

**University of Limoges**  
**ED 653 - Sciences et Ingénierie (SI)**  
**Laboratory XLIM – UMR CNRS 7252**

A thesis submitted to University of Limoges  
in partial fulfillment of the requirements of the degree of  
**Doctor of Philosophy**  
High-frequency electronics, photonics and systems

Presented and defended by  
**Ricardo CARRIZALES JUAREZ**

On January 10, 2024

**Radiation pattern reconfigurable antennas based on Phase Change  
Materials (PCM) integration**

Thesis supervisors: Priscillia DAQUIN, Laure HUITEMA, Aurelian CRUNTEANU

**JURY:**

**Reporters**

M. Philippe Ferrari, PR, TIMA - Université Grenoble Alpes  
M. Fabien Ferrero, PR, LEAT - Nice Université Cote d'Azur

**Examiners**

Mme. Anne-Claude Tarot, MCF, IETR- Université de Rennes  
M. Thierry Monédière, PR XLIM- Université de Limoges  
Mme. Daquin Priscillia, Dr. Ing, Centre National d'Etudes Spatiales- CNES Toulouse  
Mme. Laure Huitema, MCF, XLIM- Université de Limoges  
M. Aurelian Crunteanu, DR-CNRS XLIM- CNRS/ Université de Limoges



To all the people who accompanied, taught me, encouraged me, supported me, and trusted me through what was the best and most important three years of my life. Hopefully, one day, I will be able to give back everything you gave me.

*“Some might say they don’t believe in heaven.  
Go and tell it to the man who lives in hell”.*  
**Oasis00, “Some might say”, 1995**

## **Acknowledgments**

---

The author would like to thank the French National Center for Spatial Studies (CNES) and the University of Limoges for their support in this work and for the many opportunities for personal and professional development.

## Rights

---

This creation is available under a Creative Commons contract:  
« **Attribution-Non Commercial-No Derivatives 4.0 International** »  
online at <https://creativecommons.org/licenses/by-nc-nd/4.0/>



## Table of Contents

---

|  |    |
|--|----|
| Introduction .....   | 20 |
| Chapter I. Current research on reconfigurable antennas and phase change materials.....                         | 22 |
| I.1. Introduction.....   | 23 |
| I.1.1. Millimeter waves band frequencies.....  | 23 |
| I.2. The spatial context.....  | 24 |
| I.3. General characteristics of antenna devices.....   | 25 |
| I.4. Reconfigurable antennas .....   | 26 |
| I.4.1. Types of reconfiguration in antennas.....   | 27 |
| I.4.1.1. Frequency reconfiguration.....  | 27 |
| I.4.1.2. Radiation pattern reconfiguration .....   | 27 |
| I.4.1.3. Polarization reconfiguration.....   | 28 |
| I.4.2. Reconfiguration techniques .....  | 28 |
| I.4.2.1. Mechanical- based reconfiguration.....  | 28 |
| I.4.2.2. Pin-Diodes .....  | 30 |
| I.4.2.3. RF-MEMS devices .....   | 33 |
| I.4.2.4. Varactor diodes.....  | 34 |
| I.4.2.5. Ferroelectric materials.....  | 36 |
| I.4.2.6. Phase Transition Materials (PTM).....   | 37 |
| I.4.2.7. Summary of reconfigurable solutions .....   | 38 |
| I.5. Phase Change Materials (PCM) and applications .....   | 39 |
| I.5.1. General properties of chalcogenides PCMs.....   | 40 |
| I.5.2. Transformation mechanisms of PCMs.....  | 41 |
| I.5.3. Current technological uses of PCMs.....   | 45 |
| I.5.4. Particular examples of PCM compositions.....  | 46 |
| I.5.4.1. Germanium Telluride (GeTe) .....  | 47 |
| I.5.4.2. Germanium Antimonium Telluride (GeSbTe) composition.....  | 50 |
| I.5.5. PCM applications in radiofrequency circuits.....  | 52 |
| I.6. Conclusions .....   | 60 |
| Chapter II. Characterization and optical modification of the state of phase change materials (PCM).....        | 62 |
| II.1. Introduction .....   | 63 |
| II.2. Fabrication of thin PCM layers .....   | 63 |
| II.3. Electrical characterization and phase change of PCMs.....  | 65 |
| II.3.1. Phase change by direct heating.....  | 65 |
| II.3.2. Conductivity in both insulating and conductive states of GeTe and Sb <sub>2</sub> Te .....             | 66 |
| II.3.3. Stability tests of the amorphous phase in PCMs.....  | 67 |
| II.3.3.1. Activation energy and Arrhenius law .....  | 68 |
| II.3.3.2. Stability time and activation energy of GeTe and Sb <sub>2</sub> Te compositions .....               | 68 |
| II.4. Dielectric permittivity characterization of thin layers of PCM.....                                      | 70 |
| II.4.1. Methodology for the characterization of thin layers of PCM .....                                       | 71 |
| II.4.1.1. Stub resonator frequency method .....  | 72 |
| II.4.1.2. Transmission line method .....   | 73 |
| II.4.1.3. Extraction of the permittivity of the PCM layer from the effective permittivity of the CPW line..... | 77 |

|  |     |
|--|-----|
| II.4.1.4. Extraction of the loss tangent of PCM layers from the total losses of the CPW line.....                                      | 78  |
| II.4.2. Device Fabrication and measurements.....   | 78  |
| II.4.3. Extraction of PCM layers permittivity .....  | 81  |
| II.4.3.1. Resonators analysis.....   | 81  |
| II.4.3.2. Transmission line analysis .....   | 82  |
| II.4.3.3. Results synthesis and discussions .....  | 86  |
| II.5. Optical activation of the phase change in PCMs layers .....  | 86  |
| II.5.1. Optical characterization of PCMs.....  | 88  |
| II.5.1.1. Spectroscopic ellipsometry.....  | 88  |
| II.5.1.2. Optical parameters of GeTe .....   | 89  |
| II.5.2. Electromagnetic heating of PCMs using multi-physics simulations (COMSOL)....   | 90  |
| II.5.3. Optical irradiation system of PCM layers .....   | 98  |
| II.5.3.1. Laser characterization.....  | 100 |
| II.5.4. Crystallization GeTe layers by laser irradiation .....   | 102 |
| II.5.5. Amorphization of crystalline layers of GeTe by laser irradiation .....   | 106 |
| II.5.6. Arbitrary pattern written and erasing using the laser scanning system.....   | 107 |
| II.5.7. Evaluation of the quality of the optically crystallized areas.....   | 109 |
| II.6. Conclusions .....  | 111 |
| Chapter III. Design, optimization, and fabrication of a multi-reconfigurable array of antennas integrating phase change materials..... | 113 |
| III.1. Introduction .....  | 114 |
| III.2. Geometry of the antenna .....   | 114 |
| III.2.1. Material choice .....   | 115 |
| III.2.2. Performances of an array of antennas over a high permittivity superstrate and low permittivity substrate .....                | 118 |
| III.3. Numerical optimization of the antenna array .....   | 122 |
| III.3.1. Overview optimization algorithms .....  | 122 |
| III.3.1.1. Gradient-based methods.....   | 123 |
| III.3.1.2. Direct search method .....  | 125 |
| III.3.1.3. Stochastic methods.....   | 127 |
| III.3.1.4. Population methods .....  | 128 |
| III.3.2. Multi-objective optimization.....   | 130 |
| III.3.3. Selection and implementation of the optimization algorithm.....   | 132 |
| III.3.3.1. Definition of the objective functions. ....   | 134 |
| III.3.3.2. Algorithm selection.....  | 136 |
| III.3.3.3. Optimization set-up .....   | 136 |
| III.3.4. Results of the genetic algorithm run.....   | 138 |
| III.3.4.1. Selection of the solution and performance .....   | 141 |
| III.3.5. Antenna matching.....   | 144 |
| III.4. Fabrication and measurement.....  | 150 |
| III.4.1. Measure of S parameters .....   | 153 |
| III.4.1.1. Measures of S parameters on Rogers substrate .....  | 154 |
| III.4.1.2. Measures of S parameters on quartz substrate.....   | 156 |
| III.4.1.3. Summary and comparison of the measured S parameters on both substrates .....  | 157 |
| III.4.2. Far-Field measurements of the reference antennas .....  | 158 |
| III.4.3. Reconfiguration of the antenna polarization states .....  | 165 |

|                                  |     |
|----------------------------------|-----|
| III.5. Conclusions .....         | 167 |
| Conclusion and perspectives..... | 170 |
| Appendices .....                 | 174 |
| Bibliography .....               | 186 |

## List of Figures

---

|   |    |
|---|----|
| Figure 1. Applications of mmWave band frequencies. From [9].  | 24 |
| Figure 2. Attributed frequency spectrum for satellite missions with their sub-bands.  | 25 |
| Figure 3. Example of a planar rectangular antenna (microstrip antenna). a) Full view. b) Side view. Taken from [24].  | 26 |
| Figure 4. Typical distribution of the different antennas in a smartphone. Taken from [16].  | 27 |
| Figure 5. Example of a steerable beam using a linear array of antennas. From [17].  | 28 |
| Figure 6. Mechanically reconfigurable antenna with continuous tuning of the operation frequency.  | 29 |
| Figure 7. Fabrication and measure of the origami flasher antenna. a) Folding sequence to pass from the flat state to the folded state. b) Measured and simulated S-parameters in both states. c) Measured and simulated radiation pattern in both states. From [19].  | 30 |
| Figure 8. Typical electrical circuit to integrate a PIN diode into a RF circuit. a) Series configuration.   | 30 |
| Figure 9. Frequency reconfigurable antenna using PIN diodes. a) Schematic representation of the RHCP array of antennas. b) Reconfigurable band-pass filter using PIN diodes. c) Measured performances for all states. From [20].  | 31 |
| Figure 10. Radiation pattern reconfigurable SIW antenna using PIN diodes. a) Schematic representation. b) Fabricated SIW antenna with integrated diodes. c) Radiation pattern for two configurations. From [21].  | 32 |
| Figure 11. Reconfigurable pixel antenna. a) Fabricated prototype with PIN diodes. b) Measured and simulated reconfigurable resonant frequency. c) Measured and simulated reconfigurable radiation pattern. From [22].   | 32 |
| Figure 12. Typical geometry of a CPW RF-MEMS switch (Cantilever model). From [23].  | 33 |
| Figure 13. Radiation pattern reconfigurable antenna using two RF-MEMS switches. a) Schematic representation. b) Fabricated antenna with integrated RF-MEMS switches. c) Measured radiation pattern in the three states. From [25].  | 34 |
| Figure 14. Frequency rejecting reconfigurable antennas integrating varactor diodes. a) Fabricated UWB antenna (upper) and notch filter (lower) integrating varactor diodes. b) Measured and simulated $S_{11}$ performances. C) Measured and simulated gain performances. From [27].  | 35 |
| Figure 15. Frequency and polarization reconfigurable antenna integrating varactor diodes. a) Top view of the planar patch antenna integrating varactor diodes at the corners. b) Schematic representation of the whole structure. c) Measured and simulated gain performances for each state. d) Measured and simulated $S_{11}$ parameters for different voltages across the varactor diodes. From [28]. | 35 |
| Figure 16. Typical variation of the dielectric polarization in a ferroelectric material as a function of the applied electric field.  | 36 |
| Figure 17. Frequency reconfigurable antenna integrating ferroelectric capacitors. a) Schematic representation of the planar antenna and capacitors. b) Fabricated device. c)  |    |

|   |    |
|---|----|
| Close up to the ferroelectric capacitors. d) Variation of the resonant frequency as a function of the applied voltage to the capacitors. d) Variation of the gain of the antenna as a function of applied voltage. From [33].   | 36 |
| Figure 18. a) Examples of phase transition materials and the associated transition temperatures [38]. b) Variation of the normalized resistivity of a VO <sub>2</sub> film during a heating - cooling cycle [39].   | 37 |
| Figure 19. Frequency reconfigurable antenna integrating VO <sub>2</sub> for mmWave frequencies. a) Schematic representation of the antenna design. b) Fabricated device. c) Measured and simulated operation frequency in both states of the VO <sub>2</sub> switch. From [40].   | 38 |
| Figure 20. Illustration of the atomic arrangement of a a) crystalline solid and b) amorphous solid.   | 40 |
| Figure 21. Evolution of the surface resistance with temperature for different chalcogenides PCM compositions. From [42].  | 41 |
| Figure 22. Time diagram of homogeneous and heterogenous nucleation. At time t <sub>1</sub> , crystals begin to form within the material in random positions due to nucleation. At time t <sub>2</sub> , for homogenous nucleation, new crystal clusters begin to form by nucleation while the previously formed clusters grow in size. At time t <sub>3</sub> the crystal clusters have grown significantly in size while the nucleation and crystal growth continues until the whole material is crystalline. Taken from [47]. | 42 |
| Figure 23. Surface resistance evolution with temperature for different heating rates of a 90 nm thin film of a) SnSe <sub>2</sub> and b) Sn <sub>2</sub> Se <sub>3</sub> . From [46].   | 43 |
| Figure 24. Illustration showing the phase changing from a crystalline state into an amorphous state passing by a liquid state.  | 44 |
| Figure 25. Transformation temperature time (TTT) diagram showing the different state transformation of a PCM. From [48].  | 44 |
| Figure 26. a) Schematic representation of a memory PCM cell. b) Resistance of the cell as a function of programming current. c) Resistance variation as a function of number of cycles. Taken from [52].  | 45 |
| Figure 27. Schematic representation of the transformation induced by joule effect of a GeTe-based memory cell using electrical pulses. From [53].   | 46 |
| Figure 28. a) Engraving of an amorphous mark on a crystalline matrix of a PCM using a high-power laser. b) "Reading" of the encoded data by means of the reflectivity change. From [47].  | 46 |
| Figure 29. Diagram showing some of the most common (and studied) PCM compositions of the ternary Ge-Sb-Te for RF applications [33].   | 47 |
| Figure 30. Evolution of the surface resistance of a Ge-Te alloy for various compositions [62].  | 48 |
| Figure 31. Influence of the surface oxidation the evolution of the surface resistance as a function of temperature [66].  | 48 |
| Figure 32. Measured optical properties of a sample of GeTe in amorphous (as - grown) and crystalline state (250°C) [68].  | 49 |

|  |    |
|--|----|
| Figure 33. Change in reflectivity as a function of temperature for various GeTe compositions [58].   | 49 |
| Figure 34. Measured thermal conductivity of an amorphous and crystalline GeTe samples for various thickness samples. From [71].  | 50 |
| Figure 35. Crystallization time measurement of a 30-nm GeTe layer. a) Probing system using lasers. b) Crystallization time as a function of Ge percentage composition. From [72].  | 50 |
| Figure 36. Surface resistance evolution as a function of temperature for a GST composition [76].   | 51 |
| Figure 37. a) Surface resistance evolution of 80-nm thin film. b) Surface resistance evolution for a 80-nm GST thin film covered by a 4.5-nm ZnS-SiO <sub>2</sub> capping layer. From [76].  | 51 |
| Figure 38. Measured optical properties of a sample of GST in amorphous (blue trace) and crystalline state (black trace) [68].  | 52 |
| Figure 39. Measured influence of the deposition method on the optical properties of a 30-nm GST film for amorphous (as deposited) and crystalline state (annealed) [74].   | 52 |
| Figure 40. Example of a GeTe-based PCM-switch. a) Fabricated device. b) Close up to the GeTe composition. c) Schematic representation of the different layers of the circuit. From [81].   | 54 |
| Figure 41. a) Optical image of two different layouts of the PCM-based RF switch. b) S-parameters performances in both ON and OFF states from both layouts c) Switch resistance performances over 100 million cycles [78].  | 55 |
| Figure 42. a) Layout of the proposed GeTe-based RF switch. b) Measured switching time of the amorphization (left) and crystallization (right) of a GeTe-based switch 0.9 $\mu\text{m}$ length. b) Comparison of insertion loss in the ON state and isolation in the OFF state of PCM switches against other switching technologies.  | 55 |
| Figure 43. Example of fabrication process of a high-performant GeTe based PCM-switch [50].   | 56 |
| Figure 44. a) Fabricated of a simple GeTe RF-switch without heater. b) Measured performance of both states after laser irradiation for different GeTe gaps [80].   | 57 |
| Figure 45. Optically activated planar antenna integrating a GeTe composition for polarization reconfiguration. a) Fabricated device. b) Measured S <sub>11</sub> performance in all states. c) Simulated and measured realized gain in LHCP and LP state. d) Simulated and measured axial ratio in LHCP state. From [81].  | 58 |
| Figure 46. Polarization reconfigurable array of antennas integrating a GeTe composition. a) Complete geometry of the array of antennas integrating a GeTe composition. b) View of the fabricated array of antennas integrating GeTe in the amorphous state (dark gray color). c) Simulated and measured S-parameters of the LP and RHCP configurations. d) Measured and simulated gain and efficiency of the LP configuration. e) Measured and simulated axial ratio of the RHCP state. f) Measured and simulated gain and efficiency of the RHCP configuration. | 59 |
| Figure 47. a) Schematic representation of the parallel coupled half-wavelength filter b) Measured S-parameters of the filter in both states of the GeTe. c) Optical images of the filter   |    |

|   |    |
|---|----|
| integrating a GeTe pattern in the amorphous state (upper-half) and in crystalline state (lower-half). From [88].  | 60 |
| Figure 48. Evolution of the surface resistance as a function of temperature of a 250-nm, 500-nm and 1000 nm-thick layers of GeTe obtained on a c-cut (0001) sapphire substrate.   | 65 |
| Figure 49. Evolution of the surface resistance as a function of temperature of a GeTe, GST and Sb <sub>2</sub> Te PCM compositions obtained on a c-cut (0001) sapphire substrate.   | 66 |
| Figure 50. Optical images of a 250-nm layer of GeTe deposited over a 25x25 mm <sup>2</sup> sapphire substrate in a) amorphous state and b) crystalline state.   | 66 |
| Figure 51. a) Schematic representation of the 4-point probe technique to extract the conductivity of thin films. b) Measurement system employed to measure the conductivity of the film.  | 66 |
| Figure 52. Evolution of the surface resistance of a 250-nm thick layer of GeTe (using a new GeTe target) as a function of the temperature.  | 69 |
| Figure 53. a). Stress acceleration test on three samples of GeTe deposited on a sapphire substrate.   | 69 |
| Figure 54. a). Stress acceleration test on three samples of Sb <sub>2</sub> Te deposited on a sapphire substrate.   | 70 |
| Figure 55. a) Design of mmW-band stub resonators without a PCM (up) and integrating a PCM pattern (down). b) Example of a CPW line fabricated on an alumina substrate (left) and on a PCM/ alumina layer (right).   | 71 |
| Figure 56. a) Cross-section of the geometry of a CPW in a bare substrate. b) Cross-section of the geometry of a CPW integrating a PCM thin film on a substrate.   | 72 |
| Figure 57. a) Simulation of the variation of the stub's resonant frequency as a function of the permittivity of the GeTe layer. b) Simulation of the variation of the resonant frequency of the stub as a function of the GeTe layer thickness.                         | 73 |
| Figure 58. Transmission lines geometry for the standards "Thru" (left) and "Line" (right) for the TRL method.   | 74 |
| Figure 59. a) CPW lines fabricated over a layer of alumina (to the left) and over a layer of GeTe/alumina (to the right). b) Stub resonators fabricated over a layer of alumina (to the right) and a layer of GeTe/alumina (to the left).                               | 79 |
| Figure 60. Complete image of the all the fabricated CPW lines over a layer of alumina (upper left) and over a layer of GeTe/alumina (upper right) and all the fabricated stub resonators with and without a layer of GeTe (the bonding of the resonators is not shown). | 79 |
| Figure 61. Image of the test system used to measure the RF performance of all samples (VNA- vector network analyzer, DUT-device under test).  | 80 |
| Figure 62. a) Fabricated quarter-wavelength stub resonator on a sapphire substrate with a 500-nm thick GeTe pattern at the end of the resonator. b) Measured transmission of the resonator at both states of the GeTe pattern.  | 80 |
| Figure 63. a) 3D electromagnetic model of an open-circuit stub resonator integrating a thin line of GeTe and bonding wire over an alumina substrate. b) Tetrahedral mesh of the stub resonator.   | 81 |

|  |    |
|--|----|
| Figure 64. Measured $S_{21}$ parameter of a stub resonator with length of 1.3 mm showing clear changes in the parallel resonant frequency due to the addition of a 500-nm thick layer of GeTe. ....  | 81 |
| Figure 65. a) Measured $S_{21}$ parameters of all the CPW lines fabricated on an alumina substrate integrating a thin layer of a 500-nm thick GeTe (sample 2) and b) similar parameters of the CPW lines fabricated on a $\text{SiO}_2$ substrate integrating a thin layer of a 800-nm thick GeTe (sample 3). ....     | 83 |
| Figure 66. a) Measured $S_{21}$ parameters of the $L_6$ line in sample 2 (alumina substrate) with a thin layer of GeTe before and after post-processing filter and b) similar result for the $L_6$ CPW line with a thin layer of GeTe on sample 3 ( $\text{SiO}_2$ substrate). ....                                    | 83 |
| Figure 67. a) Comparison of the mean effective permittivity values extracted using the TRL method from the fabricated CPW lines on an alumina substrate, with and without a GeTe layer of 800 nm (sample 2). b) Comparison of the mean effective permittivity, with and without a GST layer of 800 nm (sample 4). .... | 84 |
| Figure 68. a) Mean and dispersion values of the extracted permittivity of GeTe using the analytical method for all samples integrating GeTe (samples 1 to 3). b) Mean and dispersion values of the extracted GST permittivity using the analytical method. ....  | 85 |
| Figure 69. a) Comparison of the mean losses values extracted using the TRL method from a fabricated transmission line on alumina substrate with and without a GeTe layer of 800 nm (sample 2) and, b) for a fabricated transmission line on alumina substrate with and without a GST layer of 800 nm (sample 4). ....  | 85 |
| Figure 70. a) Mean and dispersion values of the extracted loss tangent of the GeTe from sample 2 and, b) of the GST from sample 4. ....  | 86 |
| Figure 71. a) Schematic representation of an incident and reflected beam into a sample with a thin film. b) Change in the polarization state of an incoming light-wave after being reflected by a sample. ....   | 88 |
| Figure 72. a) Measured reflectance of two samples of GeTe over a sapphire substrate. b) Extracted refractive index and extinction coefficient for the 197-nm thick sample. ....  | 90 |
| Figure 73. a) COMSOL geometry of a PCM (GeTe) layer over a sapphire substrate. b) Spatial distribution of the laser beam. C) 2D heating profile of a 1- $\mu\text{m}$ thick GeTe sample. ...   | 94 |
| Figure 74. Simulation results of the evolution of the surface temperature in a 1- $\mu\text{m}$ thick layer of GeTe for multiple wavelengths with energy density of 10 $\text{mJ}/\text{cm}^2$ . The temporal profile of the 9-ns laser pulse is shown in the black trace. ....  | 94 |
| Figure 75. a) Temperature distribution over the surface of the GeTe layer at the time of peak temperature for different wavelengths (the violet shaded area represents the laser beam radius). ....  | 95 |
| Figure 76. a) Amorphous-to-crystalline state variable distribution over the surface of the GeTe layer at the end of the simulation. b) State variable distribution in the depth of the GeTe layer at the end of the simulation. (S = 0 for crystalline GeTe and S = 1 for amorphous state). ....                       | 96 |
| Figure 77. a) State variable distribution over the depth of the GeTe layer for different energy densities for $\lambda = 532 \text{ nm}$ . b) State variable distribution over the surface of the GeTe layer for   |    |

|   |     |
|---|-----|
| different energy densities for $\lambda = 532$ nm. (S = 0 for crystalline GeTe and S = 1 for amorphous state). .....  | 96  |
| Figure 78. Surface temperature evolution of the GeTe film over time for multiple energy densities. ....   | 96  |
| Figure 79. Simulation results of the surface temperature evolution at the center of the irradiated area for three different thickness of the GeTe layer deposited over a sapphire substrate. ....   | 97  |
| Figure 80. Temperature distribution inside the GeTe layer at the time of peak temperature at its surface for a green laser ( $\lambda = 532$ nm) and a fluence of $10 \text{ mJ/cm}^2$ , for a) 200-nm thick layer and .....  | 97  |
| Figure 81. Diagram of the complete optical irradiation set-up. ....   | 98  |
| Figure 82. Solid-state pulsed laser system working at 532 nm wavelength.....  | 98  |
| Figure 83. a) Functioning principle of the SCAN Lab system. b) Positioning and image field of the SCAN Lab system. c) Optical scanner system (SCAN Lab) with variable focus system (Vario Scan) in order to change to focus plane of the scanner and change the size of the laser spot..... | 99  |
| Figure 84. a) Principal workspace of the SCANLab software. b) Laser properties for the marking of the shapes. c) Laser control and automation of the marking process. ....  | 100 |
| Figure 85. Schematic representation of the VarioScan system. ....   | 100 |
| Figure 86. a) Average power of the laser measured over the whole frequency range. b) Average energy of the laser measured up to 200 Hz. ....  | 101 |
| Figure 87. Measured temporal pulse shape of the pulsed laser source in the a) linear region and, .....  | 102 |
| Figure 88. Crystallized area by a single 480- $\mu\text{J}$ laser pulse on a 500-nm thick GeTe layer deposited over a sapphire substrate. ....  | 102 |
| Figure 89. Crystallized zones by raster scanning with laser beam positioning speed of 1 mm/s for different laser repetition rates, at frequencies of a) 10 Hz. b) 100 Hz, c) 500 Hz and d) 1000 Hz.....   | 103 |
| Figure 90. a) Variable attenuator with beam dump. b) Normalize power transmission as a function of the half-wave plate angle position. ....   | 104 |
| Figure 91. Crystallized zone of a 250-nm thick GeTe layer for a laser power attenuation factor of .....   | 105 |
| Figure 92. Smallest observed crystallized zone using the VarioSCAN system. ....   | 105 |
| Figure 93. Amorphized area of a 250-nm thick GeTe sample using laser irradiation of a previously crystallized zone. ....  | 106 |
| Figure 94. Evolution of the surface resistance of a GeTe layer as a function of temperature after 3 complete cycles of optical induced crystallization-amorphization. ....  | 107 |
| Figure 95. Writing and erasing procedure of arbitrary shapes in a GeTe layer. a) As-deposited 250-nm GeTe layer on a $25 \times 25 \text{ mm}^2$ sapphire substrate. b) Writing of an arbitrary shape using laser engraving (CNES logo-crystalline). c) Erasing of the previously written   |     |

|  |     |
|--|-----|
| pattern by crystallizing the whole pattern d) Amorphization of the whole written surface. e) Re-write of the CNES logo (crystalline) d) Erasing and writing of another arbitrary pattern in the surface (XLIM logo-amorphous). .....   | 108 |
| Figure 96. Thermal infrared images of the a) As deposited 250-nm thick GeTe layer. b) After engraving the CNES logo. c) After erasing the previously written CNES logo and re-writing the XLIM logo. ....  | 108 |
| Figure 97. Image of the GeTe surface layer after irradiation with a) 10 pulses at 6 kHz, b) 10 pulses at 10 kHz, c) 10 pulses at 30 kHz, and d) 10 pulses at 50 kHz. ....  | 110 |
| Figure 98. Proposed geometry of the multi-reconfigurable array of antennas. a) Layered structure of the antenna. b) Array of antennas integrating a PCM composition at the top of the superstrate. ....  | 115 |
| Figure 99. a) Measured profile of the surface of a ROGERS 4003C substrate. b) Histogram and fitted gauss bell curve. ....  | 116 |
| Figure 100. Measured histogram and fitted curve of the surface profile of a quartz substrate. ....   | 117 |
| Figure 101. Measured histogram and fitter gauss bell curve of the surface profile of an alumina substrate. ....  | 117 |
| Figure 102. Simulated magnetic field distribution on the exciter patch of the double stacked array of antennas. ....   | 119 |
| Figure 103. Surface current densities on the array antennas using an alumina superstrate for a separation of $\lambda/2.25$ . a) Magnitude of $J_y$ . b) Magnitude of $J_x$ . ....   | 120 |
| Figure 104. Surface current densities on the array antennas using an alumina superstrate for a separation of $\lambda/2$ . a) Magnitude of $J_y$ . b) Magnitude of $J_x$ . ....  | 120 |
| Figure 105. Surface current densities on the array antennas using an alumina superstrate for a separation of $\lambda/3$ . a) Magnitude of $J_y$ . b) Magnitude of $J_x$ . ....  | 120 |
| Figure 106. Array of antenna integrating GeTe with asymmetric trimmed edges. ....  | 122 |
| Figure 107. Example of gradient descent method to find the minimum value on the Rosenbrock function. Each number represents an iteration. Adapted from [141]. ....   | 124 |
| Figure 108. Performance of a gradient descent method for multiple starting points. Adapted from [143]. ....  | 125 |
| Figure 109. Working principle of the Hookes-Jeeves method (adapted from [141]). a) Staring point and equally distributed neighbor points. b) New starting point with new neighbor points. c) New starting point with no best candidate solution. d) Same starting point as the previous one with a new step size. .... | 126 |
| Figure 110. Diagram showing the working principle of a genetic algorithm. ....   | 129 |
| Figure 111. Working principle of a swarm particle optimization applied to a Wheelers ridge function (Adapted from [141]). a) Initial distribution of the population and exploration of the searching space. ....   | 130 |
| Figure 112. Graphical representation of a pareto frontier of the solution space for a two-objective optimization. ....   | 132 |

|  |     |
|--|-----|
| Figure 113. Final geometry of the array of antennas to be optimized. a) Layered structure of the antenna. b) Array of antennas integrating a PCM composition at the top of the superstrate. c) Exciter patch in between the two layers. d) Ground plane and PCM filled coupling slot at the bottom of the substrate. ....  | 133 |
| Figure 114. Evolution and moving average of a) $f_1(x)$ and b) $f_2(x)$ .....  | 139 |
| Figure 115. a) Solution space of the optimization algorithm. b) Pareto front after 24 generations. ....  | 140 |
| Figure 116. Evolution of the moving average of the free variables. a) Size of the trimmed edges. ....  | 140 |
| Figure 117. Evolution of the a) directivity and b) adaptation level of the array of antennas. ....   | 141 |
| Figure 118. Simulated axial ratio at four cuts on the $\Phi$ plane for the current best configuration.....   | 143 |
| Figure 119. Simulated directivity at four cuts on the $\Phi$ plane for the current best configuration.....   | 143 |
| Figure 120. Simulated broadband performances of both CP configurations. The green rectangle corresponds to the frequency range where the AR of both circular polarizations is lower than 3dB. ....   | 144 |
| Figure 121. De-embedded matching characteristics of the selected antenna. ....   | 145 |
| Figure 122. a) Model of an impedance step change. b) Model of a smooth change in impedance using a taper line.....   | 145 |
| Figure 123. Proposed geometry for matching the antenna using two triangular taper lines a) Full view of the model. b) Dimensions of the CPW at the slot window plane integrating amorphous GeTe to obtain frequency reconfiguration. c) Dimensions of the CPW at the transition between the first and second triangular taper line. d) Dimensions of the 50 $\Omega$ input feeding line of the antenna. .... | 146 |
| Figure 124. S-parameters of the antenna using two triangular tapered transmission lines as simulated in CST-Microwave for a $L_w = 0.6$ mm.....  | 148 |
| Figure 125. Simulated behavior of input impedance of the matched antenna using the proposed matching network in for a $L_w = 0.6$ mm. ....   | 148 |
| Figure 126. Performance of the adaptation level of the RHCP configuration (solid lines) and the LHCP configuration (dashed lines) circularly polarized configuration as the effective length of the slot is changed. ....  | 148 |
| Figure 127. Performance of the far-field properties of the RHCP configuration (solid lines) and the LHCP configuration (dashed lines) as the effective length of the slot is changed. a) Directivity in the axis. b) Axial ratio in the axis. ....   | 149 |
| Figure 128. Performance linearly polarized configuration as the effective length of the slot is changed when all GeTe edges are in the crystalline state (dashed lines) and all the GeTe edges are in the amorphous state (solid lines). A) S-parameters b) Directivity. ....  | 150 |
| Figure 129. Simulated influence on the evolution of the matching properties of devices as a function of a) The thickness of the glue and, b) the permittivity of the glue layer.....   | 151 |

|   |     |
|---|-----|
| Figure 130. Fabricated antenna. a) Array of antennas integrating amorphous GeTe at the top of the alumina substrate. b) Exciter antenna at the top of the ROGERS 4003C substrate (The dark dot at the bottom right is an ink marker for orientation purposes). c) Ground planes, input transmission line and slot window integrating amorphous GeTe. .... | 152 |
| Figure 131. Fabricated full metallic array of antennas. a) RHCP array. b) LHCP array. ....  | 152 |
| Figure 132. Fabricated ground plane over a ROGERS 4003C substrate with an empty slot of 1.1 mm length. The darker region at the bottom is part of the glue that overflow during the bonding process and could not be removed. ....  | 153 |
| Figure 133. Fabricated antenna using a quartz substrate. a) Exciter antenna at the top of the substrate. b) Ground plane, input transmission line and slot window integrating amorphous GeTe. ....  | 153 |
| Figure 134. Image of the compact test range system used to measure the RF performance (matching and radiation) of the antenna under test (AUT). ....  | 154 |
| Figure 135. Measured matching performance of an array of antennas with a ROGERS 4003C substrate and a ground plane with a slot window of a) 2.4 mm length and, b) 1.1 mm length. ....   | 155 |
| Figure 136. Measured and simulated matching performance of full-metallic RHCP array of antennas with a ROGERS 4003C substrate and a ground plane with a slot window of a) 2.4 mm length and,.....   | 155 |
| Figure 137. Comparison of the measured matching performance of the three states of polarization with a ROGERS 4003C substrate.....  | 156 |
| Figure 138. Measured and simulated matching performance of an array of antennas fabricated with a quartz substrate and a ground plane with a slot window of a) 2.4 mm length and, b) 1.1 mm length.....   | 156 |
| Figure 139. Measured matching performance of a full-metallic RHCP array of antennas with a quartz substrate and a ground plane with a slot window of a) 2.4 mm length and, b) 1.1 mm length. ....   | 157 |
| Figure 140. Comparison of the measured matching performance of the three states of polarization with a quartz substrate with a ground plane with a slot window of $L_w = 2.4$ mm. ....  | 157 |
| Figure 141. Comparison of the measured matching performance with a ROGERS 4003C and quartz substrates for the a) linearly polarized antenna (all edges amorphous) and, b) Full-metal RHCP array. ....   | 158 |
| Figure 142. Simulated influence of the metal conductivity in the S-parameters of the RHCP antenna. ....   | 158 |
| Figure 143. Measured maximal directivity, axial ratio and matching level of a full-metal RHCP and LHCP configuration and LP (with all edges in amorphous state) with a ROGERS 4003C substrate. ....   | 159 |
| Figure 144. Measured realized gain and total efficiency of the full-metallic reference antennas. ....   | 160 |
| Figure 145. Measured directivity of the LP (all GeTe edges in amorphous state) array of antenna at 29.6 GHz. a) Full picture. b) Directivity at planes $\varphi = 0, 45, 90$ and $135^\circ$ . ....   | 160 |

|   |     |
|---|-----|
| Figure 146. Measured directivity of a full-metal LHCP array of antennas at 29.6 GHz. a) Full picture. ....  | 161 |
| Figure 147. Measured directivity of a full-metal RHCP array of antennas at 29.6 GHz. a) Full picture. ....  | 161 |
| Figure 148. Measured axial ratio of a full-metal RHCP array of antennas at 30 GHz. a) Full picture. ....  | 162 |
| Figure 149. Measured axial ratio of a full-metal RHCP array of antennas at 30.4 GHz. a) Full picture. b) At planes $\varphi = 0, 45, 90$ and $135^\circ$ . ....   | 162 |
| Figure 150. Measured axial ratio of a full-metal RHCP array of antennas at 29.6 GHz. a) Full picture. b) At planes $\varphi = 0, 45, 90$ and $135^\circ$ . ....   | 163 |
| Figure 151. Measured axial ratio of a full-metal LHCP array of antennas at $f = 30$ GHz. a) Full picture. b) At planes $\varphi = 0, 45, 90$ and $135^\circ$ . ....   | 163 |
| Figure 152. Measured axial ratio of a full-metal LHCP array of antennas at 30.4 GHz. a) Full picture. ....  | 164 |
| Figure 153. Measured axial ratio of a full-metal LHCP array of antennas at 29.6 GHz. a) Full picture. ....  | 164 |
| Figure 154. Optical image of the irradiated GeTe edge of the array of antennas. The black features are the out-of-focus probes. ....  | 165 |
| Figure 155. Examples of the new fabricated array of antennas using a lift-off technique. ...  | 166 |
| Figure 156. Measured far-field performances of the array of antennas after optical irradiation (as shown in Figure 155). a) Axial ratio in the axis and, b) Maximal directivity. ....                           | 166 |
| Figure 157. Simulation of the perturbation effect on the axial ratio of a RHCP antenna from a misalignment of the GeTe pattern. a) Geometry of the perturbation. b) Simulated axial ratio. ....                 | 167 |
| Figure 158. Measured far-field performances of the array of antenna shown in Figure 155 after crystallizing the remaining amorphous GeTe patterns. a) Axial ratio in the axis and, b) Maximal directivity. .... | 167 |
| Figure 159. Equivalent RLC electrical model of a patch antenna. ....  | 175 |
| Figure 160. Evolution of the input impedance of a parallel RLC circuit as a function of frequency. ....   | 175 |
| Figure 161. Evolution of the radiation efficiency and fractional bandwidth of an antenna as a function of the thickness of the substrate. Adapted from [12]. ....   | 177 |
| Figure 162. Geometrical representation of the space surrounding an antenna. ....  | 177 |
| Figure 163. Normalized radiation pattern of a patch antenna. ....   | 179 |
| Figure 164. Polarization ellipse. Adapted from [11]. ....   | 180 |
| Figure 165. Equivalent circuit representation of the coplanar waveguide shown in Figure 56. ....  | 183 |

## List of Tables

---

|  |     |
|--|-----|
| Table 1. Summary of the advantages and disadvantages of different technologies for reconfigurable antennas. ....   | 39  |
| Table 2. Parameters for the deposition of thin layers of GeTe using DC magnetron sputtering. ....  | 64  |
| Table 3. Measured conductivity in both states (amorphous and crystalline) of three samples of GeTe deposited over a sapphire substrate. ....   | 67  |
| Table 4. Measured conductivity in both states (amorphous and crystalline) of two samples of Sb <sub>2</sub> Te deposited over a sapphire substrate. ....   | 67  |
| Table 5. Comparison of the extracted permittivity of the GeTe using the analytical method and 3D electromagnetic simulations using CST microwave studio for all resonators corresponding to sample 1 (alumina substrate, 500-nm thick GeTe layer)..... | 82  |
| Table 6. Mean values of the GeTe and GST permittivities extracted from the entire sets of stub resonators, for all samples. ....   | 82  |
| Table 7. Comparison of the extracted permittivity of the GeTe for the CPW lines of sample 2 (800-nm thick GeTe on alumina substrate) using the analytical method and the 3D electromagnetic simulation. ....   | 84  |
| Table 8. Mean value of the extracted permittivity of the GeTe and GST of all fabricated samples using the analytical method. ....  | 84  |
| Table 9. Thermal parameters of a GeTe layer in amorphous and crystalline state.....  | 93  |
| Table 10. Laser pulse parameters for simulation using COMSOL.....  | 93  |
| Table 11. Deduced pulse energy from the measured average power of the pulsed laser. .  | 101 |
| Table 12. Recorded size of the crystallized zone for different focal point distances. ....   | 105 |
| Table 13. Surface resistance of the GeTe layer after optical transformation between the two states. ....   | 106 |
| Table 14. Recorded surface resistance for different frequencies (i.e different pulse energies) and number of pulses. ....  | 109 |
| Table 15. Recorded surface resistance for different focal distance points at 6 kHz.....  | 110 |
| Table 16. Desired performance of the antenna array integrating a PCM.....  | 114 |
| Table 17. Relevant electrical and thermal properties of different candidate substrates for an antenna integrating PCM.....   | 116 |
| Table 18. Parameters of the antennas in the array and the thickness of substrate. ....   | 119 |
| Table 19. Free variables for the design of the antenna and their respective ranges. ....   | 133 |
| Table 20. Acceptable solutions for the array of antennas taken from the pareto front.....  | 142 |
| Table 21. Final dimensions of the array of antennas.....   | 147 |
| Table 22. Final dimensions of the proposed matching line. ....   | 147 |

## Introduction

---

The next-generation RF systems (5G and beyond) will face increasing challenges in their performances, such as higher data rates, low latency, higher reliability, higher spectrum efficiency, even lower power consumption and low-cost implementation. In the case of future 5G front-ends, one way to achieve higher data rates is to span the allocated telecommunication frequencies toward the millimeter-wave (mmWave) spectrum (frequencies around and greater than 27 GHz) where more bandwidth is available. However, moving up to higher frequencies implies additional problems like higher atmospheric attenuation and diffraction. Therefore, the next-generation telecommunication systems will need a reconfiguration capability of their front-end constituents (filters, antennas, amplifiers) to optimize their performances at these frequency bands.

Current solutions for realizing reconfigurable antennas or filters employ semiconductor-based devices (PIN diodes, FET transistors...), functional materials such as ferroelectrics, ferrites or MEMS devices. However, the performances of these devices are severely degraded or they are not adapted at millimeter wave frequencies due to higher power losses, switching speed and power consumption. Lately, a new reconfiguration paradigm have been proposed based on the use of agile materials like phase transition materials (PTM) and phase change materials (PCM). Phase change materials are materials that present a drastic change in their physical properties (such as electrical conductivity, reflectivity, density, etc) with the application of a thermal stimulus by changing between two distinct and stable states: a crystalline state (alike to a metal) and an amorphous state (alike to a dielectric). As in the case of their early applications as non-volatile memory devices, the operation of these materials in the RF domain is based on the ability of PCM materials to be switched using short electrical or optical pulses between an OFF state (amorphous/ insulating state) and an ON state (crystalline/ conducting material). In particular, the high contrast in electrical resistivity between both states acts as a very efficient RF switch which has been extensively studied in the literature.

The bi-stability of RF-PCM devices is a key advantage of this technology as the switch does not require a permanent bias to be maintained in a specifically prepared state (ON or OFF). We have previously demonstrated bi-stable switching functions based on phase change materials using electrical or optical actuation, and confirmed the potential of these materials to realize more complex agile functions, such as filters or frequency reconfigurable antennas.

For the design of more complex RF functions (such as filters and antennas) integrating this type of materials, it is necessary to know their microwave dielectric properties, in each of their states. Some compositions of PCMs have already been characterized for frequencies less than 3 GHz and in the THz domain. Unfortunately, there is no available data on the electromagnetic properties of PCMs at millimeter-wave frequencies. Additionally, since the thickness of the PCM compositions obtained on substrates is in the order of hundreds of nanometers, a characterization by means of conventional techniques can be difficult at higher frequencies.

A common thread among current usages and studies of PCM properties is that they all are reporting layers with thicknesses in the tens of nanometers. Layers of this size may induce high losses at mmWave frequencies due to their very low equivalent cross-section area and due to losses associated with the skin depth. In order to mitigate these losses, thicker layers need to be used for RF systems. It was also established that the properties of PCMs can vary with the thickness, the fabrication method and the degree of purity of starting material, this

implies that a proper characterization of the dielectric performances of PCM films needs to be determined before their integration in practical devices.

As such, this thesis work will focus into three main aspects:

- The study and the electromagnetic characterization of PCM compositions with thicknesses of the order of hundreds of nanometers for RF applications.
- The optical characterization and activation using lasers for reversible switching between the amorphous and crystalline states of PCM samples.
- The integration of PCM composition for the design of a reconfigurable antenna working in the millimeter-wave frequency band.

These elements will receive in-depth exploration in the upcoming three chapters of the manuscript:

- Chapter 1 will introduce the basic notions and characteristics of reconfigurable antennas and the different current techniques employed to transform a single antenna into a reconfigurable one. In particular, reconfigurable antennas are of interest for the new generation of satellites applications, therefore the current context and trends of space technologies will be briefly discussed. Finally, the basics characteristics and theory regarding phase change materials will be introduced with emphasis on their use in high frequency systems.
- Chapter 2 is divided into two sections: the first one deals with basic properties of phase change materials such crystallization temperature and stability of some promising PCM candidates as well as their electromagnetic characterization (dielectric permittivity and loss tangent) of these materials. The second part of the chapter deals with the broadband optical characterization of PCMs by ellipsometry methods as well as the optical activation of PCM layers using a scanner system.
- Chapter 3 deals with the design, optimization, fabrication and measurement of a reconfigurable array of antennas working at millimeter-wave frequencies integrating a PCM composition.

Finally, in the conclusions of this work we will present a short summary and perspectives of the results obtained during this thesis work.

# **Chapter I. Current research on reconfigurable antennas and Phase Change Materials (PCM).**

---

## **I.1. Introduction.**

In this chapter, we will introduce the terms related to reconfigurable antennas in the millimeter-wave (mmWave) frequency band and their interest in this spectrum. We will focus on their characteristics, current applications and the strategies used for creating reconfigurable arrays of antennas.

First, the advantages and interest in the mmWave band are going to be explored and highlighted. During this thesis work we focus on the use of planar antennas; therefore, a short description of the most important descriptors of planar antenna performances is given in Appendix 1. The performances of an antenna are mostly fixed by their radiating elements geometry, therefore in order to provide antennas with reconfigurability capabilities, either the geometry of the antenna needs to be modified or the circuit to which it connects needs to be changed. There exist many strategies in order to provide them with reconfigurable capabilities and some of the most common ones are going to be explored in this chapter. However, all the solutions for reconfigurability presents some inconveniences that are not negligible, especially for high frequency telecommunications.

In order to counter some of these drawbacks, new solutions and design strategies have been proposed and studied. One of the most recent and interesting solutions is the use of phase change materials whose performances have been shown to be very satisfactory for high-frequency systems. In particular, their ease of integration and non-volatile nature make them very attractive for mmWave band frequencies and beyond (up to THz systems). A subchapter will be dedicated to their basic physical properties as well as theoretical studies on their nature, finalizing with their current application and performances in RF systems.

### **I.1.1. Millimeter waves band frequencies**

The exponential increase of connected systems together with the increasing demand for higher data rates and faster information transmission is saturating the currently-available radiofrequency bands [1] [2] [3]. The next-generation RF systems (5G and beyond) will face increasing challenges in their performances, such as higher data rates, low latency, higher reliability, higher spectrum efficiency, even lower power consumption and low-cost implementation. For future 5G front-ends, one way to achieve higher data rates is to migrate the allocated telecommunication frequencies toward the millimeter-wave band (frequencies greater than 27 GHz) where more bandwidth is available [4] and opens the door for enhancing current applications as well as providing new services as shown in Figure 1.

However, moving up to higher frequencies implies additional problems related to the propagation on the electromagnetic (EM) waves within the atmosphere. The conditions of the atmosphere (temperature, rain, humidity, foliage, etc) can significantly impact the propagation of the EM waves, resulting in power losses due to increased attenuation [5] [3]. In particular: the presence of rain and rain rate can significantly degrade the communication due to higher attenuations at mmWave band frequencies [6], clouds can increase the attenuation factor which is specially detrimental for satellite communications [3], water vapor and the presence of other molecules (CO<sub>2</sub>, N<sub>2</sub>, O<sub>2</sub>, etc) in the atmosphere also introduces losses to the EM propagation [7] [8].

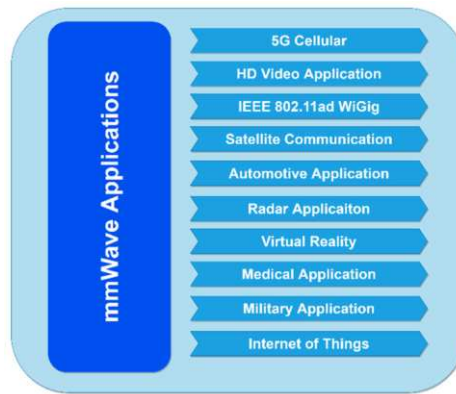


Figure 1. Applications of mmWave band frequencies. From [9].

A common characteristic between all previously mentioned points is that all of these phenomena are weather related thus unavoidable and intermittent in nature that need to be accurately predicted. In order to compensate for these detriments, the next-generation of mmWave telecommunication systems will need a reconfiguration capability of their front-end constituents to optimize their performances at these frequencies during these conditions. For example, amplifiers will need to increase their amplification level in order to compensate for the massive losses in power, antennas will need to be highly directional with beam-forming capabilities [10] and, preferably, multiband operation.

## 1.2. The spatial context

The space era started in 1957 with the launch of the first ever artificial satellite: the Sputnik. Subsequently, the first ever commercial use of satellites was with the geostationary satellite INTELSAT 1 (also called Early Bird) enabling instant communication links between any part of the Earth. Nowadays, the impact of satellites in the day-to-day life of humanity is undeniable. The original intention of satellites was only to establish very long communication links across the Earth. However, their limited performances, huge cost (construction plus launching), short lifetime and low capacity resulted in a significant high cost per telephone channel and a low reliability. Additionally, it was necessary the use of earth stations equipped with very large parabolic antennas in order to establish a link between the satellite and the earth [11].

Satellite systems work in the microwave bandwidth spectrum (1 GHz – 40 GHz) as shown in Figure 2. This spectrum is subdivided into multiple bands depending on the mission of the satellite, for example, the L band is mostly attributed for GPS (Global Positioning System) while the S band is mostly used for meteorological radars, etc. In particular, the mmWave band frequencies are a key component for the development and improvement of the current satellite communication technologies due the possibility of higher frequencies and bandwidths allowing for faster communications and a lower latency [12] [13] [14]. In addition, the use of higher frequencies implies the use of smaller antennas and therefore lower weights which reduces the cost of satellite systems.

The potential given by satellites resulted in massive investments and technological advancements as now satellites are an important key enabler for many irreplaceable technologies such as the global positioning system (GPS) or the global navigation satellite system (GNSS) [13], [15], earth observation and climate change study [16], broadcast television, global mobile communications and global internet access [17], [18], universe exploration and scientific research, etc. However, there are still several inconveniences and

obstacles limiting the use of satellite systems such a very high initial cost, considerable launching failures, limited coverage, atmospheric perturbations and low flexibility. However, these obstacles are being overcome with great success due to many new technologies such as massive satellite constellations with small satellites [19] and improved algorithms [20], reusable rockets [21], ultra directive and beam steering antennas [22], high-throughput satellites (HTS) [12], etc.

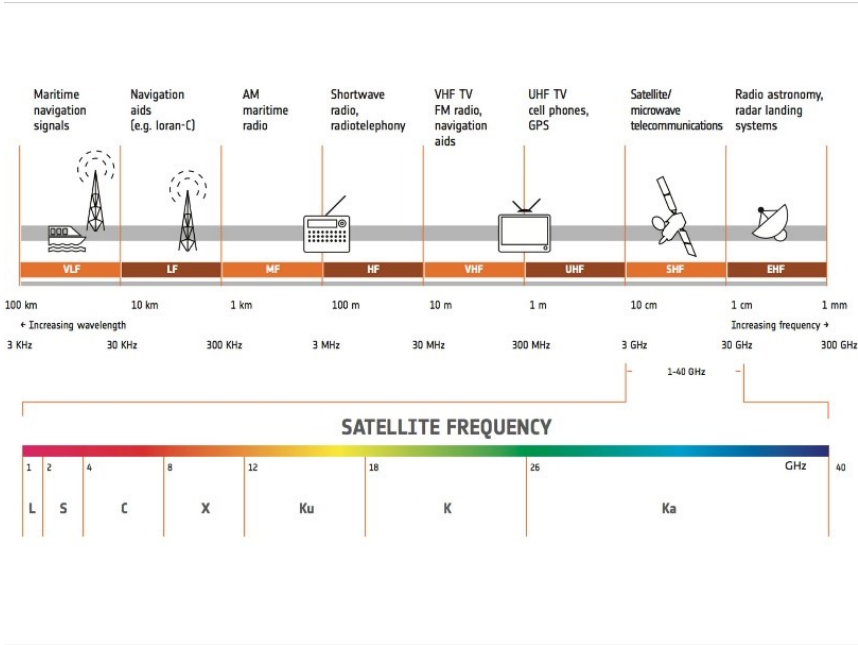


Figure 2. Attributed frequency spectrum for satellite missions with their sub-bands.

The growth of space related technology is expected to continue growing. Today, communication satellites represents a market value of \$77.1B [14] and is expected to growth higher than \$150B for 2030 due to ever higher demands of high-quality audio, image and video, lower latency, real time information (traffic, weather forecast, navigation), IOT (internet of things) for massive connectivity [23], etc. These services, together with the continuously growing facility of launching satellites (less risk and lower prices), open the way for a new kind of business and economic framework called “New Space”.

**I.3. General characteristics of antenna devices**

In order to receive and send wireless information by means of electromagnetic waves, electronic devices require antennas serving as an interface between the circuit that processes the information and the free space where the EM wave propagates. There exist many types of antennas, each one with its own advantages and disadvantages. The specialized literature is reporting many categories of antennas but most of them fall under one of the following classifications:

- **Wire antennas:** This category corresponds to antennas that are made of metallic wires or tubes. Examples include dipoles, loop antennas, Yagi-Uda arrays, etc. They are mostly used for their simplicity, low cost, and lightweight. They find most of their applications in low-frequency regimes.
- **Aperture antennas:** This category corresponds to open-ended metallic waveguides which include square or circular horns. These kinds of antennas are mostly used for

aircraft as well as spacecraft due to their ability to be easily mounted into the chassis of the device and also due to their good performances in high frequencies.

- **Reflector antennas:** These types of antennas consist of a radiator element and a metallic reflector in order to focus and redirect electromagnetic energy. The most common example is the parabolic reflector antenna. Reflector antennas can be used to send and receive information that has traveled from millions of kilometers thus very useful for long-range communication as well as satellite communications and space exploration.
- **Planar antennas (printed antennas):** These kinds of antennas correspond to metallic patterns on a substrate with a ground plane. These antennas are very low profile, very versatile in terms of geometry, and easy to integrate and fabricate on printed circuits, thus almost universally present in consumer electronics (such as cellphones).

Most of the time, a single antenna is not enough to meet the requirements imposed by the system thus an association of antennas can be used in order to improve certain properties such as range, bandwidth and overall efficiency. This association of antennas is referred as an “Array of antennas”.

In our work, we will favor the use of planar antennas due to the integration facility of phase change materials (PCM) as thin layers and the capability to fabricate them using the clean room facilities of XLIM laboratory. On the Figure 3 is shown a model of a typical rectangular microstrip patch antenna. The fundamental theory of antennas is explained in Appendix 1 in which we introduce the most important aspects and parameters of antennas in general with a focus on planar antennas (although most of the discussion can be applied to any type of antenna).

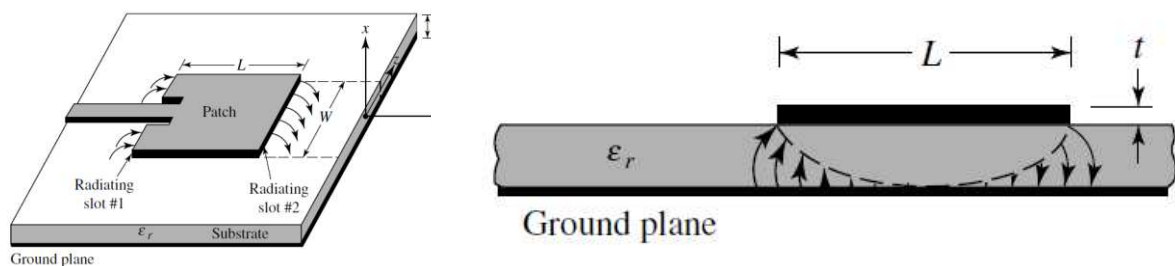


Figure 3. Example of a planar rectangular antenna (microstrip antenna). a) Full view. b) Side view. Taken from [24].

#### I.4. Reconfigurable antennas

Reconfiguration refers to the capability of a circuit to dynamically change one or more of its characteristics as a function of the operational requirements or the context in which the device is used. This characteristic allows the device to incorporate multiple functionalities or to optimize its performances in operando, as needed. In the case of antennas, the reconfiguration capabilities can be divided into three categories, according to the desired reconfigurable characteristics: operation frequency, polarization state, and radiation pattern.

## I.4.1. Types of reconfiguration in antennas

### I.4.1.1. Frequency reconfiguration

The interest in frequency reconfiguration lies in the fact that a single antenna would be used to cover multiple frequency bands and thus, multiple communication standards. For example, current cell-phones use multiple communication standards for different purposes such as Wi-Fi for internet connection, Bluetooth for data sharing and wireless connection, NFC for short-distance communication between smartphones, GPS for global positioning, cellular antennas for different communication standards (3G, 4G, 5G...), etc. Each one of these standards is regulated and confined to a particular frequency usage (Wi-Fi and Bluetooth at 2.45 GHz, GPS at 1.75 GHz, etc) and therefore requires a different antenna to access the particular frequency. The Figure 4 shows a typical example of the distribution of antennas within a smartphone. As observed, the need of multiple antennas implies a much greater surface space in order to accommodate all of them (without interfering), thus requiring larger devices. A set of frequency reconfigurable antennas can be of advantage for regrouping most of the communication standards into limited number of single antennas with reconfiguration capabilities, thus reducing their overall number. This reduces the complexity of the system as well as the size and potentially saves energy and reduces the cost of production.



Figure 4. Typical distribution of the different antennas in a smartphone. Taken from [16].

### I.4.1.2. Radiation pattern reconfiguration

This type of reconfiguration refers to the ability of the antenna to modify the shape of the radiated beam as well as the direction in which it points. For example, tracking systems such as radars and satellites need to be able to follow the source (or the target) in order to establish continuous communication link. Since the communication distances are relatively long, a communication system requires high gain antennas (with very narrow beam-widths) in order to travel such long distances, thus reducing the coverage area. In order to compensate the size of the beam, the systems need to be able to continuously steer the beam to follow the target. Traditionally, steerable antennas are created by using an array of antennas and feeding them with the same signal but with a phase delay in time, as shown in Figure 5. Then, if all the antennas are feed with equal amplitude, the beam will point in the direction  $\phi_0$  given by:

$$\alpha = k.d.\sin\phi_0 \quad (1)$$

Where  $\alpha$  is the phase difference between adjacent antennas,  $k$  is the wavenumber,  $d$  is the distance separating each antenna.

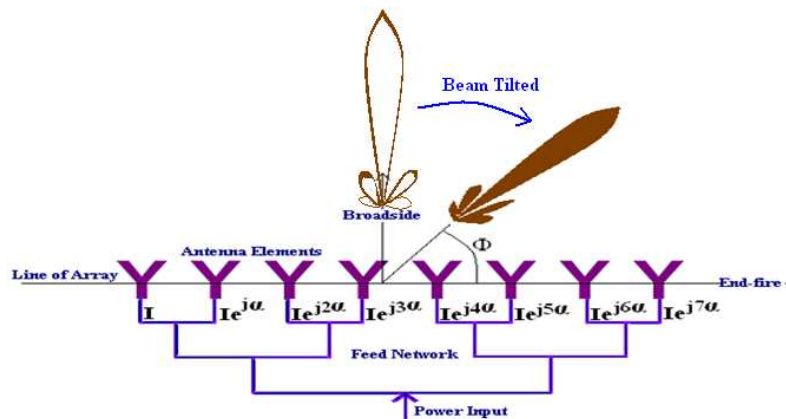


Figure 5. Example of a steerable beam using a linear array of antennas. From [17].

### I.4.1.3. Polarization reconfiguration

In this case, polarization reconfigurability refers to the capability of an antenna to change between linear and circular (C) polarizations - (LP), RHCP and LHCP. The biggest interest in polarization reconfiguration is explained by equation ( 74 ) (see Appendix 1) implying that, in order to extract as much power as possible from an EM wave, the polarization state of the receiving antenna and the EM wave must match. However, another interest of this kind of reconfigurability is the orthogonality property (for example: an antenna in RHCP state will never interact with an antenna in LHCP state) thus there is the possibility of re-using the same frequency band with orthogonal polarization state in order to use as much as possible the available bandwidth which is a very common technique employed in satellite telecommunications in order to effectively increase the available spectrum.

### I.4.2. Reconfiguration techniques

Although in the case of arrays of antennas is possible to electrically modify the radiation pattern just by changing the phase of individual antenna, most of the time the reconfiguration capability implies the modification of the geometry and physical parameters of the antenna. This can also be achieved by integrating agile components into the structure of the antenna. In the following sections, we will pass in review the solutions which have received extensive attention for achieving antenna reconfiguration.

#### I.4.2.1. Mechanical- based reconfiguration.

The radiation characteristics of an antenna are mostly determinate by the geometry of the antenna, thus, to change its properties, the physical geometry of the antenna needs to be changed. As an example, the Figure 6 shows an example of a frequency reconfigurable antenna using mechanical means, as reported in [25]. In this case, the antenna consists 3D-printed multi-leaf spring with a rotatory mechanism. By rotating the mechanism, the 3D-printed spring change geometry, thus causing the antenna to change the operation frequency continuously. The authors report a frequency operation band between 3.5 and 6.2 GHz with efficiencies better than 80% and a gain between 6 dBi and 11.5 dBi.

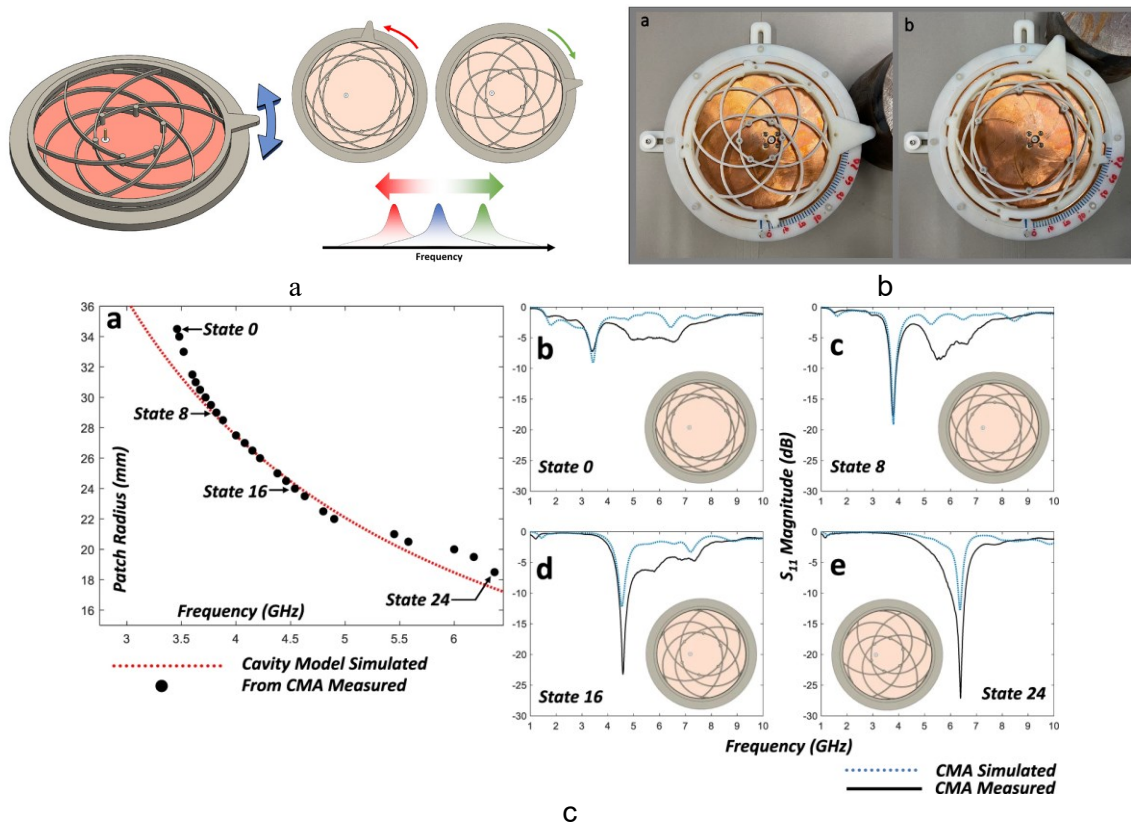


Figure 6. Mechanically reconfigurable antenna with continuous tuning of the operation frequency.  
a) Schematic representation and functioning principle. b) Fabricated device. c) Measured and simulated operation frequency variation as a function of the specific state. From [18].

One interesting example of a mechanical reconfigurable antenna is the one reported in [26] where the authors took inspiration from origami techniques in order to create a frequency reconfigurable antenna. This antenna presents two states (operation at two main frequencies), depending if the antenna is folded or not. When the antenna is in the unfolded state (step a in Figure 7a), the antenna presents an operation frequency of around 1.2 GHz. The following steps (b-n) in Figure 7a show the process of turning an un-folded state into a folded state. In this last state (step n in Figure 7a) the operational frequency shifts down to 0.75 GHz. In the flat state, the authors report efficiencies up to 90% but, when in the folded state, the efficiency reduces to 20%.

Mechanically reconfigurable antennas represent the most straightforward way of changing the characteristics of an antenna permanently (in a non-volatile manner). However, it is clear that these solutions require manual intervention from a human operator in order to change state (although, the manual intervention can be replaced by mechanical actuators at a cost of an increase in complexity in the design of the whole system). Another detriment of these types of solutions is that, as the frequencies get higher, the size of the antenna is reduced down to a few millimeters in length for mmWave band frequencies, which make manual intervention much more difficult.

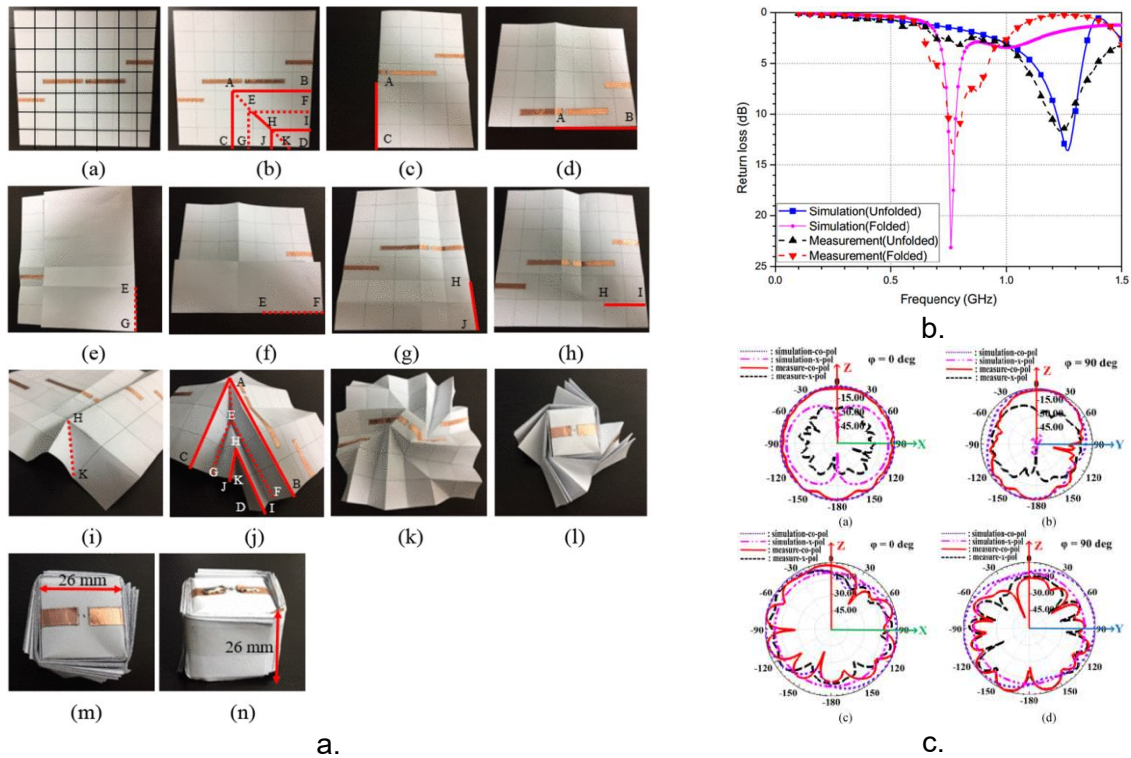


Figure 7. Fabrication and measure of the origami flasher antenna. a) Folding sequence to pass from the flat state to the folded state. b) Measured and simulated S-parameters in both states. c) Measured and simulated radiation pattern in both states. From [19].

#### I.4.2.2. Pin-Diodes

Pin diodes are semiconductor devices which can allow or block the passage of an RF signal by application of a DC voltage across its terminals, thus acting as an electrically controlled switch. The switching speed typically ranges in the tens of  $\mu\text{s}$  and the devices are extensively used in RF circuits to provide reconfiguration capabilities [5, 20]. However, their integration into RF devices is not straightforward since PIN diodes require a DC voltage polarization to be activated, which needs to be decoupled from the RF path. A typical configuration of PIN diodes is shown in Figure 8a (series configuration) and Figure 8b (shunt configuration).

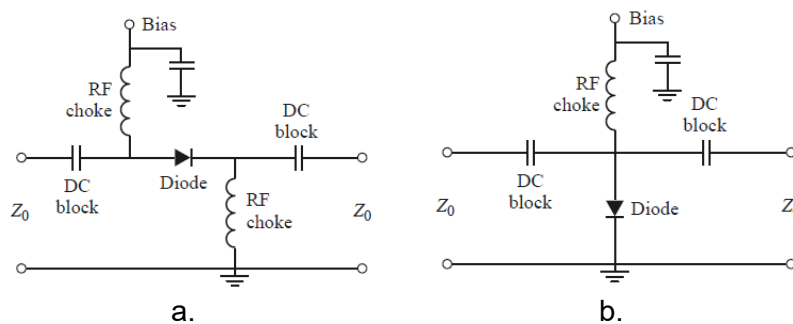


Figure 8. Typical electrical circuit to integrate a PIN diode into a RF circuit. a) Series configuration. b) Shunt configuration.

A frequency reconfigurable antenna operating above 24 GHz with reconfiguration capabilities based on the integration of PIN diodes and with wide-band RHCP was proposed in [27]. The antenna consists of two substrates, as shown in Figure 9a. At the top of the upper substrate, there is an array of sixteen planar antennas coupled to the feeding and reconfiguration circuits

on the lower substrate which is integrating a reconfigurable band-pass filter (Figure 9b). The band-pass filter integrates two PIN diodes that allows the antenna to work in four different frequencies (25, 26, 27.75 and 29 GHz) depending on their ON-OFF combination (Figure 9c). The measured gain is found to be 12 dBi, 10 dBi, 12 dBi and 13 dBi, respectively, in increasing order with frequency. The authors attribute the difference between simulated and measured results (as high as 1.2 dBi) to errors due to fabrication tolerances. This difference can also be explained by a loss introduced by the PIN diodes, which is supported by the fact that the losses increases with frequency. The radiation efficiency was not reported.

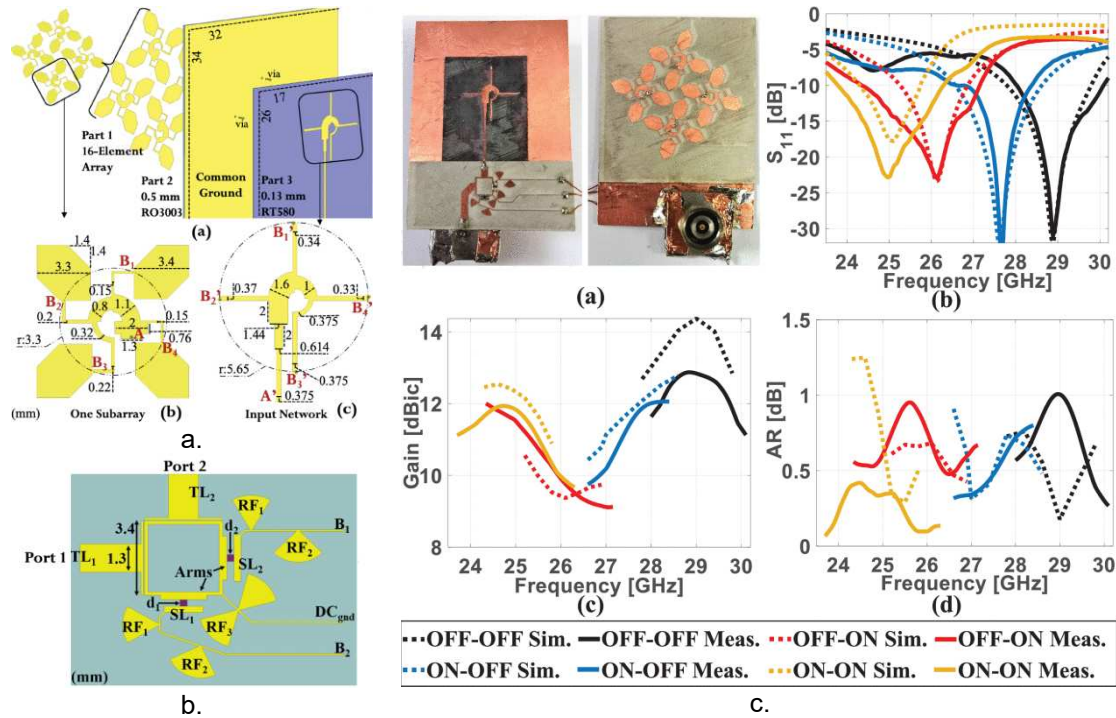


Figure 9. Frequency reconfigurable antenna using PIN diodes. a) Schematic representation of the RHCP array of antennas. b) Reconfigurable band-pass filter using PIN diodes. c) Measured performances for all states. From [20].

In [28], a radiation pattern reconfigurable SIW (substrate integrated waveguide) antenna working at 27 GHz and integrating PIN diodes is proposed. In this case, the radiating element is a slot engraved in the metallic pattern (Figure 10a). Next to the radiating slot, four circular plated-through-holes (PTH) are used as feeding system and connected to the metallic SIW via PIN diodes, which requires the integration of polarization bias (Figure 10b). Depending on the state of the PIN diodes, the PTH is connected or disconnected from the main line and thus perturbing the current flow and therefore, the radiation pattern of the device. The Figure 10c shows the radiation pattern modification at two different phase shifts induced by the different states of the diodes. The authors reported beams scanning capabilities from  $0^\circ$  to  $33^\circ$  in steps of  $8^\circ$  and efficiencies between 60% and 94%, depending on the state of the PIN diodes.

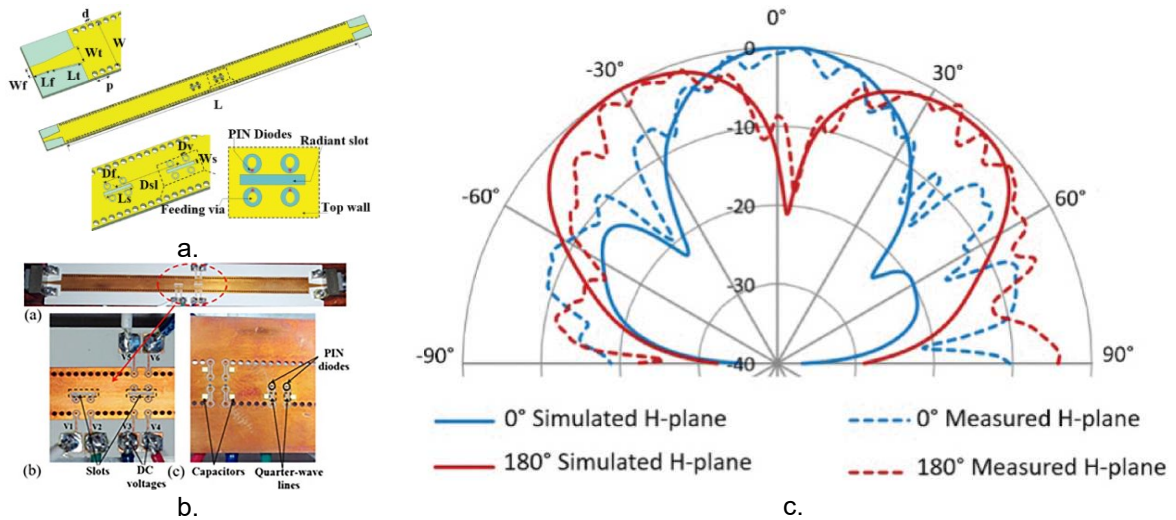


Figure 10. Radiation pattern reconfigurable SIW antenna using PIN diodes. a) Schematic representation. b) Fabricated SIW antenna with integrated diodes. c) Radiation pattern for two configurations. From [21].

A very interesting and powerful example of reconfiguration is the one shown in [29] where the authors presents a “Pixel antenna”. This concept consists of a grid of parasitic patch antennas mounted over a driven patch. Each antenna in the parasitic layer is called a “Pixel”. The pixels are connected to all the adjacent neighbors by PIN diodes (Figure 11a). This configuration works by exploiting the coupling between each pixel which can be easily modified by connecting or disconnecting the pixels using the PIN diodes. The antenna presents more than  $10^{18}$  possible switching configurations. The operational frequency can go from 2.4 GHz up to 3.0 GHz (Figure 11b). The authors also report beam-steering capabilities between  $-30^\circ$  and  $30^\circ$  in the theta plane along with the capacity of working in linear polarization or circular polarization (Figure 11c). The total efficiency of the device is reported around 50%.

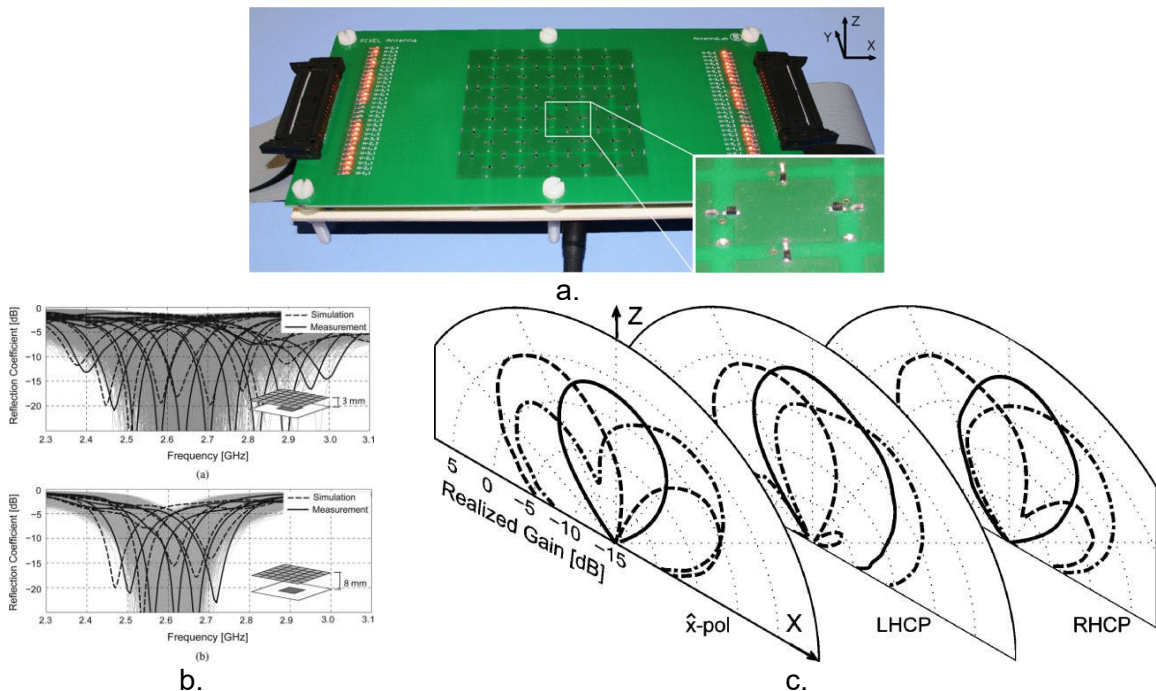


Figure 11. Reconfigurable pixel antenna. a) Fabricated prototype with PIN diodes. b) Measured and simulated reconfigurable resonant frequency. c) Measured and simulated reconfigurable radiation pattern. From [22].

Although PIN diodes offer the advantage of being very low cost and relatively easy to integrate in RF circuits, they need a constant power supply in order to remain active (their ON-states are volatile) which degrades the overall efficiency of the system. Additionally, the need of a polarization bias can complicate the design and perturb the radiation characteristics if not handled with precaution. Finally, the insertion loss increases with frequency, which make them inefficient for mmWave band applications.

### I.4.2.3. RF-MEMS devices

Switches based on micro electromechanical systems (MEMS) devices have shown remarkable performances in terms of low losses, higher isolation and very broadband operation (from DC up to THz) that are attractive for high frequency applications [30] [31]. Although in principle any kind of mechanical actuator can be created using MEMS, RF-MEMS switches are the most used for RF applications. In particular, the cantilever model shown in Figure 12 is one of the most popular options. This device uses a movable membrane that can be move down by an electrostatic force applied to the electrode thus creating a contact between the RF input port ant the output port.

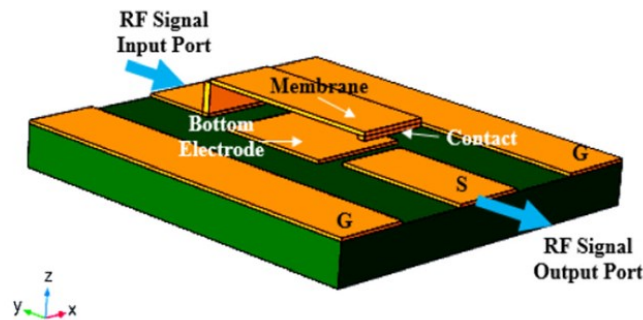


Figure 12. Typical geometry of a CPW RF-MEMS switch (Cantilever model). From [23].

In [32] the authors reports the use of RF-MEMS switch to change the angle of pointing (diagram reconfiguration) of a planar antenna working at 35 GHz. For this case, the switch is used to connect or disconnect two sub-patches at the left and right of the main patch in order to change the pointing angle of the overall antenna (Figure 13). Measurements shows that the antenna can point at the angles  $-8^\circ$ ,  $0^\circ$  and  $+8^\circ$  depending on the state of the switch, with a gain of 5 dBi in all cases. The efficiency was not reported.

RF-MEMS have shown remarkable performances up to THz frequencies, however they are not without several disadvantages. For example, the constant mechanical moving of the membrane can induce a lot of stress in the structure and reduce their life-time and reliability. Also, the material for the membrane needs to be carefully chosen in order to reduce damping and contact resistance without decreasing the displacement of the membrane and rigidity (which can increase commutation time) [31] [33]. Additionally, they require relatively high voltages in order to be activated ( $> 10$  V) and their fabrication as well as their integration can be complex [10].

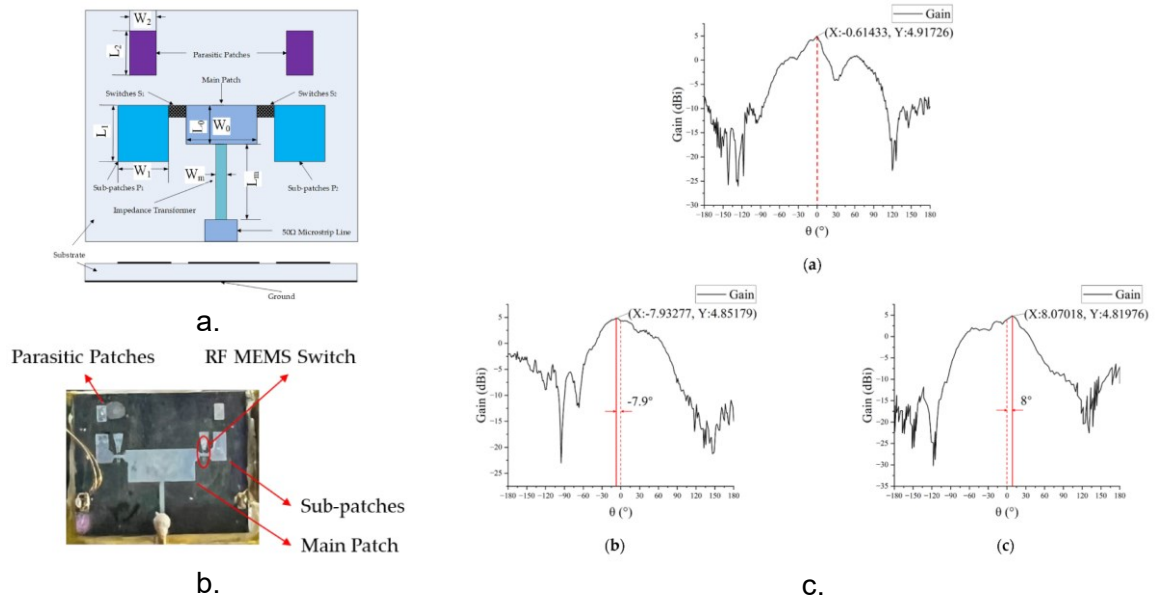


Figure 13. Radiation pattern reconfigurable antenna using two RF-MEMS switches. a) Schematic representation. b) Fabricated antenna with integrated RF-MEMS switches. c) Measured radiation pattern in the three states. From [25].

#### I.4.2.4. Varactor diodes

The solutions based on PIN diodes and MEMS have shown satisfactory results to provide reconfigurable capabilities to antennas, however, it is clear that both solutions presents a similar trend: both of them provide discrete states due to the use of switches to connect or disconnect metallic features of the circuit. One of the most common devices for continuous reconfigurable action is the use of varactor diodes which consist of a reverse-biased diode whose junction capacitance  $C_j$  is controlled by the voltage  $V$  across its terminals, according to:

$$C_j(V) = \frac{C_0}{\left(1 - V/V_0\right)^\gamma} \quad (2)$$

where  $C_0$  is the junction capacitance with no bias,  $V_0$  is a constant that depends on the type of diode and  $\gamma$  is constant that depends of the doping profile of the diode. However, as in the case of PIN diodes, varactor diodes also need a polarization circuit in order to decouple the DC bias and the RF path.

An example of varactor integration is presented in [34] for an ultra-wideband antenna (UWB) working at 7 GHz as shown in Figure 14. This antenna uses voltage-controlled varactors in order to continuously tune a notch filter which is rejecting a particular frequency band.

Another example of varactor diodes used for high frequency applications is the one presented in [35]. In this case, a square patch antenna is symmetrically connected by varactors in all corners to additional metal patterns as shown in Figure 15. The operation frequency of the device can be continuously tuned in frequency from 24 GHz up to 30 GHz by changing the bias voltages of the varactors. Additionally, this antenna can be dual-polarized, with a maximum realized gain up to 11 dBi. The maximum efficiency reported is around 56%.

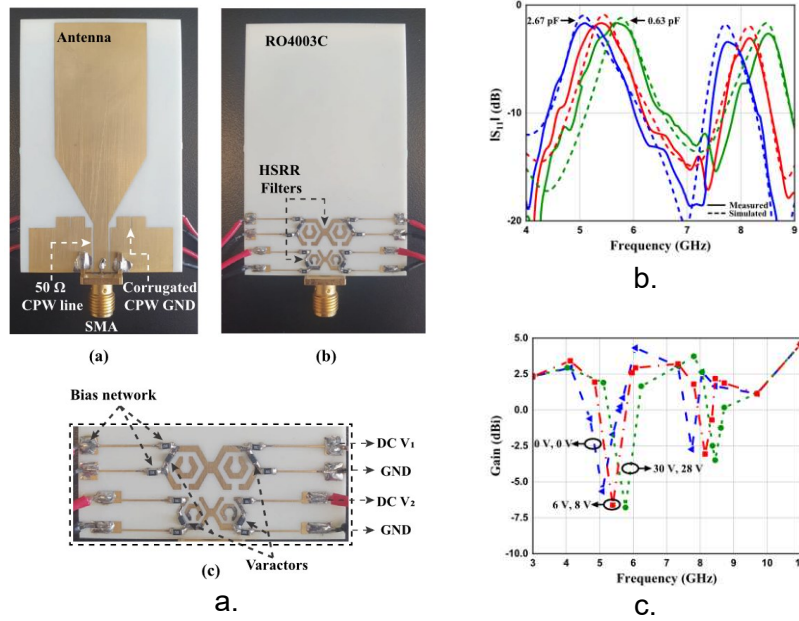


Figure 14. Frequency rejecting reconfigurable antennas integrating varactor diodes. a) Fabricated UWB antenna (upper) and notch filter (lower) integrating varactor diodes. b) Measured and simulated  $S_{11}$  performances. C) Measured and simulated gain performances. From [27].

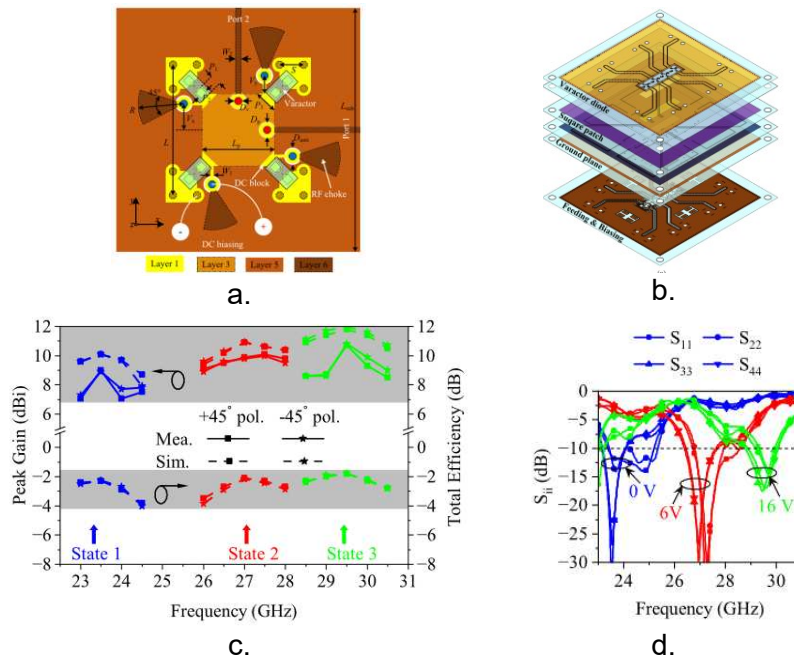


Figure 15. Frequency and polarization reconfigurable antenna integrating varactor diodes. a) Top view of the planar patch antenna integrating varactor diodes at the corners. b) Schematic representation of the whole structure. c) Measured and simulated gain performances for each state. d) Measured and simulated  $S_{11}$  parameters for different voltages across the varactor diodes. From [28].

Varactor diodes have been very present in RF circuits, most commonly for electronically tuning of local oscillators in cellphones. However, two of the biggest disadvantages of varactor diodes are their non-linearity, as seen in equation ( 2 ) and the very high voltages required to polarize them (which can go up to 20V or even higher).

### I.4.2.5. Ferroelectric materials

Other solutions like the use of ferroelectric materials have been proposed in order to create continuous reconfiguration. For ferroelectric materials, the dielectric polarization is a direct function of the electric field [36] [37], as shown in Figure 16. The most common types of ferroelectric materials are perovskites which are metallic oxides such as  $\text{BaTiO}_3$ ,  $\text{PbTiO}_3$  and  $\text{Ba}_{1-x}\text{Sr}_x\text{TiO}_3$  (BST). Since the dielectric permittivity is a direct function of the dielectric polarization, these materials have the capacity to change their permittivity value continuously by applying a voltage across the material. This phenomenon has been exploited in order to create variable capacitances [38] [39].

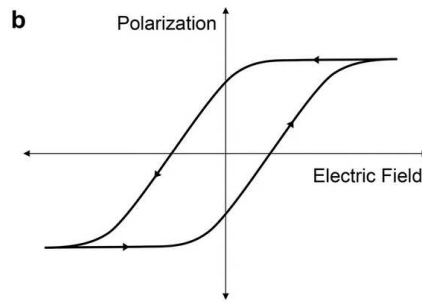


Figure 16. Typical variation of the dielectric polarization in a ferroelectric material as a function of the applied electric field.

For example, in [40] a ferroelectric composition of barium strontium titanite (BST) was used to fabricate tunable capacitors as shown in Figure 17. The antenna integrating these capacitors can be continuously tuned from 6.5 GHz up to 9.3 GHz with very good matching. The authors report a gain of less than -3 dBi over the whole frequency band, implying very high losses (which are not reported).

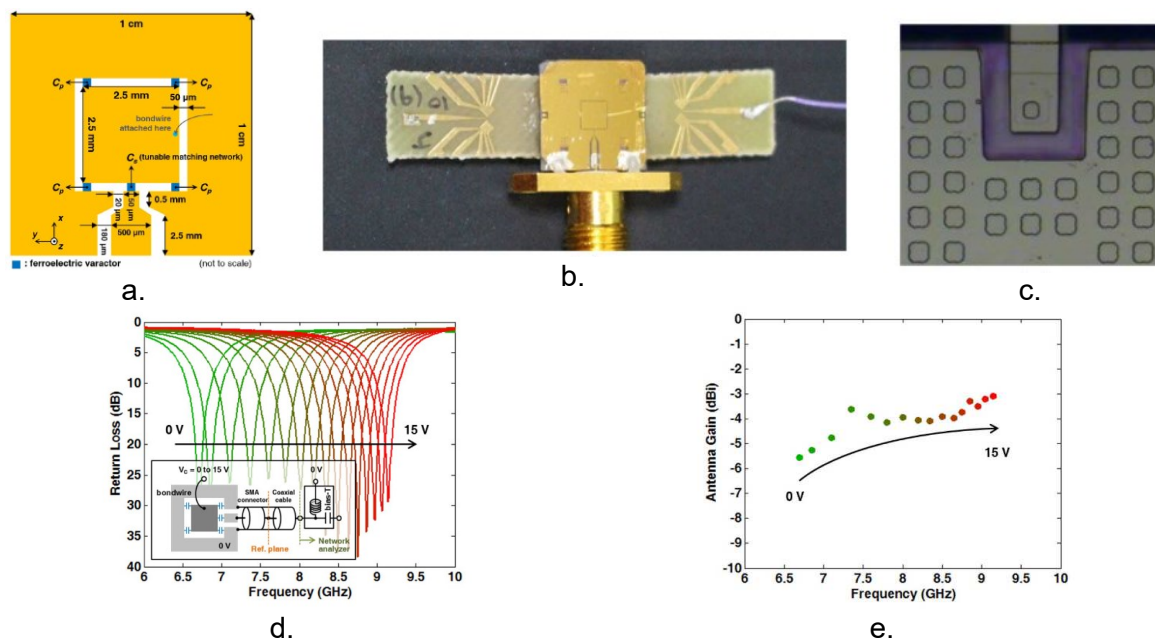


Figure 17. Frequency reconfigurable antenna integrating ferroelectric capacitors. a) Schematic representation of the planar antenna and capacitors. b) Fabricated device. c) Close up to the ferroelectric capacitors. d) Variation of the resonant frequency as a function of the applied voltage to the capacitors. d) Variation of the gain of the antenna as a function of applied voltage. From [33].

The phenomenon of field polarization in ferroelectric materials is very fast, with low consumption (very low leakage currents), they can be easily integrated at relatively low cost and have continuous reconfiguration capabilities and, therefore, have attracted a lot of attention in the RF world. However, there are some drawbacks of ferroelectric materials such as very high permittivity values ( $> 100$ ) [37], high losses for specific compositions, the need of very high polarization voltages (up to 100 V) [39] and sensibility to temperature for specific compositions [36].

#### I.4.2.6. Phase Transition Materials (PTM)

Other kind of functional materials that have gain a lot of attention for their integration as agile elements in RF devices are phase transition materials (PTM). This kind of materials are metallic oxides that undergo a drastic modification of their electrical and optical properties under thermal, optical or mechanical stimulus [41] [42] [43]. There are many such metal-insulator transition oxides that have been reported and studied in the literature, as shown in Figure 18a, but the most common one is vanadium dioxide ( $\text{VO}_2$ ) which has been extensively studied and integrated in numerous types of RF devices (switches, antennas, filters, power limiters, etc) [44]. The Figure 18b shows a typical example of the change in the electrical resistivity of  $\text{VO}_2$  as a function of the temperature during a heating then cooling cycle. It is worth noting that these materials are volatile in nature which means that the material returns to the original state after the stimulus (either thermal, electrical or optical) is removed.

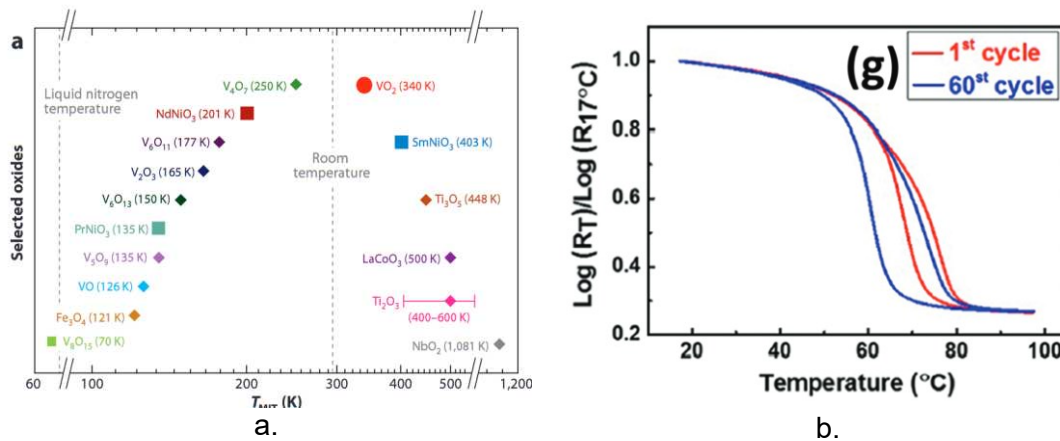


Figure 18. a) Examples of phase transition materials and the associated transition temperatures [38].

b) Variation of the normalized resistivity of a  $\text{VO}_2$  film during a heating - cooling cycle [39].

The ability of vanadium dioxide to transition between an insulating state to a metallic state has been exploited to design and realize reconfigurable antennas. As example, in [45] is reported a planar frequency reconfigurable antenna integrating a  $\text{VO}_2$  pattern, as shown in Figure 19. This slot-type antenna is based on the use of  $\text{VO}_2$  as a switching device in order to change the length of an excitation stub which in return will change the operating frequency of the antenna between 33 GHz and 37 GHz, depending on the insulating or metallic state of the  $\text{VO}_2$ . The authors report gains of 5.28 dBi and 5.41 dBi in each of the operating state with efficiencies greater than 80% in both cases.

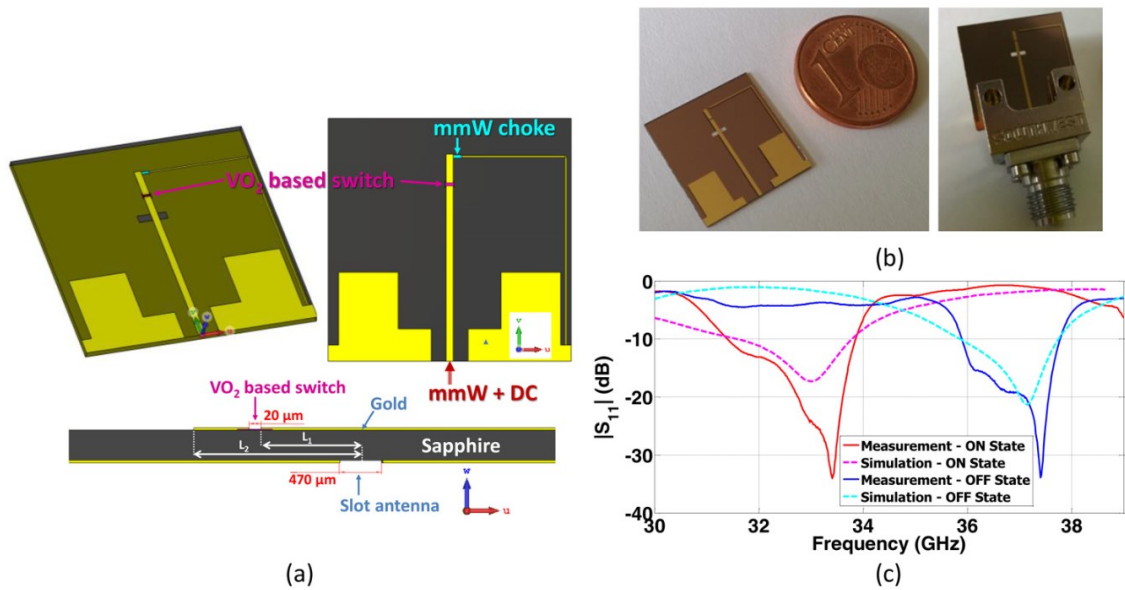


Figure 19. Frequency reconfigurable antenna integrating VO<sub>2</sub> for mmWave frequencies. a) Schematic representation of the antenna design. b) Fabricated device. c) Measured and simulated operation frequency in both states of the VO<sub>2</sub> switch. From [40].

Functional materials such as VO<sub>2</sub> allows very compact and easy integration into RF devices and possess very fast switching speeds, with very good switching properties expanding on very wide frequency bands, up to THz frequencies. Nonetheless, they have some disadvantages such as their volatile nature which requires a constant high temperature or continuous applied voltage that can lead to high energy consumption.

#### I.4.2.7. Summary of reconfigurable solutions

In the previous section, various strategies for creating reconfigurable antennas have been presented in a non-exhaustive manner. Although each technology offers interesting advantages with respect to the others, they often come in hand with some non-negligible disadvantages. Most notably, a common point between most of the presented technologies is their use of RF switches as a reconfigurable device which translate only into a finite discrete states of reconfiguration. Table 1 presents a summary of the various advantages and disadvantages of the reviewed technologies.

Another common point between of most of these technologies is their volatile nature which implies the use of a continuous stimulus in order to maintain their state. This can lead to high energy consumption over time. Recently, a new type of solution for integrate non-volatile reconfigurable capabilities to RF antennas is in the use of phase change materials (PCM). This type of materials presents similar characteristics as the PTMs but with non-volatile states which implies that no energy consumption is required in order to keep one of their specific state (insulating or metallic). In the next section, we will describe and analyze the performances of PCMs and their potential use in reconfigurable antennas.

Table 1. Summary of the advantages and disadvantages of different technologies for reconfigurable antennas.

| Device                      | Advantage   | Disadvantages   | Type of reconfiguration |
|-----------------------------|---|---|-------------------------|
| Mechanical.                 | -Low insertion losses.<br>-Non-volatile.  | -Very bulky.<br>-Difficult to design.<br>-Difficult to manufacture.   | Continuous or discrete. |
| Pin Diodes.                 | -Very low cost.<br>-Low polarization voltage.<br>-Easy to design and integrate.                             | -Moderate switching time (ns- $\mu$ s).<br>-High losses at high frequencies.<br>-Requires polarization circuit.<br>-High power consumption.<br>-Volatile. | Discrete.               |
| Varactors.                  | -Low energy consumption.<br>-Low cost.  | -Requires high voltages.<br>-Moderate switching time ( $\mu$ s).<br>-Non-linear behavior.<br>-Requires a polarization circuit.                            | Continuous.             |
| MEMS.                       | -Low insertion losses.<br>-Low power consumption.<br>-High power handling.<br>-Application up to THz bands. | -Moderate switching time ( $\sim\mu$ s).<br>-Complex to fabricate.<br>-Requires a polarization circuit and high polarization voltages.                    | Discrete.               |
| Ferroelectrics.             | -Low cost.<br>-Very fast activation time ( $\sim$ ns).<br>-Low energy consumption.                          | -Very high permittivity value.<br>-High polarization voltage.   | Continuous.             |
| Phase transition materials. | -Very fast switching (ps – ns).<br>-Application up to THz bands.  | -Quality dependent on the type of substrates (often with high permittivity).<br>-Volatile behavior.   | Discrete.               |

### I.5. Phase Change Materials (PCM) and applications

Phase change materials are solid materials that present very different physical properties (electrical, optical, thermal, etc) depending on the arrangement of their atomic structures. When the atoms within their structure are arranged in an orderly fashion, the material is in a crystalline state. On the other hand, when the structure is disordered, the material is in amorphous state, with differentiated structural, electrical and optical properties. Figure 20 presents a schematic representation of a crystalline structure (Figure 20a) and an amorphous structure (Figure 20b) of PCMs. The most attractive aspect of PCMs is that their atomic structure can be changed between a crystalline state to an amorphous state and vice-versa by application of different stimuli (thermal, electrical, optical).

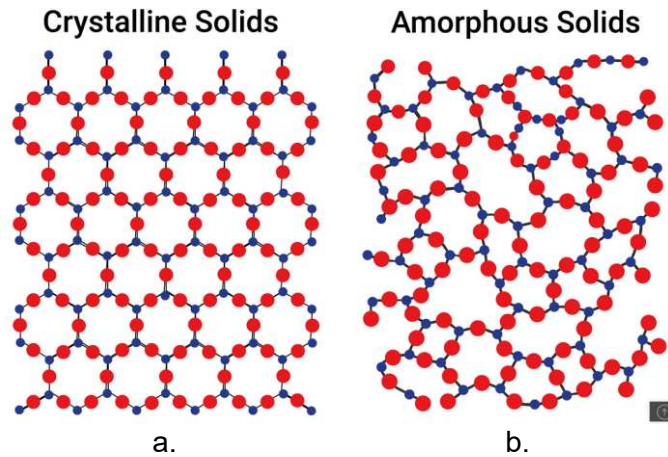


Figure 20. Illustration of the atomic arrangement of a) crystalline solid and b) amorphous solid.

The nature of PCMs was first discovered in the early 1900s by Alan Tower Waterman while studying the conductivity of a  $\text{MoS}_2$  composition. During his experiments, Waterman noticed a significant change in conductivity in a strip of  $\text{MoS}_2$  when heated using an electrical current. This change was permanent and led Waterman to point out that  $\text{MoS}_2$  existed in two phases: an  $\alpha$  state of high resistance (amorphous state) and a  $\beta$  state with low resistance (crystalline state). Indeed, the change in electrical resistance is one of the many properties of PCMs. Although initially the discovery of Waterman drew very little attention from the scientific community, it was not until the 1950s that PCMs began to attract attention from engineers and scientists due to their potential application in non-volatile solid-state memories. In particular, the interest was focus in chalcogenide-type compositions or alloys that contain at least one element of the IV group in the periodic table (most commonly sulfur, selenium, and telluride) when, in 1968, Stanford R. Ovshinsky presented the first reversible non-volatile switching memory based on a PCM composition of tellurium, arsenic, silicon, and germanium [46]. Since that moment, the study and application of PCMs based on these compositions truly surged, as PCM-based non-volatile memories have become one the key components in nowadays digital storage applications.

### 1.5.1. General properties of chalcogenides PCMs

As an example of the electrical properties change between the two states of PCMs, Figure 21 presents the evolution of the electrical resistivity of some chalcogenide PCM compositions. At low temperatures, all the samples present a high resistivity value that is characteristic of the amorphous state. As the temperature increases, the resistivity drops exponentially. When the temperature reaches a particular temperature, the material experiences a sudden drop in resistivity which is characteristic of a transformation into a highly conductive crystalline state. The temperature at which this transformation occurs is called the “crystallization temperature”. After the material has transformed into a crystalline state, the electrical resistivity does not change significantly, even when cooled back to low temperatures.

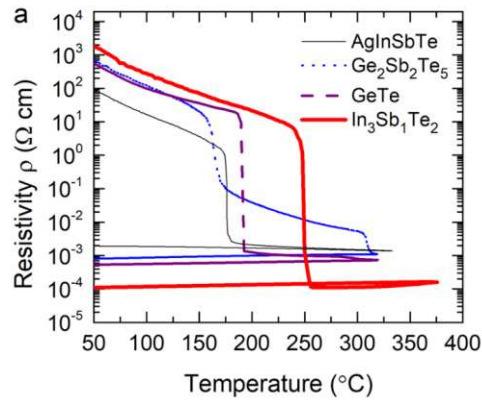


Figure 21. Evolution of the surface resistance with temperature for different chalcogenides PCM compositions. From [42].

The most interesting aspect of PCMs is that this transformation is “bi-stable” as the material retains its current state even after the heat source is removed. This characteristic gives PCM compositions an enormous advantage over classical components used for reconfiguration, as PCMs do not require a permanent bias in order to maintain one of its specific state. For RF applications, the change in resistivity is of particular interest since a high contrast between the resistance of the crystalline state and amorphous state allows one to discern very easily between a conductive metallic feature and an isolating one.

As in the case of the electrical resistivity, the optical properties of PCM compositions are also very dependent on the state of the PCM, presenting a high contrast between the two states. Thus, in the crystalline state, the PCM presents a metallic behavior evidenced by the higher conductivity and high reflectivity. In the amorphous state, the PCM behaves more like a semiconductor with high resistivity and low reflectivity. Particular examples of this contrast will be given later in our discussion.

Many other physical properties of PCMs are also modified through the phase change, like the density, heat capacity, thermal conductivity, etc. All of these changes must be considered for accurate multi-physics simulations involving PCMs.

### 1.5.2. Transformation mechanisms of PCMs

The mechanism by which a PCM transforms from the amorphous state to the crystalline state is studied by the theory of crystallization kinetics. Two processes are involved in the crystallization of an amorphous solid:

- **Crystal nucleation:** Occurs when atoms approach each other, forming crystalline clusters due to random thermodynamic fluctuations. When this process occurs in the interior of the material (without any other substance), the process is termed “homogeneous nucleation”. If the material is in contact with other substance (like impurities or doping elements), the process is called “heterogeneous nucleation”.
- **Crystal growth:** Refers to the growth of a previously formed stable crystal cluster to macroscopic sizes. This involves a re-arrangement process of the boundaries between the crystalline cluster and the amorphous region.

Both mechanisms exist simultaneously but, depending on the PCM and other factors, one can dominate the other. The Figure 22 shows a time diagram of homogeneous and heterogenous crystal formation.

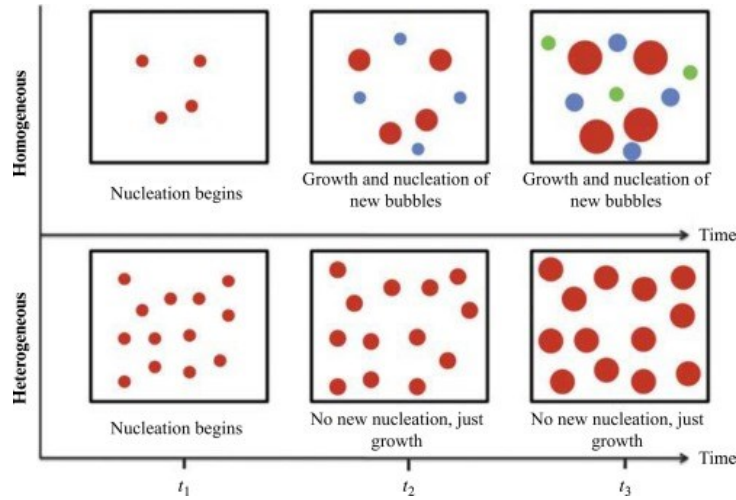


Figure 22. Time diagram of homogeneous and heterogenous nucleation. At time  $t_1$ , crystals begin to form within the material in random positions due to nucleation. At time  $t_2$ , for homogenous nucleation, new crystal clusters begin to form by nucleation while the previously formed clusters grow in size. At time  $t_3$  the crystal clusters have grown significantly in size while the nucleation and crystal growth continues until the whole material is crystalline. Taken from [47].

In the classical theory of nucleation, the crystal nucleation process is characterized by the nucleation rate which varies with time. The steady-state nucleation rate  $I$  is given by:

$$I = I_0 \cdot \exp\left(-\frac{W + E_D}{k_b \cdot T}\right) \quad (3)$$

where  $I_0$  is a pre-exponential factor,  $k_b$  is the Boltzmann constant,  $T$  is the temperature,  $E_D$  is a kinematic barrier related to the atomic diffusion and  $W$  is the thermodynamic free-energy barrier of to the nucleation which is related to the energy required to create stable crystalline clusters.

For the crystal growth mechanism, the grow velocity  $U$  is independent of time and can be stated as:

$$U = U_0 \exp\left(-\frac{E_D}{k_b T}\right) \left(1 - \exp\left(-\frac{\Delta G_c}{k_b T}\right)\right) \quad (4)$$

where  $U_0$  is a pre-exponential factor and  $\Delta G_c$  is the free-energy phase between the amorphous and crystalline states.

For temperatures much smaller than the melting temperature of the material, the thermodynamic free-energy barrier of the nucleation  $W$  is much smaller than the kinematic barrier related to the atomic diffusion  $E_D$ , therefore the nucleation rate is characterized by the diffusion activation energy. Furthermore, in the same temperature range, the second exponential in equation (19) varies very slowly with temperature and can be set as constant, therefore the crystal growth mechanism can be also characterized by the diffusion activation energy. In other words, at low temperature, the crystallization kinetics of PCMs can be mostly described by a single parameter: the activation energy  $E_D$ . It is important to notice that both equations (3) and (4) are inversely proportional to the temperature  $T$ , meaning that the nucleation and growth rates occurs faster for higher temperatures.

The overall crystallization kinematics is usually described by Johnson-Mehl-Avrami-Kolmogorov theory (JMAK) [48] in which the transformed volume fraction  $\alpha$  of a material as a function of time is given by:

$$\alpha(t) = 1 - \exp\left(-g \int_0^t I(t) \left(\int_{t'}^t U(t) dt\right)^3 dt'\right) \quad (5)$$

where  $g$  is the shape factor of the crystal,  $I$  and  $U$  are the crystal nucleation and growth rate, respectively. The volume fraction  $\alpha$  describe the percentage of volume of the material that has crystallized after a time  $t$  under isothermal conditions (at a constant temperature).

Equation ( 5 ) can be simplified depending on the nature of the nucleation rate and growth rate. Avrami [48] [49] proposed the following general relationship for isothermal crystallization process:

$$\alpha(t) = 1 - \exp(-kt^n) \quad (6)$$

where  $n$  is the “Avrami exponent” that depends on the crystallization mechanism and usually takes values between 1 and 4 [49]. The parameter  $k$  is the reaction rate that depends on the activation energy  $E_D$  and the temperature of the sample. To characterize the crystallization dynamics of a PCM, experiments search to determine the effective activation energy  $E_g$  which contains contributions from both the nucleation rate and the crystal growth. Is also worth noticing that the higher the  $E_g$ , the longer the time needed to crystallize the entire sample and therefore the material is said to be “more stable” at a particular temperature  $T$ .

The previous theory is valid under isothermal conditions (at a constant temperature). For non-isothermal conditions, the material can be studied by heating it at a constant temperature rate  $\beta$ . Under this condition, the reaction rate  $k$  is no longer constant and equation ( 6 ) has to be modified into

$$\alpha(t) = 1 - \exp\left(\left[\int_0^t -k(t) dt\right]^n\right) \quad (7)$$

Assuming  $n$  is a constant, the following equation relating the heating rate to crystallization temperature has been derived.

$$\ln\left(\frac{T_x^2}{\beta}\right) = \ln\left(\frac{E_g}{R}\right) - \frac{E_g}{RT_x} + C \quad (8)$$

where  $T_x$  is the crystallization temperature,  $R$  is the universal gas constant and  $C$  is a constant. Essentially, equation ( 8 ) describes the dependence of the crystallization temperature on the heating rate of the material. This effect has been observed for some PCM compositions. As an example, Figure 23 shows the influence of various heating rate on the crystallization of two selenium and antimony PCM alloys. Indeed, the higher the heating rate of the material, the higher the crystallization temperature.

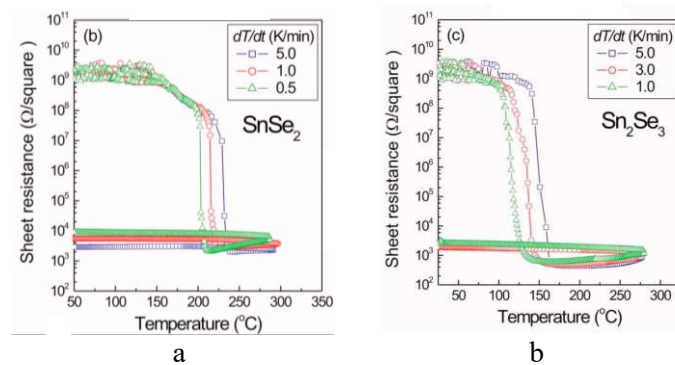


Figure 23. Surface resistance evolution with temperature for different heating rates of a 90 nm thin film of a) SnSe<sub>2</sub> and b) Sn<sub>2</sub>Se<sub>3</sub>. From [46].

On the other hand, the transformation from crystalline state to amorphous state requires heating the material at temperatures higher than its fusion point or melting temperature  $T_m$ . This process is illustrated in Figure 24. During the fusion state ( $T > T_m$ ), the material has passed from an ordered crystalline phase into a disordered quasi-liquid phase. As the PCM cools down from the liquid state, it returns into a crystalline state. However, if the crystallization process is slow compared to the cooling rate, the material may enter into a supercooled state and become a glassy solid state (amorphous state) [50]. Therefore, in order to re-transform the material into its amorphous state, the melted material has to be cold down very rapidly in order to fix the disordered structure (this action is called “fast quenching”).

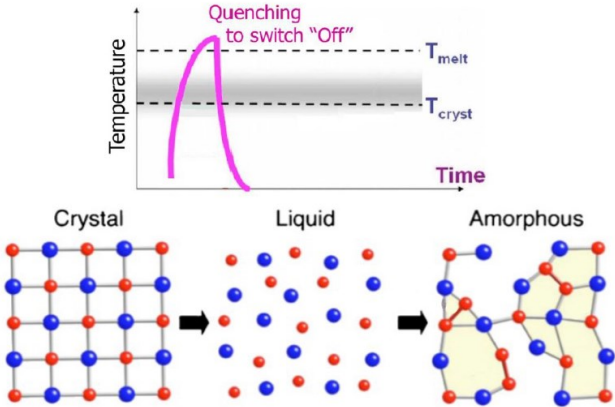


Figure 24. Illustration showing the phase changing from a crystalline state into an amorphous state passing by a liquid state.

The specifics of this process are illustrated by the transformation temperature time (TTT) diagram shown in Figure 25. In this representation,  $\Delta T$  represents the temperature difference with respect to the ambient temperature. Once the material reaches the liquid state and the heat source is removed, the temperature drops. If the curve reaches the value  $\Delta T_{melt}/e$  in a time lower than the CQT (critical quenching time) then the material transforms into a glassy amorphous state (blue trace). Otherwise, the material will transform back into a crystalline state (red trace).

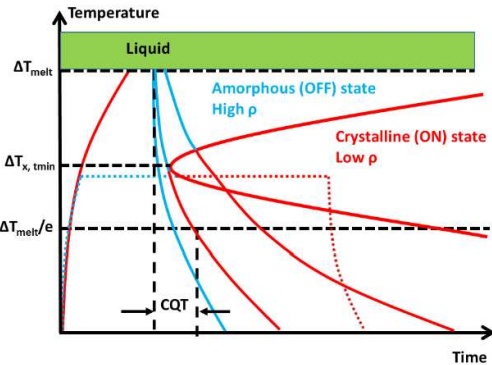


Figure 25. Transformation temperature time (TTT) diagram showing the different state transformation of a PCM. From [48].

The ability to rapidly cool down the PCM depends on the material and its environment. Typically, a PCM layer cannot dissipate the heat very quickly on their own, therefore high thermal conductive substrates are used in order to evacuate the heat more rapidly.

Although crystallization kinetics remains one of the most common models for describing the crystallization of PCMs, it still comes with some flaws. For example, some properties of PCM alloys have been observed to be dependent on the size of the material. In particular, crystallization temperature, optical constants, crystallization rate, etc. have been observed to change as the thickness of the PCM layers becomes smaller (into the tens of nanometers scale) [51] [52] [53]. This dependence of the size of PCM layers has been denoted as “scaling properties of PCMs” [50]. This dependence implies that the conclusions in the study of the PCM properties for a particular size of a PCM layer may not be the same for thicker or thinner layers.

### 1.5.3. Current technological uses of PCMs

Currently, there are three main types of digital data storage: solid-states, optical storage and magnetic storage. As mentioned previously, the original interest of PCM compositions arose from their potential to be used as non-volatile solid-states memories by profiting from their high electrical contrast between the crystalline and amorphous state. However, their high contrast in the optical properties has also been used in order to store digital information.

For solid states memories, the operation principle is based on a PCM cell as shown in Figure 26. In this case, two electrodes serve as electrical contacts of the cell. The cell operation is based on the change of phase of the PCM in within the cell ( $\text{Ge}_2\text{Sb}_2\text{Te}_5$ , in this case) [49]. The digital data is encoded in the state of the material. When the material is amorphous, the cell is characterized by a high equivalent resistance between the electrodes. When the material is crystalline, the cell is characterized by a low resistance value between the electrodes. Then, the state of the cell can be known by measuring the voltage drop between the electrodes using a very low sensing current. Since PCMs retain their state, the cell shown in Figure 26a acts as a permanent non-volatile digital memory. In order to re-write new information, the PCM needs to be transformed with the use of a high current as shown in Figure 26b (called the programming current): the action of amorphizing the material is called “reset” and the action of crystallizing the cell is called a “set” operation. One of the key advantages of PCM-based memories is their high cyclability as they are able to endure more than  $10^8$  cycles of writing and reading actions without significant degradation in their characteristics, as shown in Figure 26c.

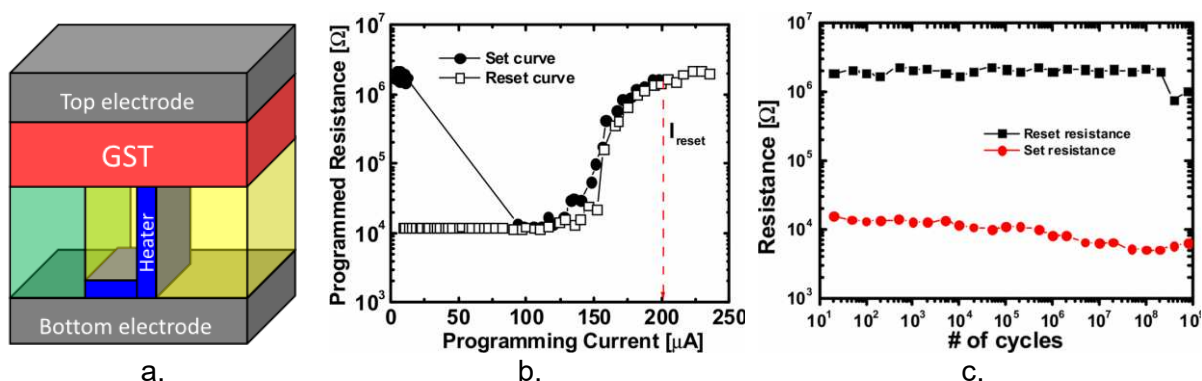


Figure 26. a) Schematic representation of a memory PCM cell. b) Resistance of the cell as a function of programming current. c) Resistance variation as a function of number of cycles. Taken from [52].

Insulator-to-metal reversible phase change induced by the Joule effect is schematically represented in Figure 27 (adapted from [54]). In order to transform the material from its amorphous state to its crystalline state, a long thermal impulsion (electrical or optical) with sufficient energy to heat the material pass its crystallization temperature is needed. To pass

from the crystalline state to the amorphous state, a short and stronger thermal impulsion sufficient to heat the material pass its melting point is needed.

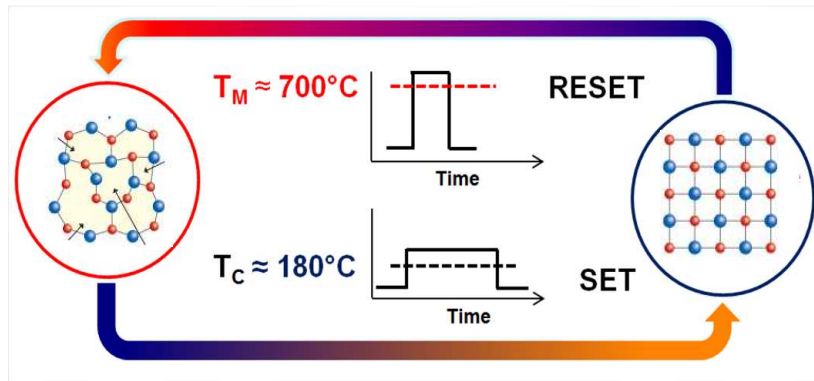


Figure 27. Schematic representation of the transformation induced by joule effect of a GeTe-based memory cell using electrical pulses. From [53].

The same basic principle is used in optical storage devices such as DVDs or blue-ray technology but in this case, is the high contrast between the reflectivity of the crystalline and amorphous state. In this case, a high-power laser is used to amorphized a region within a crystalline matrix as shown in Figure 28a. Then, a low power laser is used to sense the reflectivity of the track and “read” the encoded information as shown in Figure 28b.

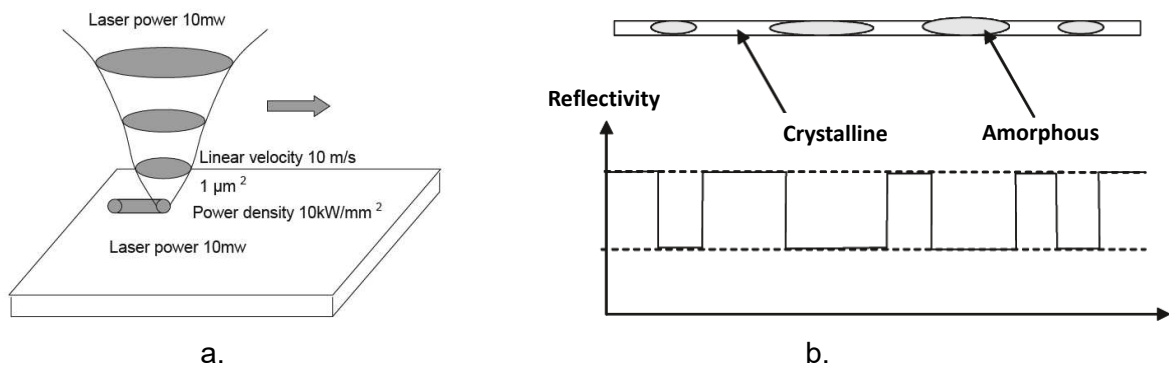


Figure 28. a) Engraving of an amorphous mark on a crystalline matrix of a PCM using a high-power laser. b) "Reading" of the encoded data by means of the reflectivity change. From [47].

#### I.5.4. Particular examples of PCM compositions

Although PCMs have been exclusive studied and used for memory storage applications, their properties are also of great interest for high frequency applications [55] [56] [57]. In particular, their high resistivity contrast between the amorphous and crystalline state allows an easy and clear distinction between a “metallic” region and “dielectric” region. In recent years, some families of PCMs have already been identified and studied for their integration into high-frequency systems. These compositions are based on the ternary Ge-Sb-Te as shown in Figure 29. In particular, the alloys GeTe and  $\text{Ge}_2\text{Sb}_2\text{Te}_5$  are the most studied and used for radio-frequency applications and will be detailed in the next sub-sections.

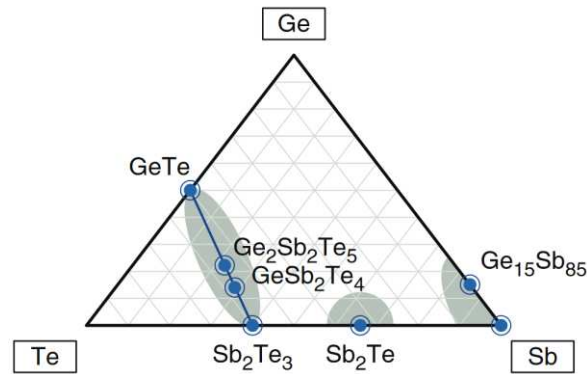


Figure 29. Diagram showing some of the most common (and studied) PCM compositions of the ternary Ge-Sb-Te for RF applications [33].

For high-frequencies applications, the PCM must respond to a certain number of requirements such as:

- High contrast between the electrical resistivity of their amorphous and crystalline state.
- A very low electrical resistivity in the crystalline state to reduce the power losses at high frequencies.
- A very low dielectric loss tangent in the amorphous state also to reduce the power losses at high frequencies.
- A very fast transition between the two states.
- A high thermal and chemical stability of both states.
- An easy technological integration into high-frequency circuits.
- A high reliability and reproducibility of the state change (high number of cycling).

#### I.5.4.1. Germanium Telluride (GeTe)

Alloys based on germanium and telluride have been studied since the 1960s [58] [59]. The crystallization mechanism for this kind of composition has been observed to be dominated by growth and thus allows for a very short crystallization time [60]. This alloy has presented very reproducible and controllable phase changings with a very high contrast in electrical resistivity. As an example, the Figure 30 shows the surface resistance behavior of a 50-nm thick GeTe alloy for various concentrations of Ge. From this figure, it can be observed that the highest resistance in amorphous state is presented by the composition with 30% Ge while the lowest resistance in crystalline state is presented by the composition with 50% Ge. In addition, is this latter composition that presents the highest contrast between the two states (around 6 orders of magnitude). Indeed, is the stoichiometric composition that is the most studied composition for RF and data storage applications [61] [62].

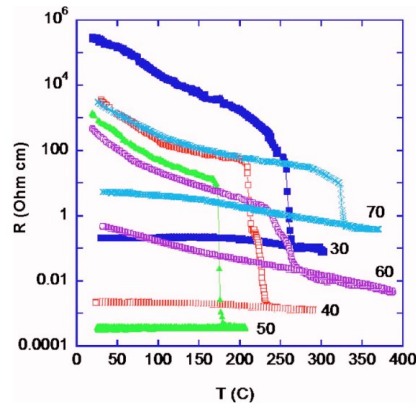


Figure 30. Evolution of the surface resistance of a Ge-Te alloy for various compositions [62].

Another interesting observation of Figure 30 is that the crystallization temperature for each composition is different, with the  $\text{Ge}_{50}\text{Te}_{50}$  being at around  $180^\circ\text{C}$ . However, there are conflicting results in the literature regarding the crystallization temperature of Ge-Te alloys. For the case of  $\text{Ge}_{50}\text{Te}_{50}$ , various authors have reported crystallization temperatures around  $180^\circ\text{C}$  [63] [64], others have reported temperatures higher than  $200^\circ\text{C}$  [65] [66] [67] with some reporting crystallization temperatures up to  $250^\circ\text{C}$  [68]. The difference between the reported crystallization temperatures may be attributed to the use of different heating rates (which was previously stated that can affect the crystallization temperature) or by oxidation of the film, which has been observed to influence the crystallization temperature, as shown in Figure 31 [66]. It has been also reported that very small differences in the concentration of Ge and Te can result in significantly high changes in the crystallization temperature [69], where variations in the Ge concentration as low as 3% can result in changes in the crystallization temperature up to  $60^\circ\text{C}$ .

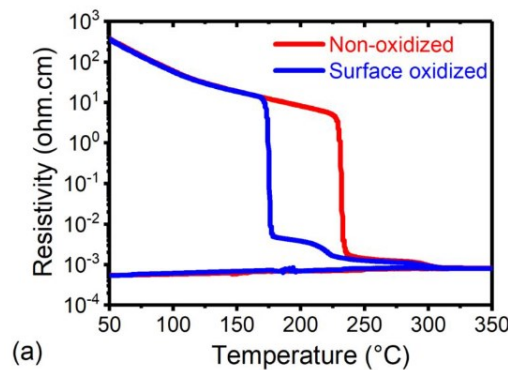


Figure 31. Influence of the surface oxidation on the evolution of the surface resistance as a function of temperature [66].

The GeTe composition has also been observed to show a high contrast of optical reflectivity between the two states, as shown in Figure 32 [70]. The biggest contrast is seen in the infrared region (around  $1000\text{ nm}$  wavelength or  $1\text{ eV}$  photon energy), with the crystalline state having the biggest reflectivity.

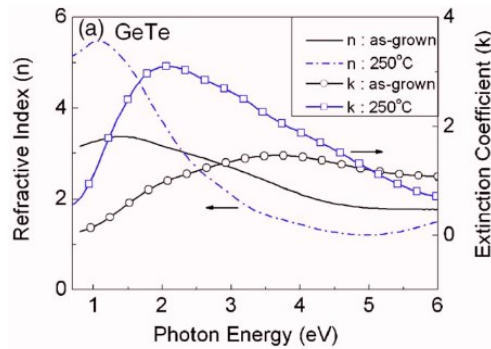


Figure 32. Measured optical properties of a sample of GeTe in amorphous (as - grown) and crystalline state (250°C) [68].

The concentration of Ge has also been observed to severely influence the reflectivity of a GeTe alloy, as shown in Figure 33. In this work the authors measured the reflectivity of a 100-nm thick GeTe alloy on a silicon substrate, for various concentrations of Ge [71]. The samples were heated up at a rate of 10 C°/min and the reflectivity was monitored with a low power laser of  $\lambda = 670$  nm. It is observed that the samples having Ge concentrations close to 50% present a crystallization temperature of around 180°C but the optical properties are slightly different, being higher for the sample with 54% concentration. Additionally, it is observed that the crystallization temperature increases with higher concentration of Ge.

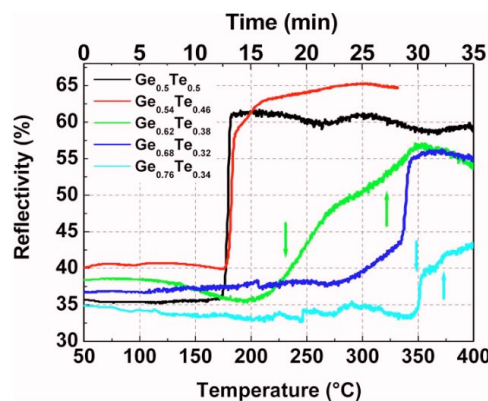


Figure 33. Change in reflectivity as a function of temperature for various GeTe compositions [58].

Other properties, such as the thermal conductivity also changes during phase change of the GeTe and have been studied in [72], which shows a conductivity of 2.3 W/m.K in the crystalline state and 0.3 W/m/K in the amorphous state, which constitutes almost one order of magnitude of contrast as shown in Figure 34.

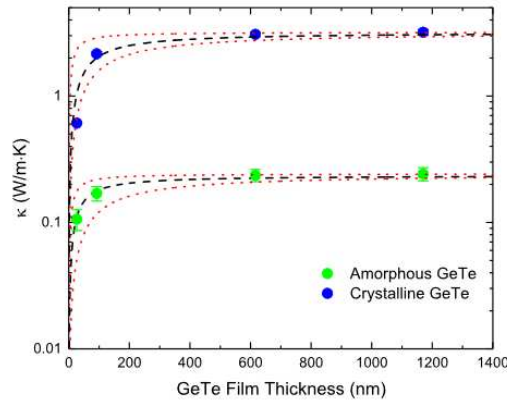


Figure 34. Measured thermal conductivity of an amorphous and crystalline GeTe samples for various thickness samples. From [71].

Studies of PCM crystallization using laser pulses have shown the need of energies as high as  $46 \text{ mJ/cm}^2$  for achieving the crystalline state using 532-nm laser, and energies as high as  $90 \text{ mJ/cm}^2$  to amorphized a 100-nm thick sample [73]. The reported crystallization time was about 20 ns and the amorphization time was about 50 ns. Other reports such as in [74] show crystallization times of around 15 ns for a 20-nm thick GeTe layer using an 8 ns green laser pulses (532 nm) with a fluence of  $28 \text{ mJ/cm}^2$ . The amorphization process is observed for a fluence of  $74 \text{ mJ/cm}^2$ .

The crystallization time of PCMs is not a fix value and depends on many parameters like the substrate on which the PCM is fabricated and its thickness. Different authors have reported different crystallization times. In [71] it is reported that a 30-nm GeTe layer obtain on a 100-nm thick  $\text{SiO}_2$  layer on a silicon substrate crystallizes in 1  $\mu\text{s}$ , for an as-fabricated layer, as shown in Figure 35. However, it seems that the crystallization time for melt-quenched sample (switched to the amorphous phase after initial crystallization) is much lower. For example in both [71] and [64] a crystallization time lower than 30 ns is reported for the same 30-nm thick GeTe layer, respectively. Efforts are still done in order to reduce as much as possible the crystallization time, as for example in [75], where the crystallization time of the as-obtained 20-nm GeTe layer was reduced up to 20 ns by fabricated the GeTe over a 5-nm thick  $\text{Sb}_2\text{Te}_3$  crystalline layer.

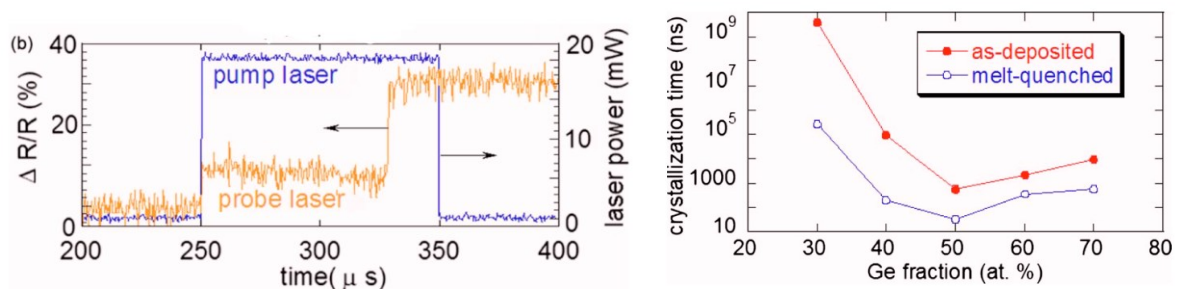


Figure 35. Crystallization time measurement of a 30-nm GeTe layer. a) Probing system using lasers. b) Crystallization time as a function of Ge percentage composition. From [72].

#### 1.5.4.2. Germanium Antimonium Telluride (GeSbTe) composition

Alloys based on Ge-Sb-Te compositions have been one of the most studied and used composition for optical storage applications. The first identified compositions for optical storage are  $\text{GeSb}_2\text{Te}_5$  and  $\text{Ge}_2\text{Sb}_2\text{Te}_5$  in 1990s [76]. These compositions were deemed useful due to a long-term stability and fast crystallization rates (around 50 ns) using fast laser pulses

irradiation. Thus,  $\text{Ge}_2\text{Sb}_2\text{Te}_5$  (commonly referred as GST-225 or GST) has been particularly studied due to their high number of cyclability, up to  $10^6$  in memory applications [77].

In terms of electrical properties, GST compositions have been shown to presents a resistivity contrast of around 5 orders of magnitude as shown in Figure 36. In this figure, the evolution of the surface resistance as function of temperature is recorded. As the material is heated up, an exponential decrease of resistance is observed until the crystallization temperature. An interesting observation is that the transition occurs in two phases: a first transitions occurs at around  $160^\circ\text{C}$  where the amorphous sample transforms into a crystalline state with rhombohedral structure followed by a gradual transition to a cubic structure form.

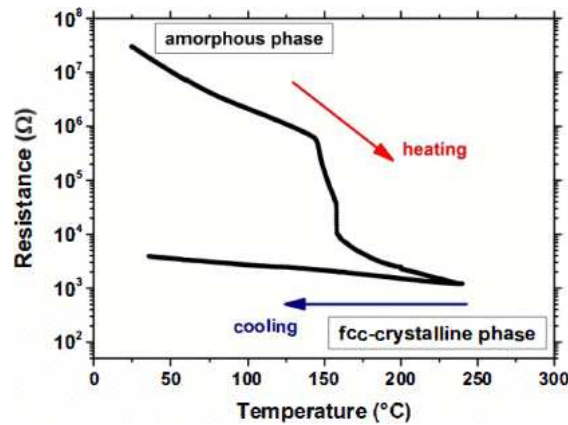


Figure 36. Surface resistance evolution as a function of temperature for a GST composition [76].

As in the case of GeTe, the crystallization temperature of the sample depends on many factors as for example the heating rate or the environment (stack of materials), as observed in Figure 37 [78].

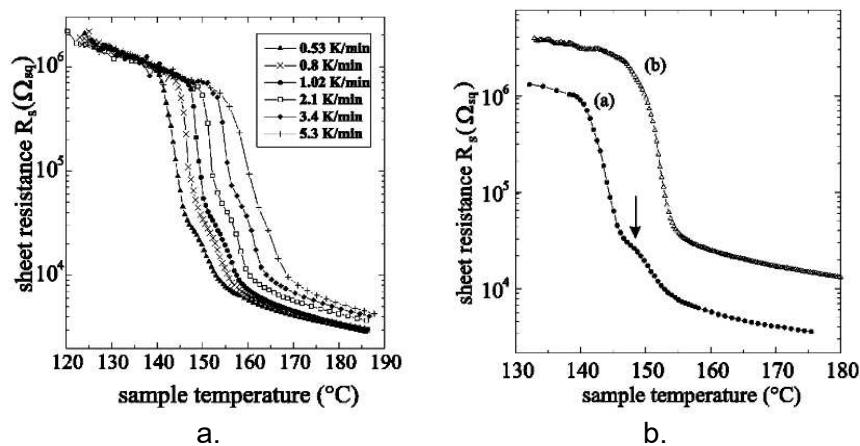


Figure 37. a) Surface resistance evolution of 80-nm thin film. b) Surface resistance evolution for a 80-nm GST thin film covered by a 4.5-nm ZnS-SiO<sub>2</sub> capping layer. From [76].

As is the case with GeTe composition, GST material has a high contrast of optical reflectivity between the two states, as shown in Figure 38 [70].

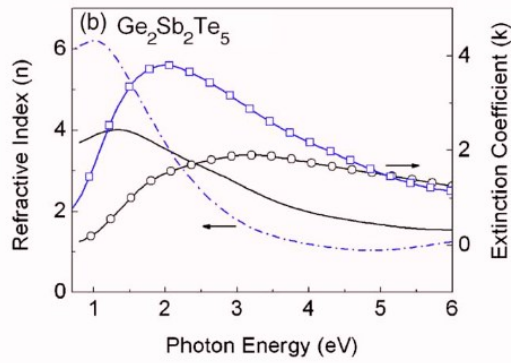


Figure 38. Measured optical properties of a sample of GST in amorphous (blue trace) and crystalline state (black trace) [68].

However, the deposition method of GST have been showed to influence the structure of the sample as shown in Figure 39 [79]. In this work, it was observed that different deposition methods influence the stoichiometric composition of GST samples and therefore induce small but notable differences in its properties (for example, the optical properties [74]).

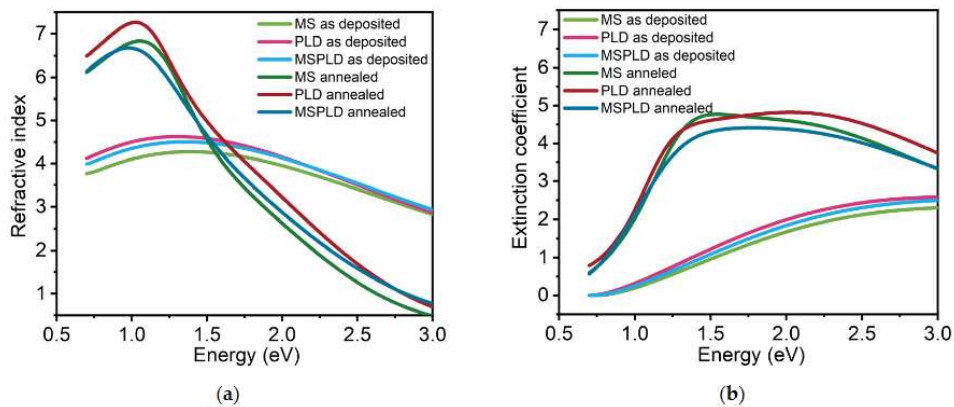


Figure 39. Measured influence of the deposition method on the optical properties of a 30-nm GST film for amorphous (as deposited) and crystalline state (annealed) [74].

Other properties such as thermal conductivity changes have also been reported as in [80], where GST is recorded to have a thermal conductivity of 0.4 W/m.K in the crystalline state and 0.19 W/m.K in the amorphous state.

### 1.5.5. PCM applications in radiofrequency circuits

The most common and direct application of PCMs into radiofrequency systems is their use as RF-switches. For high frequency applications, RF switches must respond to various requirements to be deemed useful such as:

- Low insertion losses in the ON state.
- High isolation in the OFF state.
- Low return losses.
- Fast switching between the ON and OFF state.
- High power handling.
- Long operational life (high number of cycles).

Unfortunately, most of the time, a trade-off needs to be done between these requirements. For example, in order to achieve high power handling, devices need to be significantly big and bulky, which decreases the switching time and may induce higher losses in the ON state. Another trade-off example is the low insertion loss versus high isolation. For this case, very low insertion losses in the ON state can be achieved by reducing the size of the switch but this may hinder the isolation in the OFF state. For these reasons, many different technologies exist in the market for RF-switches, such as semiconductors (CMOS or diodes) or mechanical components such as RF-MEMS, mechanical or magnetic relays. Each solution brings its own sets of advantages and disadvantages. The interest of RF switches based on PCM compositions came from their noteworthy properties such as:

- Their bi-stability as they retain their conductive or insulating state without the need to maintain polarization (non-volatile memory effect), leading to low overall energy consumption.
- Abrupt switching of electrical resistivity (5-6 orders of magnitude) on a very wide frequency ranges (microwaves, millimeter-wave range and THz).
- Long-term stability of each of the states of the material (usually greater than 10 years).
- Very fast switching (electrical and/or optical activation - on a time scale of ns or even ps for optical switching).
- RF figure of merit for simple switches ( $FOM \approx R_{ON} \times C_{OFF}$  where  $R_{on}$  is the resistance of the switch in the ON state and  $C_{off}$  is the capacitance of the switch in the OFF state) superior to current semiconductor-based solutions.
- Easiness of integration (thin-film manufacturing at temperatures at or below 200°C, compatible with CMOS integration, on a wide variety of substrates).

These properties represent a real technological breakthrough in the high-frequency field, and may lay the foundations for numerous telecommunication-oriented applications. The first ever RF-PCM switch was demonstrated in [81] and since then, the use and interest in PCM-switches has increased dramatically as these devices have shown exceptional performances in RF-frequencies. In particular, the biggest advantage of PCM-based switches is that they do not require permanent bias thus no additional consumption of energy.

The basic operational principle of a PCM-based RF switch in the form of a four-terminal device can be easily understood thanks to Figure 40 from [82]. The Figure 40a shows a coplanar waveguide (CPW) transmission line integrating a GeTe pattern that serves as a switch. The GeTe pattern is inserted in between the RF path as shown in Figure 40b. When the GeTe is in the crystalline state, the GeTe act as a conductor, thus the path is closed allowing the RF signal to flow between the contacts. When the GeTe is in amorphous state, it behaves as an insulator and the RF path is open, therefore no signal is transmitted through the contacts. In order to transform the GeTe, a thin film resistor layer (TFR) of molybdenum under the GeTe is used as heater. The Mo layer is connected to two DC electrodes from which a DC current can be injected. This current heats-up significantly the Mo layer thus heating the surroundings. When the temperature is high enough, the GeTe layer is transformed to a specific state by indirect heating. The silicon nitride (SiN) layer act as an insulator between the DC heater path and the RF signal and allows a thermal coupling between the GeTe layer and the heater as shown in Figure 40c.

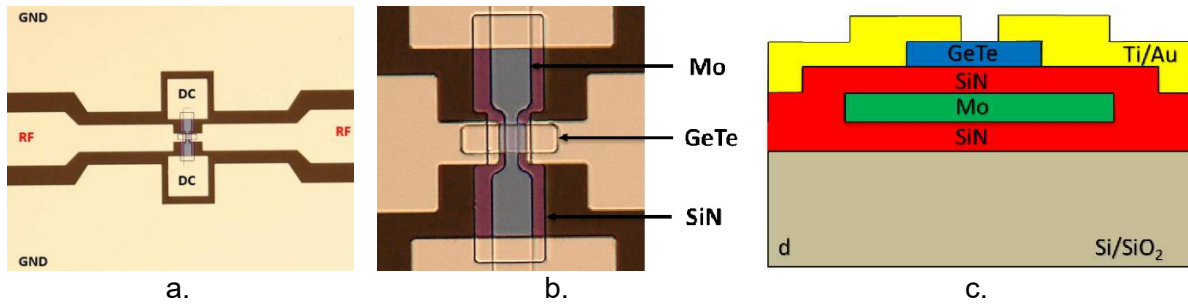


Figure 40. Example of a GeTe-based PCM-switch. a) Fabricated device. b) Close up to the GeTe composition. c) Schematic representation of the different layers of the circuit. From [81].

The device presented in Figure 40 shows isolations better than -22 dB up to 24 GHz but the insertion losses can go as high as 3 dB which can be attributed to very narrow size of the switch. This example demonstrates the trade-off that needs to be done between the performances of GeTe based switch and that the integration of PCM compositions in RF devices is not straight forward as one needs to consider not only the composition acting as a switch but also the surrounding elements (heaters), bias (DC electrodes) and type of substrate in order to activate the PCM, elements which may drastically influence the performance of the devices.

One of the most important aspects is that the need of the DC electrodes interferes with the shape of the ground plane thus degrading the performances of the device. By carefully choosing the size of CPW dimensions as well as the position of the bias, one can significantly improve the performances of the devices.

One of the key characteristics of PCM-based RF switches is their exceptional cyclability and reproducibility. Recently, in [83] is demonstrated that PCM-based RF switches (shown in Figure 41a) were functional after 1 billion cycles of commutation without noticeable degradation of the switches characteristics (Figure 41b). While in the ON state, the switch presents insertion losses smaller than 0.25 dB up to 40 GHz and isolation better than 15 dB in the OFF state as shown in Figure 41c.

As the fabrication technology improves, new and more performant RF-switch layouts are proposed, increasing the overall performances of PCM-based RF switches. In the current state of the art, PCM switches have shown switching times of 100 ns when passing from the crystalline state to the amorphous state with a 100 ns 20 V pulse (peak current of 100 mA) and switching times less than 2  $\mu$ s when passing from the amorphous state to the crystalline state with a 2  $\mu$ s 20 V pulse [84] (Figure 42 a).

The Figure 42b shows a comparison of the insertion losses in the ON state and isolation in the OFF state for various switching technologies [55]. From this image it can be noticed that RF switches based on PCMs present the lowest insertion losses (less than 1 dB) with the highest bandwidth (up to 67 GHz). However, the isolation performances of PCM-based RF switches, although good (better than 15 dB), is not as good as the performances of switching technologies based on silicon transistors which can reach up isolations better than 35 dB.

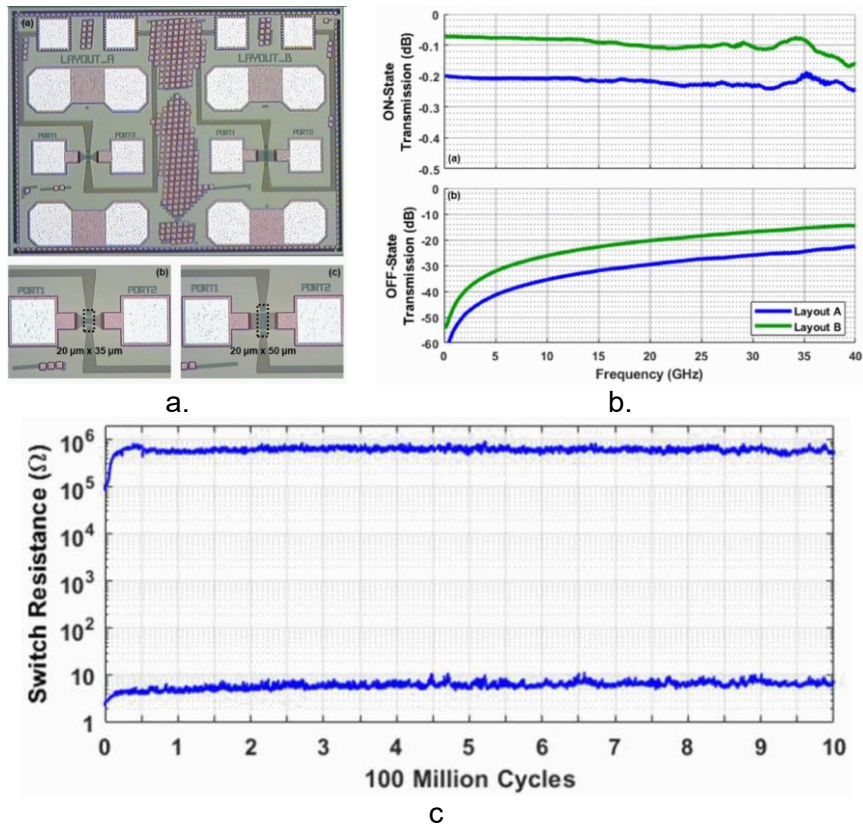


Figure 41. a) Optical image of two different layouts of the PCM-based RF switch. b) S-parameters performances in both ON and OFF states from both layouts c) Switch resistance performances over 100 million cycles [78].

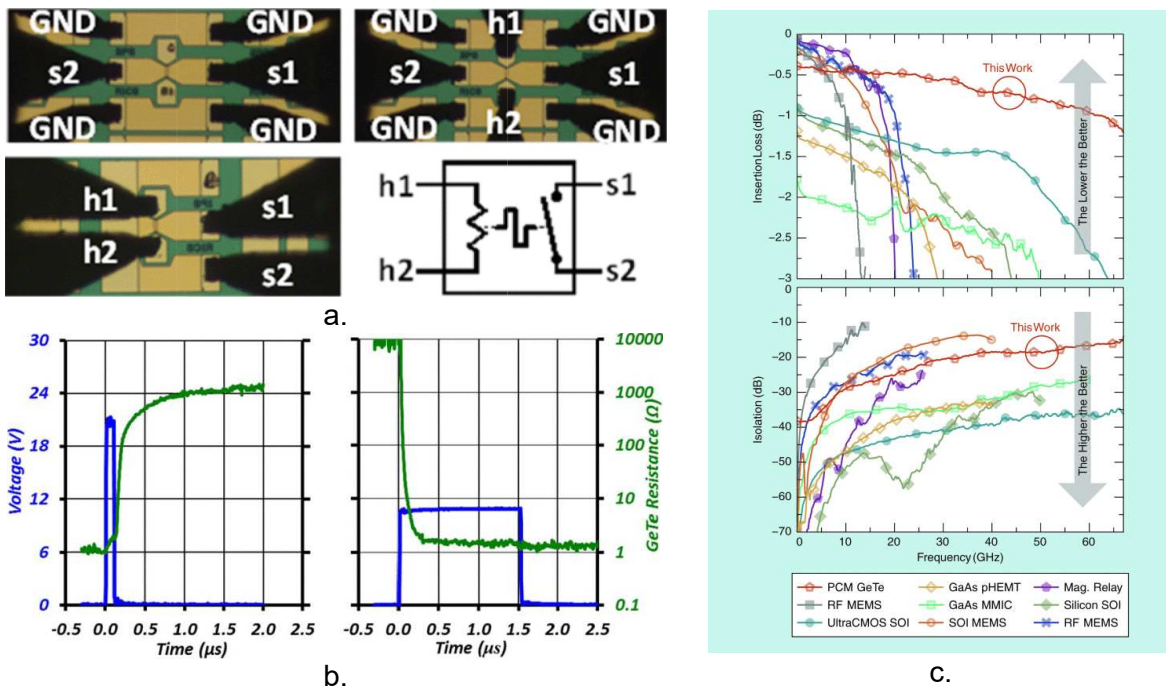


Figure 42. a) Layout of the proposed GeTe-based RF switch. b) Measured switching time of the amorphization (left) and crystallization (right) of a GeTe-based switch 0.9 μm length. c) Comparison of insertion loss in the ON state and isolation in the OFF state of PCM switches against other switching technologies.

However, more performant PCM-based RF switches often come together with a more complex and time-consuming fabrication process. As an example, Figure 43 shows the 14 steps fabrication process of an state-of-the-art PCM RF-switch developed in [55]. The fabrication process requires the sputtering deposition, photolithography patterning and lift-off of many different layers, which in turn requires highly specialized equipment and careful alignment between the different layers.

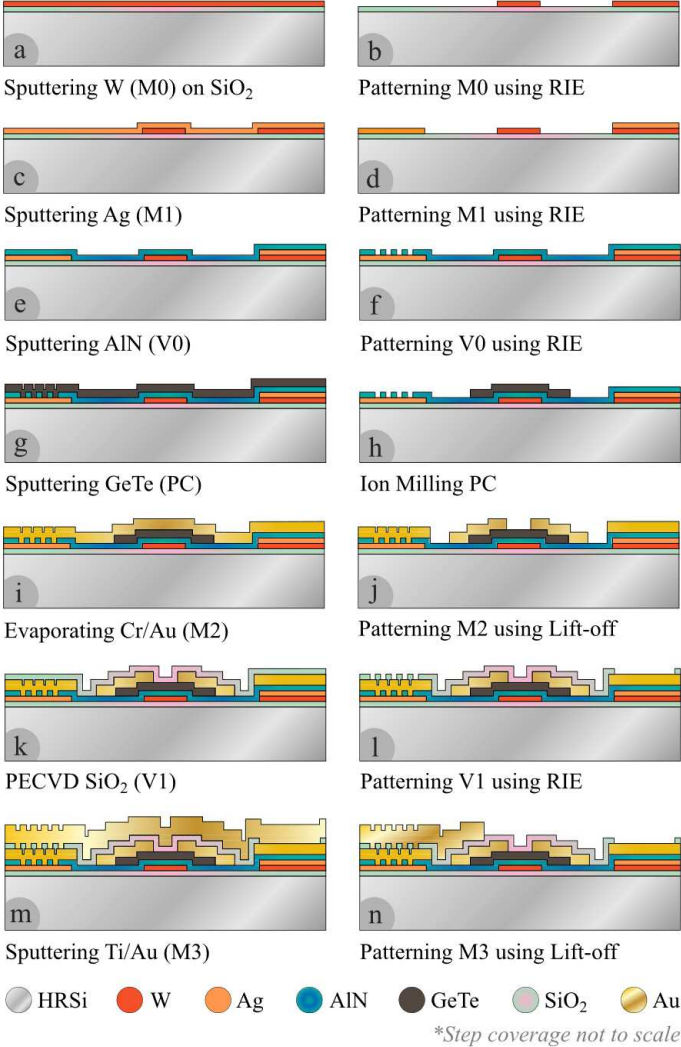


Figure 43. Example of fabrication process of a high-performant GeTe based PCM-switch [50].

Most of the difficulty of electrically activated PCM switches comes from the fabrication of the patterned thin-film heater and its excitation bias. An interesting alternative is the use of optical excitation using single laser pulses in order to transform the material. An example of this concept of activation has been presented in [85] where the state of the switch can be changed by using a single UV laser pulse of 30 ns. The use of laser pulses massively simplifies the layout and the fabrication process of the device, as shown in Figure 44a, as the need of polarization lines and a heater are no longer required. This device presents insertion losses as low as 0.6 dB up to 67 GHz for a 3 μm size pattern and isolations as high as 17 dB for 60 μm size patterns as shown Figure 44b.

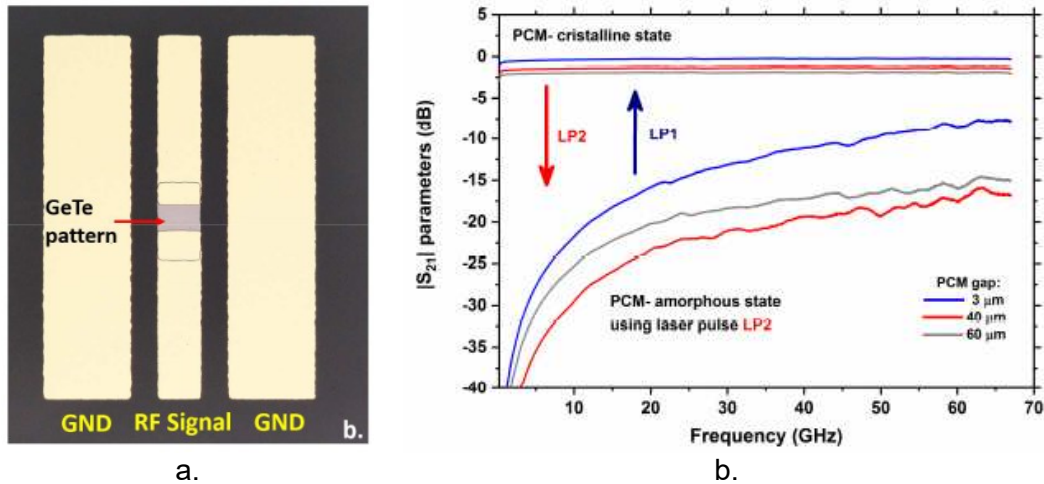


Figure 44. a) Fabricated of a simple GeTe RF-switch without heater. b) Measured performance of both states after laser irradiation for different GeTe gaps [80].

The excellent performances of PCM-based RF-switches has attracted the attention of these materials for their use in other high frequency devices such as antennas and filters.

In [86], a mmWave antenna with polarization state reconfiguration integrating a GeTe pattern is presented. The reconfiguration is possible by replacing the metallic edges of a square patch with a GeTe composition that is transformed by laser irradiation. Depending on the state of the GeTe (amorphous or crystalline) different polarization states are possible as seen in Figure 45a. This device takes advantage of the optical activation strategy presented previously to simplify the design and minimize any perturbation in the radiation characteristics of the antenna. When the upper-right and lower-left edges are crystalline while the rest are amorphous, the antenna presents circular polarization of type LHCP. When the upper-left and lower-right edges are crystalline while the rest are amorphous, the antenna presents circular polarization of type RHCP. When all the edges are crystalline or amorphous, the antenna presents linear polarization. The X-shaped slot is used to align the resonance frequency with the AR minimum. The Figure 45b shows the  $S_{11}$  measurements of all states of polarization from which it can be seen that the first three states (LHCP, RHCP and LP) can exist in the same frequency band. The antenna exhibits a  $S_{11}$  passband better than 5% for all configurations with a gain better than 6.4 dBi and efficiencies better than 67% as shown in Figure 45c. The axial ratio of the RHCP and LHCP is better than 3 dB with a fractional bandwidth of 1.7% as shown in Figure 45d (only the performances in the LHCP state are reported since, due to the symmetry of the antenna, the RHCP performances are expected to be identical as the LHCP case). The work reported in [86] is, to our best knowledge, the first ever report of a reconfigurable antenna integrating a PCM composition.

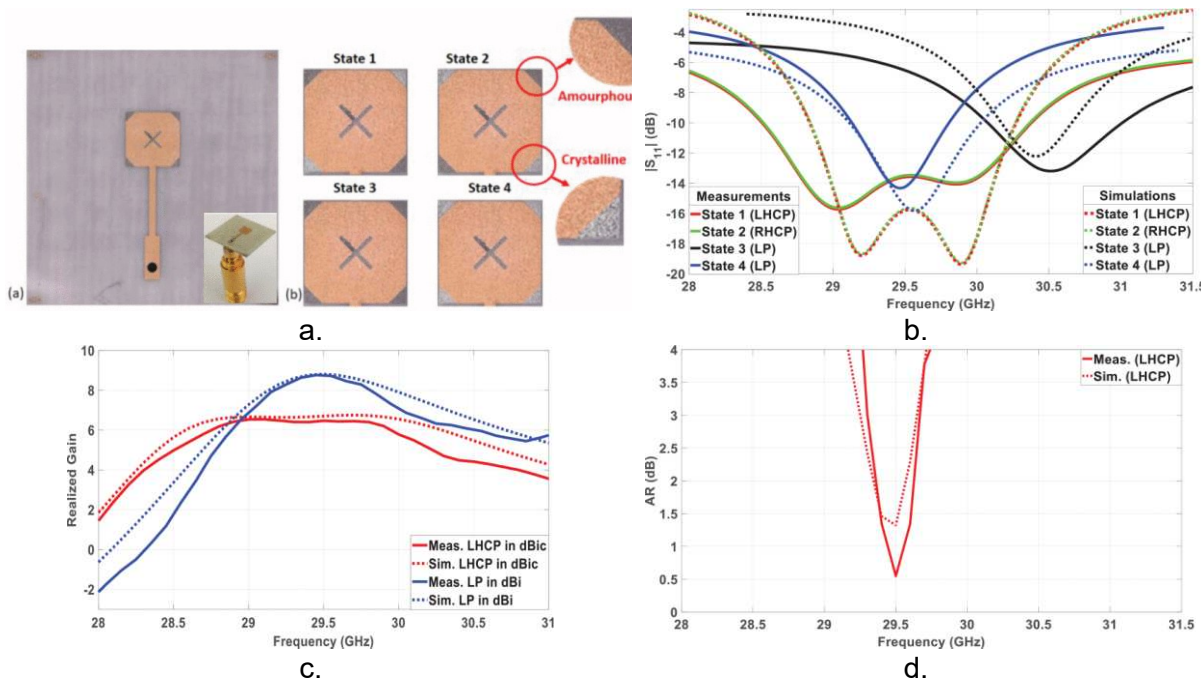
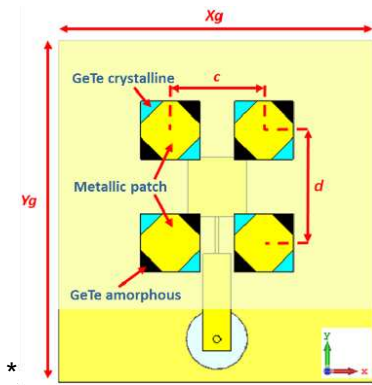


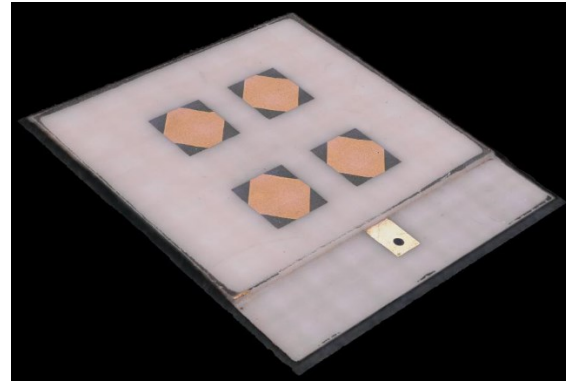
Figure 45. Optically activated planar antenna integrating a GeTe composition for polarization reconfiguration. a) Fabricated device. b) Measured  $S_{11}$  performance in all states. c) Simulated and measured realized gain in LHCP and LP state. d) Simulated and measured axial ratio in LHCP state. From [81].

However, the performances, although acceptable, can be enhanced notably by using an array of antennas in order to increase the gain and the bandwidth. Indeed, this solution has been extensively studied at the XLIM laboratory [87]. The proposed device consists of a  $2 \times 2$  array of antennas over two stacked substrates of ROGERS 4003C as shown in Figure 46a. Both substrates have a thickness of  $406 \mu\text{m}$  and are bonded together with a  $102\text{-}\mu\text{m}$  thick adhesive film (RO4450F). The edges of the four antennas at the top surface have been replaced by a  $1\text{-}\mu\text{m}$  thick GeTe composition. The distance separating the array in the y and x directions have been extensively studied in [87] and chosen such that the  $\text{TM}_{01}$  mode is correctly excited in each antenna ( $c = 3,8 \text{ mm}$ ,  $d = 4,6 \text{ mm}$ ). The array is excited by a coupling patch antenna in between both substrates. The coupling patch is matched to a  $50 \Omega$  impedance line by a quarter-wavelength impedance transformer. The  $50 \Omega$  line is connected to a  $50 \Omega$  coaxial connector. The fabricated device is shown in Figure 46b.

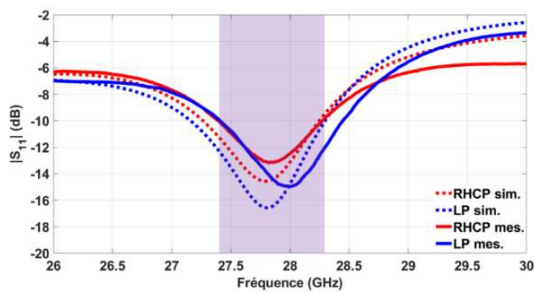
The Figure 46c shows the measured and simulated S-parameters of the LP and RHCP configurations of the array from which we can observe a matching level better than  $-10 \text{ dB}$  for both configurations at the same frequency range (from  $27.4 \text{ GHz}$  up to  $28.3 \text{ GHz}$ ). The measured and simulated gain and efficiency for the LP configuration are shown in Figure 46d from which a maximum gain of  $9.2 \text{ dBi}$  with an efficiency of  $64\%$  is observed at  $28 \text{ GHz}$ . The Figure 46e shows the measured and simulated axial ratio of the RHCP configuration from which we can observe an axial ratio lower than  $3 \text{ dB}$  from  $27.4 \text{ GHz}$  up to  $28.6 \text{ GHz}$ . The Figure 46f shows the measured and simulated gain and efficiency of the array from which we can observe a maximum gain of  $8.7 \text{ dBi}$  with an efficiency of  $67\%$  at  $27.7 \text{ GHz}$ .



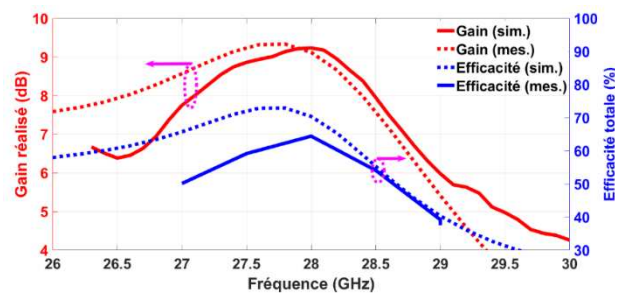
a.



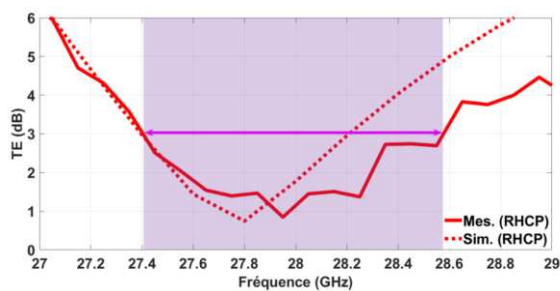
b.



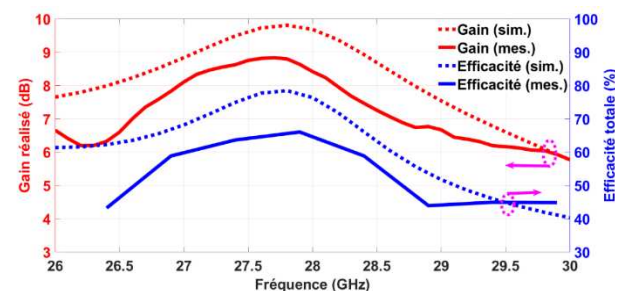
c.



d.



e.



f.

Figure 46. Polarization reconfigurable array of antennas integrating a GeTe composition. a) Complete geometry of the array of antennas integrating a GeTe composition. b) View of the fabricated array of antennas integrating GeTe in the amorphous state (dark gray color). c) Simulated and measured S-parameters of the LP and RHCP configurations. d) Measured and simulated gain and efficiency of the LP configuration. e) Measured and simulated axial ratio of the RHCP state. f) Measured and simulated gain and efficiency of the RHCP configuration.

Another example of a complex RF function is shown in [88] a where a frequency reconfigurable band-pass filter integrating a GeTe composition is presented. The topology of the microstrip filter is the one of a third-order parallel-coupled half-wavelength resonators fabricated on a 0.45-mm thick c-cut sapphire substrate as shown in Figure 47a. The frequency reconfigurability is obtained by adding a GeTe pattern of length  $\delta l$  at the end of each resonator. In the amorphous state (as shown in the upper-half of Figure 47c), the GeTe is non-conductive and therefore the total length of the resonator is given by  $L$  with a resonance frequency of 34 GHz as shown in Figure 47b. When the GeTe is transformed to its crystalline state (as shown in the bottom half of Figure 47c) the total length of the resonator becomes  $L + \delta l$  thus lowering

the resonance frequency of the resonator resulting in a shift down of the band-pass frequency as shown in Figure 47b.

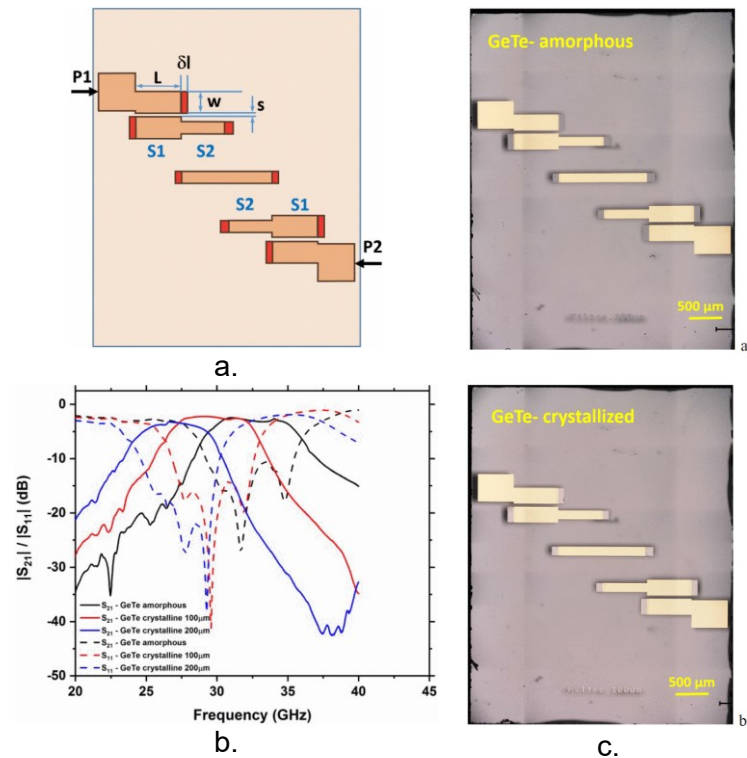


Figure 47. a) Schematic representation of the parallel coupled half-wavelength filter b) Measured S-parameters of the filter in both states of the GeTe. c) Optical images of the filter integrating a GeTe pattern in the amorphous state (upper-half) and in crystalline state (lower-half). From [88].

It is clear that high frequency devices integrating PCM compositions have shown remarkable performances most notably for RF-switches. Their ease of fabrication, fast commutation, bi-stability and relatively high conductivity even up to mmWave frequencies allows the integration into more complex devices such as metasurfaces or reconfigurable intelligent surfaces (RIS). In particular, the capability of activate them by using laser pulses, thus avoiding the need of polarization lines, further simplify their integration into these complex devices.

## 1.6. Conclusions

In this first chapter we have presented a brief introduction to mmWave-band communication and its advantages as well as its drawbacks. This frequency band has shown potential for high speed digital communication allowing for additional communication frequencies and applications. Furthermore, the use of high frequencies allows for devices that are much smaller. On the other side, mmWave frequencies suffers from a high amount of attenuation due to atmosphere and weather-related phenomena. Thus, in order to counter these impairments, high performance reconfigurable RF devices are needed in order to optimize their properties in situ.

We introduced the notion of reconfigurable antennas and the different strategies used for provide the devices with reconfiguration capabilities. Most common techniques uses RF switches such as PIN diodes, varactors, MEMS switches in order to modify either the shape of the antenna or of the feeding circuit connected to the antenna. These solutions have proved suitable for creating reconfigurable antennas for low-frequency applications, but present many drawbacks at high-frequency, such as high losses for PIN diodes or slow switching action for

MEMS. More notably, the nature of this type of RF switches only allows for discrete states which limits the capabilities of reconfigurable antennas. Other alternatives are the use of varactor diodes and functional materials like ferroelectrics. These solutions have the advantages of providing a continuous reconfiguration for the antenna, but they still present some disadvantages, more notably the need of very high polarization voltages and high losses at high frequencies. Finally, new solutions such as the use of phase transition materials (PTM) have shown promising performances for their integration into RF reconfigurable devices due to their high contrast in conductivity between both states, easiness of integration and very fast switching, up to very high frequencies (including THz). However, PTMs also suffers from sensitivity to temperature and require deposition compatible substrates, which often implies the use of high permittivity substrates that can be detrimental to the antenna performances.

Indeed, many strategies for reconfigurable antennas have been evaluated, each with their own merits and drawbacks; nonetheless a common point between all these previous solutions is their volatile nature which implies the use of a constant energy supply in order to retain a specific state (usually the ON state). Thus, constant energy supply implies a continuous consumption of power that, in the long term, can lead to very inefficient performances of the device. For these reasons, a new solution for reconfigurable devices is the use of phase change materials (PCMs) which, like the PTMs, presents a very high contrast between their insulator and metallic states, with the advantages of been bi-stable, meaning that they retain their specific state even after the energy source of excitation is removed.

Then next part of the chapter was focused on the description and properties of PCM compositions. The process by which a PCM transforms between an amorphous phase to a crystalline state (and vice-versa) was introduced, as well as the parameters describing this transformation. In summary, at temperatures lower than the melting temperature, the crystallization dynamics is described by a single parameter, the activation energy  $E_g$ . This parameter describes the speed at which the crystallization occurs and gives a sense of the "stability" of the sample. In order to complete the amorphous-to crystalline transition, the PCM composition has to be heated up above its melting point (transform it into a quasi-liquid state) and then cool it down very fast (fast quenching).

PCMs are largely used in non-volatile solid-states memory applications due to their ease of integration and fabrication. For RF applications, the most used and studied compositions are alloys of GeTe and  $\text{Ge}_2\text{Sb}_2\text{Te}_5$ . In particular, GeTe presents a high contrast in resistivity up to 5 or 6 orders of magnitude. This composition has already shown excellent performances in RF switches with very low insertion losses, switching times less than 2  $\mu\text{s}$  and cycling reliability up to 100 million cycles without significant degradation.

However, more performant devices using PCM-based RF switches often comes with a more complex fabrication process in order to integrate the required polarization circuit meant to indirectly heating the material. As these polarization and activation circuits may perturb the performances of PCM devices, an alternative for the activation of PCM devices is the use of laser irradiation in order to locally heat the material, which massively simplifies the integration of PCMs into reconfigurable systems. Additionally, the use of laser irradiation has other advantages over electrical activation such as nanosecond (or even faster) switching times.

# Chapter II. Characterization and optical modification of the state of Phase Change Materials (PCM).

---

*“A theory is something nobody believes, except the person who made it. An experiment is something everybody believes, except the person who made it.”*

*Albert Einstein*

## II.1. Introduction

In this chapter, we will focus primarily on the characterization of the electrical and dielectric properties of phase change thin-films for their integration into radiofrequency systems as well as the study of reversible optical activation of insulator-to-metal transitions of PCMs fabricated at XLIM laboratory.

The electromagnetic characterization will focus primarily on the amorphous (metallic) state of the PCM and the extraction of the permittivity value and the loss tangent. The knowledge of these values in the millimeter-wave band is important to evaluate the performances of complex radiofrequency systems integrating PCMs by means of 3D electromagnetic simulations. The stability of the materials is also an important system requirement and was explored for GeTe and Sb<sub>2</sub>Te PCM compositions.

Finally, the use of a laser system is explored to locally crystallize and amorphize the PCM layers. For these experiments, we will focus exclusively on the GeTe composition. The GeTe was characterized in the optical domain and the extracted data was then used in multi-physics COMSOL simulations to explore the heating effects of laser pulses in PCMs while considering a thermally driven phase change mechanism. Additionally, an optical scanner system was implemented in order to write and erase crystalline specific zones on large surface area PCM surfaces using fast raster scanning.

## II.2. Fabrication of thin PCM layers

Radiofrequency circuits integrating PCM thin films are fabricated by means of microfabrication techniques. These techniques consist of stacking and patterning layers of materials until the desired structure is completed. The dimensions of these layers can go from 0.1 nm (atomic layers) up to hundreds of micrometers, depending on the deposition technique, but typical thicknesses range from 10 nm up to 1 μm [89]. The process of microfabrication consists of four basic operations (although not all of them are required to fabricate RF circuits):

1. High-temperature processes or ion implantation: Used for diffusion process and modification of the distribution of dopant atoms (crucial for the fabrication of transistors).
2. Thin-film deposition: Used for fabrication of thin layers on wafers/ substrates.
3. Patterning: Used to define specific areas of thin films over the wafer using electron-beam or photolithography.
4. Layer transfer and bonding: Refers to the attachment of wafers to another one via physical or chemical processes.

Microfabrication takes place under carefully controlled conditions of air purity (lack of air contaminants, particles etc.), temperature, humidity, and vibration. Otherwise, micrometer-scale structures would be damaged by air contaminants/ particles, or vibrations or temperature and humidity fluctuations will drastically affect the reliability of the lithographic processes. Even though extreme care is taken to ensure cleanliness during microprocessing, some devices will always be defective due to stochastic errors. Other kinds of errors are systematic, like equipment and operator failures, or impurities in starting materials or design errors.

The quality of RF systems integrating PCM thin films depends greatly on the quality of the deposited films. At the same time, the properties of the obtained PCM are dependent on the fabrication method as seen in chapter 1. Deposition conditions strongly affect the thin film properties either by incorporating impurities during the deposition or the temperature at which

the deposition occurs. In addition, the materials (both the substrate and the thin film) must be amenable to microfabrication patterning techniques like etching and tolerate various types of thermal, physical, and chemical treatments (like reactions or diffusions during wet or dry etching). The substrate on which the thin film is deposited plays an important role in the film's quality; in particular, substrates with low roughness are desired to mitigate the losses in the circuit at millimeter-wave band frequencies. Substrate cleaning using specific recipes by chemical and physical methods is very important, specifically for thin ( $\leq 500$  nm) films.

There are many different techniques for the deposition of thin films. In our work, we used the DC magnetron sputtering technique since it allows us to grow uniform and large surfaces of materials. Magnetron sputtering belongs to the class of physical vapor deposition (PVD) techniques, in which a plasma discharge is initiated in an inert gas atmosphere (usually argon, Ar) from a cathode (the sputtering target). The atoms of the target are ejected toward the substrate situated in close vicinity, which is collecting the sputtered material and will form the thin film. Many parameters of the deposition process must be optimized in order to grow high-quality films. These parameters are:

1. Pressure of the chamber and gas flow: This parameter influences the structural properties of the film.
2. Temperature of the substrate: Higher temperatures during the deposition process favor the mobility of atoms on the surface of the substrate, thus creating a more homogeneous film.
3. Power of the magnetron: The power of the magnetron defines the rate at which the thin film is grown; a higher power will result in a faster deposition rate. However, very high power may result in unstable plasma as well as damage of the sputtered target.

These parameters are material dependent. For the GeTe thin-film deposition using DC magnetron sputtering, these parameters have been optimized at XLIM laboratory in previous works [90] on a Plassys MP 300 system and are summarized in Table 2:

Table 2. Parameters for the deposition of thin layers of GeTe using DC magnetron sputtering.

| Parameter             | Value  |
|-----------------------|--|
| Target                | GeTe, 50:50 wt/, 2" diameter                 |
| Chamber pressure      | $5 \times 10^{-3}$ mbar                      |
| Gas flux (Argon)      | 60 sccm                                      |
| Substrate temperature | 150 °C - 250 °C (depending on the substrate) |
| Magnetron power       | 50 W   |

These parameters produce a stable plasma with a deposition rate of around 50 nm/min. Before each deposition process, the substrates are cleaned using an ultrasonic bath in acetone, then isopropyl alcohol followed by an osmosis-purified water bath. Finally, the substrates are dried with a flux of dry compressed air. Additionally, before each deposition, a 10-minute long pre-sputtering step is performed in order to remove the eventual oxidation of the target.

To define the structure of the circuit, the material has to be etched away locally, which constitutes the patterning process. This process defines the structures of interest by firstly

applying a photoresist film over the obtained layer, then using photolithographic patterning of the resist (lithographic mask and UV exposure using a Suss Microtec MJB4 mask aligner), which then acts as a mask for wet or dry etching or modification of the underlying material.

## II.3. Electrical characterization and phase change of PCMs

### II.3.1. Phase change by direct heating

GeTe layers of different thicknesses (250 nm, 500 nm, and 1000 nm) were initially obtained in the amorphous insulating state and can be easily transformed into their crystalline conducting phase by a direct heating cycle from 23°C to 300°C, on a hot plate with a 5°C/min ramp, followed by cooling at room temperature. The evolution of the surface resistance of the layers with the three dissimilar thicknesses is shown in Figure 48. The change in resistance of GeTe layers as a function of temperature was recorded using two electrical probes spaced 1 mm apart. The material undergoes a sudden and irreversible change in resistance toward the metallic phase at ~180°C (crystallization temperature), with a decrease in resistance of about five orders of magnitude. During the cooling cycle, the material retains its crystalline state with low resistance, showing the bi-stability or the non-volatile behavior of GeTe.

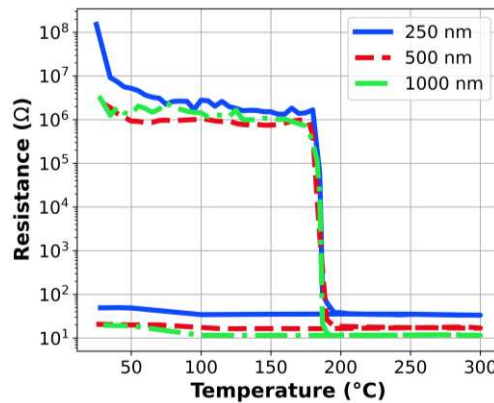


Figure 48. Evolution of the surface resistance as a function of temperature of a 250-nm, 500-nm and 1000 nm-thick layers of GeTe obtained on a c-cut (0001) sapphire substrate.

Similar experiments were performed on other PCM compositions like  $\text{Ge}_2\text{Sb}_2\text{Te}_5$  (GST) and  $\text{Sb}_2\text{Te}$ , shown in Figure 49. The three compositions (obtained under similar experimental conditions mentioned in Table 2 -except for  $\text{Sb}_2\text{Te}$  which requires a magnetron power of 20 W) were transformed to their crystalline states using the same procedure). The  $\text{Sb}_2\text{Te}$  composition presents the lowest temperature transitions at around 135 °C which is an advantage over the other compositions since a lower crystallization temperature translates into a need for lower energy to activate the material to its crystalline state. For the GST, a gradual transition is observed starting from around 180°C and completely crystallized at 350 °C, this gradual transformation is characteristic of the GST composition. Another important observation is the surface resistance at both the GST and  $\text{Sb}_2\text{Te}$  amorphous and crystalline states also presents the lowest conductivity ratio between the two states (4 orders of magnitude) while the GeTe presents the highest one (up to 7 orders of magnitude).

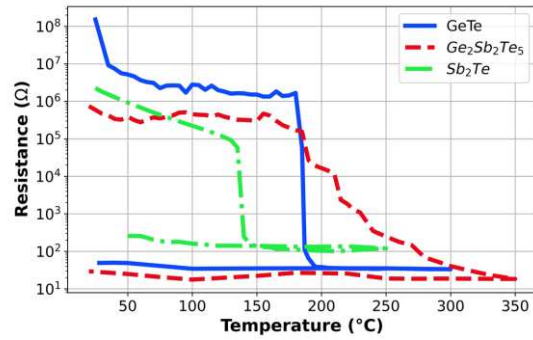


Figure 49. Evolution of the surface resistance as a function of temperature of a GeTe, GST and Sb<sub>2</sub>Te PCM compositions obtained on a c-cut (0001) sapphire substrate.

The Figure 50 shows an optical image of a sample of a 250-nm thick GeTe layer deposited over a sapphire substrate in the amorphous state (as deposited) and crystalline state (after baking).

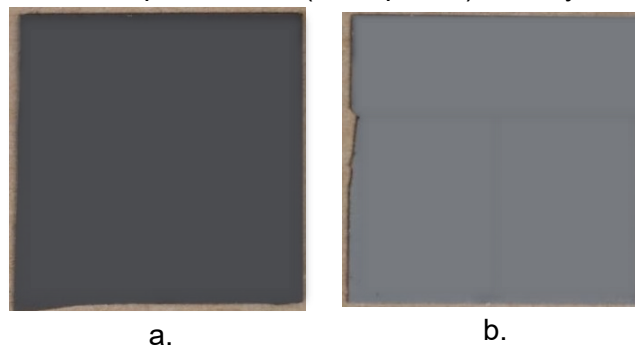


Figure 50. Optical images of a 250-nm layer of GeTe deposited over a 25x25 mm<sup>2</sup> sapphire substrate in a) amorphous state and b) crystalline state.

This capability of changing between a non-conductive to a conductive state can be exploited in order to create reconfigurability in RF circuits, as already illustrated in the introductory chapter 1.

### II.3.2. Conductivity in both insulating and conductive states of GeTe and Sb<sub>2</sub>Te

When the thickness of the PCM layer deposited on a substrate is known, the electrical conductivity of the PCM layer is determined by measuring its surface resistance or square resistance. A simple and non-destructive method to determine the conductivity of a thin PCM layer is the four-point probe method shown in Figure 51.

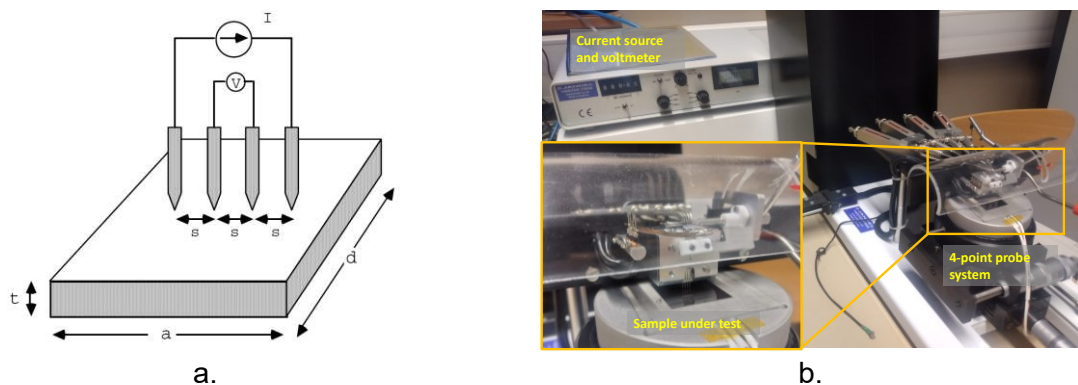


Figure 51. a) Schematic representation of the 4-point probe technique to extract the conductivity of thin films. b) Measurement system employed to measure the conductivity of the film.

This method consists in placing four inline metal probes separated by a length  $s$  of 1 mm in contact with the surface of the layer to be studied. The two outer probes are used to inject a current  $I$  while the inner probes are measuring the voltage drop  $V$ . Thus, we can deduce the square surface resistance and the conductivity of the layer using the following equations:

$$R_s = \frac{V}{I} \cdot C_{fd} \cdot C_{ft} \quad (9)$$

$$\sigma = \frac{1}{R_s \cdot t} \quad (10)$$

where  $t$  is the thickness of the layer and  $C_{fd}$  and  $C_{ft}$  the geometrical correction factors depend on the dimensions of the layer.

Table 3 shows the extracted conductivities (using equations (9) and (10)) of three GeTe layers and two Sb<sub>2</sub>Te layers with different thicknesses obtained on sapphire substrates in both amorphous and crystalline states. From the results shown in Table 3, we can notice a change in conductivity greater than 6 orders of magnitude for GeTe. The difference in the observed measurements can be explained by an error in the estimation of the actual thickness of the GeTe layer with respect to the nominal value. Table 4 shows the same measures with two samples of Sb<sub>2</sub>Te from where it can be seen that the Sb<sub>2</sub>Te composition presents a change in conductivity of 4 orders of magnitude.

Table 3. Measured conductivity in both states (amorphous and crystalline) of three samples of GeTe deposited over a sapphire substrate.

| Thickness (nm) | Conductivity (S/m)   |                   |
|----------------|----------------------|-------------------|
|                | Amorphous            | Crystalline       |
| 250            | $1.8 \times 10^{-2}$ | $8.4 \times 10^4$ |
| 500            | $2.3 \times 10^{-2}$ | $2.3 \times 10^5$ |
| 1000           | $3 \times 10^{-2}$   | $4.5 \times 10^5$ |

Table 4. Measured conductivity in both states (amorphous and crystalline) of two samples of Sb<sub>2</sub>Te deposited over a sapphire substrate.

| Thickness (nm) | Conductivity (S/m) |                   |
|----------------|--------------------|-------------------|
|                | Amorphous          | Crystalline       |
| 130            | 3                  | $1.6 \times 10^5$ |
| 260            | 5                  | $1.2 \times 10^5$ |

From the two previous tables, it can be seen that both compositions have similar levels of conductivity in the crystalline state. However, it is also clear that the GeTe composition shows a bigger ratio of conductivity while having a lower conductivity in the amorphous state. Although a high conductivity in the crystalline state is desired in order to reduce the losses in RF circuits integrating PCMs, a low conductivity in the amorphous state is also desired, for example, to increase the isolation in RF switches [91] [92]. This difference makes the GeTe composition more suitable for RF applications. However, the use of Sb<sub>2</sub>Te composition may be interesting for applications where low activation energies between the two states are required.

### II.3.3. Stability tests of the amorphous phase in PCMs

One of the key advantages of PCMs is the bi-stability of both phases or the non-volatile character of each state. In this context, we refer to the stability as the ability of the amorphous material to remain in this state for long periods of time at a particular temperature [93] [94]. For information storage applications (where data is encoded in the amorphous regions), the PCM

must be able to keep its amorphous state for a minimum of 10 years at the operating temperature [95]. For optical disk storage, the operating temperature is the ambient temperature, but for embedded memory applications typical operating temperatures are around 85°C (or up to 150 °C for automotive applications [93]). For satellite applications, temperature can rise up to 130°C depending on the orbit of the satellite [96].

Obviously, waiting 10 years to verify if an amorphous region transforms into the crystalline state, is not feasible in practice. Therefore, accelerated tests on amorphous PCM samples are performed by baking the sample at a constant high temperature (called stress acceleration test) and monitoring the sample over time until it crystallizes. This analysis has been used extensively to estimate the lifetime of PCM-based memories for decades [97] [98]. The monitoring can be done electrically (by monitoring the surface resistance of the sample) or optically (by monitoring the reflectivity of the sample). By extrapolating the time taken to crystallize at higher temperatures, we can estimate the stability time at any desired operating temperature by means of the Arrhenius law.

### II.3.3.1. Activation energy and Arrhenius law

The time of reaction of many chemical and physical processes depends on the temperature  $T$  at which the reaction occurs. This dependence is described by the Arrhenius equation:

$$R(T) = A \cdot \exp\left(\frac{E_a}{k_b T}\right) \quad (11)$$

Where  $A$  is the pre-exponential factor,  $k_b$  is the Boltzmann constant,  $E_a$  is the activation energy for the reaction and  $R(t)$  is the reaction rate (which can be understood as the speed of the process or the time needed to finish the process). For our purposes, the reaction of interest is the crystallization time at a constant temperature of an amorphous sample. By taking the natural logarithm of equation ( 11 ), we obtain

$$\ln R = E_a \left(\frac{1}{k_b T}\right) + \ln A \quad (12)$$

If we define the quantity  $1/k_b T$  as the free variable, we observe that equation ( 12 ) defines a straight line where  $E_a$  is the slope of the line. By knowing the crystallization time  $R$  at (at least) two different temperatures, a straight line can be traced and  $E_a$  can be extracted directly from the slope of the line.

By analyzing ( 11 ), we can see that an amorphous sample will crystallize faster at higher temperatures. Another observation of interest is that the bigger the activation energy  $E_a$ , the slower the reaction time and therefore more time is required for the amorphous sample to crystallized which means that the sample is more stable.

### II.3.3.2. Stability time and activation energy of GeTe and Sb<sub>2</sub>Te compositions

Accelerated stress test were performed on three samples of a 250-nm thick GeTe deposited on sapphire substrates by magnetron sputtering using a new GeTe target with respect to the results previously shown. For this test, the PCM sample was kept to a constant temperature close to the crystallization temperature while recording the surface resistance evolution with time. The resistance-temperature behavior of this new batch of samples is shown in Figure 52, from which we notice a significant difference in the crystallization temperature ( $\approx 250$  °C) of the material with respect to previous sample, the difference coming out probably from the

different batches of the target material offered by the supplier (although similar composition and purity).

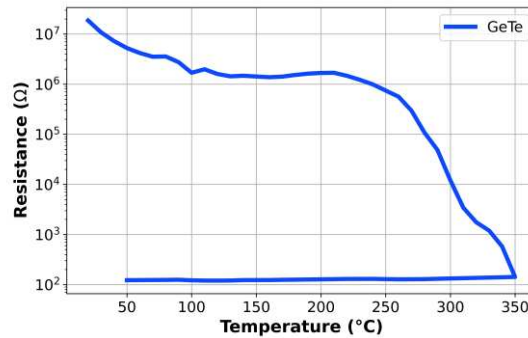


Figure 52. Evolution of the surface resistance of a 250-nm thick layer of GeTe (using a new GeTe target) as a function of the temperature.

The test was performed within a Linkam heating system at a constant temperature and the surface resistance was monitored over time with a two-probe system. For this test, the crystallization time is defined as the time needed for the surface resistance of the sample to fall under 50% of its initial value. Figure 53a show the results on the accelerated stress test at 230°C, 235°C and 240°C where it can be observed that the higher the temperature of the test, the fastest the amorphous sample crystallizes. The sudden increase in resistance at the end of the sample kept at 230°C is due to the heating plate turning off and cooling of the sample implying the increase of its resistance to the nominal value. A small increase with time of the surface resistance of the GeTe sample at 230°C can be observed and can be explained by resistance drift [99].

The crystallization time data points are shown in Figure 53b. By fitting a straight line, we can deduce an activation energy  $E_a = 2.69$  (eV) which is in agreement to similar reports in the literature [100]. By extrapolating the fitted line, we can estimate a stability time greater than 10 years for working temperatures under 164°C, which makes the GeTe composition suitable for memory applications, automotive or satellite applications.

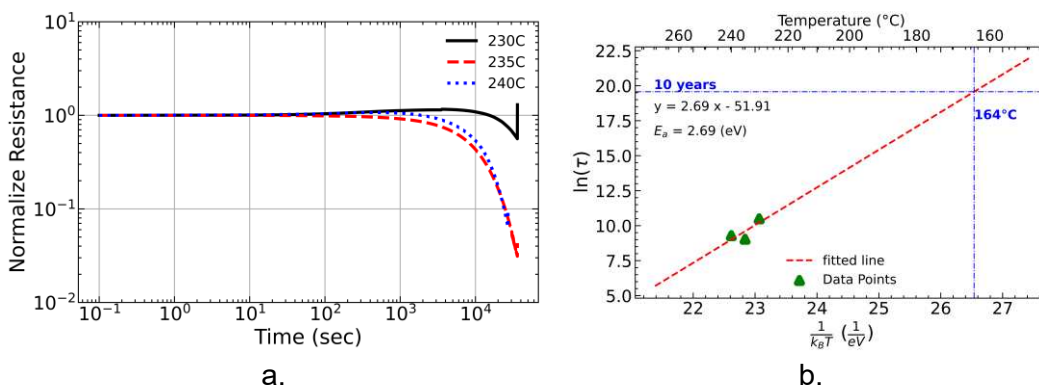


Figure 53. a). Stress acceleration test on three samples of GeTe deposited on a sapphire substrate. b) Linear plot of the Arrhenius equation showing the crystallization time of the accelerated temperature stress test on the three samples.

A similar stress test was performed on a 130-nm thick  $Sb_2Te$  composition over a sapphire substrate. The Figure 54a. shows the behavior of the normalize resistance over time while Figure 54b shows the three data points and the fitted straight line. We can extract an activation energy of  $E_a = 1.96$  (eV) (which agrees with other measurements in the literature [101]) and a

stability time greater than 10 years for temperatures lower than 47 °C. This low temperature threshold makes Sb<sub>2</sub>Te less suitable for reliable memory applications or any other application with operational temperatures above 50°C.

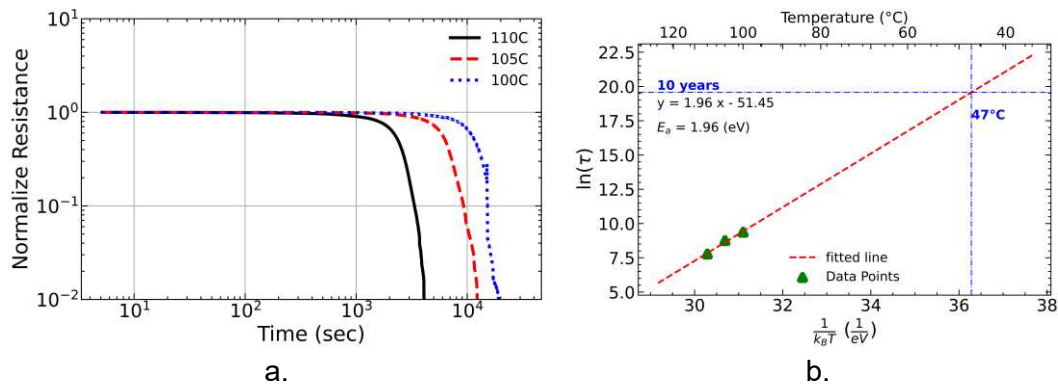


Figure 54. a). Stress acceleration test on three samples of Sb<sub>2</sub>Te deposited on a sapphire substrate. b) Linear plot of the Arrhenius equation showing the crystallization time of the accelerated temperature stress test on the three samples.

#### II.4. Dielectric permittivity characterization of thin layers of PCM

For an accurate design and analysis of complex RF functions (such as filters or antennas) integrating PCMs compositions, it is necessary to know their microwave properties in each of their states. Some compositions of PCM have been already characterized for frequencies less than 3 GHz and in the THz domain [102] [103] [104]. Unfortunately, there is no available data on the electromagnetic properties of PCMs at millimeter-wave frequencies. Additionally, since the thickness of the PCM compositions obtained on substrates is in the order of hundreds of nanometers, a characterization by means of conventional techniques can be difficult at higher frequencies, as shown in [102] and [104], where the fluctuations in the permittivity values can reach values as high as 20% for some compositions. Current techniques for measuring the dielectric permittivity are mostly based on cavity resonant techniques allowing accurate extraction of the permittivity value and the loss tangent of the material [105] [106]. However, these methods can only extract the permittivity of the material at a single frequency and the results are prone to substantial errors when the thickness of the layer to be measured is in the order of hundreds of nanometers, unless the permittivity of the material is very high. Alternative methods involve the measuring of transmission and reflection coefficients in a waveguide charged by the material to be characterized [107], [108]. However, these methods require a substantial volume of material and a proper installation of the fundamental propagating mode in the structure.

Other methods allows to extract the permittivity of thin films over a wide bandwidth by measuring the S-parameters of a single CPW integrating a thin layer of the material [109]. Then, the permittivity of the material can be extracted by comparing the propagation constant of the CPW to the one calculated by the method of Spectral Domain Approach [110]. However, this technique requires a full knowledge of the electromagnetic properties of the structure in which the thin film is integrated, such as the conductivity of the metal or the permittivity and losses of the substrate at the measurement frequencies.

### II.4.1. Methodology for the characterization of thin layers of PCM

We present here the broadband electromagnetic characterization of very thin layers of GeTe and  $\text{Ge}_2\text{Sb}_2\text{Te}_5$  phase change materials (less than  $1\ \mu\text{m}$ ) using two independent methods, allowing to extract the effective dielectric permittivity.

Assuming that equivalent fabricated devices are identical and if the only difference between the two devices is a thin layer of PCM, then by knowing the thickness of each layer in the stacks, the effective permittivity variation corresponding to the dissimilar devices should only reflect the influence of the PCM layer. This assumption can be satisfied if the devices (with and without a thin PCM film) are fabricated on the same substrate with the same metallic layer at the same time. Using this differential measurement procedure for a similar device fabricated on a bare substrate and on a substrate covered with a PCM layer, we can then evaluate the permittivity of the PCM without actually considering the losses of the metallic structure of the devices. We propose two complementary methods, one for a single frequency evaluation and other for a wide frequency evaluation of dielectric properties of PCMs, based on:

1. a comparison between the modification of the resonant frequency of a simple stub resonator operating in the mmW domain with and without a PCM pattern integrated in the stub's structure as shown in Figure 55a, and
2. a differential measurement of the propagation constant of a simple coplanar waveguide transmission line (CPW) fabricated on a bare substrate and on the same substrate covered by a thin PCM layer shown in Figure 55b. The propagation constant is measured using the mathematical development of the "Through-Reflect-Line" method.

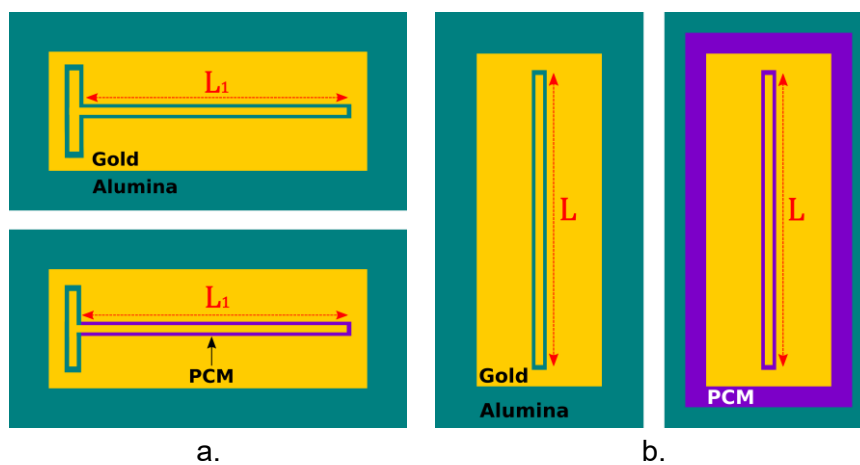


Figure 55. a) Design of mmW-band stub resonators without a PCM (up) and integrating a PCM pattern (down). b) Example of a CPW line fabricated on an alumina substrate (left) and on a PCM/ alumina layer (right).

The dielectric permittivity of these compositions in amorphous state were extracted by comparing the measurements of their millimeter-wave performances with device retro-simulations using either analytical methods or full-wave electromagnetic simulations using CST-Microwave Studio. However, the extraction of the permittivity values using full-wave electromagnetic simulations requires precise knowledge of the other parameters of the devices used for the characterization like the permittivity and losses of the substrate or the exact thickness and conductivity of the metallic layers. In order to circumvent these limitations, we are also proposing a differential approach measurements allowing to eliminate the absolute knowledge of the above-mention device parameters. Our proposed approach is based on the

extraction of the effective permittivity of specific planar devices (coplanar waveguides CPW and stub resonators) fabricated on bare substrates and, additionally, on substrates covered with the thin PCM film to be characterized, as shown in Figure 56.

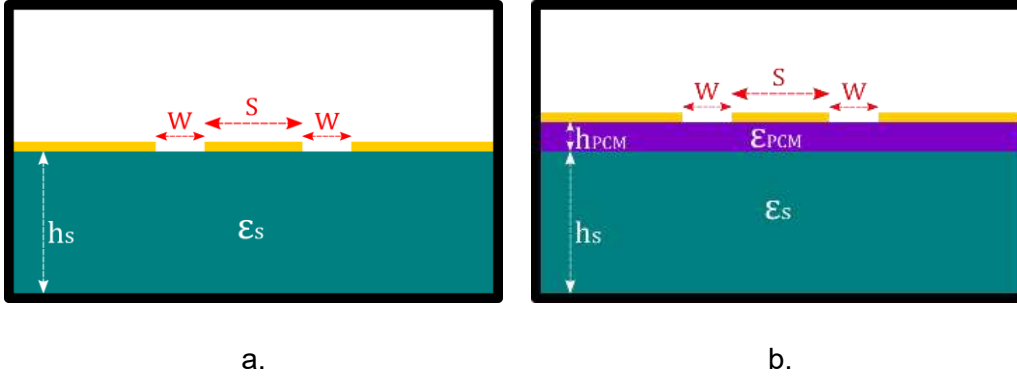


Figure 56. a) Cross-section of the geometry of a CPW in a bare substrate. b) Cross-section of the geometry of a CPW integrating a PCM thin film on a substrate.

We fabricated different samples integrating the devices presented on Figure 55. Various stub resonators of length  $L_1$  and CPW of lengths  $L$  were fabricated in order to cross-check the measured characteristics of the circuits. Three devices were fabricated by deposition of thin layers of GeTe using the DC magnetron sputtering of a 50:50 GeTe target, on  $25 \times 25 \text{ mm}^2$  substrates. Since the method of dielectric properties extraction requires us to first calculate the permittivity of the substrate on which the PCM is obtained from the effective permittivity of the line, the use of an anisotropic material (e.g. sapphire) will complicate a precise extraction of the PCM permittivity. Therefore, to accurately extract the permittivity of the PCM layer, we favor the use of isotropic materials. Thus, two samples (samples 1 and 2) were fabricated on alumina substrates while a third one (sample 3) was fabricated on a  $\text{SiO}_2$  substrate. The magnetron sputtering technique can be used to obtain PCM layers up to several micrometers in thickness, however the time required for film's fabrication with these thicknesses can be considerable long. We therefore explored films properties with thicknesses under or around micrometer range, which were previously shown to be adapted for integration in devices for millimeter-wave domain. Samples 1 and 3 correspond to devices with a GeTe layer having a thickness of 500 nm and sample 2 correspond to devices with a GeTe layer of 800 nm.

#### II.4.1.1. Stub resonator frequency method

In the first case, the stub resonator will resonate at a particular frequency given by:

$$f_r = \frac{c_0}{4 \cdot \sqrt{\epsilon_{eff}} \cdot L_1} \quad (13)$$

where  $L_1$  is the length of the stub,  $c_0$  is the speed of light and  $\epsilon_{eff}$  is the effective permittivity of the line which is a function of the substrate permittivity and its thickness.

By adding a layer of PCM, the effective permittivity of the resonator will be modified and its resonance frequency will shift as a function of the permittivity of the PCM, as shown in the Figure 57a for a device with  $L_1 = 1.1 \text{ mm}$ . The change in the  $\epsilon_{eff}$  is also dependent on the PCM layer thickness, meaning that the resonant frequency values will depend on these two parameters, as shown in Figure 57b. The permittivity of the PCM layer at the stub's resonant frequency can be then straightforwardly extracted by analytical and electromagnetic retro-

simulations of the devices and knowing the dimensions of the stub, the thickness of the PCM layer and by measuring the resonance frequency of the device.

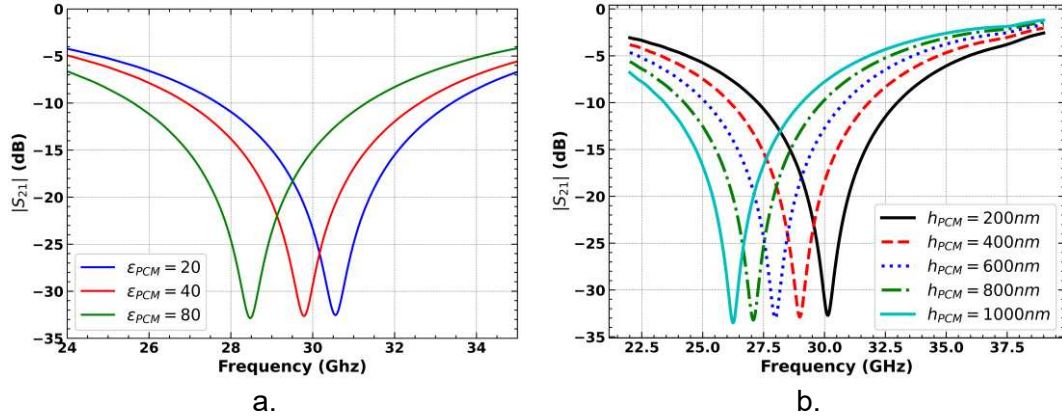


Figure 57. a) Simulation of the variation of the stub's resonant frequency as a function of the permittivity of the GeTe layer. b) Simulation of the variation of the resonant frequency of the stub as a function of the GeTe layer thickness.

#### II.4.1.2. Transmission line method

The second method employed for extracting the PCM permittivity over a wide frequency band is based on the evaluation of the complex propagation constant  $\gamma$  of a CPW line fabricated on a bare substrate and on a substrate covered by a PCM layer, using the multiline Thru-Reflect-Line (TRL) technique [111]. The analytical model of the TRL technique allows calculating the propagation constant of the transmission line by measuring the “Line” and “Thru” standards (Figure 58). The cascade parameters of an ideal transmission line are given by:

$$[L^i] = \begin{bmatrix} e^{-\gamma \cdot l_i} & 0 \\ 0 & e^{+\gamma \cdot l_i} \end{bmatrix} \quad (14)$$

where  $l_i$  is the length of the line and  $\gamma$  is the complex propagation constant of the line which can be calculated using the eigenvalues of (14). In practice however, the measurement of a transmission line produces the cascade matrix:

$$[M^i] = [X] \cdot [T^i] \cdot [Y] \quad (15)$$

where  $X$  and  $Y$  are the cascade parameters of the (unknown) “error boxes” at the detector plane and  $T^i$  is the actual matrix of the transmission (non-ideal) line given by:

$$T^i = (I + \delta^{1i}) L^i \overline{(I + \delta^{2i})} \quad (16)$$

where  $[I]$  is the identity matrix and  $[L^i]$  is the ideal cascade matrix of the transmission line. The terms  $[\delta^{1i}]$  and  $[\delta^{2i}]$  represent small perturbations at port 1 and port 2, respectively, on the ideal transmission line described in [111]. Therefore, the extraction of the propagation constant from a single line measurement is not so straightforward.

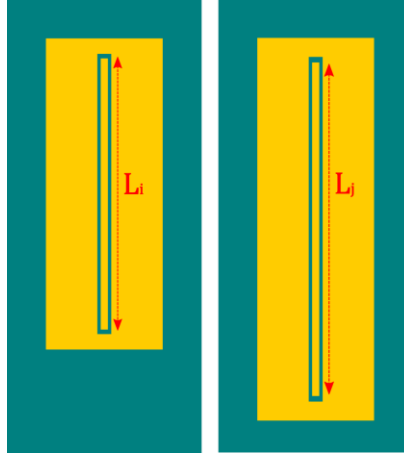


Figure 58. Transmission lines geometry for the standards “Thru” (left) and “Line” (right) for the TRL method.

Measuring two lines (or two standards)  $[L^i]$  and  $[L^j]$  of lengths  $l_i$  and  $l_j$  will produce the matrices  $[M^i]$  and  $[M^j]$  which can be combined to form the following matrix equation:

$$[M^{ij}] \cdot [X] = [X] \cdot [T^{ij}] \quad (17)$$

where:

$$[M^{ij}] = [M^j] \cdot ([M^i])^{-1} \quad (18)$$

and:

$$[T^{ij}] = [T^j] \cdot ([T^i])^{-1} \quad (19)$$

If the perturbations on the line are small, the  $[T]$  matrix can be expressed as:

$$[T^{ij}] \approx [L^{ij}] + [\epsilon^{ij}] \quad (20)$$

where:

$$[L^{ij}] = \begin{bmatrix} e^{-\gamma \cdot (l_j - l_i)} & 0 \\ 0 & e^{+\gamma \cdot (l_j - l_i)} \end{bmatrix} \quad (21)$$

and  $[\epsilon^{ij}]$  is a small error term which can be neglected if the perturbations on the line are small enough. Once again, the propagation constant of the line can be calculated from ( 21 ) using the eigenvalues of the matrix and the length difference of the two measured transmission lines.

However, as mentioned previously, in practice we have access to the measurements of matrices  $[M^i]$  and  $[M^j]$ . On the other hand, in [111] it is demonstrated that the eigenvalues of the  $[M^{ij}]$  and  $[T^{ij}]$  matrices are the same (although their eigenvectors are different), therefore calculating the eigenvalues of  $[M^{ij}]$  provides a good approximation of the propagation constant of the line provided that the error terms in ( 20 ) are small enough. The eigenvalues of  $[M^{ij}]$  are calculated using:

$$\lambda_{1,2}^{ij} = \frac{1}{2} \left[ (M_{11}^{ij} + M_{22}^{ij}) \pm \sqrt{(M_{11}^{ij} - M_{22}^{ij})^2 + 4 \cdot M_{12}^{ij} \cdot M_{21}^{ij}} \right] \quad (22)$$

where  $M_{mn}$  are the element of the matrix  $[M^{ij}]$ . We can associate one eigenvalue to the negative exponential in ( 21 ) and the other with the positive exponential. This estimation can be improved by taking a simple average of the eigenvalues given by:

$$\lambda^{ij} = \frac{1}{2}[\lambda_1^{ij} + 1/\lambda_2^{ij}] \quad (23)$$

Then, the propagation constant can be calculated using the following equation:

$$\gamma^{ij} = \frac{\ln(\lambda^{ij})}{(l_i - l_j)} \approx \gamma + \Delta\gamma^{ij} \quad (24)$$

where  $\gamma$  is the propagation constant of the line and  $\Delta\gamma^{ij}$  is a linear error term described in [111] which can be neglected if the error terms are small or by maximizing the difference between the transmission lines, according to [111].

Once  $\gamma$  is known, one can extract the effective permittivity of the transmission line by using:

$$\varepsilon_{eff} = \left(\frac{\beta}{k_0}\right)^2 \quad (25)$$

where  $k_0$  is the wave number and  $\beta$  is the imaginary part of the complex propagation constant. Additionally, from the real part of the propagation constant, the total losses of the CPW can be extracted. For a CPW, the total losses  $\alpha_t$  of the line are expressed as:

$$\alpha_t = \alpha_c + \alpha_s + \alpha_{PCM} \quad (26)$$

where  $\alpha_c$ ,  $\alpha_s$  and  $\alpha_{PCM}$  are the losses due to conductors, the substrate and PCM, respectively.

As in the previous case, the effective permittivity is a function of the substrate and the PCM layer permittivity and thickness. The measurement of the physical dimensions of the line and the PCM layer thickness will allow us to obtain their permittivity  $\varepsilon_{PCM}$ .

We have employed an additional analytic method based on the equivalent network representation [112], [113] which allows calculating the effective permittivity of the CPW. Moreover, electromagnetic retro simulations of the measured scattering parameters of the CPW line will validate the previous analytical values.

The fundamental theory on the ‘‘Equivalent Network Representation’’ can be found in [112] and [113]. It allow us to derive the integral equations for electromagnetic boundary problems by applying the Kirchhoff and Ohm’s law to a circuit representation of the boundary value problem in question (called ‘‘Equivalent network’’) where voltages represent the tangential components of the electric field at the boundaries and currents represent the density currents at the boundaries. This integral equation is then solved by the application of the Galerkin method [113], which produces an equation that can be solved for the propagation constant  $\beta$ . The details are explained in Appendix 2.

The advantage of this analytical method is that the model is considering the anisotropy of the substrate, multiple layers, the thickness of the metal and the losses of the conductors [113]. Nonetheless, in this work we will be using a simpler formulation where the conductor is a lossless thin layer as we are only interested in the shift in the effective permittivity caused by the addition of a thin layer of PCM.

Thus, following the extended development integrated in the Appendix 2, we deduce the following expression:

$$\sum_n |\langle \vec{g}_e | f_n^{TE} \rangle|^2 \left( (Y_{1,n}^{TE} + Y_{2,n}^{TE}) + (n\pi/\beta a)^2 (Y_{1,n}^{TM} + Y_{2,n}^{TM}) \right) = 0 \quad (27)$$

where:

$$|\langle \vec{g}_e | f_n^{TE} \rangle|^2 = \frac{8}{a} \frac{\beta^2 w^2}{\left(\frac{n\pi}{a}\right)^2 + \beta^2} \left( \sin \left( n \frac{\pi(s+w)}{2a} \right) \right)^2 \left( \text{sinc} \left( n \frac{\pi w}{2a} \right) \right)^2 \quad (28)$$

The expression for the free space admittances for the TE and TM modes  $Y_{1,n}^{TE}$  and  $Y_{1,n}^{TM}$  are given by:

$$Y_{1,n}^{TE} = \frac{p_{1,n}}{j2\pi f \mu_0} \coth(p_{1,n}(b-h)) \quad (29)$$

and :

$$Y_{1,n}^{TM} = \frac{j2\pi f \epsilon_0}{p_{1,n}} \coth(p_{1,n}(b-h)) \quad (30)$$

where  $h = h_s$  for a single layer substrate and  $h = h_p + h_s$  for a multilayer substrate. The expression for  $p_{1,n}$  is given by

$$p_{1,n} = \sqrt{\left(\frac{n\pi}{a}\right)^2 + \beta^2 - k_0^2} \quad (31)$$

The expression for the admittance in the substrate region  $Y_{2,n}^{TE}$  and  $Y_{2,n}^{TM}$  is more complicated for a multilayer substrate as we need to consider a third region (the region where the PCM exist). We will note  $Y_{2s,n}^{TE}$  and  $Y_{2s,n}^{TM}$  the admittances for a single layer case and  $Y_{2m,n}^{TE}$  and  $Y_{2m,n}^{TM}$  the admittances for a multilayer case. For a single layer substrate, the admittances of the substrate region are given by :

$$Y_{2s,n}^{TE} = \frac{p_{2,n}}{j2\pi f \mu_0} \coth(p_{2,n}h_2) \quad (32)$$

and :

$$Y_{2s,n}^{TM} = \frac{j2\pi f \epsilon_0 \epsilon_r}{p_{2,n}} \coth(p_{2,n}h_2) \quad (33)$$

where :

$$p_{2,n} = \sqrt{\left(\frac{n\pi}{a}\right)^2 + \beta^2 - \epsilon_r k_0^2} \quad (34)$$

For a multilayer substrate, the substrate and PCM admittances for the TE and TM modes are given by :

$$Y_{2m,n}^{TE} = \frac{p_{3,n}}{j2\pi f \mu_0} \left[ \frac{\frac{p_{3,n}}{j2\pi f \mu_0} + Y_{2s,n}^{TE} \coth(p_{3,n}h_1)}{Y_{2s,n}^{TE} + \frac{p_{3,n}}{j2\pi f \mu_0} \coth(p_{3,n}h_1)} \right] \quad (35)$$

and :

$$Y_{2m,n}^{TM} = \frac{j2\pi f \epsilon_0 \epsilon_{PCM}}{p_{3,n}} \left[ \frac{\frac{j2\pi f \epsilon_0 \epsilon_{PCM}}{p_{3,n}} + Y_{2s,n}^{TM} \coth(p_{3,n}h_1)}{Y_{2s,n}^{TM} + \frac{j2\pi f \epsilon_0 \epsilon_{PCM}}{p_{3,n}} \coth(p_{3,n}h_1)} \right] \quad (36)$$

where :

$$p_{3,n} = \sqrt{\left(\frac{n\pi}{a}\right)^2 + \beta^2 - \epsilon_{PCM} k_0^2} \quad (37)$$

With this system, equation ( 27 ) can be solved for  $\beta$  using numerical techniques. Once  $\beta$  is known, one can calculate the effective permittivity of the line using equation ( 25 ) for any frequency.

### II.4.1.3. Extraction of the permittivity of the PCM layer from the effective permittivity of the CPW line

As stated in the previous section, a direct and accurate extraction of the permittivity of the PCM using the transmission line geometry presented in Figure 59 will require full knowledge of some properties such as conductivity of the metal layer, its thickness, the permittivity of the substrate and its dielectric losses. The roughness of the PCM must be also known, as it may modify the effective permittivity of the line and the conductivity of the metallization [114] [115].

Therefore, to accurately extract the permittivity of the PCM layer we propose a differential measure using the following procedure:

1. We set the following equation:

$$\varepsilon_{eff}(f, \varepsilon_{Substrate}) - \varepsilon_{eff,m}(f) = 0 \quad (38)$$

where  $\varepsilon_{eff}$  is the effective permittivity calculated from equations ( 27 ) and ( 25 ) or by electromagnetic simulation of a CPW fabricated on a bare substrate. The  $\varepsilon_{eff,m}$  is the measured effective permittivity extracted from the CPW lines using the TRL procedure or from the resonance frequency of a stub resonator fabricated on a bare substrate. Both values are calculated for a single frequency  $f$ .

2. Equation ( 38 ) is then solved for  $\varepsilon_{Substrate}$ .
3. We set another equation:

$$\varepsilon_{eff-PCM}(f, \varepsilon_{Substrate}, \varepsilon_{PCM}) - \varepsilon_{eff-PCM,m}(f) = 0 \quad (39)$$

where  $\varepsilon_{eff-PCM}$  is the effective permittivity calculated from equations ( 27 ) and ( 25 ) or by electromagnetic simulation for a CPW fabricated on the same substrate covered by a PCM layer. The  $\varepsilon_{eff-PCM,m}$  is the measured effective permittivity extracted from the CPW lines using the TRL procedure or from the resonance frequency of a stub resonator fabricated on a similar bilayer substrate. Both values are calculated for a single frequency  $f$ .

4. Equation ( 39 ) is then solved for  $\varepsilon_{PCM}$  using the  $\varepsilon_{Substrate}$  calculated in step 2.

This approach allows us to calculate the permittivity of the PCM just from the change in the effective permittivity of the CPW lines and resonators consequent to the addition of a PCM layer, without needing to consider other parameters described previously (like the thickness of the metal, the roughness of the substrate and the losses of the substrate and metal).

Note that  $\varepsilon_{Substrate}$  calculated from ( 38 ) using the analytical method is not necessarily the permittivity of the substrate, as this formulation does not take into consideration the losses and the thickness of the metal or any other perturbation in the CPW line. Nonetheless, if the losses in the lines are negligible, then the extracted  $\varepsilon_{Substrate}$  can be a good approximation of the real permittivity of the substrate. As an example, at 30 GHz, the extracted  $\varepsilon_s$  of the alumina substrate from the 3D electromagnetic simulation is 9.47, while the extracted  $\varepsilon_s$  using the analytical method is 9.39. It should be mention that the extraction from the electromagnetic simulation approach takes a considerable amount of time due to the need of a finer mesh in the boundary of the metallization.

#### II.4.1.4. Extraction of the loss tangent of PCM layers from the total losses of the CPW line

In a similar way to the extraction of the permittivity, the accurate extraction of the losses of the PCM will also require a full knowledge of the electromagnetic properties of the structures, in particular the losses of the metal and substrates. However, since the CPW with and without PCM are fabricated over the same substrate and during the same process of metal deposition, the terms  $\alpha_c$  and  $\alpha_s$  in equation ( 26 ) should be, in average, similar for both type of devices. Therefore, any supplementary losses in the CPW may be considered as introduced by the PCM layer.

To accurately extract the loss tangent of PCM we also propose a differential method by solving the equation:

$$\alpha_{PCM}(f, \tan(\delta)) - (\alpha_{t-PCM}(f) - \alpha_t(f)) = 0 \quad (40)$$

where  $\alpha_{t-PCM}$  and  $\alpha_t$  are the total losses measured by the TRL method with and without a PCM layer respectively. Since we do not dispose of an analytical model for evaluating the losses of a bi-layer CPW, equation ( 40 ) is solved using 3D electromagnetic simulations.

#### II.4.2. Device Fabrication and measurements

We fabricated different samples integrating the devices presented on Figure 55. Three devices were fabricated by deposition of thin layers of GeTe using the DC magnetron sputtering of a 50:50 GeTe target, on 25×25 mm<sup>2</sup> substrates. As indicated before, since the method of dielectric properties extraction developed in section II requires us to first calculate the permittivity of the substrate on which the PCM is obtained from the effective permittivity of the line, the use of an anisotropic material (e.g. sapphire) will complicate a precise extraction of the PCM permittivity. Therefore, to accurately extract the permittivity of the PCM layer, we favor the use of isotropic materials. Thus samples 1 and 2 were fabricated on alumina substrates while sample 3 was fabricated on a SiO<sub>2</sub> substrate. Samples 1 and 3 correspond to devices with a GeTe layer having a thickness of 500 nm and sample 2 correspond to devices with GeTe layer of 800 nm.

The fabricated circuits corresponding to the two types of designs shown in Figure 55a and Figure 55b are shown on Figure 59a and Figure 59b, respectively. The complete image of all fabricated circuits is shown in Figure 60. For each sample with different PCM and thicknesses, two sets of seven stub resonators (with and without a layer of PCM) were fabricated. The stubs' lengths  $L$  have dimensions of 0.8 mm, 0.9 mm, 1.0 mm, 1.1 mm, 1.2 mm, 1.3 mm and 1.4 mm, corresponding to specific resonant frequencies in the band 20 to 40 GHz on the alumina substrate and 30 to 50 GHz on the SiO<sub>2</sub> substrate. The ground planes aside the stub resonators were connected using gold wire bonding (not shown on Figure 59b) for suppressing the propagation of higher order modes and prevent the structure to radiate.

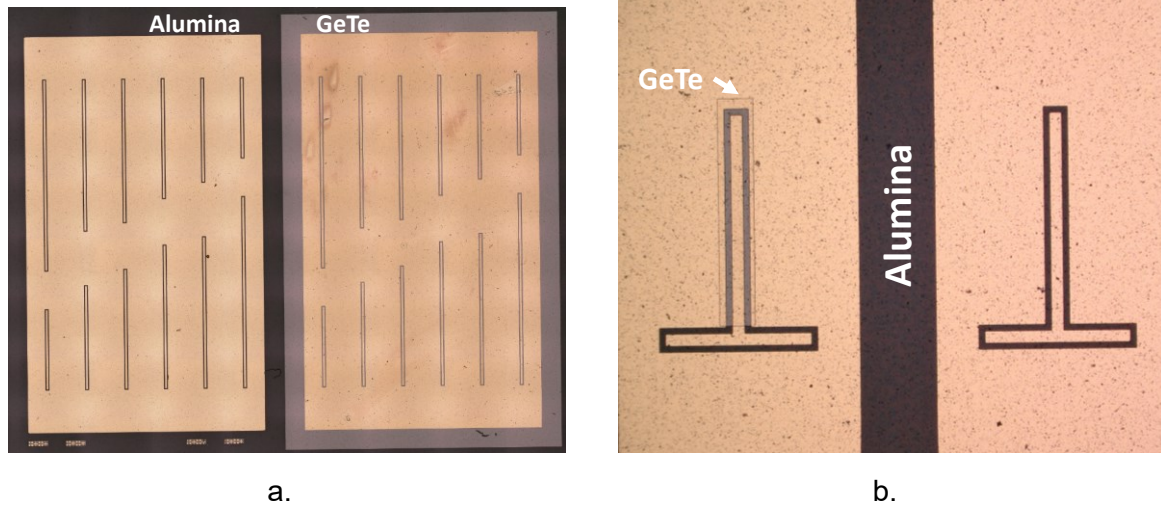


Figure 59. a) CPW lines fabricated over a layer of alumina (to the left) and over a layer of GeTe/alumina (to the right). b) Stub resonators fabricated over a layer of alumina (to the right) and a layer of GeTe/alumina (to the left).

Two sets of CPW lines (on the bare substrate and on a PCM sub-layer) were also realized on each of the samples mentioned before. Three sets of similar lines with different lengths were designed and fabricated to introduce phase variations around  $90^\circ$  between specific pairs of lines at 30 GHz ( $\approx 1.2$  mm, on the alumina substrate). The lengths  $L$  of the CPW transmission lines are  $L_1 = 2.0$  mm,  $L_2 = 2.4$  mm,  $L_3 = 3.2$  mm,  $L_4 = 3.6$  mm,  $L_5 = 3.8$  mm and  $L_6 = 4.6$  mm. The pairs used for evaluation of the propagation constant are the lines  $L_1$ - $L_3$ ,  $L_2$ - $L_4$  and  $L_5$ - $L_6$ .

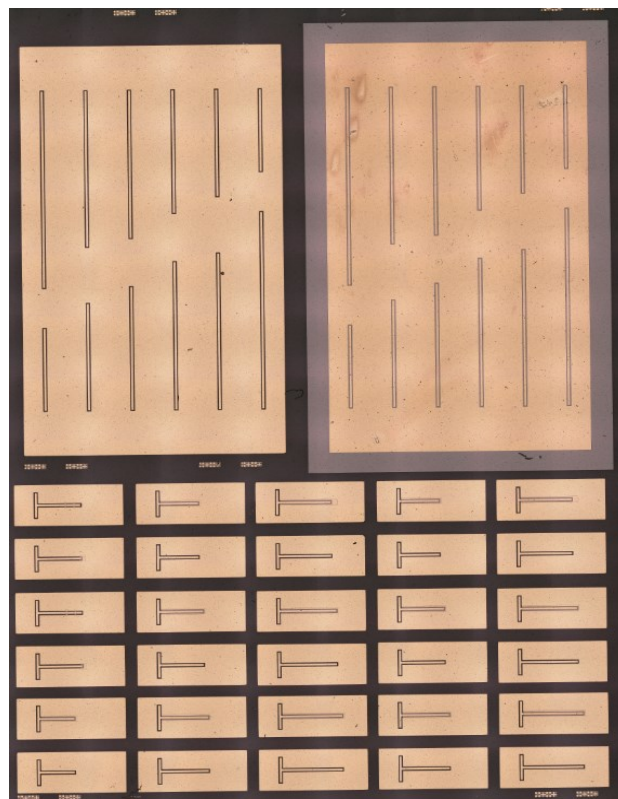


Figure 60. Complete image of the all the fabricated CPW lines over a layer of alumina (upper left) and over a layer of GeTe/alumina (upper right) and all the fabricated stub resonators with and without a layer of GeTe (the bonding of the resonators is not shown).

The RF characteristics of the investigated devices (stubs and CPW lines) were measured in the 100 MHz-67 GHz range using Ground-Signal-Ground (GSG) Cascade probes connected to a vector network analyzer (ZVA Rohde & Schwarz) allowing to extract the experimental S-parameter matrices, as shown in Figure 61.

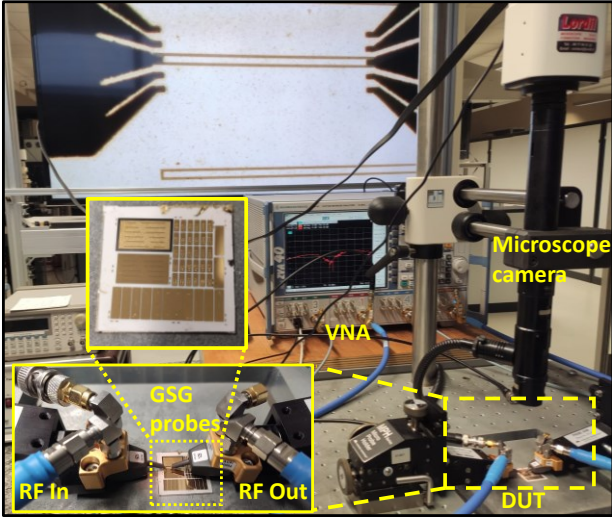


Figure 61. Image of the test system used to measure the RF performance of all samples (VNA- vector network analyzer, DUT-device under test).

Additionally, Figure 62a shows a quarter-wavelength stub resonator working in the millimeter-wave band (around 30 GHz) in which a GeTe pattern added at the end of the stub. When this pattern is in the amorphous state, the stub is equivalent to an open-circuit resonator which presents a notch in the transmission at the resonant frequency as evidenced by the black trace in Figure 62b. When the GeTe pattern is transformed into its crystalline state, the resonator element is connected to the ground and thus shorted. In this state, the circuit is equivalent to a short-circuit stub quarter-wave resonator which presents a transmission at the resonance frequency as evidenced by the red trace in Figure 62b. It is important to note that, at this high frequency, resonators in CPW technology require a bonding between the adjacent ground planes in order to equalize the ground planes and avoid higher-order modes [116]. If this bonding is not done with caution, the performances of the resonator can be significantly altered which can explain the anomaly observed at 40 GHz in transmission during the amorphous state on Figure 62b.

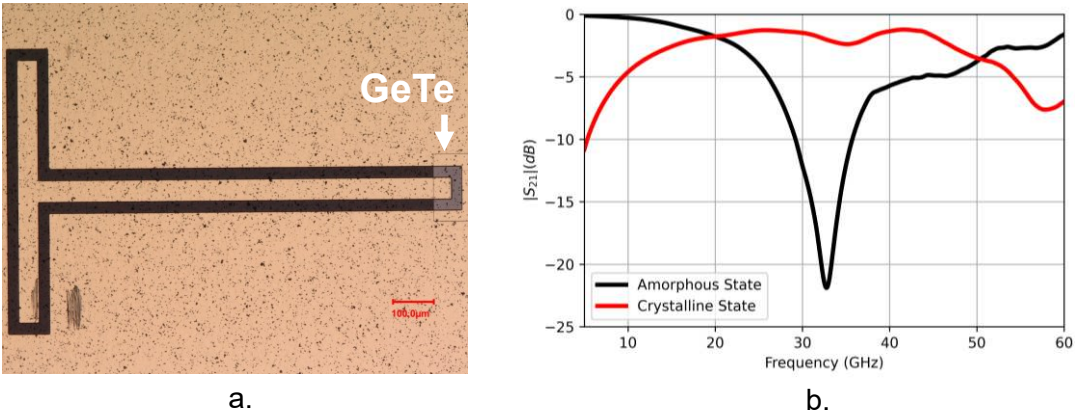


Figure 62. a) Fabricated quarter-wavelength stub resonator on a sapphire substrate with a 500-nm thick GeTe pattern at the end of the resonator. b) Measured transmission of the resonator at both states of the GeTe pattern.

### II.4.3. Extraction of PCM layers permittivity

#### II.4.3.1. Resonators analysis

By measuring the resonant frequency of both resonators (with and without a 500-nm thick GeTe layer) and using the equation ( 13 ) to calculate the effective permittivity for each device, we can deduce the permittivity of the PCM layer generating the change in the effective permittivity. The PCM permittivities were extracted using the proposed analytical method and the 3D electromagnetic simulations of the devices (the latter also takes into consideration the conductivity of the metal and its thickness) as show in Figure 63. Since the PCM layer is very thin with respect to the size of the substrate and smaller than the thickness of the metallization, the 3D electromagnetic simulation requires a very fine mesh at the boundaries of the PCM. The effects of adding a thin layer of GeTe within a stub resonator structure is clearly shifting its resonant frequency, as shown in the experimentally recorded responses of a typical stub resonator device in Figure 64.

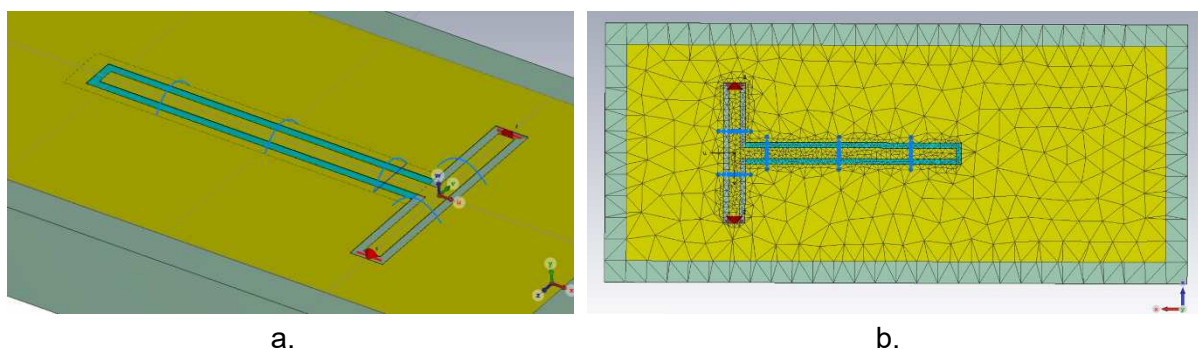


Figure 63. a) 3D electromagnetic model of an open-circuit stub resonator integrating a thin line of GeTe and bonding wire over an alumina substrate. b) Tetrahedral mesh of the stub resonator.

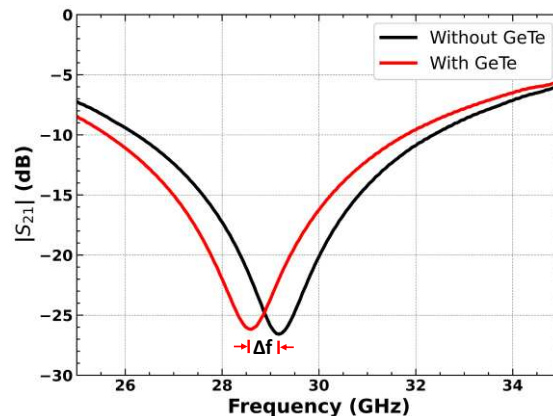


Figure 64. Measured  $S_{21}$  parameter of a stub resonator with length of 1.3 mm showing clear changes in the parallel resonant frequency due to the addition of a 500-nm thick layer of GeTe.

The results presented in Table 5 for devices with stubs having different dimensions show that the permittivity values obtained using both methods agree very well. Most of the values in Table 5 are close to a value of 21, however the extracted permittivity from the resonators of length 1.2 and 0.9 mm is showing a large dispersion from the value of 21. This dispersion between permittivity values reported in Table 5 can be explained by variations on the thickness of the PCM layer or by undesirable perturbations due the bonding of gold wires used to equalize the ground planes as well as inaccuracies in the reading of the resonance frequency.

In fact, as shown in Figure 57 and demonstrated in Appendix 3 (which is describing the sensibility of the resonance frequency to the geometrical parameters of the structure), the resonance frequency is sensible to the thickness of the PCM layer, therefore any inhomogeneity in the thickness of the layer will cause a change in the resonance frequency of the resonator. The errors may be also increased by the rough surface of the alumina substrate on which the PCM layer is obtained.

Table 5. Comparison of the extracted permittivity of the GeTe using the analytical method and 3D electromagnetic simulations using CST microwave studio for all resonators corresponding to sample 1 (alumina substrate, 500-nm thick GeTe layer).

| Resonator length (mm) | Resonant frequency (GHz) |           | GeTe Permittivity |                   |
|-----------------------|--------------------------|-----------|-------------------|-------------------|
|                       | Without GeTe             | With GeTe | 3D EM Simulation  | Analytical method |
| 1.4                   | 23.11                    | 22.67     | 22.0              | 21.9              |
| 1.3                   | 24.89                    | 24.45     | 20.6              | 20.9              |
| 1.2                   | 26.83                    | 26.42     | 17.7              | 17.6              |
| 1.1                   | 29.28                    | 28.77     | 20.8              | 21.0              |
| 1.0                   | 32.16                    | 31.61     | 20.7              | 19.8              |
| 0.9                   | 35.68                    | 35.23     | 18.1              | 18.4              |

The results on the GeTe permittivity in Table 6 shows the permittivity of the GeTe and GST compositions for the entire set of resonators (different thicknesses and substrates). For the GeTe compositions we can observe that most of the extracted values are around 21, however there are certain values that are far away from the mean value which (as stated previously) can be attributed to variations on the thickness of the PCM layer and the influence of the bonding wires. Nonetheless, these values agree very well with the ones found in [102] where the permittivity of the GeTe was evaluated to be around 24.4 using the impedance spectroscopy method from 10 MHz up to 100 MHz. Other measurements in the THz domain [104] suggest that the permittivity of the GeTe is around 19 at 250 GHz. These results suggest that permittivity of the GeTe has little dispersion in the frequency band from 10 MHz up to 250 GHz. The same conclusions can be made for the GST composition permittivity, where the value reported by [102] is around 34 for frequencies from 10 MHz up to 100 MHz.

Table 6. Mean values of the GeTe and GST permittivities extracted from the entire sets of stub resonators, for all samples.

| Resonator length (mm) | GeTe                       |                           |                           | GST                       |
|-----------------------|----------------------------|---------------------------|---------------------------|---------------------------|
|                       | Sample 1 (250 nm, alumina) | Sample 2 (500nm, alumina) | Sample 3 (800nm, alumina) | Sample 4 (800nm, alumina) |
| 1.4                   | 22.6                       | 19.6                      | 18.5                      | 33.2                      |
| 1.3                   | 21.6                       | 19.9                      | 19.2                      | 34.8                      |
| 1.2                   | 17.6                       | 22.2                      | 23.9                      | 36.0                      |
| 1.1                   | 21.7                       | 22.4                      | 20.2                      | 28.2                      |
| 1.0                   | 21.33                      | 18.2                      | 15.5                      | 30.8                      |
| 0.9                   | 18.4                       | 19.3                      | 17.3                      | 28.3                      |
| 0.8                   | ----                       | 23.9                      | 24.3                      | 38.6                      |

### II.4.3.2. Transmission line analysis

The measured  $S_{21}$  parameters of the six CPW fabricated over a bi-layer of alumina or  $\text{SiO}_2$  substrate and the GeTe film are shown in Figure 65a and Figure 65b, respectively. The curves

measured on an alumina substrate are noisier than the ones measured on a SiO<sub>2</sub> substrate, due to the higher roughness of the alumina substrate. Therefore, before applying the permittivity extraction methodology described previously, the data were filtered by applying a Savitzky-Golay filter [117] using a third-degree polynomial with a window of 2000 frequency points. This filter was applied separately to the real and imaginary parts of the measured S-parameters of each line. The results of the post-processed measured S-parameters for the L<sub>6</sub> line are displayed in Figure 66a and Figure 66b for an alumina and a SiO<sub>2</sub> substrate, respectively. From both figures, it can be seen that the noise has been filtered out while preserving the overall trending of the S<sub>21</sub> curve (as clearly shown in Figure 66b).

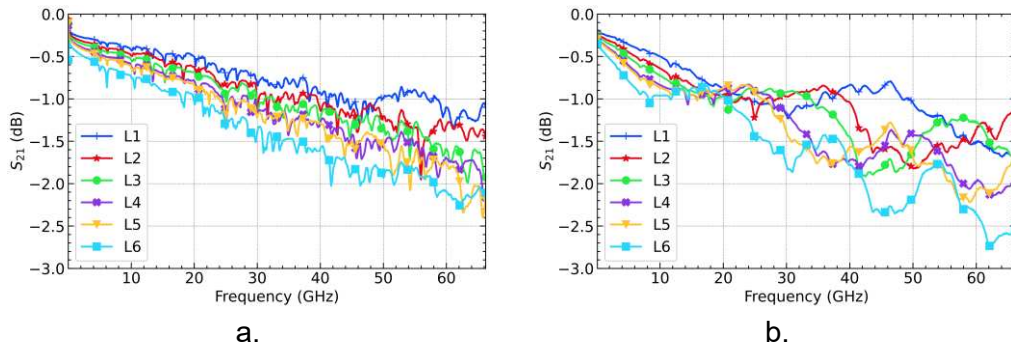


Figure 65. a) Measured S<sub>21</sub> parameters of all the CPW lines fabricated on an alumina substrate integrating a thin layer of a 500-nm thick GeTe (sample 2) and b) similar parameters of the CPW lines fabricated on a SiO<sub>2</sub> substrate integrating a thin layer of a 800-nm thick GeTe (sample 3).

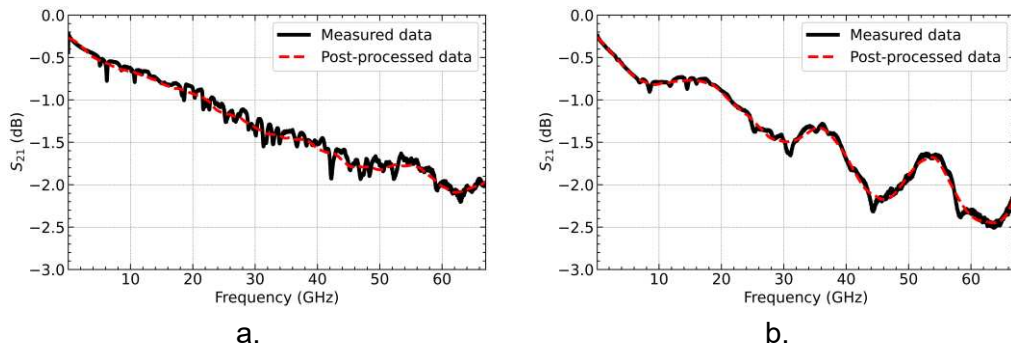


Figure 66. a) Measured S<sub>21</sub> parameters of the L<sub>6</sub> line in sample 2 (alumina substrate) with a thin layer of GeTe before and after post-processing filter and b) similar result for the L<sub>6</sub> CPW line with a thin layer of GeTe on sample 3 (SiO<sub>2</sub> substrate).

The effect of adding a thin layer of GeTe and GST under the transmission line devices and their influence on the effective permittivity of the fabricated coplanar waveguide is shown on Figure 67a for GeTe and on Figure 67b, for GST respectively. The mean value of CPW's effective permittivity is represented as a function of frequency in the 5-60 GHz frequency domain and was evaluated using the analytical method from each of the two sets of three pairs of CPW lines (pairs L<sub>1</sub>-L<sub>3</sub>, L<sub>2</sub>-L<sub>4</sub> and L<sub>5</sub>-L<sub>6</sub>). The standard error of the mean values calculated at every frequency value is also shown for each permittivity trace. One can notice that the addition of PCM layers (GeTe or GST) increases proportionally the values of  $\epsilon_{eff}$  without changing its overall shape, suggesting that the permittivities of both GeTe and GST are rather constants over the investigated frequency band.

Table 7 shows a comparison of the extracted permittivity of the GeTe layer using both the analytical method and 3D electromagnetic simulations for sample 2 (800-nm thick GeTe layer). It can be seen that both methods agree very well, especially at low frequencies. Following the

same approach and using the analytical estimation method, Table 8 summarizes the values of the extracted permittivity for both PCM compositions and for all fabricated samples. To solve the propagation constant, we use the “waveguide port” utility of CST Microwave Studio. The time domain simulations were performed using a hexahedral mesh.

Table 7. Comparison of the extracted permittivity of the GeTe for the CPW lines of sample 2 (800-nm thick GeTe on alumina substrate) using the analytical method and the 3D electromagnetic simulation.

| Frequency (GHz) | Effective permittivity |           | GeTe permittivity |                   |
|-----------------|------------------------|-----------|-------------------|-------------------|
|                 | Without GeTe           | With GeTe | 3D EM Simulation  | Analytical method |
| 20              | 5.17                   | 5.50      | 23.2              | 22.2              |
| 30              | 5.15                   | 5.47      | 22.3              | 21.7              |
| 40              | 5.10                   | 5.42      | 21.7              | 21.6              |
| 50              | 5.13                   | 5.43      | 20.4              | 20.1              |
| 60              | 5.14                   | 5.47      | 21.0              | 22.7              |

The complete picture of frequency-dependent GeTe and GST permittivities is shown in Figure 68a for GeTe and on Figure 68b for GST, where it can be noticed that the permittivity values of both GeTe and GST, although having different values, are mostly constant over the investigated frequency band. This feature is supporting the conclusions from the results obtained using the resonant method and strongly suggest that the permittivity of the GeTe and GST are little dispersive in the investigated frequency band and from 10 MHz up to 250 GHz [102] [103] [104].

Table 8. Mean value of the extracted permittivity of the GeTe and GST of all fabricated samples using the analytical method.

| Frequency | GeTe                       |                            |                            | GST                       |
|-----------|----------------------------|----------------------------|----------------------------|---------------------------|
|           | Sample 1 (250 nm, alumina) | Sample 2 (500 nm, alumina) | Sample 3 (800 nm, alumina) | Sample 4 (800nm, alumina) |
| 20        | 19.7                       | 22.2                       | 26.3                       | 32.7                      |
| 30        | 20.6                       | 22.0                       | 25.9                       | 32.4                      |
| 40        | 19.5                       | 22.3                       | 26.2                       | 32.6                      |
| 50        | 18.0                       | 20.7                       | 26.0                       | 30.0                      |
| 60        | 20.7                       | 22.7                       | 25.8                       | 34.3                      |

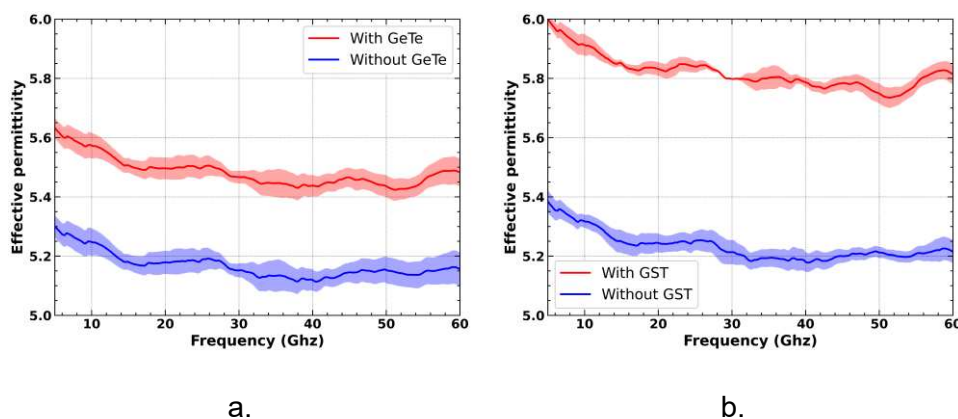


Figure 67. a) Comparison of the mean effective permittivity values extracted using the TRL method from the fabricated CPW lines on an alumina substrate, with and without a GeTe layer of 800 nm (sample 2). b) Comparison of the mean effective permittivity, with and without a GST layer of 800 nm (sample 4).

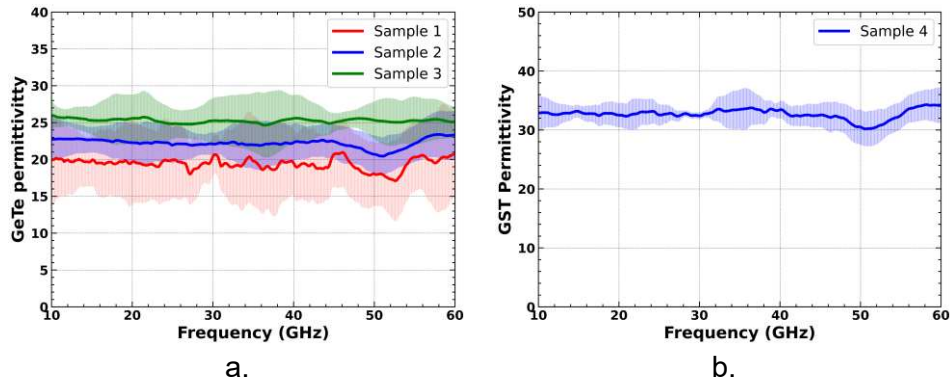


Figure 68. a) Mean and dispersion values of the extracted permittivity of GeTe using the analytical method for all samples integrating GeTe (samples 1 to 3). b) Mean and dispersion values of the extracted GST permittivity using the analytical method.

The difference in the values of GeTe permittivity for the dissimilar samples 1-3 can be explained by errors introduced in the estimation of the GeTe thickness under a specific device, which may vary from the expected values across the surface of each sample (center to edges). Considering the small deviations from the expected values of the PCM thicknesses and the standard error of the mean permittivity values extracted from each line pairs, Figure 68 also takes in consideration the dispersion of the permittivity values of the PCM layers.

Finally, Figure 69a and Figure 69b shows a comparison of the losses of the CPW with and without a layer of PCM. From these figures, we can notice that the addition of a very thin layer of PCM does have a noticeable impact on the losses of the CPW, however, the uncertainties associated with the measurement can make the extraction of the loss tangent of the PCMs difficult. Additionally, we notice that the uncertainties are increasing at higher frequencies, which can be mostly attributed to the substrate roughness and local variations on the thickness of the PCM layers. Since the difference in the attenuation constant values from samples 1 and 3 is very small, they were not considered for the extraction of the loss tangent of the PCM. By comparing the shift on the real part of the propagation constant, from 3D electromagnetic retro-simulation we can extract the loss tangent variation with frequency, as shown in Figure 70a and Figure 70b. The extracted values of the loss tangent at 30 GHz for the GeTe and GST layers are of  $3.4 \times 10^{-2}$  and  $3.2 \times 10^{-1}$ , respectively.

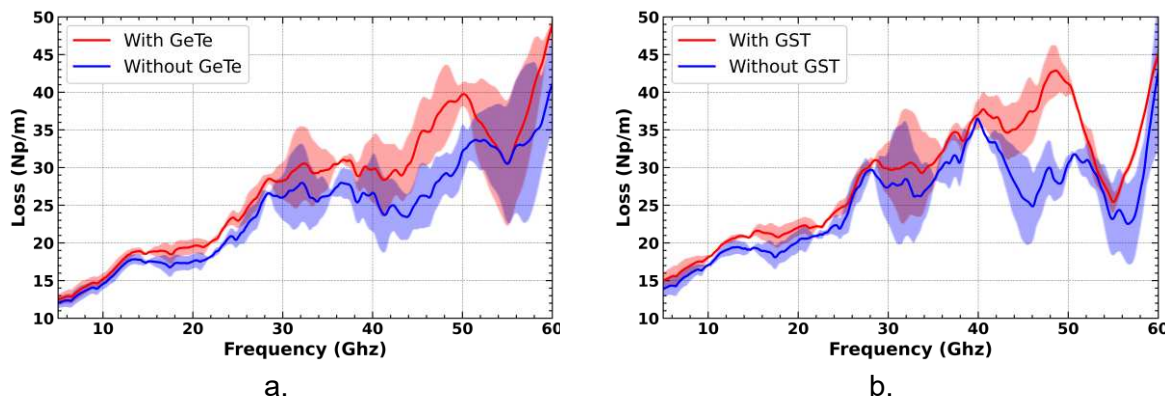


Figure 69. a) Comparison of the mean losses values extracted using the TRL method from a fabricated transmission line on alumina substrate with and without a GeTe layer of 800 nm (sample 2) and, b) for a fabricated transmission line on alumina substrate with and without a GST layer of 800 nm (sample 4).

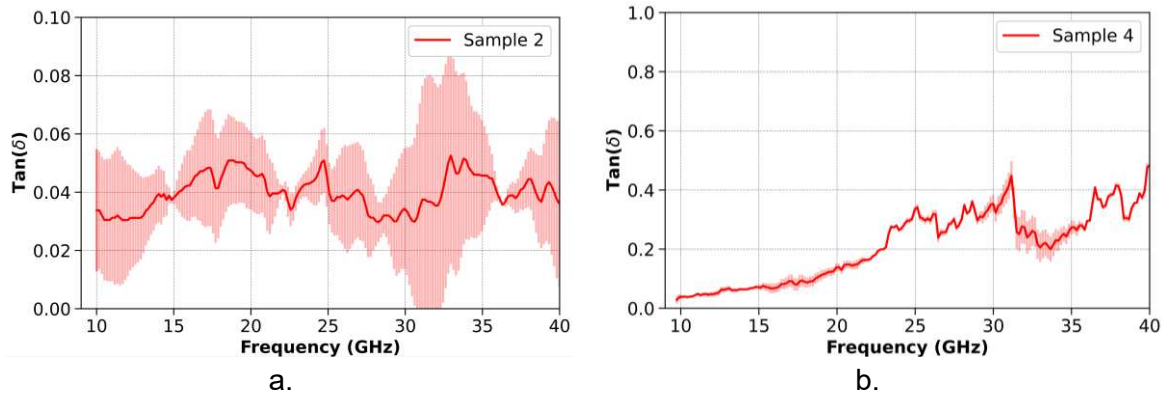


Figure 70. a) Mean and dispersion values of the extracted loss tangent of the GeTe from sample 2 and, b) of the GST from sample 4.

### II.4.3.3. Results synthesis and discussions

From Table 5 and Table 8, it can be seen that the dielectric permittivity extracted from both methods agrees quite well on average. Since the procedure for extracting the permittivity from the stub resonators is very straightforward, these results allow us to cross-validate the results from the CPW method and the post-processing step required by the later.

From Figure 68a and Figure 68b one can notice that the permittivity of the PCM composition are mostly constant over the studied frequency bandwidth. The mean values recorded for the sample 3 (GeTe obtained on an optically polished SiO<sub>2</sub> substrate) produce a smoother frequency-dependent permittivity curve, which can be explained by the fact that the surface of this substrate has a much lower roughness than the alumina ones (around 4 nm rms roughness against ~30 nm for alumina substrates). The extracted loss tangent values for the GeTe sample are mostly constant values, especially at low frequencies, nonetheless, the high roughness and variations of the layer thickness add a high degree of uncertainty to these values at high frequencies especially since the loss tangent value is low. For the GST composition, we can observe a monotonic increase of the loss tangent with increasing frequency. For both layers, the evaluated uncertainties can be greatly reduced by using longer lines with thicker PCM layers, on smoother substrates.

The results presented in Figure 68a and the permittivity dispersion values extensively analyzed in Appendix 3 suggest that the devices fabricated on SiO<sub>2</sub> have the lowest dispersive permittivity values, followed by the devices fabricated on a thick (800 nm) GeTe layer (which may alleviate the initial roughness of the alumina substrate). The roughness of the substrate produces small local variations on the thickness of the PCM and therefore, induces a small change in the effective permittivity of the line. These changes are quantified and analyzed in Appendix 3. Assuming a nominal permittivity value of 22 for the GeTe composition and 32 for the GST composition, and using equations (83) and (85) (see Appendix 3) we can estimate that for the extraction of the permittivity value within an error of 1%, the thickness of the PCM layer must be known within 10-nm precision for an alumina substrate. On the other hand, for a SiO<sub>2</sub> substrate, the thickness of the PCM must be known within 1-nm precision.

## II.5. Optical activation of the phase change in PCMs layers

The term “optical activation” implies the use of a laser pulse to transform a PCM from its amorphous state to its crystalline state and vice-versa. The interest of this approach is that the use of laser pulses reduces the commutation time between the two states [118] [119] [120].

Additionally, it simplifies the process of fabrication and avoids design complexity especially in the case of designs integrating a large number of PCM switching elements, which would require a complex network of heating elements and their polarization lines to transform the material between the two states.

Several important parameters must be considered when using laser irradiation for PCM activation:

1. The **energy density of the laser** which will proportionally induce the rise in temperature of the material. A suitable value must be chosen such that the PCM is heated enough to be crystallized/ amorphized. If the energy density is very high, it will result in damage of the PCM sample or even ablation.
2. The **laser's spot size** defines the system's resolution (size of the crystallized or amorphized zone). A higher resolution allows creating smaller features that are necessary for higher frequency systems (like terahertz devices [121] [122]). However, the energy density of a laser pulse is proportional to the laser power and inversely proportional to the size of the laser spot. Therefore, for a given laser power, there will be a minimum laser spot size before the PCM gets damaged due to a very high energy density. Additionally, smaller spots require raster scanning specially for large surface areas.
3. The efficiency of the material transformation is determined also by the **extinction coefficient  $k$  of the material**. Therefore, lasers of different wavelengths will not heat up equally the PCM. A suitable wavelength must be chosen such that the PCM should be not transparent (with a low  $k$ ) but also not very opaque (high  $k$ ). In the case of a very opaque substrate, all the energy will be transformed into heat only at the surface of the material which means that the depth of crystallization will not be very high. Additionally, the extinction coefficient defines the **optical or thermal penetration coefficient of the material**. This parameter defines the depth at which the PCM heats up significantly and therefore the depth at which the PCM can crystallize by laser pulses, implying that there is a maximum PCM layer thickness that can be crystallize by optical means for a given wavelength at a given power, with a single pulse.
4. The spatial profile of the laser beam can also have an influence on the resolution and the uniformity of the crystallized/amorphized spot as well as the depth of the crystallization. Usually, the single-mode laser beams are gaussian but flat-top square or circular profiles can be prepared by using additional optical elements.
5. To transform the PCM to the amorphous phase using laser pulses, the PCM must be heated up to its melting point and then quench very rapidly. This implies the use of a high thermal conductivity substrate for the heat to be evacuated as fast as possible (fast quenching). Additionally, the duration of the laser pulse and the layer thickness may have a strong influence on the amorphization of the PCMs as pointed out in I.5.
6. For RF applications, the PCM must be in contact with the metallic layer in which the RF signal travels. For most applications, a small metallic layer is superposed to the PCM layer to ensure electrical contact. Unfortunately, this means that the laser cannot be used to heat up the underlying PCM since is covered by a metallic pattern. This zone can still be heat up due to heat diffusion from the surrounding space or must be previously crystallized by direct heating over a hot plate before adding the metallic layer.

### II.5.1. Optical characterization of PCMs

When a laser beam hits the surface of a material, part of it will be reflected, absorbed or transmitted through the material. The amount of reflection is characterized by the material's reflectivity  $R$  at a specific wavelength while the leftover passing through the material is absorbed and/or transmitted by the material. The decrease of light speed within the material is characterized by the refraction index  $n$  while the energy absorbed is usually transformed into heat. The heat absorption is characterized by the extinction coefficient  $k$  of the material: if  $k$  is low, the material is transparent at the corresponding wavelength and therefore the heating will be negligible. Both  $n$  and  $k$  define the complex refraction index  $N$  as:

$$N = n + j.k \quad (41)$$

where  $j$  is the imaginary unit.

The refraction index and extinction coefficient are wavelength-dependent and therefore the amount of heating in the material is also dependent on the wavelength of the laser. Additionally, the reflectivity  $R$  is a function of  $N$  hence also wavelength-dependent. Thus, the optical activation of PCM materials implies an understanding of the interaction between light (laser) and materials as well as their optical properties. Ideally, we would like to work with a wavelength where  $R$  is low to minimize the energy loss due to reflections, and where  $k$  is high enough to ensure all the energy passing through the material is absorbed by it.

#### II.5.1.1. Spectroscopic ellipsometry

Ellipsometry is an optical analysis technique based on the modification of the polarization state of light when it is reflected on a surface, as shown in Figure 71. This technique has been used for many decades to determine the optical parameters of materials as well as the thickness of a film obtained over a substrate [123] [124], depending on the specific model used to process the ellipsometry data. We consider a substrate in which a thin film has been deposited, as shown in Figure 71a. An incident beam arrives onto the substrate with an angle  $\varphi$  with respect to the normal of the sample. The reflected wave travels outwards with the same angle but at the opposite direction while the transmitted wave travels through the film until is reflected back at the film-substrate interface and travels back to the ambient-film interface, where the transmitted-then reflected wave adds to the first wave reflected at the surface. The incident and reflected beams at the surface define a plane called the incidence plane, and then any linearly polarized incoming wave can be decomposed into a component parallel to this plane (called the "p-wave") and a component perpendicular to the plane (called the "s-wave"), as shown in Figure 71b.

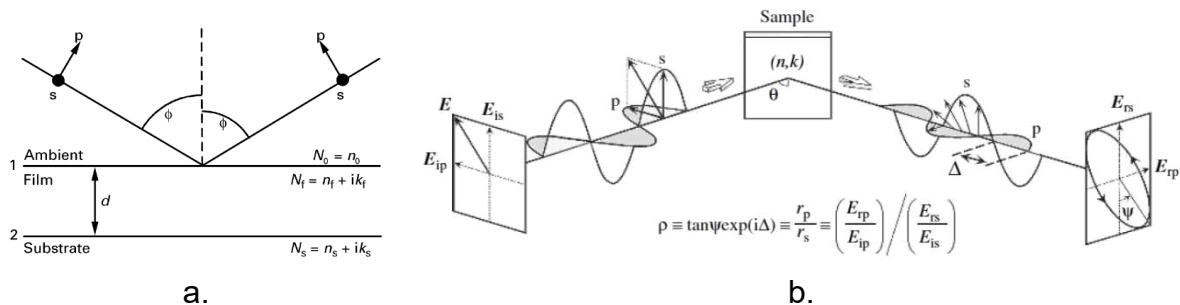


Figure 71. a) Schematic representation of an incident and reflected beam into a sample with a thin film. b) Change in the polarization state of an incoming light-wave after being reflected by a sample.

The total reflection of each component at the surface of the film is described by the Fresnel coefficients, noted  $r_p$  for the parallel component and  $r_s$  for the perpendicular component where

both components are function of the wavelength  $\lambda$ , the complex refraction index of the substrate  $N_s$  and film  $N_f$  as well as the thickness  $d$  of the film according to:

$$r_x = \frac{r_{1x} + r_{2x} \cdot \exp(-j \cdot 2 \cdot b)}{1 + r_{1x} \cdot r_{2x} \cdot \exp(-j \cdot 2 \cdot b)} \quad b = \frac{2\pi d N_f \cos(\phi_f)}{\lambda} \quad (42)$$

where  $x = s$  for an s-wave and  $x = p$  for a p-wave,  $\phi_f$  is the transmitted angle at the ambient-film interface (defined by Snell law),  $r_{1x}$  and  $r_{2x}$  are the reflection coefficients at the ambient-film interface and film-substrate, respectively.

Since the Fresnel coefficients are complex values, the reflected s-wave and p-wave suffer not only an amplitude change but also a phase shift. The combination of these two waves produces an elliptically polarized wave as shown in Figure 71b. This wave is characterized by two angles  $\psi$  and  $\Delta$  where the first one is the angle formed between the two components of the wave while the latter is the angular shift between the two waves. Ellipsometry measurements are based on the determination of the parameters of the ellipse characterizing the polarization of the reflected wave which are characteristic of the optical properties of the sample. This relationship is given by:

$$\rho = \frac{r_p}{r_s} = \tan \Psi \cdot \exp(j\Delta) \quad (43)$$

The refractive index  $n$  and the extinction coefficient  $k$  of the material constituting the layer as well as its thickness  $d$ , are determined by comparing the measured ellipsometric parameters to those calculated on the basis of the configuration shown in Figure 71a, using ( 42 ). If the measures are broadband, a model for the behavior of  $n$  and  $k$  as a function of the wavelength must be established [125].

Is important to notice that ( 42 ) assumes that both materials are homogeneous with perfectly smooth surfaces and interfaces. The use of anisotropic materials is possible if ( 42 ) is appropriately modified to take it into account the anisotropies [125]. Additionally, any imperfections like roughness, inhomogeneities on the thickness of the samples or non-smooth interfaces introduces a substantial amount of incertitude to the calculated  $N$  unless considered in the model.

### II.5.1.2. Optical parameters of GeTe

The ellipsometry method was applied to two sapphire samples in which a GeTe layer was deposited by magnetron sputtering. The measures were performed with an UVisel Ellipsometer (Horiba) with a wavelength ranging from 200 nm to 1500 nm at an incident angle of  $45^\circ$ . The optical parameters data were fitted using a Tauc-Lorentz model. The roughness was considered by adding a thin layer at the surface of the film and assuming their optical properties are the average of the layer above (air) and the layer below (GeTe). The measured reflectivity of both samples is shown in Figure 72a and the extracted optical parameters as a function of wavelength are shown in Figure 72b, as well as their measured thickness. The roughness of the film was evaluated at 7 nm for both samples.

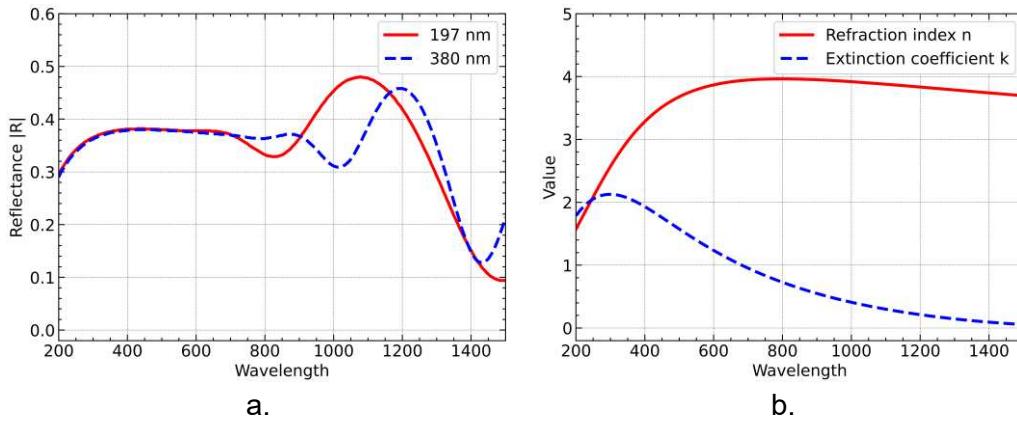


Figure 72. a) Measured reflectance of two samples of GeTe over a sapphire substrate. b) Extracted refractive index and extinction coefficient for the 197-nm thick sample.

From Figure 72a we see that both GeTe layers have a mostly constant reflection (around 0.38) from 350 up to 700 nm wavelengths, after which the reflectance behavior changes for each sample. To explain this difference, we notice from Figure 72b that the extinction coefficient of the GeTe decreases with increasing wavelength, meaning that the GeTe is becoming transparent at longer wavelengths and therefore the effect of multiple reflections inside the GeTe layer are more pronounced. These multiple reflections inside the GeTe produce constructive and destructive interference to the reflected beam at the surface which changes the total reflected power, thus the reflectance. At shorter wavelengths, the GeTe extinction coefficient is greater, which means that the PCM is opaque and therefore the multiple reflections inside the GeTe attenuates enough to not influence the total reflectance seen at the surface. This behavior in the extinction coefficient explains why the reflectance at shorter wavelength is the same but changes with the thickness of the GeTe at longer wavelengths.

With this information we can conclude that the ideal range of wavelengths for efficient GeTe activation lies between 200 and 600 nm (from ultraviolet to red lasers) where  $k$  is high enough and the reflectance is mostly constant. Working with wavelengths greater than 600 nm will result in the material been semi- or completely transparent and hence the efficiency of optical activation will be dependent on the thickness of the GeTe layer. Additionally, the knowledge of the GeTe refractive index  $n$  will allow us to fabricate an anti-reflection layer to further increase the efficiency of the transformation.

## II.5.2. Electromagnetic heating of PCMs using multi-physics simulations (COMSOL)

We are interested in how the properties of a pulsed laser (energy density, wavelength, size of the beam, repetition frequency, etc.) influence the local crystallization properties of a GeTe layer. These questions can be answered by solving the heat equation and assuming a heat source term that depends on the characteristic of the laser. In its most general form, the heat equation is written as:

$$\rho C_p \frac{dT}{dt} - \nabla \cdot k \nabla T = Q(x, y, z, t) \quad (44)$$

where  $\rho$  is the density of the material,  $C_p$  is the heat capacity,  $k$  is the thermal conductivity and  $Q$  is an arbitrary heat source.

The equation ( 44 ) can be solved for an arbitrary shape of the laser. Assuming that there is no transmission, the source term can be written as:

$$Q(x, y, z, t) = \alpha I_0(x, y, t)(1 - R)\exp(-\alpha z) \quad (45)$$

where  $I_0$  is the power density of the laser,  $R$  is the reflectance at the surface of the material given by equation ( 41 ) and  $\alpha$  is the optical absorption of the material which is related to the extinction coefficient  $k$  by the equation:

$$\alpha = \frac{4\pi}{\lambda} k \quad (46)$$

The power density of the laser is given by its shape, in the case of a gaussian laser beam, it is given by :

$$I_0(x, y, t) = \frac{P(t)}{A} \exp\left(-\frac{x^2 + y^2}{w_0^2}\right) \quad (47)$$

where  $P(t)$  is the instantaneous power of the laser and  $A$  is the irradiated area by the laser. For a symmetric gaussian laser, the irradiated area is given by:

$$A = \frac{\pi}{2} w_0^2 \quad (48)$$

where  $w_0$  is the beam waist (or half of the beam diameter). It is important to remark that, due to the gaussian spatial profile of the pulse, only 86% of the laser irradiated power is contained in an area of a circle with radius  $w_0$ . The area needed to contain all the power (at least 99%) is the one of a circle with radius of 1.52 times  $w_0$ .

However, many difficulties arise when trying to apply this model to the heating of a PCM laser:

1. To begin with, as the PCM reaches the crystallization temperature, the thermal properties of the material change, which modifies the heat distribution. This characteristic of the PCM makes it very difficult to solve equation ( 44 ) analytically.
2. Additionally, PCM layers are always deposited over a substrate with very different thermal properties with respect to the PCM layer. This change in the medium must also be considered in equation ( 44 ).
3. Finally, typical sizes of the PCM layers are in the hundreds of nanometers which is comparable to the wavelengths of typical lasers used for PCM activation. In this case, Maxwell's equations for the electric field inside the GeTe laser must be solved without assuming any preferred direction of propagation inside the material.

This is effectively an electromagnetic heating problem that can only be solved by numerical methods. In this case, we use the software COMSOL in order to simulate, at the same time, the electromagnetic field produced by a laser and how it heats the PCM layer. In this case, equation ( 44 ) is solved numerically while considering that the source term is given by

$$Q(x, y, z, t) = \text{Re}\{\vec{E} \cdot \vec{J}\} \quad (49)$$

Where  $E$  is the electric field inside the material and  $J$  is the current density inside the material. Equation ( 49 ) effectively means that the heating of the PCM is caused by the electromagnetic losses inside the PCM.

We consider a gaussian pulse with circular symmetry. The laser is simulated by assuming an electromagnetic source (assuming TEM propagation) of the form:

$$\vec{E}(r, z) = E_0 \frac{1}{w_0^2} \exp\left(-\left(\frac{r}{w_0}\right)^2\right) \exp(-j k_0 z) (\hat{r} + j\hat{\phi}) \quad (50)$$

Where  $E_0$  is the amplitude of the source,  $k_0$  is the wavenumber,  $r$ , and  $\varphi$  are the unit vectors,  $w_0$  is the diameter of the beam and  $r$  is the radial distance from the source center.

To accurately model the process of heating the PCM, the change of phase must be considered. Indeed, the physical properties (heat capacity, thermal conductivity, and density) of the PCM are different in both states. To model this change of state, a state variable is used, then the parameters of the PCM are generally defined as

$$\begin{bmatrix} k(T) \\ \rho(T) \\ C_p(T) \end{bmatrix} = s(T) \begin{bmatrix} k_{amorphe} \\ \rho_{amorphe} \\ C_{p_{amorphe}} \end{bmatrix} + (1 - s(T)) \cdot \begin{bmatrix} k_{crystalline} \\ \rho_{crystalline} \\ C_{p_{crystalline}} \end{bmatrix} \quad (51)$$

where  $s(T)$  is a state variable that depends on the temperature  $T$ . When the material is amorphous, the state variable is set to 1 and therefore the properties of the material are the ones in amorphous state. When the temperature  $T$  is greater than the crystallization temperature, the state variable is set to 0 and the properties of the material are the ones in crystalline state.

To ensure that the PCM retains its state when crystallized, the state variable must possess a memory effect such that when the temperature decreases below the crystallization temperature, the state variable remains at 0. This memory effect can be applied by the following pseudo code:

```

s = 1
While Simulating:
  If T > Tx:
    s = 0
  Else:
    if T < Tx:
      s = 1
    Else s = s

```

without this memory effect, the material behaves as a phase transition material. A model for the amorphization of the PCM has not yet been establish since this requires not only to model the melting of the PCM but also needs to consider the quenching time of the PCM layer.

Typical laser impulsions can be approximated by a gaussian temporal shape. Therefore, the instantaneous power of the laser can be described by:

$$P(t) = P_p \cdot \exp\left(-\left(\frac{t}{\tau}\right)^2\right) \quad (52)$$

where  $P_p$  is the peak power of the laser and  $\tau$  is the duration of the pulse which is related to the full width at half maximum (FWHM) by:

$$\tau = \frac{FWHM}{2\sqrt{\ln(2)}} \quad (53)$$

The peak power of the laser can be calculated from the electromagnetic source as:

$$P_p = \frac{\pi w_0^2 |E_0|^2}{4 \eta} \quad (54)$$

where  $\eta$  is the impedance of the vacuum.

The energy density of the laser pulse is given by :

$$\varphi = \frac{E}{A} \quad (55)$$

Where  $E$  is the energy of the pulse which is related to the power of the laser by:

$$E = \sqrt{\pi} \cdot \tau \cdot P_p \quad (56)$$

where  $T$  is the period of the pulse repetition.

By combining equations ( 53 ) to ( 56 ), the peak power of the pulse for a given energy density can be defined as:

$$P_p = \frac{1.47 w_0^2}{FHBW} \varphi \quad (57)$$

The values used for the parameters of the GeTe are summarized in Table 9. It should be noted that these values might depend on the sample and the deposition conditions, which in turn will affect the heat and temperature profiles of the heating of the PCM.

Table 9. Thermal parameters of a GeTe layer in amorphous and crystalline state.

| Parameter | Value  | Reference |
|-----------|--|-----------|
| $k$       | 0.24 J/m.K(amorphous)<br>3.2 J/m.K (crystalline)                           | [72]      |
| $C_p$     | 25.4 J/mol.K (amorphous)<br>33.8 (crystalline)                             | [126]     |
| $\rho$    | 5600 kg/m <sup>3</sup> (amorphous)<br>6170 kg/m <sup>3</sup> (crystalline) | [127]     |

The temperature rise of the material due to a single laser pulse was simulated using the parameters shown in Table 10.

Table 10. Laser pulse parameters for simulation using COMSOL.

| Parameter         | Value                 |
|-------------------|-----------------------|
| FHBW              | 9 ns                  |
| $W_0$             | 50 $\mu$ m            |
| Energy density    | 10 mJ/cm <sup>2</sup> |
| $h_{\text{GeTe}}$ | 1000 nm               |
| $T_x$             | 240 °C                |

The geometry of the structure is the one presented in Figure 73a while the laser beam profile is shown in Figure 73b and the heat distribution profile of the thin film is shown in Figure 73c. The thickness of the air layer must be at least three times bigger than the laser's wavelength in free space to ensure the correct propagation of the electromagnetic wave. In our simulations we have used five times the wavelength. The thickness of the substrate was truncated to 10  $\mu$ m to reduce the memory consumption and reduce the simulation time, although a heat continuity equation is used in the bottom to ensure that the heat propagates. The width of the layers (in the  $r$  dimension) are also truncated up to 100  $\mu$ m with the same continuity equations.

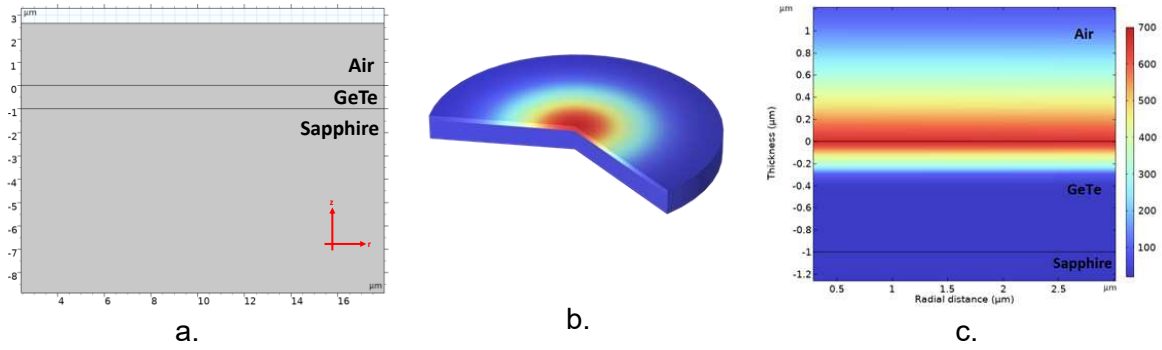


Figure 73. a) COMSOL geometry of a PCM (GeTe) layer over a sapphire substrate. b) Spatial distribution of the laser beam. c) 2D heating profile of a 1- $\mu\text{m}$  thick GeTe sample.

The rise of temperature at the center of the surface for three different wavelengths with energy density of  $10 \text{ mJ/cm}^2$  is shown in Figure 74 from which it can be seen that a laser of wavelength of  $1024 \text{ nm}$  (infrared) produces the least amount of heating compared to a laser with a wavelength of  $532 \text{ nm}$  (green) or  $248 \text{ nm}$  (ultraviolet). This is expected since, according to the ellipsometry results, at  $1024 \text{ nm}$  wavelength, the reflectance of the material is higher with respect to the other ones and thus less energy is available to heat up the material, resulting in a lower temperature rise. At wavelengths of  $532 \text{ nm}$  and  $248 \text{ nm}$ , the reflectance at the surface is almost equal, therefore the available energy is similar, resulting in a similar temperature rise.

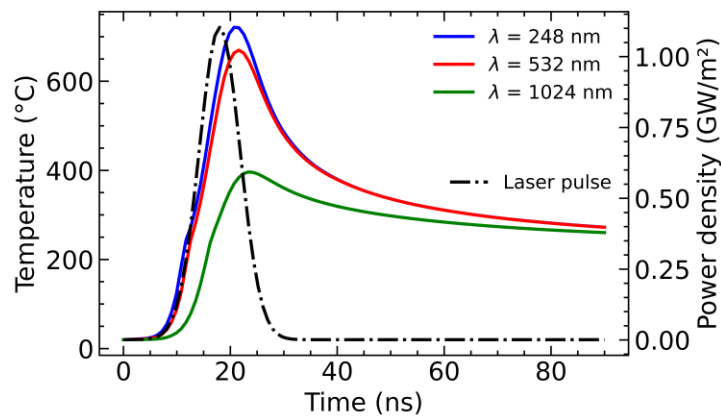


Figure 74. Simulation results of the evolution of the surface temperature in a  $1\text{-}\mu\text{m}$  thick layer of GeTe for multiple wavelengths with energy density of  $10 \text{ mJ/cm}^2$ . The temporal profile of the 9-ns laser pulse is shown in the black trace.

Figure 75 shows the distribution of the temperature on the surface of the layer (Figure 75a) and within the depth of the GeTe (Figure 75b) at the time of the maximum temperature increase at the surface after application of the laser pulse ( $t \approx 22 \text{ ns}$ ). In Figure 75a it is clear that the temperature distribution decays rapidly the further away we are from the center, this is expected since the laser pulse has a gaussian shape. We also notice that, for the wavelengths of  $532 \text{ nm}$  and  $248 \text{ nm}$ , the temperature distribution curves are discontinuous at around  $50 \mu\text{m}$  away from the center which can be explained by the phase change in the GeTe (change in thermal properties) since this perturbation occurs at the crystallization temperature.

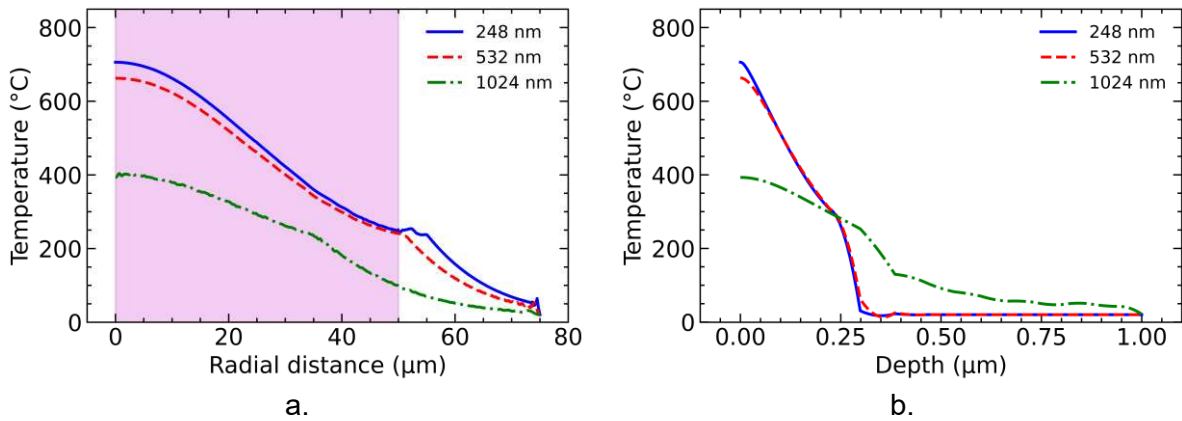


Figure 75. a) Temperature distribution over the surface of the GeTe layer at the time of peak temperature for different wavelengths (the violet shaded area represents the laser beam radius). b) Temperature distribution in the depth of the GeTe layer at the center of irradiation beam at the time of peak temperature for different wavelengths.

From Figure 75 we can observe that the profile of temperature for wavelengths of 248 nm and 532 nm is similar and also that the temperature decays very rapidly as we go deeper into the material. This is due to the high extinction coefficient of the GeTe at both wavelengths. Additionally, a sharp transition is observed at a depth of around 300 nm which is due to the crystallization of the GeTe layer. It is worth noticing that for wavelengths of 1024 nm the temperature distribution does not decay as fast as the other two wavelengths which is explained by the fact the GeTe is more transparent at this wavelength. This transparency allows the energy to penetrate deeper into the material thus heating more easily the deeper parts of the layer, on the expense of a lower temperature increase in the layer, for similar incident power.

As the laser impulsion is over, the excess heat in the material will propagate to its surroundings and extend the crystallized zone. Although the depth and extent of the crystallization can be approximated from Figure 75, looking at the state variable at the end of the pulse will provide a much clear image of the crystallized zone. The value of the state variable at the interior of the GeTe is shown in Figure 76 for all three wavelengths. From this image it can be seen that an infrared laser (1024 nm) produces the smallest crystallized zone (radius of around 35 μm) with respect to the other two wavelengths, because the rise in temperature is lower. The green (532 nm) and ultraviolet (248 nm) lasers produce similar sizes of the crystallized zone (around 50 μm to 55 μm in radius, respectively) comparable to the radius of the pulse.

From Figure 76 it can be seen that, for the specific incident energy, all wavelengths produce similar depths of crystallization (of around 500 to 550 nm). as explained earlier, the transparency of the layer at this wavelength is bigger which allows the deepest part of the laser to heat up easier. This to effects compensated each other such that, after diffusion of the surrounding heat, the crystallization depth is mostly similar.

Naturally, increasing the energy density of the laser will increase the depth of the crystallized zone and the radius of the crystallized zone, as shown in Figure 77a and Figure 77b, respectively for  $\lambda = 532$  nm. However, increasing the energy density will also increase the maximum temperature at the surface (as shown in Figure 78) which could lead to damage of the PCM film. It is also worth noting that the boundaries of the crystallized area do not grow linearly with the power of the laser.

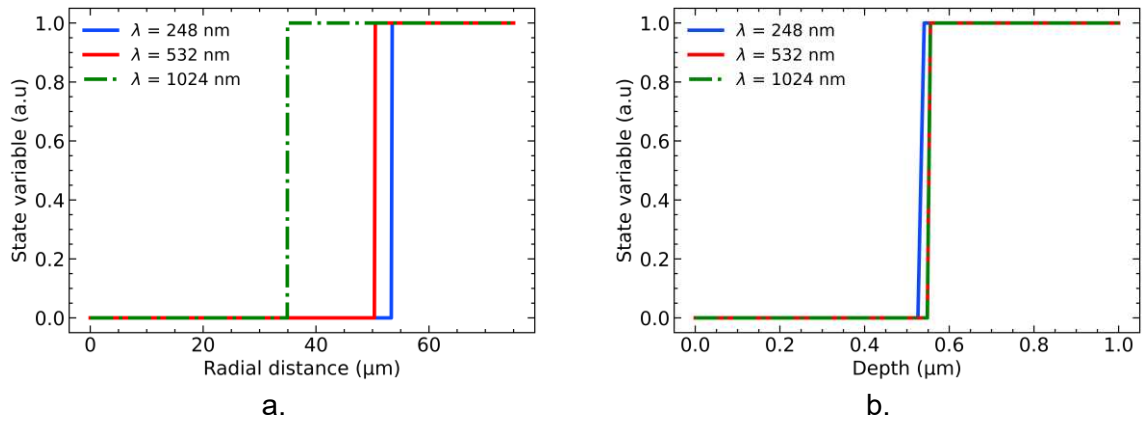


Figure 76. a) Amorphous-to-crystalline state variable distribution over the surface of the GeTe layer at the end of the simulation. b) State variable distribution in the depth of the GeTe layer at the end of the simulation. ( $S = 0$  for crystalline GeTe and  $S = 1$  for amorphous state).

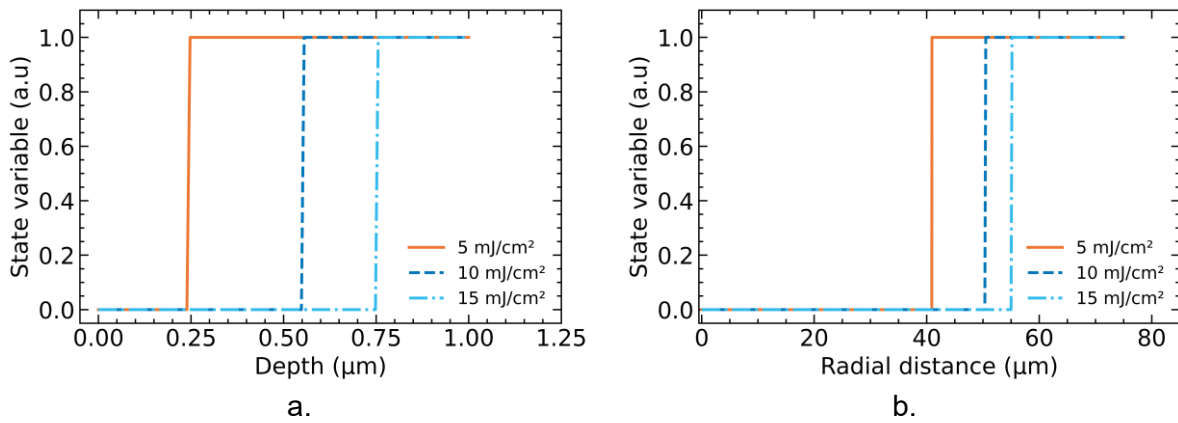


Figure 77. a) State variable distribution over the depth of the GeTe layer for different energy densities for  $\lambda = 532$  nm. b) State variable distribution over the surface of the GeTe layer for different energy densities for  $\lambda = 532$  nm. ( $S = 0$  for crystalline GeTe and  $S = 1$  for amorphous state).

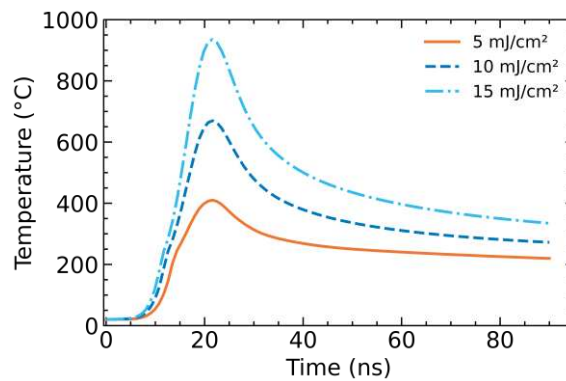


Figure 78. Surface temperature evolution of the GeTe film over time for multiple energy densities.

Another important aspect is the thickness of the PCM layer. The Figure 79 shows the simulation results of the heating at the surface of the GeTe for various thicknesses of the layer for a wavelength of 532 nm and a fluence of 10 mJ/cm<sup>2</sup>. From this image is clear that the rise in temperature is almost independent of the thickness of the layer, however the cooling speed is greatly dependent on its thickness. We can see that the thinner the layer, the faster is the cooling rate.

This can be explained by observing the temperature distribution at the time of reaching the peak temperature. As explained previously, the laser energy decays exponentially when enters the material which means that not all the material is heated up significantly within its depth. When the thickness of the layer is lower, the heated part of the GeTe is in contact with the sapphire substrate and therefore there is a significant heat transfer between the PCM and the substrate (as shown in Figure 80a), which increases the cooling rate of the PCM. When the thickness of the PCM layer is higher, there is no contact between the heated part of the GeTe and the substrate as shown in Figure 80b, hence there is low or no heat transfer, and the cooling of the GeTe layer is slower. It can be concluded that the thickness of the layer plays a significant role in the cooling of the PCM. This is a very important issue, since the amorphization of PCM layers requires quenching the material very rapidly. This result implies that thinner layers of PCM are easier to amorphise.

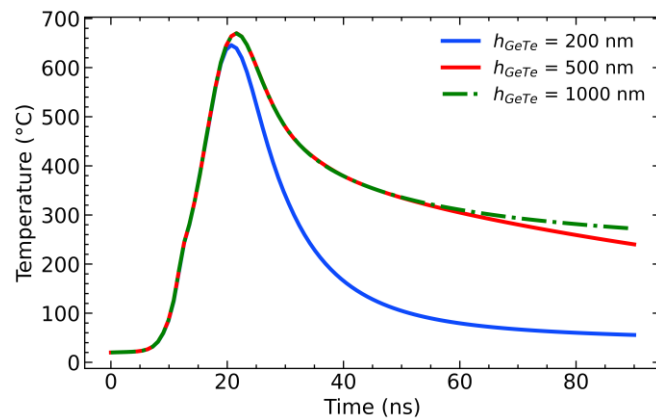


Figure 79. Simulation results of the surface temperature evolution at the center of the irradiated area for three different thickness of the GeTe layer deposited over a sapphire substrate.

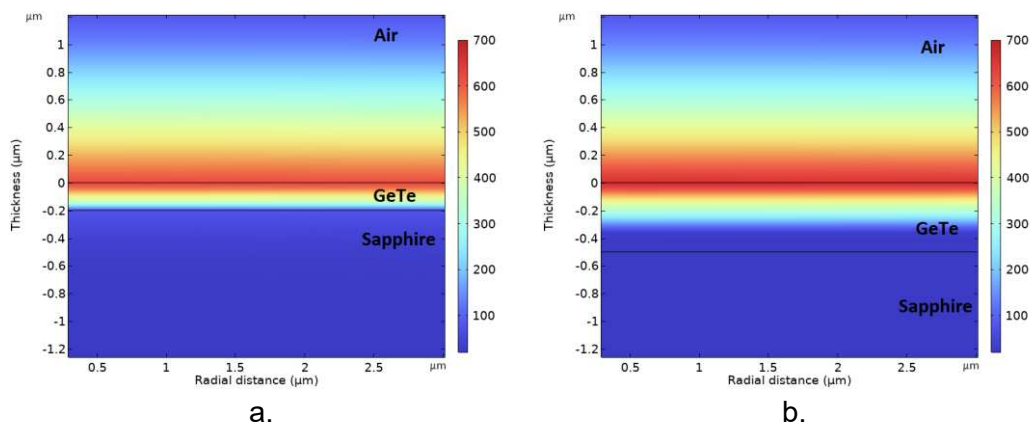


Figure 80. Temperature distribution inside the GeTe layer at the time of peak temperature at its surface for a green laser ( $\lambda = 532 \text{ nm}$ ) and a fluence of  $10 \text{ mJ/cm}^2$ , for a) 200-nm thick layer and b) 500-nm thick layer.

To summarize, we can conclude that the depth of crystallization of PCM layers seems to be almost independent of the laser's wavelength. However, an efficient reversible activation (crystalline to amorphous states) requires the use of relatively thin layers of GeTe. As previously explained, for infrared lasers, the reflectivity of the layers depends on their thicknesses which only adds complexity to the mechanism of activation and reduces the overall energy efficiency of the process. The use of green or ultraviolet lasers is much more adequate and efficient since the reflectivity of the layers does not depend on their thickness.

Additionally, the depth of the crystallization is likely to play an important role in the overall electrical resistance of the PCM layer in the crystallized state: the deeper the crystallized zone, the lower the resistance of the layer and therefore less losses at millimeter-wave frequencies. To create a deep crystallized zone, one could increase the power of the laser during the irradiation process at the expense of risking to damage the surface of the layer. Another strategy may be the use of subsequent multiple low-power laser pulses or the addition of an antireflection capping layer which, beside the increase of the energy delivered to the layer may also protect its surface from oxidation or other adverse environmental conditions.

### II.5.3. Optical irradiation system of PCM layers

The optical irradiation system developed for our PCM activation experiments is the one shown in Figure 81.

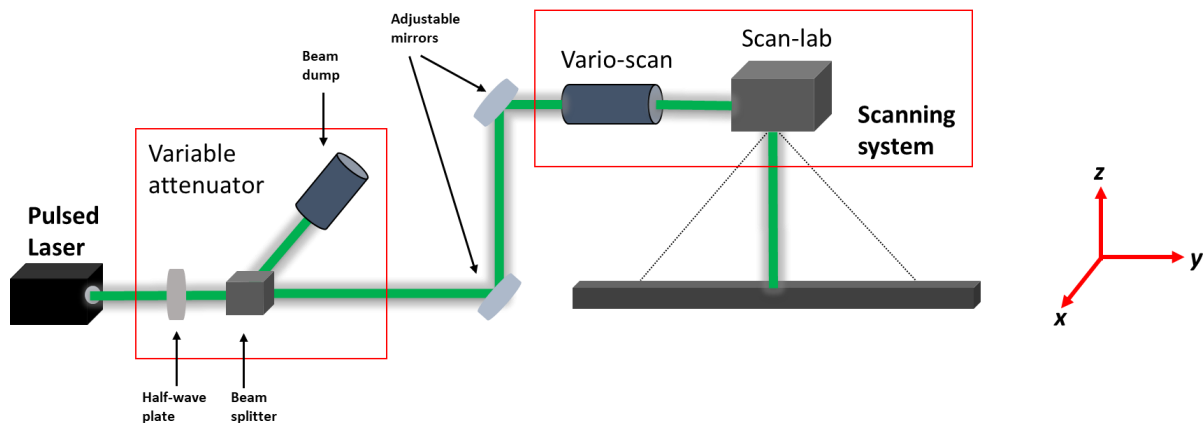


Figure 81. Diagram of the complete optical irradiation set-up.

This system basically consists of the following elements:

1. A solid-state pulsed laser source from Compact Laser Solutions manufacturer. The laser model is a monolith 532\_3\_HE (shown in Figure 82) working at a wavelength of 532 nm (green beam laser) with a variable repetition frequency from 1 Hz up to 50 KHz. The nominal average power is 3 W at 6 kHz with a maximum pulse energy of 550  $\mu$ J and 60 kW of maximum peak pulse power. The nominal beam diameter is 0.8 mm with an  $M^2$  value less than 1.3. The nominal temporal pulse width is 9 ns.

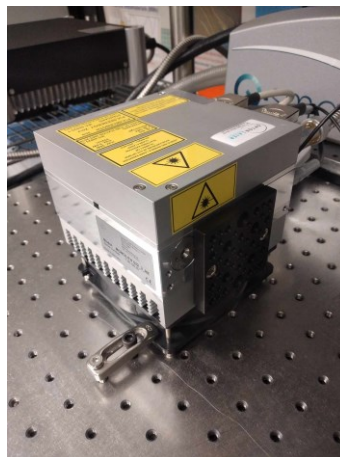


Figure 82. Solid-state pulsed laser system working at 532 nm wavelength.

- An optical scanner system (SCANLAB) with galvanometric mirrors and a F-theta lens which allows directing the laser beam over a flat surface (Figure 83a) by a moving set of mirrors. This capability will allow to write patterns over large surfaces of PCM layers. The scanner F-theta objective lens allows to correct deformations on the beam when the beam is projected at different distant points on a flat surface limited to a maximum written area of  $10 \times 10 \text{ cm}^2$  (Figure 83b). The focal point of the F-theta lens is 160 mm which be adjusted by the Vario Scan system (which will be described later in the discussion) (Figure 83c).

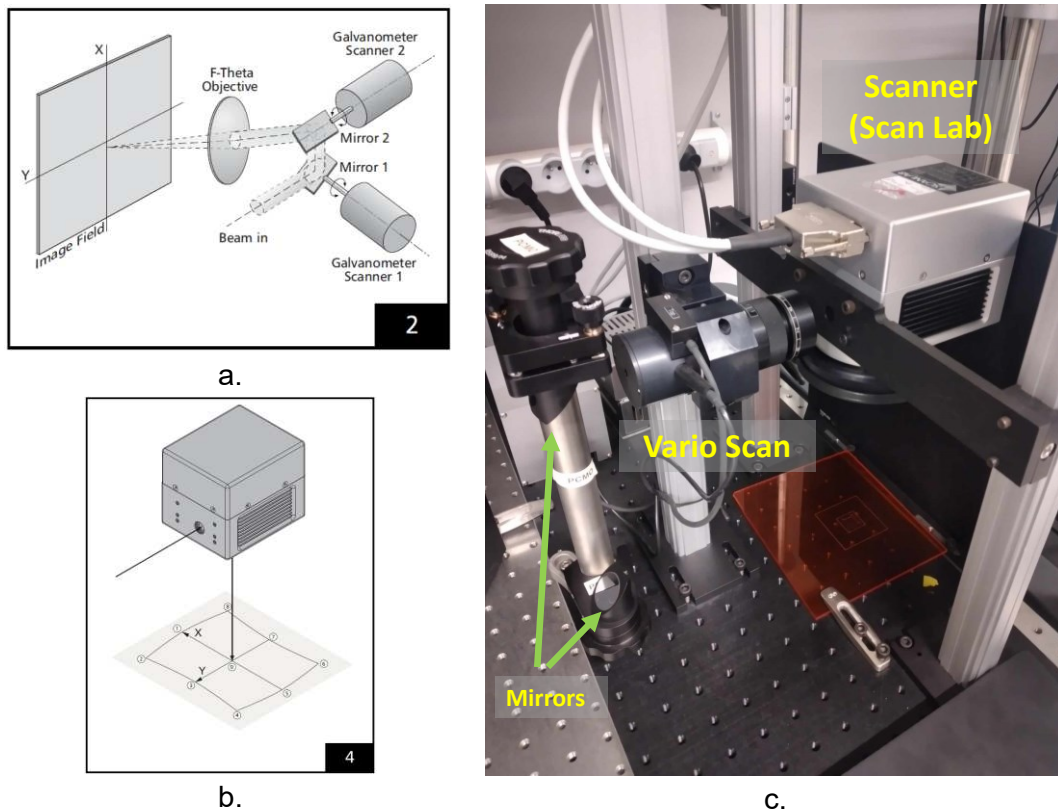


Figure 83. a) Functioning principle of the SCAN Lab system. b) Positioning and image field of the SCAN Lab system. c) Optical scanner system (SCAN Lab) with variable focus system (Vario Scan) in order to change to focus plane of the scanner and change the size of the laser spot.

- Software control: The ScanLab system as well as the laser can be digitally controlled by a powerful software that can take advantage of all the functionalities of the scanner system. This software comes with graphical interface that allows the creation and editing of arbitrary shapes and images (Figure 84a) as well as complete control and automation of the irradiation parameters on demand (Figure 84b and Figure 84c, respectively).

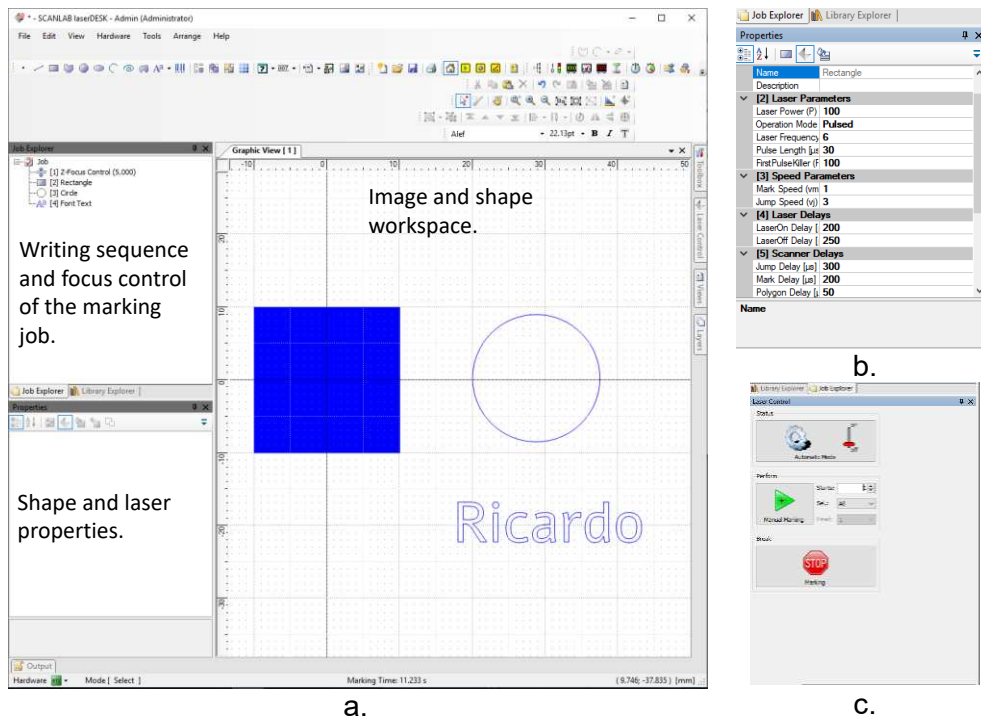


Figure 84. a) Principal workspace of the SCANLab software. b) Laser properties for the marking of the shapes. c) Laser control and automation of the marking process.

4. VarioScan system: This is a mechanical optical system that allows to dynamically modify the focal length in the z-plane. The Figure 85 shows the functioning principle of the device. In this case, a motor moves a divergent lens (at the middle of the device) which then goes into a fixed convergent lens. Depending on the distance between the two lenses, the effective focal length can be adjusted.

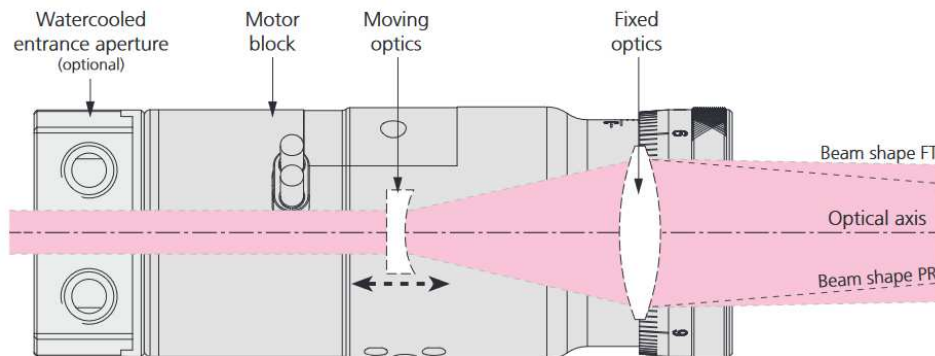


Figure 85. Schematic representation of the VarioScan system.

### II.5.3.1. Laser characterization

The Figure 86a shows the measured average power and energy of the laser as a function of frequency repetition rate. The average power was measured using a thermopile power detector. The average energy of the pulse was measured with a pyroelectric joulemeter using 500 pulses (this detector can only be used up to repetition frequencies of 200 Hz). From Figure 86b it can be seen that the average power increases linearly with the frequency up to 6 kHz (the nominal operation frequency). This is the linear region of the laser where the energy of the pulse is constant as shown in Figure 86b. For repetition frequencies higher than 6 kHz, the

average power of the laser increases up to 30 kHz but in a non-linear manner, which implies a decrease of pulse energy, this is the saturated region of the laser.

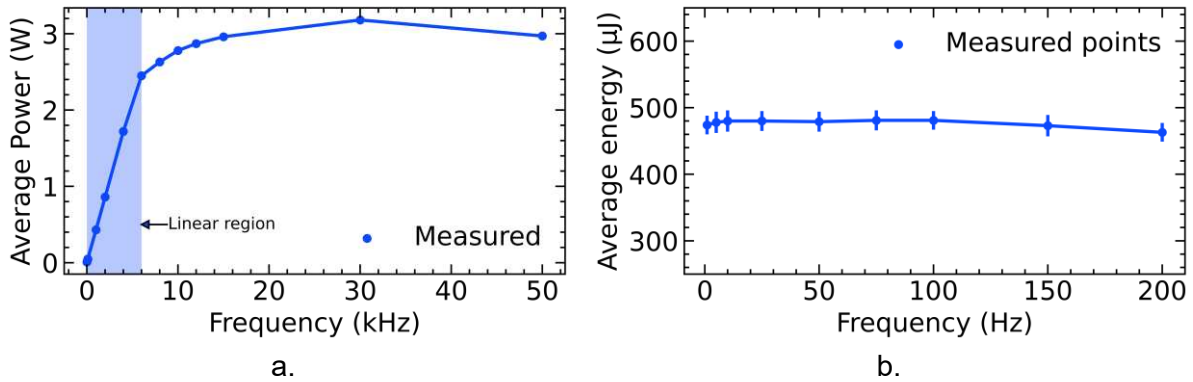


Figure 86. a) Average power of the laser measured over the whole frequency range. b) Average energy of the laser measured up to 200 Hz.

For frequencies greater than 200 Hz, the energy of the pulse can be deduced from the average power  $P_{avg}$  and the frequency by using the relationship:

$$E = \frac{P_{avg}}{f} \quad (58)$$

The Table 11 summarizes the deduced pulse energies up to 50 kHz. From this table, it can be seen that the energy of the pulse decreases very slowly up 6kHz and then it drops significantly in the saturated region.

Table 11. Deduced pulse energy from the measured average power of the pulsed laser.

| Frequency (Hz) | Pulse energy (µJ) |
|----------------|-------------------|
| 1000           | 450               |
| 2000           | 445               |
| 4000           | 438               |
| 6000           | 413               |
| 8000           | 335               |
| 10000          | 283               |
| 15000          | 201               |
| 30000          | 107               |
| 50000          | 60                |

The Figure 87a shows the measured pulse temporal profiles of the laser, using a high speed silicium photodetector (DET025A from Thorlabs, connected to an DSO Tektronix oscilloscope) in the linear region, while the Figure 87b shows the pulse profile in the saturated region. It can be seen that the shape of the pulse is rather constant in the linear region with a FWHM of less than 13 ns. In the saturated region the amplitude of the pulse decreases as the frequency increases, additionally the FWHM increases with frequency, which further supports the claim that the energy of the pulse decreases in this region.

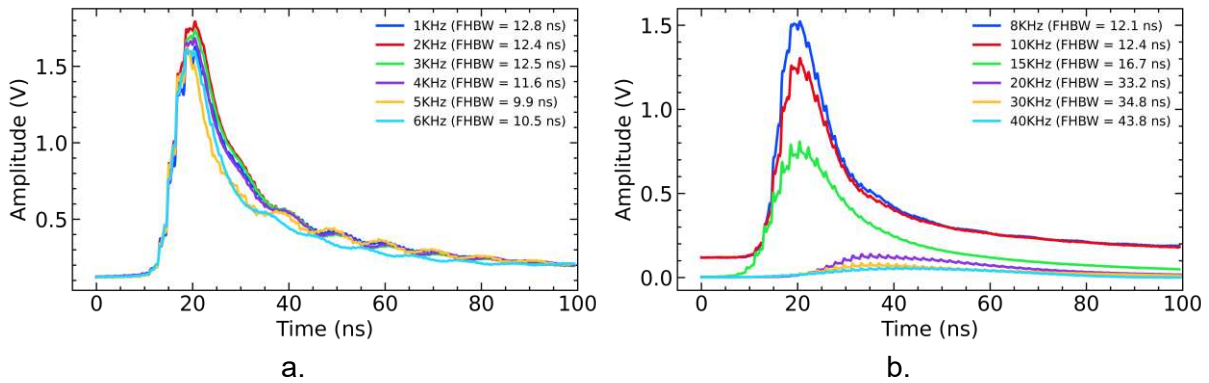


Figure 87. Measured temporal pulse shape of the pulsed laser source in the a) linear region and, b) saturated region.

### II.5.4. Crystallization GeTe layers by laser irradiation

An amorphous sample of a 500-nm thick layer of GeTe obtained on a sapphire substrate was irradiated using a single 480  $\mu\text{J}$  laser pulse with a repetition frequency of 10 Hz. As shown in Figure 88, the irradiated area has been transformed to the crystalline state, as indicated by the change of color. The nominal size of the beam is around 0.8 mm (according to manufacturer specifications) however the size of the transformed area is 0.59 mm. This is expected since only the area in which the temperature reaches the crystallization temperature is transformed. The surrounding area, although also irradiated, did not reach the crystallization temperature and therefore is not transformed. Trying to deduce the energy density from the size of the crystallized area is ill-advice since, according to equations ( 48 ) and ( 55 ), the energy density is inversely proportional to the square of the beam radius and, therefore, any inaccuracy in the estimation of the diameter of the beam will results in much bigger energy density. Additionally, the size of the crystallized area does not correspond to the actual size of the laser pulse, as shown by simulation results. Assuming a beam diameter of 0.8 mm (beam waist radius of  $w_0 = 0.4$  mm) and multiplying by 1.52 to consider 99% of the beam power, the energy intensity of the pulse would be around 77.8  $\text{mJ}/\text{cm}^2$ . The loses of energy due to additional optics was not considered. Is important to notice that the shape of the crystallized zone is not completely circular, this can be explained by misalignment of the optics.

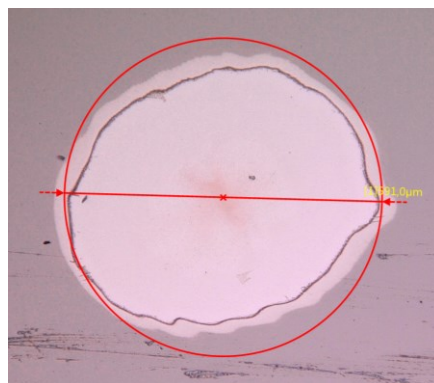


Figure 88. Crystallized area by a single 480- $\mu\text{J}$  laser pulse on a 500-nm thick GeTe layer deposited over a sapphire substrate.

Arbitrary continuous and larger-area patterns can be created using the scanner system by irradiating adjacent zones. The separation between pulses is dictated by the laser frequency as well as the speed of the beam displacement operated by the scanner system. Figure 89 shows examples of a laser crystallization of a GeTe amorphous layer following multiple pulse

irradiations with different spacing. The speed of beam positioning of the scanner is set to 1 mm/s while the frequency of the laser irradiation is gradually increased.

The Figure 89a shows that if the laser frequency is very slow with respect to the scanning speed, the crystallized zones will not overlap and therefore a continuous pattern cannot be formed. As the laser frequency increases, the crystallized zones overlap and a continuous pattern is formed (Figure 89b, Figure 89c and Figure 89d). However, as the pulses overlap, damages on the center area of the scanned line are observed. This is due to fact that, for a gaussian pulse, most of the energy is concentrated in the center and therefore the increase in temperature is more important. As the irradiation pulses becomes closer in space, some areas are irradiated multiple times with a very high energy density, which leads to damage of the film. Another important aspect is that the time needed to complete a specific pattern depends on the scanning speed. Indeed, the slower the scanning speed the more time is required to complete the pattern.

In order to reduce the damage associated to an area irradiated multiple times, a variable attenuator is used between the laser and the scanning system (as shown in Figure 90a) which consist of a half-wave plate, a polarizer (a cube beam split polarizer, in our case) and a beam dump. This combination of optical components attenuates the power of the laser by a factor:

$$\frac{P_{out}}{P_{in}} = (\cos(2\theta - \varphi))^2 \quad (59)$$

where  $\theta$  is the angular difference between the axis of the beam splitter and the half-wave plate and  $\varphi$  is a correction angle for the case when the fast axis of the half-wave plate is not aligned with the graduation of its support. Figure 90b shows the power characterization of the variable attenuator.

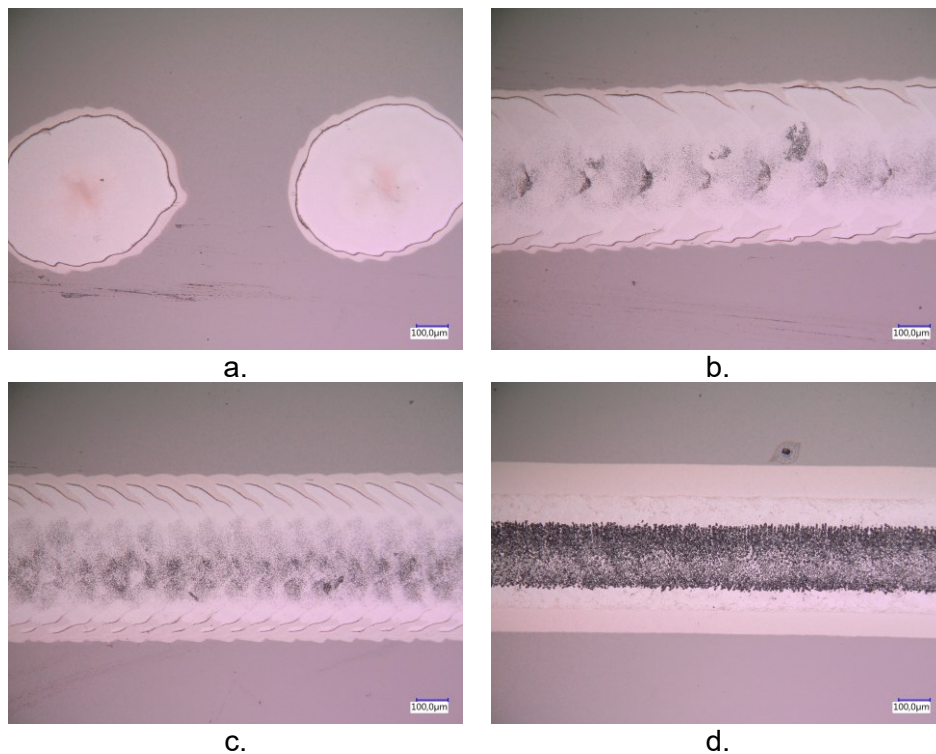


Figure 89. Crystallized zones by raster scanning with laser beam positioning speed of 1 mm/s for different laser repetition rates, at frequencies of a) 10 Hz. b) 100 Hz, c) 500 Hz and d) 1000 Hz.

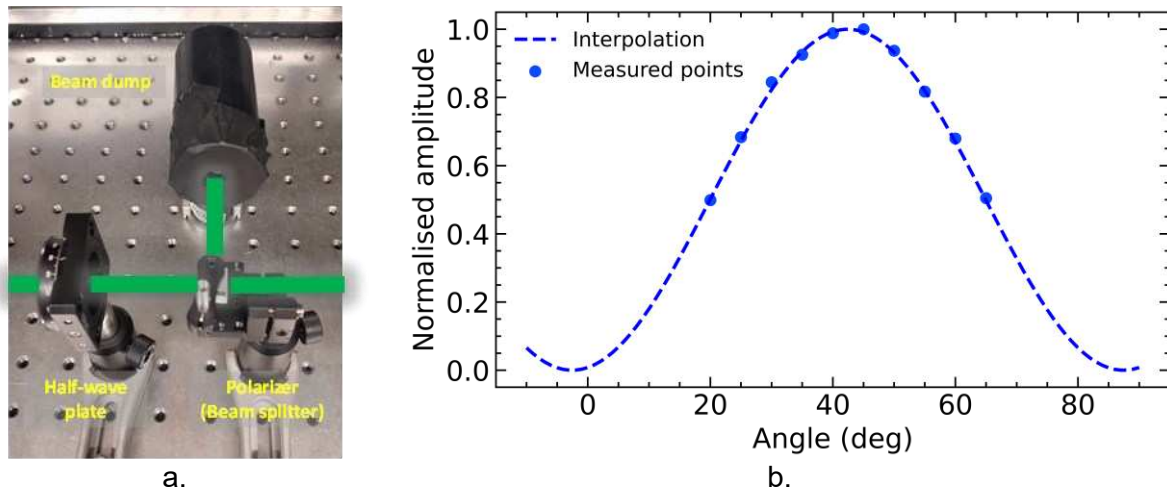


Figure 90. a) Variable attenuator with beam dump. b) Normalize power transmission as a function of the half-wave plate angle position.

In practice, the attenuation factor is reduced gradually until a clear and undamaged irradiated area is observed. Additionally, the frequency of irradiation and speed of scanning is increased to 6 kHz and 30 mm/s, respectively in order to reduce the pattern fabrication time. Thus, on Figure 91 are shown the results following irradiation with different attenuation factors. From Figure 91a and Figure 91b it can be seen that the damaged areas can be greatly reduced by reducing the overlapping, unfortunately, the damage is still observed. As the energy is further reduced, the surface damage is also reduced. For power attenuations lower than 20% (Figure 91c and Figure 91d), we observe a smooth crystallized zone that corresponds to an energy density of less than 40 mJ/cm<sup>2</sup> by assuming a beam diameter of 1.52 times the size of the crystalline region (0.9 mm).

The size of the crystallized area defines the resolution of the system. In the case of Figure 91, the size of the pattern is defined by the size of the laser beam after passing through the scanning system. The spatial dimension of the pulse can be reduced by focusing, however, decreasing the area of the irradiation without decreasing the energy of the impulsion will lead to an increase in the energy density which can lead to damage in the material. If the diameter of the irradiated beam is reduced 5 times, then the energy density is increased by 25 times.

The use of the VarioSCAN system is used to change the position of the focal point in the vertical dimension which normally lies in the irradiation plane situated at 163 mm below the scanning system. Unfortunately, for very high attenuation factors, the sensitivity of the variable attenuator becomes very high which leads to difficulties in the precise control of the attenuation. Therefore, the frequency of the irradiation was also increased into the saturation region in order to further decrease the original energy of the impulse and decrease the need for high attenuation factors.

Tests were performed in a 250-nm thick layer of GeTe over a sapphire substrate with a frequency of irradiation of 30 kHz and an attenuation factor of 80% (transmission of 20%) corresponding to a pulse energy of 20 μJ. The absolute value of the focal point is changed and the results of the irradiation experiments are recorded in Table 12.

From this table, it can be seen that for a focal distance greater than 10 mm no crystallization is observed which is due to the fact that the energy density is not enough to reach the crystallization temperature. As the focal distance decreases, the energy density increases and crystallization is observed. The minimum crystallization zone observed is around 46 μm as

shown in Figure 92. For focal distances at and below 4 mm, some damages of the PCM layer are observed.

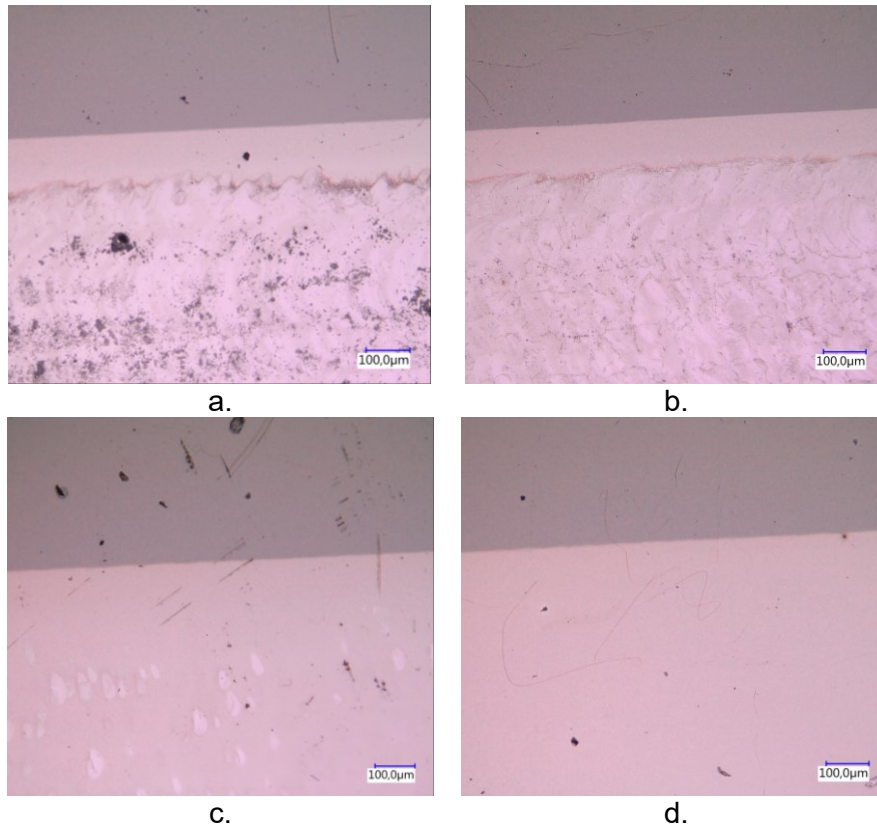


Figure 91. Crystallized zone of a 250-nm thick GeTe layer for a laser power attenuation factor of a) 100% transmission ( $E_{\text{pulse}} = 450 \mu\text{J}$ ), b) 50% transmission ( $E_{\text{pulse}} = 225 \mu\text{J}$ ), c) 20% transmission ( $E_{\text{pulse}} = 90 \mu\text{J}$ ) and d) 5% transmission ( $E_{\text{pulse}} = 22.5 \mu\text{J}$ ).

Table 12. Recorded size of the crystallized zone for different focal point distances.

| Focal point distance | Diameter of the crystallized zone | Observations                |
|----------------------|-----------------------------------|-----------------------------|
| 10 mm                | N.A                               | No crystallization observed |
| 8 mm                 | 127 $\mu\text{m}$                 | Crystallization observed    |
| 6 mm                 | 147 $\mu\text{m}$                 | Clean crystallized zone     |
| 4 mm                 | 93 $\mu\text{m}$                  | Damage is observed          |
| 2 mm                 | 46 $\mu\text{m}$                  | Damage is observed          |
| 0 mm                 | 74 $\mu\text{m}$                  | Damage is observed          |



Figure 92. Smallest observed crystallized zone using the VarioSCAN system.

### II.5.5. Amorphization of crystalline layers of GeTe by laser irradiation

From the simulation results presented before, it is expected that a thinner layer of GeTe will be easier to transform from the crystalline to the amorphous state. The amorphization of a crystallized 250 -nm thick GeTe area is achieved by gradually increasing the pulse energy (by varying the attenuation factor). A test to transform to the amorphous state a previously crystallized GeTe area was performed using a laser frequency of 30 kHz with a transmission factor of 40% (42.8  $\mu$ J) and a VarioScan focal distance of 6 mm. The Figure 93 shows a clear laser transformed amorphous area next to an initially crystallized zone. We notice that the required energy needed for amorphization is around the double of the energy required for crystallizing the sample.

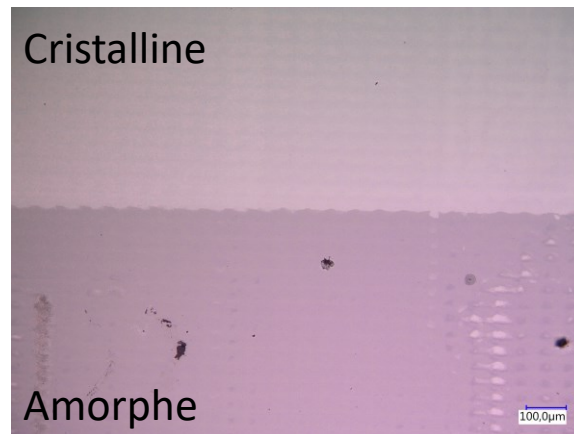


Figure 93. Amorphized area of a 250-nm thick GeTe sample using laser irradiation of a previously crystallized zone.

The surface resistance of the irradiated sample was recorded using the 4-point probe method before and after amorphization and is indicated in Table 13. From this table we can observe that the surface resistance after re-amorphization is significantly lower with respect to the as-deposited state.

Table 13. Surface resistance of the GeTe layer after optical transformation between the two states.

| State                       | Surface resistance        |
|-----------------------------|---------------------------|
| As-deposited (Amorphous)    | 27 M $\Omega$ $\square$   |
| After laser crystallization | 59 $\Omega$ $\square$     |
| After laser amorphization   | 2.45 M $\Omega$ $\square$ |

Finally, a 250-nm thick GeTe layer over a 10x10 mm<sup>2</sup> sapphire substrate was sequentially crystallized and amorphized three times and the evolution of the resistance with respect to the temperature was recorded. The results shown in Figure 94 demonstrates that the crystallization temperature does not change after the subsequent transformations between the different phases. Still, more conclusive experiments with multiple optical transformation cycles between the two states will be needed in order to assess the reliability of the process. The sudden increase in resistance of the as-deposited sample at 200°C was caused due to a probe manipulation error during the experiment.

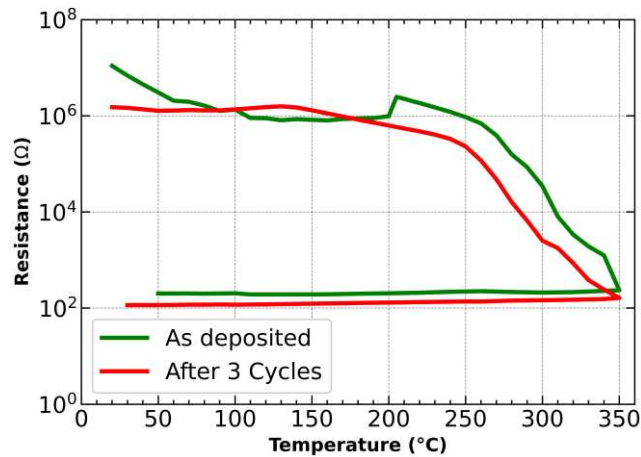


Figure 94. Evolution of the surface resistance of a GeTe layer as a function of temperature after 3 complete cycles of optical induced crystallization-amorphization.

### II.5.6. Arbitrary pattern written and erasing using the laser scanning system

In order to illustrate the optical activation of GeTe layers using large and complex patterns, an arbitrary pattern was written in a 250-nm layer of GeTe obtained on a 25x25 mm<sup>2</sup> substrate sapphire. The frequency of irradiation was 30 kHz with a transmission of 20% (pulse energy of  $\approx 21.4 \mu\text{J}$ ). In Figure 95a, the as-deposited GeTe layer is shown. Then, the logo of CNES was optically written in the GeTe by crystallization, as shown in Figure 95b.

To erase the pattern, the whole surface was crystallized (Figure 95c) and then re-amorphized (Figure 95d) using the same irradiation frequency but with a transmission of 40% (pulse energy of  $\approx 42.8 \mu\text{J}$ ). After amorphization, it can be seen that the CNES logo has been almost completely erased but some traces are still visible. These traces may be explained by some local areas damaged by the high energy pulses which may be due to instabilities of the laser as we are forced to work in the saturated region in order to comply with the necessary energy levels for amorphization. Then, the logo of CNES was re-written in the previously erased surface (Figure 95e). Afterwards, the pattern is erased following the same procedure and a new pattern (XLIM laboratory logo) is written in the layer (Figure 95f).

The Figure 96 shows a thermal infrared image of the engraved logos on a GeTe/sapphire substrate the profile of the emissivity of the GeTe layer. The figure shows a large contrast between the amorphous and crystalline irradiated regions. From Figure 96c, it can be seen that CNES logo was not completely erased and therefore optimization of the parameters still needs to be carried out.

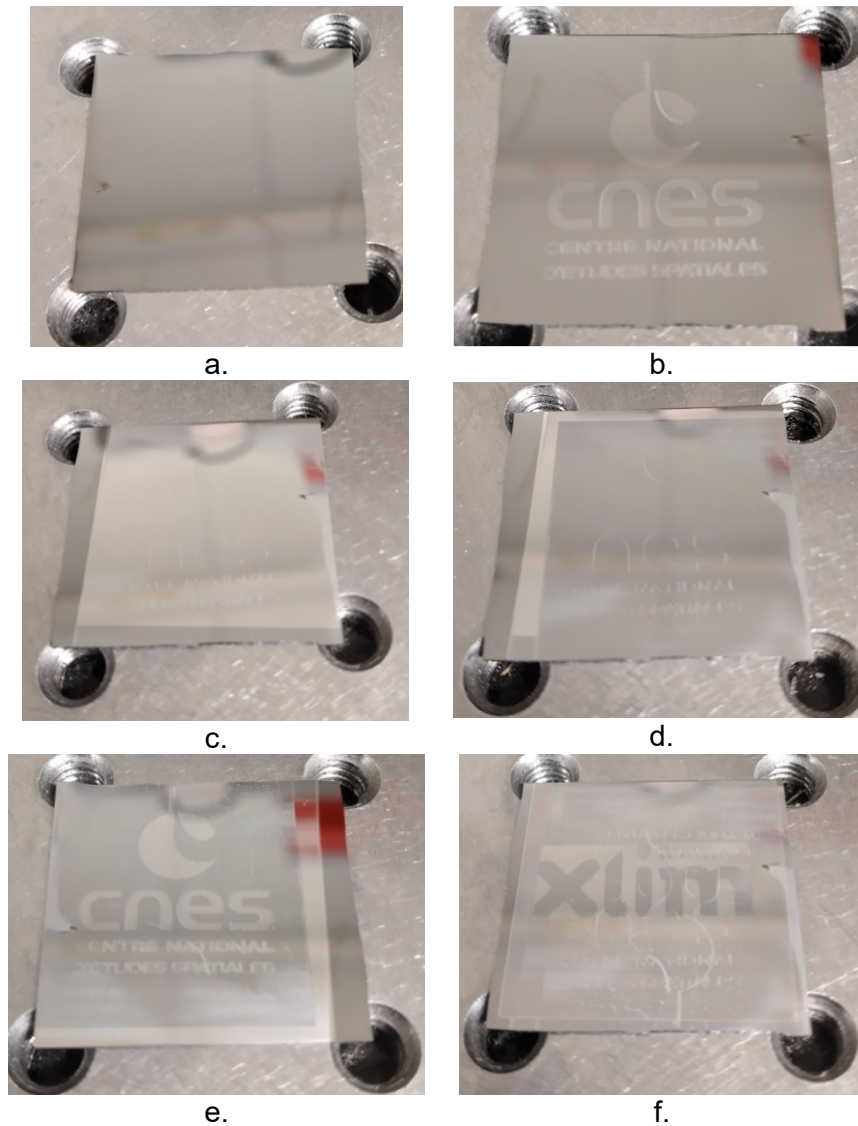


Figure 95. Writing and erasing procedure of arbitrary shapes in a GeTe layer. a) As-deposited 250-nm GeTe layer on a 25x 25 mm<sup>2</sup> sapphire substrate. b) Writing of an arbitrary shape using laser engraving (CNES logo-crystalline). c) Erasing of the previously written pattern by crystallizing the whole pattern d) Amorphization of the whole written surface. e) Re-write of the CNES logo (crystalline) d) Erasing and writing of another arbitrary pattern in the surface (XLIM logo-amorphous).

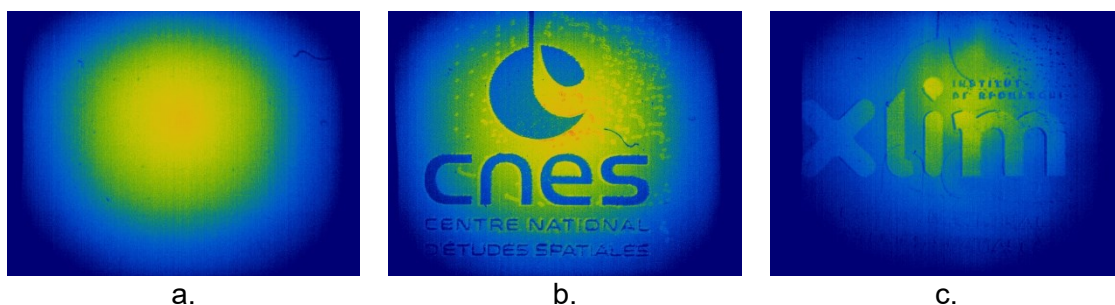


Figure 96. Thermal infrared images of the a) As deposited 250-nm thick GeTe layer. b) After engraving the CNES logo. c) After erasing the previously written CNES logo and re-writing the XLIM logo.

This experiment shows for the first time to our knowledge the capability of writing and erasing, an arbitrary pattrer in a PCM layer. This procedure can be exploited for different applications,

for example to design reconfigurable metasurfaces directly in the GeTe layer (all-dielectric metadevices) or within devices with hybridized metal-PCM structures. It is important to notice that the erasing procedure must be further optimized by proper choose of irradiation and scanning parameters) since some traces of the previously written patter are still observed (as shown in Figure 95d) which leads to visible traces in the newly written pattern (Figure 95f).

### II.5.7. Evaluation of the quality of the optically crystallized areas

A single pulse irradiation with sufficient energy is enough to crystallize an amorphous region at the surface of the GeTe. However, as shown by the multi-physics simulation results, the fact the surface is crystallized does not ensures that all the volume of the material is crystallized (i.e within the entire thickness of the fabricated layer). This is important, since the thinner the crystallized region, the lower the overall conductivity of the sample, which implies higher losses when used for millimeter wave band applications.

One strategy to increase the depth of the crystallized zone is to increase the energy of the pulse. However, this implies also an increase in the surface temperature which can lead to film damages. Another strategy is to irradiate the same area with multiple low-energy pulses in order to heat up progressively the film. To evaluate the quality of the crystallization, we can use the concept to layer resistivity. Indeed, according to equation ( 9 ), the resistance of the layer depends on the thickness of the conductive region: for a given conductive surface, the thicker this conductive layer is, the lower the resistance.

Different optical irradiation tests for investigating the change in surface resistivity were performed on a GeTe layer (250-nm thick) by varying the laser frequency from 6 kHz to 50 kHz (in the saturated region) with various numbers of pulses applied on the same area. A VarioScan focal distance of 10 mm was chosen, such that the size of the pulse is large enough to avoid damaging the layer's surface when using high-energy pulses. The surface resistance of the irradiated areas was evaluated on a surface of 8x4 mm<sup>2</sup> with a 4-point probe method and the overall results along with the irradiation parameters are presented in Table 14. The results indicate that the higher the pulse number, the lower the surface resistance which implies a deeper crystallization in the film. However, as shown in Figure 97a and Figure 97b, higher energies imply a higher rise in temperature at the GeTe film surface, which can lead to damage. As the energy of the pulse decreases (higher frequencies), the damage to the surface is reduced (Figure 97c and Figure 97d) but the surface resistance is increased as indicated in Table 14.

Table 14. Recorded surface resistance for different frequencies (i.e different pulse energies) and number of pulses.

| Frequency (Energy) | 10 pulses | 50 pulses | 100 pulses |
|--------------------|-----------|-----------|------------|
| 6 kHz (408 μJ)     | 51 Ω□     | 20 Ω□     | 18.67 Ω□   |
| 10 kHz (408 μJ)    | 24 Ω□     | 41 Ω□     | 24 Ω□      |
| 20 kHz (280 μJ)    | 172 Ω□    | 202 Ω□    | 106 Ω□     |
| 30 kHz (106 μJ)    | 536 Ω□    | 546 Ω□    | 260Ω□      |
| 40 kHz (76 μJ)     | 21 KΩ□    | 710 Ω□    | 386Ω□      |
| 50 kHz (60 μJ)     | 1.22 MΩ□  | 695.7 Ω□  | 525 Ω□     |

Another important system aspect of the scanner is the writing speed: as the frequency of the irradiations increases, the scanner must move faster in order to reposition the next pulse. This fast movement can lead to errors in the size of the written area for very small features. Additionally, the laser can become unstable if working in the saturated region.

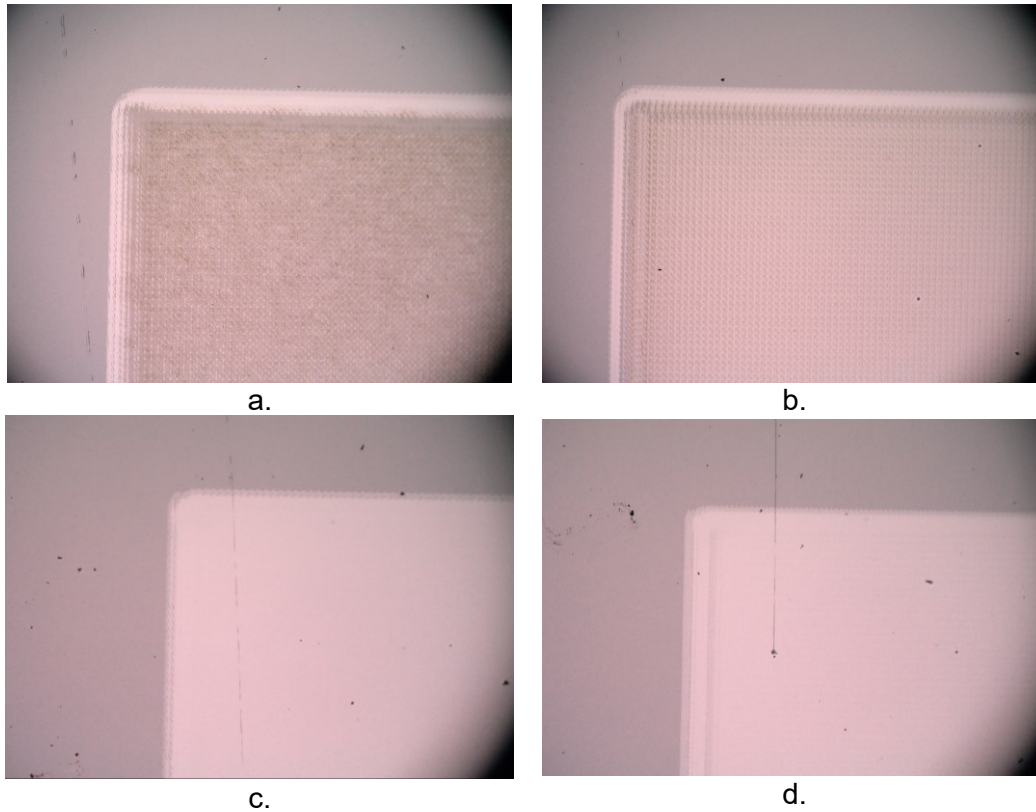


Figure 97. Image of the GeTe surface layer after irradiation with a) 10 pulses at 6 kHz, b) 10 pulses at 10 kHz, c) 10 pulses at 30 kHz, and d) 10 pulses at 50 kHz.

In order to reduce the written speed, the laser frequency must be decreased (ideally to the linear zone where the laser is more stable). However, as shown in the previous test, this increase in energy can lead to damage to the GeTe layer. To counter this energy increase, a second variable attenuator was installed in series with the initial one. Table 15 indicate the measured surface resistance of the crystallized areas on the same GeTe layer after a laser irradiation using a frequency set to 6 kHz and a scanner speed positioning of 300 mm/s. The attenuation factor is set to 99% (pulses of  $\approx 4.5 \mu\text{J}$ ) while the VarioScan focal distance was gradually decreased. The quality of the crystallization was evaluated using the measured surface resistance of an  $8 \times 4 \text{ mm}^2$  rectangular area and a 4-point probe system.

Table 15. Recorded surface resistance for different focal distance points at 6 kHz.

| Focal distance | 10 pulses                       | 50 pulses              | 100 pulses             |
|----------------|---------------------------------|------------------------|------------------------|
| 7.0 mm         | 25.6 $\text{M}\Omega_{\square}$ | 200 $\Omega_{\square}$ | 150 $\Omega_{\square}$ |
| 6.5 mm         | 13.5 $\text{M}\Omega_{\square}$ | 124 $\Omega_{\square}$ | 87 $\Omega_{\square}$  |
| 6.0 mm         | 13.1 $\text{M}\Omega_{\square}$ | 78 $\Omega_{\square}$  | 57 $\Omega_{\square}$  |
| 5.5 mm         | 10.8 $\text{M}\Omega_{\square}$ | 87 $\Omega_{\square}$  | 44 $\Omega_{\square}$  |
| 5.0 mm         | 10.1 $\text{M}\Omega_{\square}$ | 100 $\Omega_{\square}$ | 11 $\Omega_{\square}$  |

As the focal distance is decreases, the spot size also decreases thus the energy density of the pulse is increased. From the results presented in Table 15, we notice that for very low energy densities, 10 pulses are not enough to crystallize the film. However, as the number of pulses increases, the surface resistance decreases which implies a thicker crystallized zone, evidenced by the decrease in surface resistance. For focal distances smaller than 5.0 mm, the layer surface is presenting visible damages. Thus, the minimum recorded surface resistance is 11  $\Omega_{\square}$  obtained in conditions which are preserving the destruction of the layer surface during laser irradiation. These optimized parameters (irradiation frequency of 6kHz, focal distance of

5 mm, writing speed 300 mm/s and attenuation of 99%) will be used for the rest of the experiments presented in this manuscript.

## II.6. Conclusions

This chapter focuses on three main parts:

- the electromagnetic characterization of thin-film phase change materials for millimeter-wave band applications,
- the optical characterization of GeTe, and
- the optical activation of states changes of GeTe thin films using a green-colored laser (wavelength of 532 nm).

A brief and general introduction to microfabrication technologies and the parameters used for fabrication of the GeTe thin layers and of the devices, which will be developed in the next chapter, was presented before describing the approaches we employed for the electrical and electromagnetic characterization of phase change materials. The mechanism of phase change in different PCM compositions was presented and illustrated by the evolution of their surface resistance with respect to the temperature. It was shown that the phase change characteristics are independent of the thickness of the layer. The capability of the materials to retain a specific insulating or conducting state in the absence of an applied stimulus (bi-stable or non-volatile behavior) allows the exploitation of these materials for reconfigurable circuits with low energy consumption, high speed and overall promising RF performances.

For the three investigated compositions (GeTe, GST, Sb<sub>2</sub>Te) it was shown that the composition Sb<sub>2</sub>Te presents the lowest crystallization temperature (at around 130°C) while the GeTe and GST possess a crystallization temperature of around 180 °C. However, the GeTe composition presents the highest ratio of electrical conductivity change between the two states (greater than 6 orders of magnitude), with conductivity values in the metallic state which are adapted for RF devices integration. Additionally, accelerated thermal stress tests were performed on GeTe and Sb<sub>2</sub>Te compositions shows that the GeTe presents a stability greater than 10 years for operating temperatures below 160°C, which makes it more suitable for memories and spatial applications.

We focused our efforts on the dielectric characterization of PCM thin-films in the amorphous state, e.g. the extraction of their permittivity and loss tangent in the millimeter-wave band frequency. The knowledge of these properties is important to evaluate their RF performances (particularly, the losses) during 3D-electromagnetic simulations of RF devices designs integrating these materials. The biggest challenge is the fact that, PCM thin-films have normally thicknesses of less than 1 μm, which makes them very difficult to characterize using traditional methods. We developed a methodology for characterizing very thin films of PCMs (under 1 μm) using planar devices integrating them and a differential approach to minimize the impact of additional unknown parameters of the circuits. This approach was used to characterize thin-films of GeTe and GST at frequencies around 30 GHz, allowing us to extract permittivity values of 21 and 32, respectively, and loss tangents of  $3.4 \times 10^{-2}$  and  $3.2 \times 10^{-1}$ , respectively. These values and the associated characterization methodology are, to the best of our knowledge, the very first-ever reported electromagnetic properties of PCM materials at millimeter-wave frequencies.

Finally, we investigated the reversible phase change activation of GeTe thin layers using a laser irradiation system integrating a laser operating at 532 nm wavelength and an optical scanner. Following multi-physics simulations of laser beam interaction with the material, we showed the capability of the system to locally crystallize areas of GeTe and the capacity of reversible writing arbitrary crystalline GeTe patterns in the amorphous layer (optical write-erase capacity of the GeTe thin-film). However, the irradiation system and the writing mechanism are still subject to optimization for reliable, multicycle reversible changes between the two states. Thus, the use of diffractive optical elements for transforming the spatial profile of the incident laser beam to a flat-top profile will allow increasing the writing uniformity while the use of protective capping layers on the PCM material will avoid their oxidation and subsequent decrease of their electrical performances. Nevertheless, the presented approach implying a large area modification of PCM thin layers and inscription of arbitrary patterns with dissimilar conductivities represents a completely innovative concept in the field of millimeter-wave devices. It will enable to extend the methodology to the design of complex antenna systems and metasurfaces whose optical control will be a promising solution for millimeter-wave and space-based wireless communications (programmable antennas or beam-forming circuits).

In the next chapter, we will employ the PCM's measured electromagnetic characteristics to design a multi-reconfigurable antenna using a GeTe sample. The antenna will be optically activated using the irradiation banc that was implemented as well as the irradiation parameters that were characterized and optimized in this section.

# Chapter III. Design, optimization, and fabrication of a multi-reconfigurable array of antennas integrating phase change materials.

---

*Anything that can go wrong will go wrong, and at the worst possible time»*

*Arthur Bloch: Murphy's Law, and Other Reasons Why Things Go WRONG*

### III.1. Introduction

In I.5.5, it is shown that a single patch antenna can be used to create right-hand circular polarization (RHCP), left-handed circular polarization (LHCP) and linear polarization by replacing the corner edges of the patch antenna with a GeTe-based phase change composition. However, a single patch antenna may present some drawbacks such as low directivity and very narrow bandwidth. Therefore, it is of interest to integrate this antenna into an array in order to achieve better performances. The use of the array with a double ROGERS substrate proves to be very satisfactory as the axial ratio bandwidth was enhanced successfully as shown at a previous work at XLIM laboratory. However, the main drawback with this array of antennas is that the used substrate is not adapted for the use of PCMs due to its high rugosity and very low thermal conductivity which is a detrimental for the amorphization of the PCM and therefore a change of substrate needs to be considered.

Thus, the main objective of this chapter is to upgrade the previously presented array with substrates that are more suitable for reversible transformation of PCMs, while enhancing the aperture of the axial ratio and adding the capacity of reconfiguration in frequency. The desired performances of the antenna are summarized in Table 16.

Table 16. Desired performance of the antenna array integrating a PCM.

| Parameter                 | Value   | Comments   |
|---------------------------|---|--|
| Operating frequency       | Around 30 GHz   | For all configurations                                       |
| $ S_{11} $ level          | <-10 dB   | For all configurations                                       |
| Boresight directivity     | > 10 dB   | For all configurations                                       |
| Boresight axial ratio     | < 3dB   | For both RHCP and LHCP                                       |
| Axial ratio angular range | $-50^\circ < \theta < 50^\circ$<br>(for all $\varphi$ planes) | For both RHCP and LHCP.<br>Must be as symmetric as possible. |

### III.2. Geometry of the antenna

The full geometry of the proposed multi-reconfigurable antenna is shown in Figure 98. The antenna consists of two main layers: the superstrate in the upper part with height  $h_2$ , the substrate at the bottom part with height  $h_1$ . A thin glue layer is needed to bond the superstrate and the substrate together. This layer has height  $h_g$  to bond the two layers (Figure 98a). All the layers have dimensions of  $X_g \times Y_g$ . Achieving a directivity of 10 dBi with a single patch antenna is impossible therefore, at the top of the superstrate, four patch antennas of size  $X_a \times Y_a$  form an array of antennas separated by a center-to-center distance of  $D_x$  in the x direction and  $D_y$  in the y direction as shown in Figure 98b. Each antenna has their edges trimmed-off and replaced with a PCM composition such that, depending of the state of the trimmed edges (crystalline/conductive or amorphous/insulator), the patch antenna will present a different state of polarization. Normally, each antenna requires a proper feedline which can be done by incorporating microstrip lines in the superstrate. However, the radiation characteristics can be hugely impacted by unwanted radiation due the microstrip-antenna transition. Additionally, the feeding lines of each antenna need to be joint together in order to excite the antenna with only one source thus complicating the design. To avoid these problems, the array is electromagnetically coupled to another patch antenna between the substrate and superstrate (and bellow the glue layer) of size  $X_e \times Y_e$  as shown in Figure 98c. This antenna is excited by a slot window of length  $L_w$  and width  $W_w$ . embedded in the ground plane at the bottom of the substrate (Figure 98d). This strategy is justified by the fact that the slot is filled with a PCM composition meaning that the effective length of the window can be changed by choosing

which part is crystalline (conductive) and which stays amorphous (isolator) thus changing the resonance frequency of the antenna.

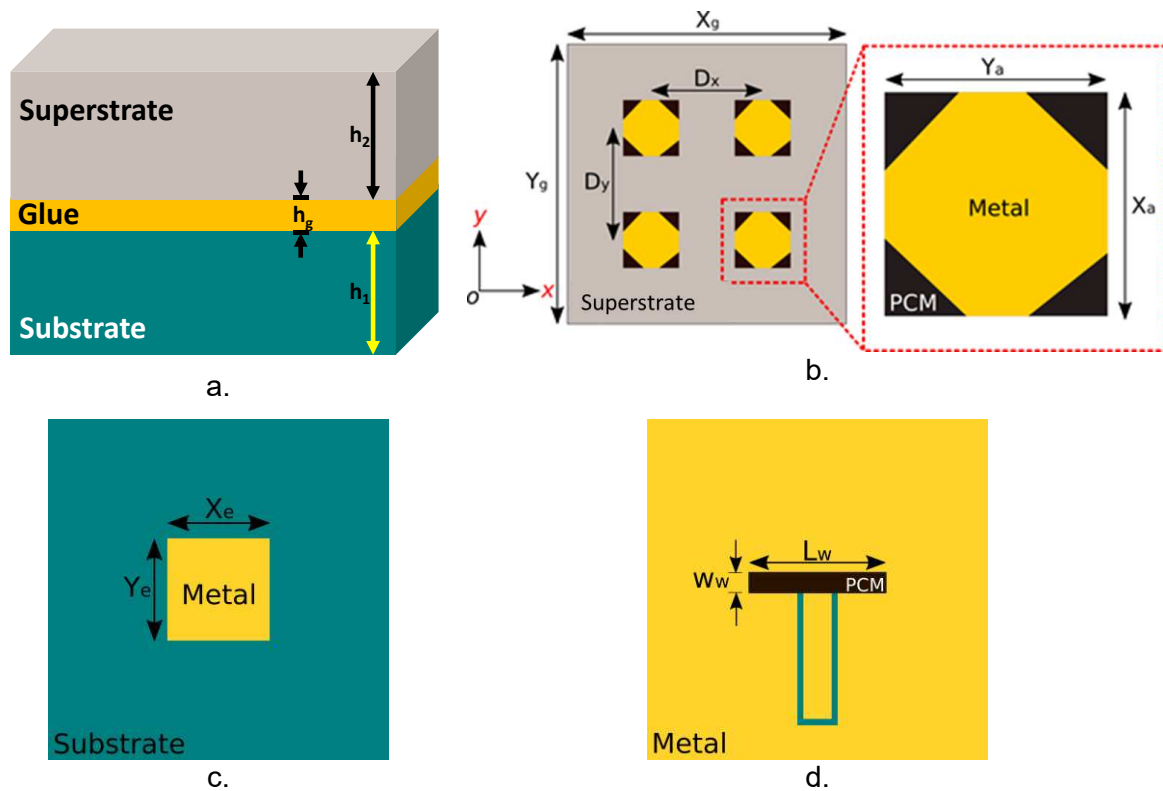


Figure 98. Proposed geometry of the multi-reconfigurable array of antennas. a) Layered structure of the antenna. b) Array of antennas integrating a PCM composition at the top of the superstrate. c) Excitation patch between the two layers. d) Ground plane and PCM filled coupling slot at the bottom of the substrate.

### III.2.1. Material choice

As explained previously, the superstrate of the array of antennas must be a high thermal conductive substrate to favor amorphization. Normally the same conclusion should apply to the substrate, nevertheless the existence of a metallic ground plane surrounding the PCM in the slot window should also help to evacuate heat very rapidly. In our case, the ground plane (and all other metallic patterns) will be made of a thin layer of titanium and gold, the latter presenting a thermal conductivity value higher than 300 W/m.K [128]. In order to choose a suitable material, Table 17 summarizes the relevant properties of some candidate materials for antenna applications integrating PCMs. Ideally, we would like a substrate with low permittivity, low roughness profile, and very high thermal conductivity. In addition, the use of low-dense materials with low specific heat capacity values will also help the heat dissipate faster in the substrate due to a higher thermal diffusivity constant.

Normally, as explained in Appendix 1, antenna designers favor the use of thick substrates with low permittivity values since these characteristics provide better efficiency and larger bandwidths. However, the main drawback of substrate like ROGERS 4003C is its low thermal conductivity and its very rough surface which is a detriment in the mm-wave frequency band. The Figure 99a show the profile of the surface of a ROGERS 4003 substrate as measured by a Dektak XT profilometer from which it can be observed a very rough surface with peaks and valleys in the order of the micrometers. Since the profile of the surface is, essentially, random in nature the quantification of the surface roughness is done via statistical metrics like the root

mean square value (sometimes abbreviated as RMS or  $R_q$ ) which is given by the standard deviation of the height of the profile. The Figure 99b shows the histogram of the profile to which a gauss bell curve can be fitted. From this latter, we can deduce an RMS value of 834 nm which is significantly high value (even higher than the deposited GeTe layer).

Table 17. Relevant electrical and thermal properties of different candidate substrates for an antenna integrating PCM.

| Property                             | Typical values                      |                        |  |                                    |
|--------------------------------------|-------------------------------------|------------------------|--|------------------------------------|
|                                      | Rogers 4003C                        | Alumina                | Sapphire   | Quartz                             |
| Dielectric constant ( $\epsilon_r$ ) | 3.55                                | 9.4*                   | $\epsilon_{r\perp} = 9.4$<br>$\epsilon_{r\parallel} = 11.5$                              | 3.8*                               |
| Loss tangent (Tan $\delta$ )         | $2.7 \times 10^{-3}$<br>(at 10 GHz) | $6 \times 10^{-4}$ *   | Tan $\delta_{\perp} = 8.6 \times 10^{-8}$<br>Tan $\delta_{\parallel} = 3 \times 10^{-8}$ | $< 1 \times 10^{-4}$<br>(at 1 MHz) |
| Thermal conductivity (k)             | 0.71 W/m.K                          | 27 W/m.K               | $k_{\perp} = 23.1$ W/m.K<br>$k_{\parallel} = 25.2$ W/m.K                                 | 1.4 W/m.K                          |
| Density ( $\rho$ )                   | 1790 kg/m <sup>3</sup>              | 3800 kg/m <sup>3</sup> | 3980 kg/m <sup>3</sup>   | 2200 kg/m <sup>3</sup>             |
| Specific heat                        | N.A                                 | N.A                    | 761 J/kg.K   | 670 J/kg.K                         |
| Glass temperature ( $T_g$ )          | >280 °C                             | ----                   | ----   | ----                               |

N.A: Not available in the datasheet

\*Measured at XLIM laboratories

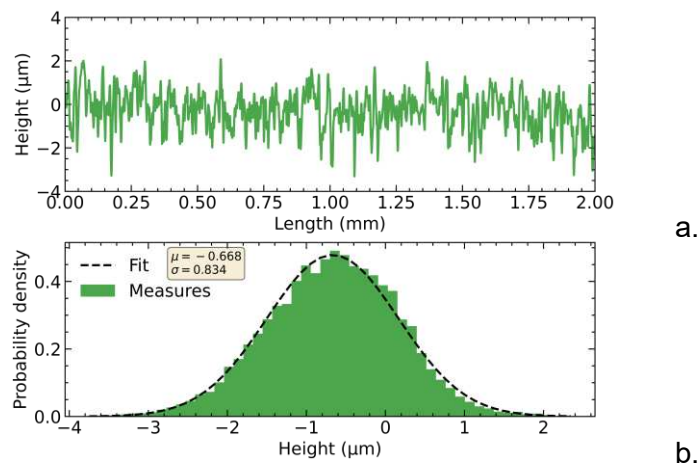


Figure 99. a) Measured profile of the surface of a ROGERS 4003C substrate. b) Histogram and fitted gauss bell curve.

Sapphire is the most common option as a substrate for PCM deposition presenting a very high thermal conductivity as well as an ultra-low loss tangent together with a very low roughness profile. Unfortunately, it also presents a high degree of anisotropy and a very high permittivity which will add a lot of complexity to the design of an array of antennas. Another option may be the use of a quartz substrate which presents a low permittivity value, low loss tangent, and low rugosity (around 4 nm) as shown in Figure 100a. However, the thermal conductivity, although double the Rogers 4003C, is still very small compared to the sapphire substrate. Additionally, this substrate is very fragile and should be managed with precaution. Finally, an alumina substrate presents also a very high thermal conductivity and low loss tangent value. Its permittivity value, although still high, is isotropic and the roughness of the substrate is much lower than the Rogers 4003C with a measured value of around 34 nm as shown in Figure 100b (but slightly higher than sapphire or quartz substrates).

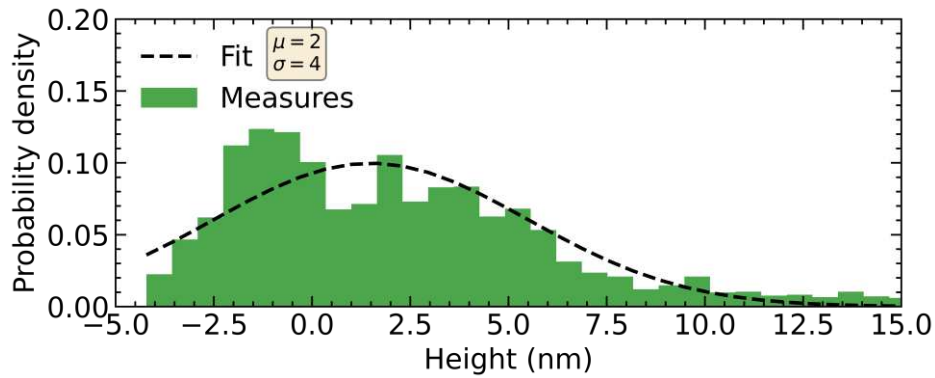


Figure 100. Measured histogram and fitted curve of the surface profile of a quartz substrate.

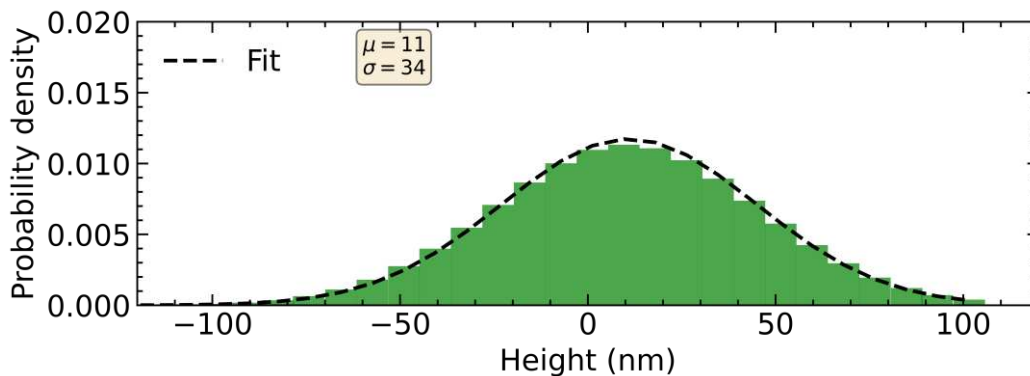


Figure 101. Measured histogram and fitted Gaussian bell curve of the surface profile of an alumina substrate.

Considering all these arguments, a sensible choice to replace Rogers 4003C in the superstrate for antenna applications integration PCM is the alumina substrate due to its isotropic nature and very high thermal conductivity.

In the case of the substrate, two cases need to be considered: when both the superstrate and the substrate have a high permittivity value (alumina) and when the superstrate has high permittivity and the substrate has low permittivity value. Arguments against and in favor of the two cases can be done. To choose a suitable configuration, many parameters need to be discussed. For example, the dimensions of an antenna in an alumina substrate are much smaller than the ones in Rogers 4003C (due to its high permittivity). However, this high permittivity will also favor the existence of surface waves modes in the boundary of substrate and the air [129] [130]. Indeed, the interaction (or coupling) between elements in the array can be mostly attributed to the existence of surface waves [24] [131] [132] and a lot of work is still being done to eliminate or mitigate this coupling [133] [134] [135]. The first surface wave mode (fundamental mode) is a TM wave with a cut-off frequency of 0 Hz. This mode is then followed by alternating TE and TM modes whose cut-off frequencies are inversely proportional to the thickness of the layer and its permittivity. The thicker the substrate, the lower the cut-off frequencies of higher order modes [129] [136]. Similarly, the higher the permittivity, the lower the cut-off frequency. It is clear then that replacing a low permittivity superstrate with a high permittivity superstrate (while keeping the same thickness) increases the probability of exciting higher order surface wave modes which will be detrimental for the radiation of the antenna. For the case where both the superstrate and substrate are made of alumina, the whole structure can be considered made of an even thicker substrate which will only result in the excitation of

even higher order modes, degrading even more the performances of the array. In addition, the glue layer acts as another dielectric slab whose influence needs to be considered.

Although, this detriment caused by the increase in permittivity may be counterbalanced by using thinner substrates, the original structure uses layers with thickness of 305  $\mu\text{m}$ . This means that the structures created with alumina substrate will need even thinner layers (less than 200  $\mu\text{m}$ ) which will result in very fragile substrates who can be very difficult to manipulate during fabrication and prone to breaking. Considering the added difficulty in fabrication and the fact that the metal in the ground plane can also help evacuate the heat very rapidly, we will proceed by using a high dielectric superstrate together with a low permittivity substrate.

As stated previously, the quartz substrate is a very fragile material that has to be managed with a lot of precaution under the risk of breaking. Thus, we will proceed with a ROGERS 4003C as substrate. Although very rough, the metallic ground plane deposited under the substrate can help reduce the roughness. Nevertheless, if needed, the Rogers 4003C can be substituted for a quartz substrate. This is because both materials present very similar permittivity values while been isotropic which means that the use of a quartz substrate will not perturbate very substantially the performances of the device designed for a Rogers 4003C substrate.

### III.2.2. Performances of an array of antennas over a high permittivity superstrate and low permittivity substrate

The first difficulty lies in the fact that the antennas in the array and the exciter antenna are situated in different mediums which means that they see different effective permittivity values, thus different dimensions for the same resonant frequency. For this case, the array of antennas is situated at the top of a multilayer substrate (Alumina + Rogers 4003C) while the exciter patch is in between the alumina and the Rogers 4003. The glue layer is not considered and will be ignored since it will only add more difficulty to this study. The goal is to ensure that all antennas are excited in the fundamental TM<sub>01</sub> mode. For the design of the dimensions of the antennas we can follow the procedure outline in [24] where the resonance frequency is calculated by using equation ( 75 ):

$$f_r = \frac{c_0}{2(L + 2 \cdot \Delta L) \sqrt{\epsilon_{eff}}} \quad (75)$$

where  $c_0$  is the speed of light,  $\epsilon_{eff}$  is the effective permittivity of the medium and  $\Delta L$  is the contribution of the fringing fields at the edge of the patches given by equation ( 76 ):

$$\Delta L = 0.412 \cdot h \cdot \frac{(\epsilon_{eff} + 0.3) \left( \frac{w}{h} + 0.264 \right)}{(\epsilon_{eff} - 0.258) \left( \frac{w}{h} + 0.8 \right)} \quad (76)$$

where  $h$  is the height of the substrate and  $w$  is the width of the antenna.

The effective permittivity value depends if we are considering the array patches or the exciter patch and can be evaluated either by numerical simulation or by following the procedure outlined in [137]. The dimensions of the array of antennas are resumed in Table 18.

The TM<sub>01</sub> mode of a patch antenna is characterized for only having one component of magnetic field in the surface. The Figure 102 shows the magnetic field of the exciter patch antenna from which it can be seen that the x-component of the magnetic field is predominant

implying that the excited mode is the TM01. The small perturbation at the lower end is caused by the discrete port existence.

Table 18. Parameters of the antennas in the array and the thickness of substrate.

| Parameter                  | Value    |
|----------------------------|----------|
| $X_{array}, Y_{array}$     | 1.25 mm  |
| $X_{exciter}, Y_{exciter}$ | 1.73 mm  |
| $X_{gnd}, Y_{gnd}$         | 10 mm    |
| $h_1, h_2$                 | 0.305 mm |

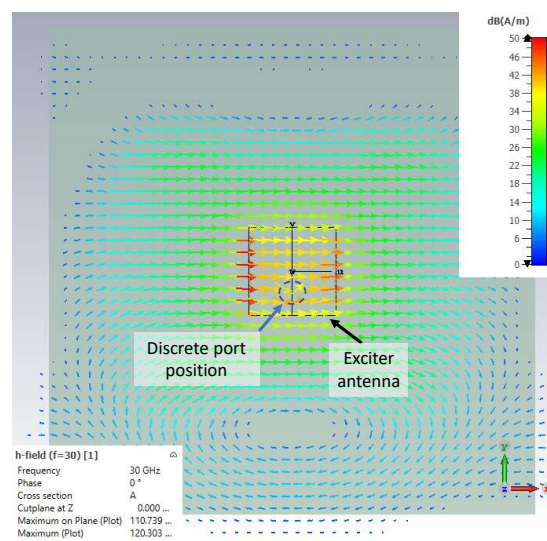


Figure 102. Simulated magnetic field distribution on the exciter patch of the double stacked array of antennas.

The correct excitation of only the TM01 mode is very important since the strategy used to generate circular polarization requires the existence and a small perturbation of the fundamental mode [138]. It was previously established that, for the case when both superstrate and substrate are made of Rogers 4003C, an optimal distance between the antenna array exists such that the antennas are excited in their fundamental mode TM01. This distance is around  $\lambda_0/2.25$  where  $\lambda_0$  is the free-space wavelength. This may be no longer the case when using an alumina substrate due to its different permittivity value which means that the same study must be done for this new superstrate. This can be confirmed by observing the current density at the parasitic patches in the surface. For the desired TM01 mode, only the component  $J_y$  of the current density should be excited. From Figure 103a we can observe a current distribution who resembles the one of a TM01 mode, unfortunately, the currents in the array are not in phase as there is a slight dissymmetry between the antennas at the top of the figure and the bottom. Additionally, as shown in Figure 103b a strong non-zero  $J_x$  component exists in the array which implies that other modes in the antenna had been excited as well.

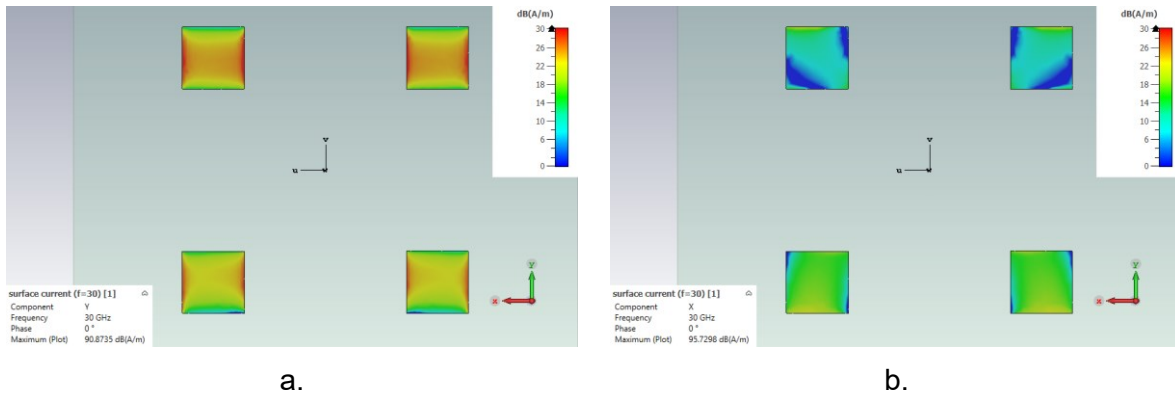


Figure 103. Surface current densities on the array antennas using an alumina superstrate for a separation of  $\lambda/2.5$ . a) Magnitude of  $J_y$ . b) Magnitude of  $J_x$ .

As the distance between the antennas is increased, the  $J_y$  component are more out of phase while the  $J_x$  component seems to increase as shown in Figure 104.

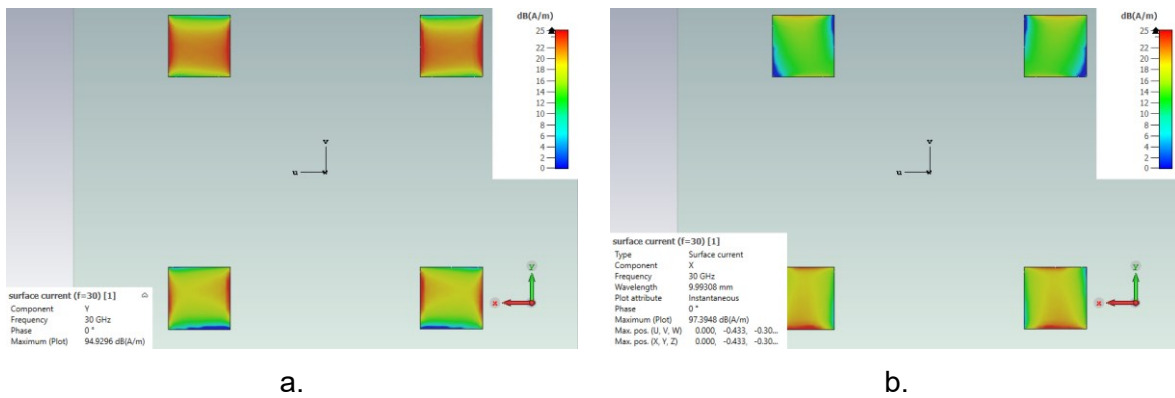


Figure 104. Surface current densities on the array antennas using an alumina superstrate for a separation of  $\lambda/2$ . a) Magnitude of  $J_y$ . b) Magnitude of  $J_x$ .

Contrary, if the distance between the patches is decreased, the  $J_y$  components seems closer to be in phase but the component  $J_x$  is still present, as shown in Figure 105. However, as the antennas becomes closer, the interaction between them can become stronger (particularly in the E-plane).

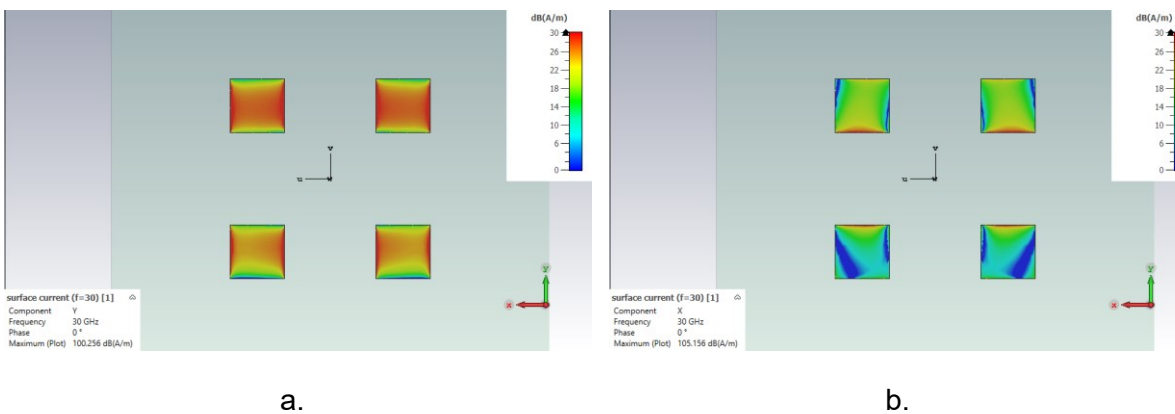


Figure 105. Surface current densities on the array antennas using an alumina superstrate for a separation of  $\lambda/3$ . a) Magnitude of  $J_y$ . b) Magnitude of  $J_x$ .

From the three previous simulations, we can observe a tendency that the  $J_y$  component seems to be stronger and closer to be in phase when the antennas are closer in the array. However, the existence of a non-zero  $J_x$  component in all cases is only detrimental to the performance of the antenna array. In order to improve the performance of the array many parameters can be optimized. For example, the separation of the array in the x and y directions can be changed independently in order to improve the correct excitation of the TM01 mode in the y direction while ensuring that the antennas do not interact strongly between them in the E or H planes. Another parameter that can be optimized are the size of the antennas themselves, by changing the size of the antennas in the x and y directions, the excitation of different modes can be pushed to higher frequencies so that they do not degrade the radiation performances at the desired 30 GHz frequency. Additionally, the use of rectangular patches instead of squares ones can improve the quality of the circular polarization [138].

More importantly, as seen in the literature, in order to correctly generate circular polarization of good quality, the trimmed patches need to be excited at a particular position within the array [136] [24]. There exist methodologies to choose the size of the trimmed edges as well as the excitation point of the antenna as a function of the desired parameters of the antenna (like substrate thickness, quality factor and radiation efficiency). However, these constraints assume that the antenna is to be fed by either a coaxial probe or a transmission line and that the trimmed edges have all the same dimensions. These methodologies may no longer be valid for an antenna that is excited by proximity and where the electric field may not be uniform in the antenna or when there exist surface waves in the substrate due to its high permittivity value. In order to increase the probability of finding a configuration that can satisfy the requirements imposed in Table 16 we can add additional degrees of liberty by allowing different sizes of the trimmed edges. It is also worth remarking that the trimmed edges also have an influence in the resonant frequency of the array patch but taking into consideration the fact that edges are not symmetrically cut, an analytical formulation to predict the influence on the resonance frequency cannot be properly stated.

The final geometry of the array of antennas is the one showed by the Figure 106. Each antenna array is placed on an alumina superstrate with dimensions of 10 mm×10 mm and a thickness of 0.305 mm and a Rogers 4003C substrate also with a thickness of 0.305 mm. The four patch antennas of dimensions  $X_a \times Y_a$  form the array of antennas separated by a center-to-center distance of  $D_x$  in the x direction and  $D_y$  in the y direction. The edges of each patch antenna have been unsymmetrized to counter the non-uniform field on the patch and enhance the quality of the circular polarization. For the RHCP antenna, the size of the trimmed edges is  $S_{R1x} \times S_{R1y}$  and  $S_{R2x} \times S_{R2y}$  for the bottom and upper edges, respectively for all antennas. For the LHCP antenna, the size of the trimmed edges is  $S_{L1x} \times S_{L1y}$  and  $S_{L2x} \times S_{L2y}$  for the bottom and upper edges, respectively and for all antennas in the array.

In order to comply with the performances stated in Table 16, each configuration (LP, RHCP and LHCP) must be also compliant with all the required parameters meaning that all the configurations must be designed in parallel. However, as stated in the previously, all antennas should be designed such that they possess the same dimensions, i.e distance between individual patches and similar core dimensions for each patch while disregarding the trimmed edges. All of these while ensuring that all states are matched in  $S_{11}$  and all pointing in boresight.

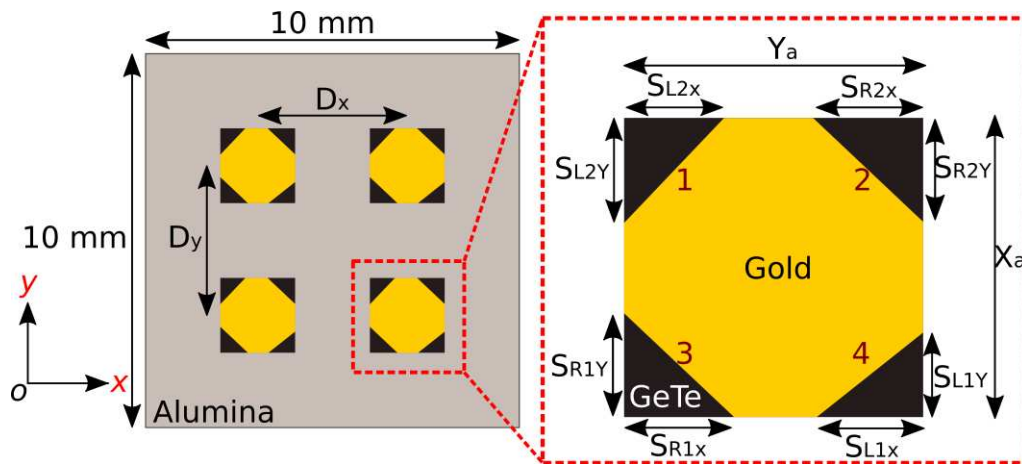


Figure 106. Array of antenna integrating GeTe with asymmetric trimmed edges.

Problems like the one stated previously are very difficult to solve due to the high number of free variables and the now unsymmetrized edges of the antenna patches. There exist analytical formulations to properly choose the dimensions of patch antennas and separation between its elements, given a resonant frequency [138]. The reality is that these formulations do not take into consideration the coupling between the array elements, which, as stated previously, can become really detrimental for the radiation of the antenna.

In summary, since we do not dispose of any analytical formulation, the optimization of this antenna array needs to be carried out via 3D electromagnetic simulation. For this reason, the design must be done via optimization algorithms based on numerical models.

### III.3. Numerical optimization of the antenna array

There exist many different mathematical strategies used for optimization. Each strategy presents its own advantages and disadvantages that need to be considered in order to ensure the success of the optimization. In the next subsections we will present an introduction and survey to some common optimization strategies as well as some difficulties, considerations and trade-offs to be made in order to choose the most appropriate one.

#### III.3.1. Overview optimization algorithms

Optimization is the process of finding and selecting the best possible solution (or set of parameters), with respect to one or multiple criteria's, to a particular problem from a set of possible solutions. For engineering and scientific optimization, most of the time not all the solutions are possible as the parameters must comply with some restrictions imposed by the nature of the problem or the feasibility of the fabrication. For example, for the array of antennas shown in Figure 106 all dimensions must be positive real numbers and the separation between the array elements must be greater than the size of the individual patches (or else they will overlap).

In general, optimization problems consist of minimizing or maximizing a particular function  $f(x)$  by finding suitable  $x$  values where  $x$  is a vector containing  $n$  values:  $x = (x_1, x_2, \dots, x_n)$  and subject to constraints involving these variables. In the context of engineering, the objective function represents a parameter or metric that needs to be optimized. For example, in the context of antennas, we may want to maximize the gain in a particular direction, or minimize the reflection coefficient at a particular frequency or find the minimum number of radiating elements needed

for a particular gain value, etc. In some cases, even an arbitrary combination of multiple metrics needs to be optimized.

In mathematical terms, the optimization problem can be stated as

$$\begin{aligned} & \min_x f(\vec{x}) \\ & \text{subject to } \begin{cases} x \in X \\ g(\vec{x}) \geq 0 \end{cases} \end{aligned} \quad (77)$$

where  $g(x)$  is a constraint involving the free variables that the solution must satisfy and  $X$  is the space search. Of course, there can be multiple objective functions  $f(x)$  values with multiple constraints  $g(x)$ . In general, a maximization problem can be transformed into a minimizing problem by a proper transformation of the objective function.

There exist many strategies for optimization in the literature. Some popular examples are the gradient-based approaches, direct searching methods, stochastic methods and population methods. The choice of a particular algorithms depends on the problem at hand. One needs to take into consideration many parameters in order to choose an ideal optimization strategy, for example the number of free variables, the constraints and type of constraints imposed to the variables, the nature of the objective function, ease of implementation, etc. In particular, the nature of the objective function is arguably the most important aspect in the choice of an optimization strategy. Is important to know if the objective function is linear or non-linear, continuous or discontinuous, discrete, differentiable, monotone, difficult to calculate, etc.

### III.3.1.1. Gradient-based methods

This kind of algorithms focus on finding the minimum of an objective function by evaluating its gradient and it is the most straightforward path to take when the function to be optimized is known. They are mostly used for machine learning applications as they are able to find an optimal solution for problems involving thousands of free parameters [139] [140]. Logically, the use of the gradient implies that the objective function must be differentiable and continuous within the searching space.

When an analytical formulation is known for the objective function, an optimal point can be found by solving the equation ( 78 )

$$\nabla f(\vec{x}) = 0 \quad (78)$$

The nature of the solution (i.e a maximum, a minimum or a saddle point) can be deduced from the second-order gradient. For the case of single variable functions, the equation ( 78 ) becomes finding the first-order derivative then an optimal point by solving for when the derivative is equal to zero. However, most often than not, we do not dispose of an analytical formulation for the objective function thus we are not capable of solving ( 78 ) analytically. For that reason, most optimization algorithms use numerical methods based on the gradient descent method (GD).

GD methods are a family of gradient based strategies which relies on information given by the gradient of a function in order to iteratively converge to an optimal solution. For this case, we assume that we are interested only in finding the minimum of an objective function. The basic idea is shown in Figure 107. First, we start at any point  $x$  (represented by the red star), then we move to a new position such that the objective function at a new point  $x$  represents an improvement over the previous point  $x$ . Then we iteratively follow this procedure until an

improvement of the function cannot be made, in which case we assume that we have reached a minimum (represented by the blue star).

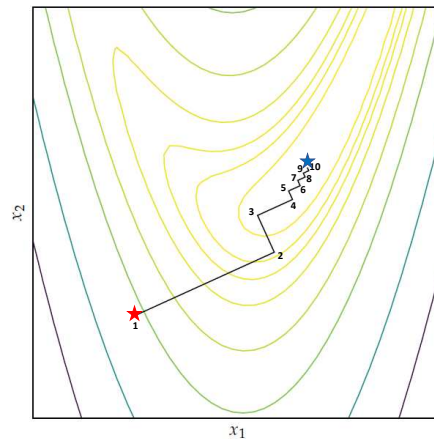


Figure 107. Example of gradient descent method to find the minimum value on the Rosenbrock function. Each number represents an iteration. Adapted from [141].

In mathematical form, this procedure is described by equation ( 79 ) :

$$x^{(k+1)} = x^{(k)} + \alpha \cdot d^{(k)} \quad ( 79 )$$

where  $x^{(k)}$  is the current point at the  $k$ -th iteration,  $x^{(k+1)}$  is the new point,  $\alpha$  is the step size and  $d^{(k)}$  is the direction of the step. At each iteration, the direction choose is the one with steepest descent i.e. the direction in which the value function decreases the fastest which is calculated by equation ( 80 ).

$$d^{(k)} = - \frac{\nabla f(x^k)}{\|\nabla f(x^k)\|} \quad ( 80 )$$

Although, this method creates a powerful methodology to find optimal solutions, there are several difficulties and inconveniences that need to be addressed or discussed before its implementation. First of all, we need access to the gradient of the function which can be difficult to obtain if we do not dispose of an analytical formulation for the problem. We can approximate the gradient of a function by using multiple data points by means of numerical differentiation although this may produce inaccurate gradients unless a huge amount of data points are used [19] [140]. Another problem is when the current  $x$  value falls into saddle points (also called the “vanishing gradient” problem) which are points where the gradient of a function is zero without been neither a maximum nor a minimum. In such cases, the algorithm cannot make any further progress [142] [21]. In addition, the size of the step  $\alpha$  also plays a role in the performance of the algorithm, a big step size can make the algorithm converge more rapidly but at the risk of skipping solutions that are very narrow within the search space. On the other hand, a small step size can increase the duration of the optimization process.

Arguably, the most important problem with these kinds of algorithms (and many other types of optimization strategies) is that they can easily fall into local-minima points. As an example, Figure 108 shows the performance of a gradient descent method for multiple starting points (represented by the hollow blue stars) over a known topology. The objective function to be optimized presents five extreme points: four local minimums at points  $(0,0)$ ,  $(0,6)$ ,  $(6,0)$  and  $(6,6)$ , a global maximum at point  $(2,2)$  and a global minimum at point  $(6,6)$ . Ideally, we want to

find the global minimum, however as shown in Figure 106, the end point strongly depends on the initial position as the end point tend to finish at the closest minimum. In real-world applications we do not know a priori where the local minimums nor global minimum are located thus optimization algorithms using gradient descend methods have to be run multiple times from multiple starting points to assure finding a global minimum.

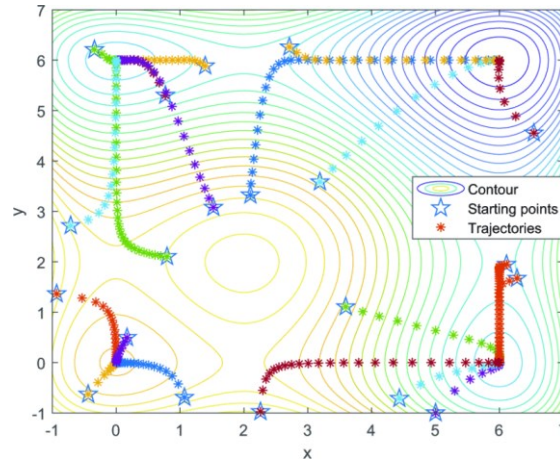


Figure 108. Performance of a gradient descent method for multiple starting points. Adapted from [143].

### III.3.1.2. Direct search method

Although many improvements can be made to GD methods in order to tackle its weakness, sometimes the increase on the computation complexity can made them not worthy to implement them. Specially if the objective function is very difficult to calculate. For this reason, optimization methods that do not rely on derivatives are of interest. These alternative methods are called zero-order methods, direct search methods or pattern search methods. These strategies rely only on the current value of the objective function in order to explore the solution space while searching for the global minimum value.

Although there are different strategies, most zero-order methods follow the same principle in which several points close to any given starting position need to be evaluated in order to choose the new point. One of the most popular examples is the one proposed by Hookes and Jeeves [144] [23]. The working principle is shown in Figure 109 where the global minimum of two variable functions is been searching for. First, a starting point is chosen, then a set of neighbor points equally distributed along each direction are evaluated as shown in Figure 109a. From these neighbor points, the best solution is chosen and the corresponding point becomes the new starting position, then the process is repeated (Figure 109b). If neither of the new neighbor points offers an improvement over the current starting point, the step size is reduced then the new neighbor points are evaluated as shown in both Figure 109c and Figure 109d. This process is repeated iteratively until the function decreases below a certain level, or a sufficiently small step is achieved or until no further improvement is made on the objective function.

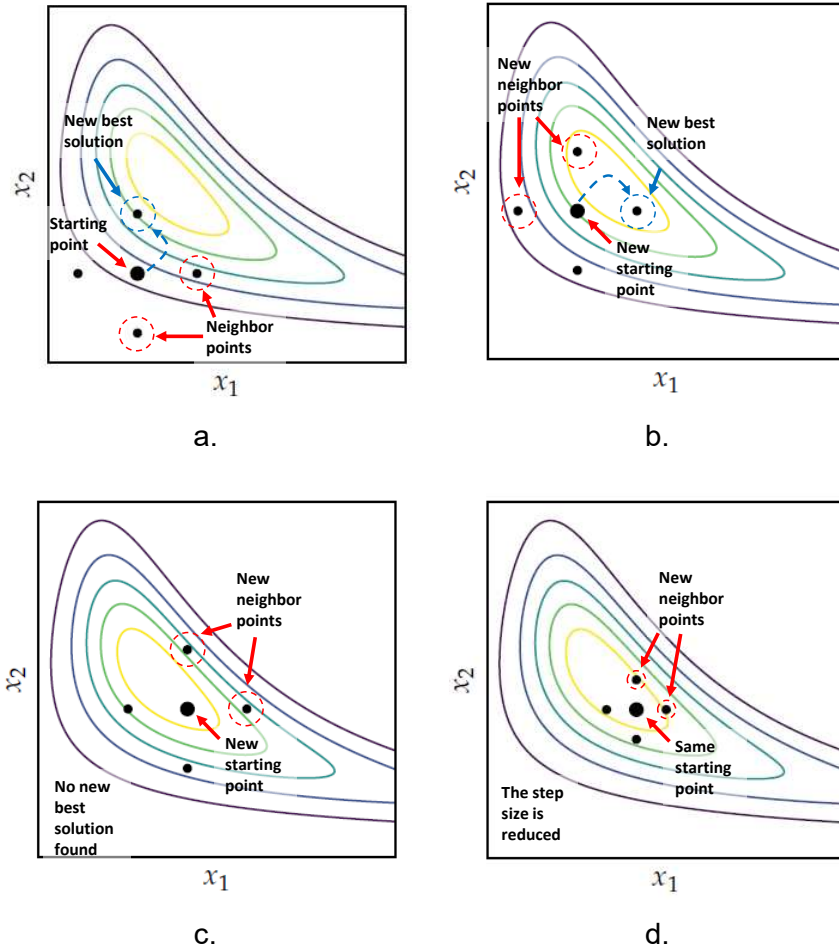


Figure 109. Working principle of the Hookes-Jeeves method (adapted from [141]). a) Starting point and equally distributed neighbor points. b) New starting point with new neighbor points. c) New starting point with no best candidate solution. d) Same starting point as the previous one with a new step size.

In mathematical form, the Hookes-Jeeves method can be stated by iteratively solving and comparing the current value of the objective function  $f(x^{(k)})$  to the values found by calculating

$$f(x^{(k)} \pm \alpha e^{(i)}) \quad (81)$$

where  $\alpha$  is the step size and  $e^{(i)}$  is the unit vector in the  $i$ -th direction. Then the new  $x$  value is given by equation (82) :

$$x^{(k+1)} = x^{(k)} + \alpha e^{(i^*)} \quad (82)$$

where  $e^{(i^*)}$  is the direction in which the value of the function decreases the most.

Others zero-order methods follows a similar procedure to the Hookes-Jeeves methods. For example, Powell's method [145] follows the same operation principle but it can search in directions that are not necessarily orthogonal to each other. It can also adjust for the step size in order to avoid narrow or long valleys which otherwise will need an important number of evaluations using the Hookes-Jeeves methodology. In general, the generalized pattern search conducts the same searching principle but it can perform the search in any arbitrary direction with any arbitrary step size. Unfortunately, the convergence to a local minimum of these algorithms is not assured unless certain conditions are met [146].

Although these methods have proven to be strong alternatives to GD optimization, they also present their own weakness and problematics that need to be addressed. First, it has the same problematic as GD methods in which is also prone to fall into local minimum points as well as that the finish position depends strongly on the initial position. Another aspect to consider is the number of evaluations of the objective function at each iteration. In the example shown in Figure 109 the objective function needs to be evaluated four times before choosing the new location. In general, the Hooke-Jeeves algorithm needs to evaluate the objective function at least  $2n$  times at each iteration where  $n$  is the number of free variables. This can be a problem if the objective function is difficult to calculate or if the number of variables is high. However, this methodology can be significantly speed up by using parallel computing techniques in order to evaluate multiple times the objective function in a single run.

Finally, another problem worth to be remarked (from an engineering point of view) is the fact that the step size is the same in each direction meaning that all variables are modified equally. This is a problem when the variables do not possess the same order of magnitude as this procedure will result on some variables been changed significantly, while others suffer from small changes that may not produce a significant change in the objective function, although Powell's method can adjust this step size.

### III.3.1.3. Stochastic methods

The previous two strategies fall under the category of deterministic methods, meaning that the procedure used to search for a global minimum of the objective function follows a well-established and predictable sequence of steps. This means that, if the process is repeated using the same initial point and parameters, the final answer is always going to be the same. Although this may be desirable from a research reproducibility point of view, it is beneficial to add some sort of randomness to the procedure in order to avoid falling under common problems like the aforementioned local minima and saddle points or even to escape them. This randomness can help increase the probability of finding a global minimum by forcing the algorithm to explore regions that were not previously considered by the deterministic nature of the algorithm.

Some examples are stochastic gradient descend methods in which a random variable with zero mean is added to equation ( 79 ). This change provides the algorithm with capability of escape local minimum points or the capacity to produce changes in the current point even when facing the “vanishing gradient” problem. Another modification to GD is to approximate the gradient of the function using randomly selected subset of points (called batch) instead of using the complete dataset in order to enhance the accuracy of the approximated gradient (which is a very common approach in machine learning algorithms).

Another example is the mesh adaptative direct search which is a modification to the zero-order methods. This change consists in, at every iteration, to look at randomly chosen directions instead of the previously defined ones. This in order to force the algorithm to explore more the local search space. In this case, care must be exercise in order to avoid looking at very similar directions as well as producing very large or short step sizes.

Another interesting strategy worthy to mention is “simulated annealing optimization” in which the amount of stochasticity (randomness) added to the system depends on a temperature-like parameter that decreases over time. The idea is that, at the beginning of the optimization process, the temperature of the system is high thus there is a huge amount of randomness in the system. This high randomness can help the algorithm to explore more freely the searching

space in order to find a suitable region close to the global minimum. As the optimization progress, the temperature is reduced thus the stochasticity in the system is reduced. This allows the algorithm to carefully search the global minimum in a previously identified suitable region.

#### **III.3.1.4. Population methods**

Instead of using a single point to explore and search for an optimal solution, population methods use a collection of points called individuals. The basic idea is to distribute these individuals over the searching space in order to explore it. Then, the information obtained by the individuals can be shared between them in order to identify possible regions where a global minimum is likely to be found. This shared information helps these kinds of algorithms to avoid local minimum points. This is because individuals who have not yet fallen into a local minimum can avoid places near where other individuals have found a minimum to instead continue exploring other regions within the searching space. It is also worth noting that these kinds of algorithms do not need to calculate the gradient of the function.

The way in which the individuals explore the searching space and how the information is shared within individuals depends on the specific strategy used. Nevertheless, all of these methods began with an initial population that is distributed over the searching space. The way this distribution takes place can be random or follow a heuristic approach like, for example, all the individuals can be evenly distributed across the searching space or follow a normal distribution centered around an area of interest. The bigger the population, the higher the chances of finding a global minimum point but at the cost of a higher computational time.

Among these population methods, genetic algorithms are one of the most popular methodologies. These algorithms are a subset of evolutionary algorithms based on evolutionary biology concepts like natural selection, mutation, inheritance, and recombination. The basic working principle of a genetic algorithm is detailed in Figure 110. The algorithm starts with a randomly distributed population. Each individual is characterized by properties called “chromosomes” or “genotypes”, which are the free-variables that need to be optimized. Each individual is then evaluated according to the objective function (in this context, the objective function is also called the “fitness” of the individual), then the chromosomes of the best individuals are selected then passed to new individuals via inheritance or modified through two operations: recombination and random mutations. Recombination (also called crossover) refers to the action of combining the chromosomes of two individuals in order to form a new one. Random mutation refers to the action of randomly changing the chromosomes of a new individual. It is possible that a single individual suffers all three operations.

The new individuals born from the previous population form a new population and the process is repeated. Each new population is called a “generation”. This process repeats iteratively until a desired fitness value is reached or until a certain number of generations have passed. The idea of genetic algorithms is that, by continuously choosing and slightly modifying and recombining the best individuals in the current generation, eventually the best possible individual (representing the global minimum) will be born.

Of course, this process is completely random in nature as the performance of this algorithm depends on the distribution of the first generation (which is random) as well as the strategies used for the recombination and mutation (the former being also random in nature). Nevertheless, if the population is sufficiently big, diverse and if enough generations are evaluated, GA will eventually find the global minimum. Another important aspect of this strategy

is that the individuals that are close to local minima cannot be further significantly improved no matter how much mutation and recombination their chromosomes suffer thus, eventually, better individuals will be born such that they will outperform the individuals located at local minimums effectively avoiding stagnation like GD and pattern search algorithms.

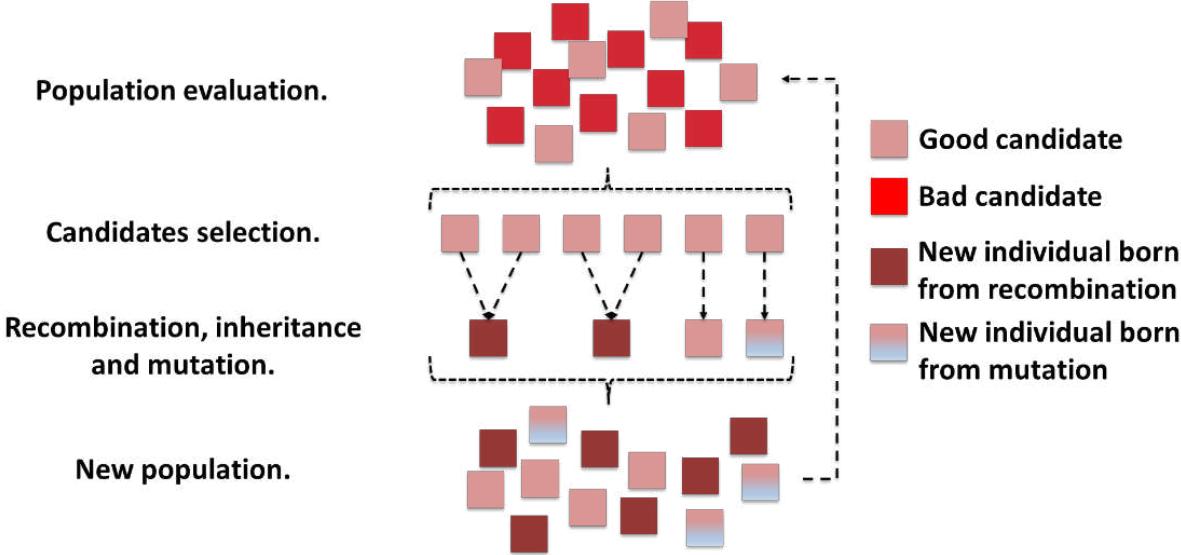


Figure 110. Diagram showing the working principle of a genetic algorithm.

Another popular population method is the particle swarm optimization. This strategy works by continuously moving the individuals across the searching space. This movement is parametrized by the current position of the individual as well as a “velocity” term and an “acceleration” term with some degree of randomness. The working principle of this method is illustrated on Figure 111. The basic idea is that each individual will explore the searching space (Figure 111a) and keep trace of the current best-known position (Figure 111b) then all the other individuals are attracted to the current best position until a new best position is found (Figure 111c). At the end of the optimization, is expected that most individual will end close to the global minimum (Figure 111d) while the rest will end stuck in local minimum points or outside the searching space. Similar to GA, the success of this strategy depends on the size and diversity of the initial population although this process is much less random. However, care must be exercise in regards to the velocity and acceleration terms which may cause the algorithm to explode (i.e all the individual will gain such speed and acceleration that they will either leave the searching space or oscillates between regions) effectively causing the process to end prematurely without any useful solution.

Similar to zero-order methods, the optimization process using population methods can be significantly speed up by using parallelization techniques.

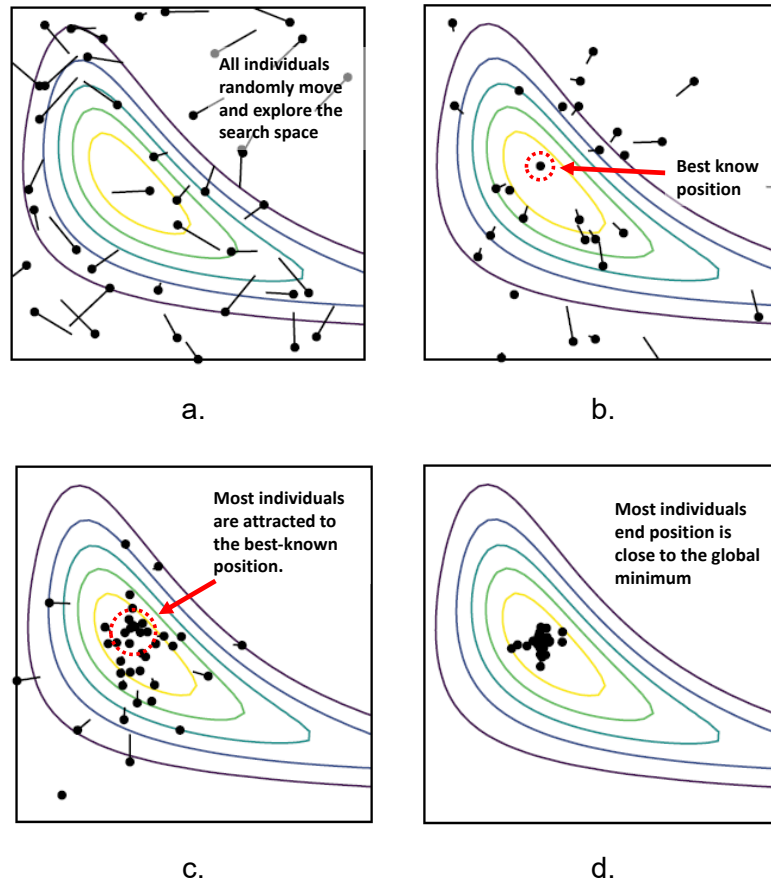


Figure 111. Working principle of a swarm particle optimization applied to a Wheelers ridge function (Adapted from [141]). a) Initial distribution of the population and exploration of the searching space. b) An individual stays on the current best-known position. c) Most of the other individuals are attracted towards the current best-known position. d) Most of the individuals (if not all) end close to the global minimum.

### III.3.2. Multi-objective optimization

Although optimization algorithms can search for optimal solutions simultaneously for multiple objective functions, this is not a straightforward task. This is because, most often than not, trade-offs need to be done between the objective functions. Even if we find the best possible solution for some set of objective functions, the rest of the objectives may not even be acceptable, thus an approach must be established in order to choose a suitable design point with a reasonable trade-off between all the objective functions.

One strategy to solve these kinds of difficulties can be to transform a multi-objective optimization problem into a single objective optimization via a weighted sum of all the objective functions (equation ( 83 )).

$$f(\vec{x}) = \frac{1}{N} \sum_{i=0}^N w_i f_i(\vec{x}) \quad ( 83 )$$

where  $w_i$  is the weight assigned to the objective function  $f_i(x)$  and  $N$  is the number of objective functions. The bigger the weighting coefficient, the more emphasis the algorithm will make in order to minimize that particular objective.

The difficulty with this approach is to choose a suitable weighting coefficient. Most of the time, the selection of these coefficients becomes a matter of experience and multiple test runs. Another aspect to be aware of equation ( 83 ) is that the numerical values of the objective functions need to be around the same order of magnitude, otherwise there will be a natural bias towards the function that produces the biggest values. Furthermore, as with any averaging process, extreme values (i.e a function producing extremely high or low values with respect to the other functions) can skew the average and produce false tendencies for the algorithm run.

Another approaches to transform a multi-objective problem into a single objective problem is to use a minimax approached (or a maximin if we want to maximize an objective). In this case, the value of the objective function is simply the maximum value between all objective functions. Mathematically, this operation is stated by equation ( 84 ):

$$f(x) = \min_x \max_x (f_1(x), f_2(x), \dots, f_N(x)) \quad ( 84 )$$

This approach searches to minimize the worst-case scenario (i.e the function that produces the biggest value). With this strategy, there is no need to search for suitable weighting coefficients nor the function is skewed by extremely low values. However, the minimax operators render the objective function non-linear. Additionally, the objective functions need to produce numerical outputs with the same order of magnitude or else the optimization process will then to focus on the function that produces the biggest numerical outputs.

Although the previous approaches may be suitable strategies for treating multi-objective optimization problems, with these approaches we lose information on the behavior of all the objective functions which an experience user can profit in order to make appropriate trade-offs during the process. In order to identify and solve trade-offs, the concept of dominance is established. We say that a point  $x_1$  dominates another point  $x_2$  if the two conditions ( 85 ) and ( 86 ) are met.

$$f_i(x_1) \leq f_i(x_2) \text{ for all } i \quad ( 85 )$$

$$f_i(x_1) < f_i(x_2) \text{ for some } i \quad ( 86 )$$

That is,  $x_1$  is objectively a better design point than  $x_2$  because it improves at least one objective without degrading the rest. For a single objective optimization problems,  $x_1$  dominates  $x_2$  whenever  $f(x_1) < f(x_2)$ . Unfortunately, for multi-objective optimization, the concept of dominance can be ambiguous. For example, in a two-objective optimization, an ambiguity occurs between two points when  $f_1(x_1) < f_1(x_2)$  and  $f_2(x_1) > f_2(x_2)$ . In this case, we cannot say that the point  $x_1$  dominates the point  $x_2$ , therefore a compromise must be made between the two objectives.

To deal with this trade-off, the concept of pareto optimality is very useful. In mathematical terms, we say that a point  $x$  is pareto optimal if it is not dominated by other points in the searching space. Multiple pareto optimal points can exist at a time. Each point in the solution space represents a possible solution for the problem and everything outside this region is an impossible solution. The dimension of the solution space is equal to the number of objective functions. The set of pareto optimal points (or non-dominated solutions) constitute the pareto frontier as shown in Figure 112 which can be understood as the “best” or “most efficient” possible solutions to the problem.

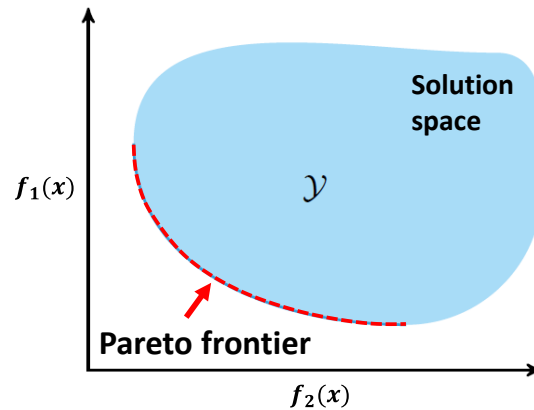


Figure 112. Graphical representation of a Pareto frontier of the solution space for a two-objective optimization.

Thanks to Pareto optimality concept, the trade-off problem is transformed into selecting a point within the Pareto frontier which can be done via other information that was not considered during the optimization process like, for example, the facility of implementing of the solution. For two or three objective optimization problems, the Pareto front represents a convenient graphical tool to choose an appropriate compromise.

It is important to be aware that, in a numerical optimization problem, the Pareto frontier is formed as the optimization progress thus we do not know, a priori, the shape of the Pareto frontier nor at which point the frontier cannot be extended furthermore. Nonetheless, a good criterion to end the optimization progress can be when the Pareto frontier does not improve significantly from one iteration to another or when a sufficient number of “satisfactory” solutions are found.

### III.3.3. Selection and implementation of the optimization algorithm

In order to choose the right strategy from the ones introduced in the previous section, the nature of the problem as well as the objective function (or functions) must be established. In addition, the number of free variables, the type of constraints and the searching space must be explicated. Moreover, due to development time constraints, we desire an algorithm that is easy to implement in an off-the-shelf numerical software like MATLAB as well as capable of providing useful answers within the first run.

The full structure to be optimized is the superstrate with the unsymmetrized array shown in Figure 106 together with the substrate shown in Figure 98. The final structure to be optimized is reminded in Figure 113 to facilitate the reading of this section.

At first glance, the structure presented in Figure 113 possesses twenty-one parameters that need to be optimized (twenty-three if we consider the dimensions of the input transmission line). Each time a new variable is added, the dimensions of the problem increases thus increasing the complexity of the problem as well as the development time. In order to minimize the development time, and due to fabrication constraints, some variables are fixed from the start. The fixed parameters are the height of the substrate and superstrate which are both fixed to 305  $\mu\text{m}$  thick. The size of the ground plane is fixed to a squared form of 10x10 mm (around one lambda at 30 GHz). The glue layer is supposed to be a 100  $\mu\text{m}$  thick layer with a permittivity value of 3.7. Additionally, the input impedance is fixed such that the line impedance is around

50 Ohms. The rest of the dimensions cannot be fixed and will need to be optimized giving a total of 17 free variables.

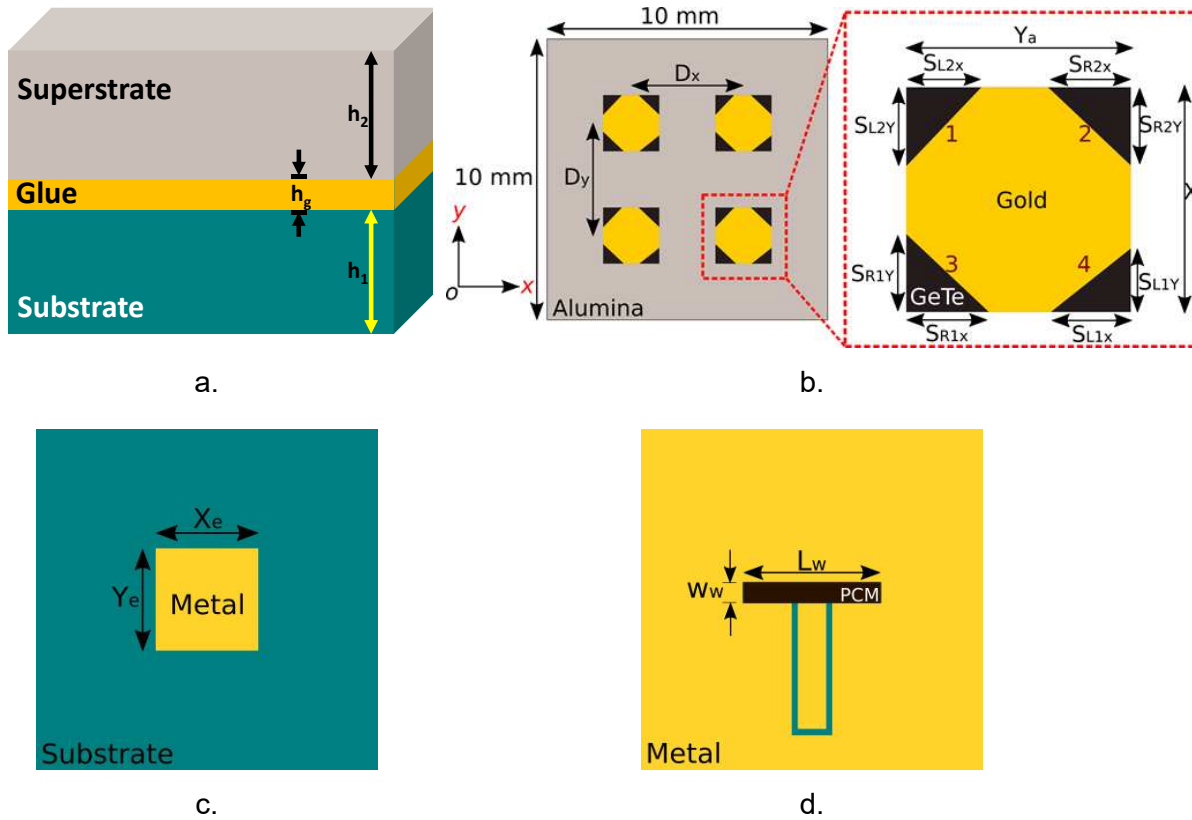


Figure 113. Final geometry of the array of antennas to be optimized. a) Layered structure of the antenna. b) Array of antennas integrating a PCM composition at the top of the superstrate. c) Exciter patch in between the two layers. d) Ground plane and PCM filled coupling slot at the bottom of the substrate.

The variables to be optimized and their respective searching ranges are detailed in Table 19. The separation of the array ( $D_x$  and  $D_y$ ) are constrained such that they are never bigger that  $\lambda_0/2.5$  at 30 GHz.

Table 19. Free variables for the design of the antenna and their respective ranges.

| Variables  | Range            |
|--|------------------|
| $D_x, D_y$   | 1 mm – 4 mm      |
| $X_a, Y_a, X_e, Y_e$   | 1 mm – 3 mm      |
| $S_{R1x}, S_{R1y}, S_{L1x}, S_{L1y}, S_{R2x}, S_{R2y}, S_{L2x}, S_{L1y}$ | 0.1 mm – 1 mm    |
| $L_w, L_{wt}$  | 0.5 mm – 3 mm    |
| $W_w$  | 0.01 mm – 0.1 mm |

However, not all combinations of parameters are valid for the antennas shown in Figure 113. These impossible combinations define the constraints of the problem. One of these constrains has already been established at the beginning of the section, in which we established that the

center-to-center distance in the x direction  $D_x$  must be greater than the size of the patch  $X_a$  or else the patches will superpose with the same logic applying to the y direction. In summary, the allowed combination of parameters must satisfy the following relationships:

$$D_x - X_a > 0 \quad (87)$$

$$D_y - Y_a > 0 \quad (88)$$

$$X_a - S_{R1X} - S_{L1X} > 0 \quad (89)$$

$$X_a - S_{L2X} - S_{R2X} > 0 \quad (90)$$

$$Y_a - S_{R1Y} - S_{L1Y} > 0 \quad (91)$$

$$Y_a - S_{L2Y} - S_{R2Y} > 0 \quad (92)$$

$$L_{wt} - L_w > 0 \quad (93)$$

Equations ( 87 ) and ( 88 ) ensure that the antennas in the array do not superpose in any direction. Equations ( 89 ) to ( 92 ) ensure that the trimmed edges do not overlap. Finally, equation ( 93 ) ensures that the size of amorphous patch is never bigger than the total length of the slot.

### III.3.3.1. Definition of the objective functions.

In order to comply with the objectives proposed here, appropriate objective functions need to be established. In summary, we desire an antenna working at the millimeter-wave frequency band in all states (LP, RHCP and LHCP) with an axial ratio as symmetric as possible and under 3 dB in both states with circular polarization. To minimize the axial ratio while assuring its symmetry, we define the following auxiliary equations:

$$S(\vec{x}, \Phi_0) = \int_{-\theta_0}^{\theta_0} (AR(\vec{x}, \theta, \Phi_0) - AR(\vec{x}, -\theta, \Phi_0))^2 d\theta \quad (94)$$

$$L(\vec{x}, \Phi_0) = \int_{-\theta_0}^{\theta_0} AR(\vec{x}, \theta, \Phi_0) d\theta \quad (95)$$

where  $AR(x, \theta, \Phi_0)$  is the axial ratio in dB of the antenna evaluated at an arbitrary frequency,  $x$  is a vector containing all the dimensions of the antenna and  $\phi_0$  is a particular direction in the  $\phi$ -plane.

Equation ( 94 ) measures the degree of dissymmetry by means of comparing the axial ratio with its reflected image. If the AR is symmetric in the  $\phi_0$  plane, the reflected image is equal to the original axial ratio hence the subtraction results is zero everywhere in the  $\phi_0$  plane. However, if the AR is not symmetric, then the subtraction is non-zero in the  $\phi_0$  plane. In order to quantify the amount of dissymmetry, the area under the curve is evaluated by the integral between the angles  $-\theta_0$  and  $\theta_0$  in the  $\phi_0$  plane. The subtraction is squared in order to avoid negative numbers.

Similarly, equation ( 95 ) measures the level of the axial ratio in the plane  $\phi_0$  by measuring the area under the curve of the AR between the angles  $-\theta_0$  and  $\theta_0$ . With these two equations, we can define the function:

$$f(\vec{x}) = \frac{1}{N} \sum_{i=1}^N (S(\vec{x}, \varphi_i) + L(\vec{x}, \varphi_i)) \quad (96)$$

where we evaluate (94) and (95) for N-cuts in the  $\Phi$ -plane. Effectively, equation (96) is an average over all the phi planes. In this case,  $N = 11$  as the  $\Phi$ -plane is evaluated every  $15^\circ$  from  $0^\circ$  to  $165^\circ$ .

Each circular polarized antenna will have an associate value of  $f(x)$  for a particular set of physical parameters. For the linearly polarized case, equations (94) to (96) are meaningless. In order to evaluate (96), a full-wave simulation must be performed at each state of polarization. To optimize both states of polarization simultaneously, we use a minimax approach between  $f(x)$  value produced by each antenna. With this set-up, we define our first objective function to be minimized as:

$$f_1(\vec{x}) = \max(f_{RHCP}(\vec{x}), f_{LHCP}(\vec{x})) \quad (97)$$

where  $f_{RHCP}(x)$  and  $f_{LHCP}(x)$  are the results obtained from evaluating equation (96) for the right-hand circular polarization and left-hand circular polarization, respectively.

At the same time, we want to maximize the gain of the antenna at boresight direction in all states. Since the effect of unsymmetrized the edges of the antennas may have an influence in the radiation characteristics of the array, a trade-off is to be expected between the maximum gain of the antenna and quality of the circular polarization of the antenna, therefore a second objective function is to be defined.

Maximizing the gain of the antenna will result in maximizing simultaneously the directivity and minimizing the adaptation level of the antenna at frequency of interest. To assure that the antenna effectively points in the axis, we can maximize the gain only in this direction. Since the optimization algorithms can only minimize functions, this objective needs to be transformed into a minimizing problem which can be easily done by multiplying the function by negative one. In summary, we define our second function as :

$$g(\vec{x}) = -\text{Gain}(\vec{x}, \theta = 0) \quad (98)$$

For this case, we will assume that if the maximum gain of both circular polarized states points in the axis, then the linearly polarized antenna will also point in the same direction since the trimmed edges do not affect significantly the radiation pattern. This means that we do not need to perform a full-wave simulation on the LP case, thus speeding up the development. Then to optimize simultaneously both structures, we minimize the worst-case scenario. Therefore, our second objective function can be expressed as :

$$f_2(\vec{x}) = \max(g_{RHCP}(\vec{x}), g_{LHCP}(\vec{x})) \quad (99)$$

A suitable trade-off between equations (97) and (99) will be chosen post-optimization after evaluating the pareto frontier of the problem.

One can argue that a third objective function need to be added in order to ensure that all states of polarization operates the same resonance frequency. However, equation (99) can ensure that both the RHCP and LHCP operates at the same frequency by means of the gain as a proxy parameter. On the other hand, the trimmed edges of the square patch have an influence on the resonance frequency of a patch, therefore we do not expect that the LP configuration

will operate exactly at the same resonance frequency as the circular polarized cases. However, this perturbation is small and any deviation from the desired resonance frequency can be finely tuned by changing the length of the slot within the ground plane. In order to reduce the simulation time, we will not simulate the LP case under the assumption that the performance in directivity and matching of this configuration will be very similar to the circular polarized case thus this third objective function is not necessary.

### III.3.3.2. Algorithm selection

The fact that the optimization needs to be carried out via 3D full-wave electromagnetic simulations implies that the objective functions are very difficult and time consuming to calculate. In order to minimize the simulation time, the antenna will be only optimized at the frequency of 30 GHz. In addition, this means that we will not have access to gradients of the function since we will require, either a lot of data points to numerically approximate it or evaluated it via very small changes in the structure. This detriment, together with the fact that the objective functions are non-linear functions immediately rules out the use of gradient descend methods as an option to optimize this structure.

Moreover, the huge number of free variables and the non-linear nature of equations ( 97 ) and ( 99 ) may require a lot of effort and computational time in order to be solved by zero-order algorithms due to the high number of variables. Furthermore, according to Table 19, the magnitudes of the design variables are very dissimilar meaning that the steps taken using a pattern search methodology have to be carefully managed. This problem can be easily avoided by normalizing the range of free variables, however, in this case the mathematical formulations of the algorithm must be changed accordingly. Finally, given that we do not possess any information on the topology of the searching space, the probability of falling into a local minimum can be very high thus implying that multiple runs of the optimization problem will need to be performed. With this information, we consider that the best option to solve this problem is the use of population methods.

Swarm particle optimization has been used effectively to optimize structures in electromagnetic problems, however the possibility of the algorithm exploding needs to be addressed properly and there is no warranty of obtaining useful solutions within the first run of the algorithm if the velocity and acceleration terms are not appropriately handled. For these reasons, our chosen optimization strategy must be the genetic algorithm approach.

Genetic algorithms (GA) have been a popular choice due to their simplicity and ease of implementation in numerical off-the-shelf software, most notably MATLAB. GA have been successfully used to optimize structures in electromagnetism, in particular for arrays of antennas, as shown in [147] and [148] although by using an analytical formulation. GA have also been used to optimize a single circular polarized antenna focusing on minimizing the axial ratio (AR) over a large bandwidth, as shown in [149] while others such as [150] focus on minimizing the axial ratio over a broad angular region.

### III.3.3.3. Optimization set-up

To start the GA, we need to *i*) define the objective functions to be optimized, *ii*) define the free variables and, *iii*) define the parameters of the genetic algorithm (size of the population, mutation rate, number of generations, etc). The first two steps were already discussed and fixed in previous sections. In this section we will deal with the parameters of the optimization

algorithm as well as the preparation of the structure to be optimized and its implementation in MATLAB.

Since we have two objective functions with possible trade-off, the concept of pareto front will be implemented within the run of the optimization algorithm. For population methods, the optimization of the objective functions is usually performed by dividing the population into subpopulations equal to the number of objective functions, then each subpopulation tries to minimize an objective function. The pareto front is constructed by identifying the non-dominated solution from each subpopulation. The search of the non-dominated solutions as well as the creation of the pareto front is automatically managed by MATLAB.

The mutation is governed by a power mutation rule. For this case we use a modified version as stated in [151] to take account of the boundaries. With this formulation, the mutation of a variable  $x$  is given by:

$$x = \begin{cases} x^* - s^p(x^* - x^l) & \text{if } t < r \\ x^* + s^p(x^u - x^*) & \text{if } t \geq r \end{cases} \quad (100)$$

where  $x^*$  is the value of the current variable,  $x^l$  and  $x^u$  are, respectively, the lower and upper limits of the variable  $x$ ,  $r$  and  $s$  are uniformly distributed distinct random numbers between 0 and 1,  $p$  is the index of mutation governing the strength of the perturbation and  $t$  is a variable defined in equation (101).

$$t = \frac{x^* - x^l}{x^u - x^*} \quad (101)$$

The crossover of the individuals is governed by equation (102).

$$x = x_1 + h.(x_2 - x_1) \quad (102)$$

where  $x_1$  and  $x_2$  are the parents of the new offspring  $x$  and  $h$  is another uniformly distributed random variable from 0 to 1. The most important aspect of equation (102) is the selection of the parents. One may think only the best individuals within the population should be eligible for creating offspring however this approach risks destroying the diversity of the population thus increases the probability of falling into a local minimum. A popular alternative is to use "Tournament selection" in which the population is randomly divided into multiple subgroups and only the best individuals from each group are chosen as the parents of the next generation.

The size of the population is, arguably, the most important parameter who defines most of the performances of the GA. A small population will not have enough diversity in their chromosomes thus it exists the risk that the algorithm will not find the best solution unless a lot of generations are evaluated. On the other hand, if the size of the population is very big, the amount of time needed to find the optimal solution may be prohibitively long. Many works have been performed in order to choose an appropriated number of individuals for GA algorithms ([152] [153] [154]) but the reality is that this parameter is dependent on the problem. More specifically, it depends on the number of objective functions, the number of free variables and the size of the searching space, and is usually fixed after various trial runs. A very common "rule of thumb" found in the literature is to set a population with at least three times the number of variables, although most of the time the number of variables to be optimized is less than five in these examples. Numerical software's like MATLAB recommend at least ten times the number of variables for more than five variables while other works go as high as 50 times the number of variables. For this work, we choose ten times the number of variables multiply by the expected number of subpopulations. For multi-objective optimizations, MATLAB creates a

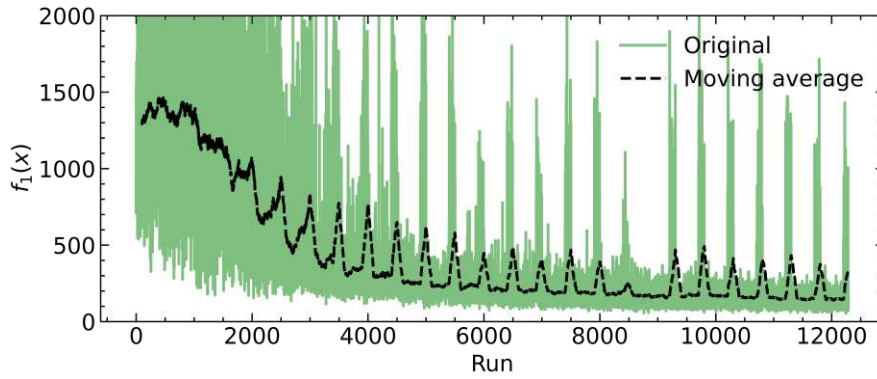
subpopulation for each objective, in addition it also creates an additional subpopulation that is randomly generated at each generation in order to randomly explore the solution space independently of the other objectives. This is with the intention of keeping a high diversity on the global population and reducing the chances stagnation due to a local minimum. In summary, we define the total population as ten times the number of subpopulations times the number of variables, giving a total of 510 individuals which is rounded to 500 individuals.

It is expected that the most time-consuming task during optimization is the electromagnetic simulation. Therefore, in order to accelerate the development time, the simulation time must be optimized to take the least amount of time possible. This can be achieved by choosing an appropriate mesh into the structure and ensure that the least amount of adaptive mesh is performed. The average time per individual evaluation within the GA is around 120 seconds giving a total of around 17h average time per generation.

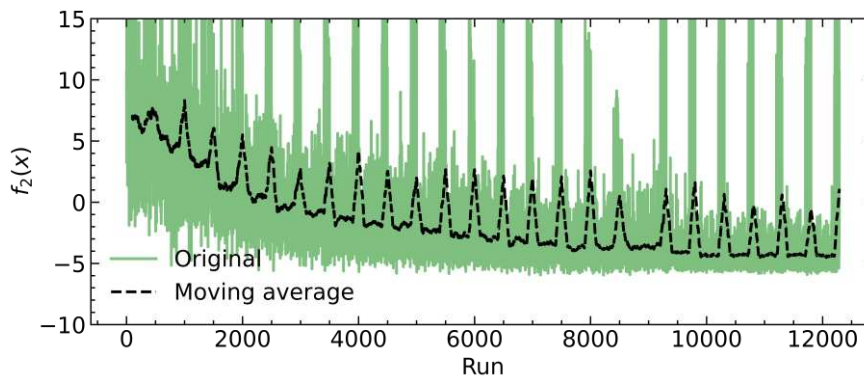
The optimization algorithm was implemented using MATLABs optimization toolbox with a maximum of 50 generations, and the electromagnetic 3D simulation of the antennas (using the physical parameters of the device) was performed using CST Microwave Studio. At each generation, MATLAB will create a population with their respective chromosomes. Each set of parameters are then imported to CST Microwave to perform an electromagnetic 3D simulation of both circularly polarized configurations. Once the simulations are finished, the far-field results of both arrays are then imported back to MATLAB to perform the fitness evaluation of the individual by using ( 96 ) and ( 97 ). This process is repeated for each member of the current population. Afterward, the MATLAB algorithm will select the best candidates to create a new population and repeat the entire process.

#### **III.3.4. Results of the genetic algorithm run**

The genetic algorithm has been evaluated for over 24 generations. The total run time is around 1200 hrs. (or around of nine weeks) of continuous computational power. The evolution of both objective functions during the optimization process is shown the Figure 114. Due the stochastic nature of the algorithm, the behavior of functions  $f_1(x)$  and  $f_2(x)$  is also random as shown in the green trace. The black trace on both graphs shows a moving average of the objective function using 100 individuals to show the trending of the function. From this black trace we can see that both objective functions are still decreasing although very slowly. The sudden spikes are most probably due to the randomly generated subpopulation exploring the searching space. It is also observed that both functions rapidly decrease during the first half of the process and then slowly decrease during the second half indicating a slow convergence rate to a minimum value. Additionally, from both figures a lower limit of both objective functions can be observed (around 100 for the first objective function and -6 for the second objective function) from which we can conclude that there is a high probability that the best solutions have already been found and therefore the optimization process can be stopped. In order to definitely decide to stop the optimization process more information is needed which can be obtained from the pareto front as well as the evolution of the variables.



a.



b.

Figure 114. Evolution and moving average of a)  $f_1(x)$  and b)  $f_2(x)$ .

Figure 115a shows the solution space of the whole optimization process where it can be seen that a clear frontier has been created at the lower left side. Figure 115b shows the pareto front of this generation from which it can be observed that all points align very well in a parabolic shape from which no individual is significantly far away. This is a strong indication that we are close (if not already into) to the global minimum in each objective function. This is because if we were not close to the global minimum of neither of the objective functions we will expect the apparition of even a single point significantly far away to the left of this frontier after this number of generations due the random nature of the algorithm. This shape of the pareto front confirms that, indeed, there is a strong trade-off to be made between the gain of the antenna ( $f_2(x)$ ) and the quality of the circular polarization ( $f_1(x)$ ).

Figure 116a shows the moving average of the size of the trimmed edges from which it can be observed that any of the variables has yet converged to a particular value meaning that the mean value of the first objective function can still be improved. However, as mentioned previously, there seems to be a lower limit with respect to the quality of the circular polarization and most probably, the solutions close to the minimum are already part of the pareto front in Figure 115b. That means that, even if the size of the trimmed edges has not converged yet, the probability of finding better solutions that the ones shown in Figure 115b is very low and even if we find better solutions we do not expect a much greater improvement in the pareto front as previously discussed.

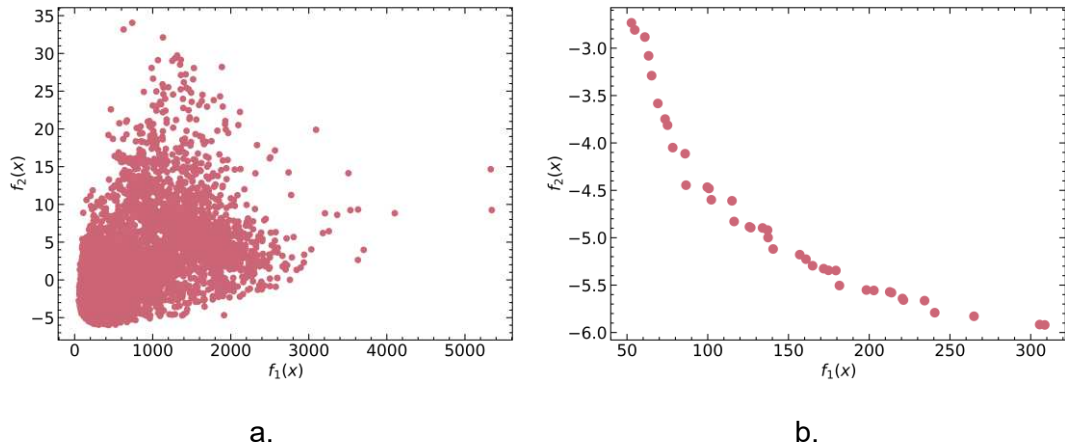


Figure 115. a) Solution space of the optimization algorithm. b) Pareto front after 24 generations.

Figure 116b and Figure 116c show the evolution of the variables controlling the size of the array and the size of the coupling slot. Figure 116b shows that the dimensions of the array already converge to a value which implies that the directivity also converge to a particular value. This is confirmed by Figure 117a showing the evolution of the directivity confirming that the algorithm rapidly converged to solutions presenting the best possible directivities values at 30 GHz. It can be observed that it seems to be an upper limit of 11 dBi in the directivity.

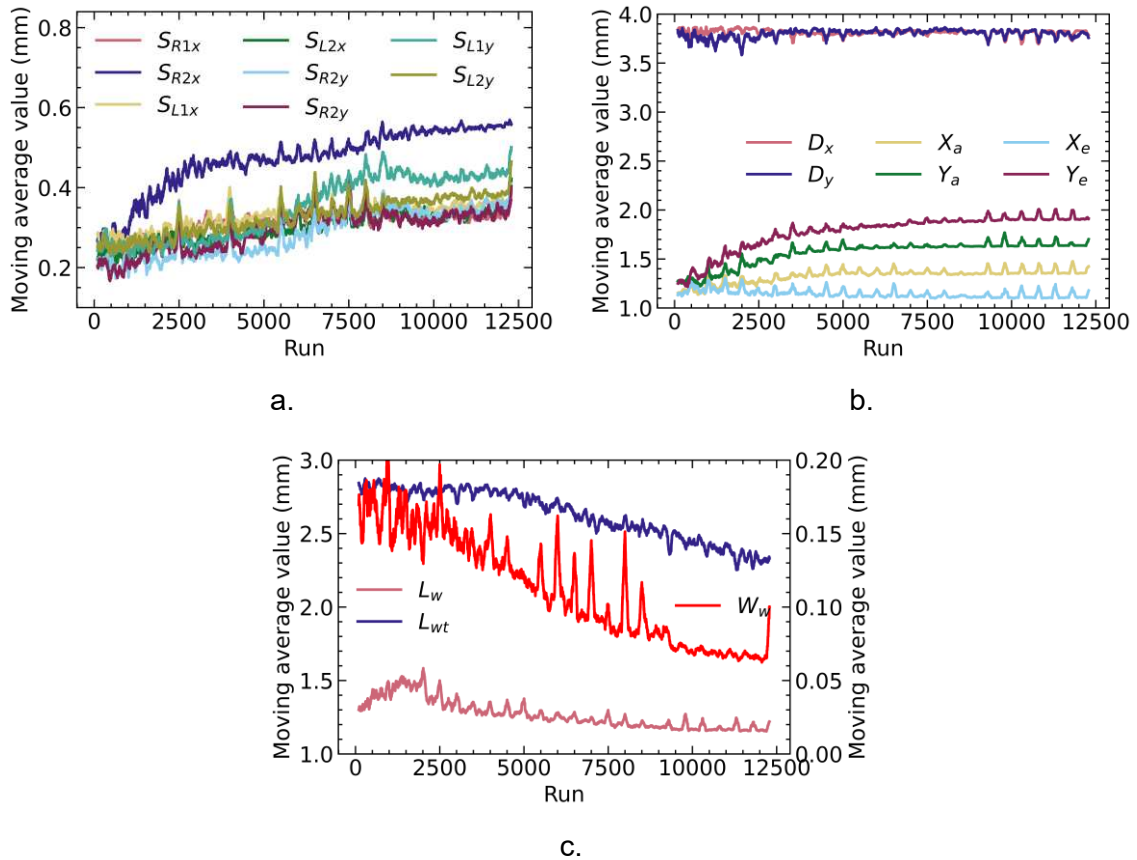
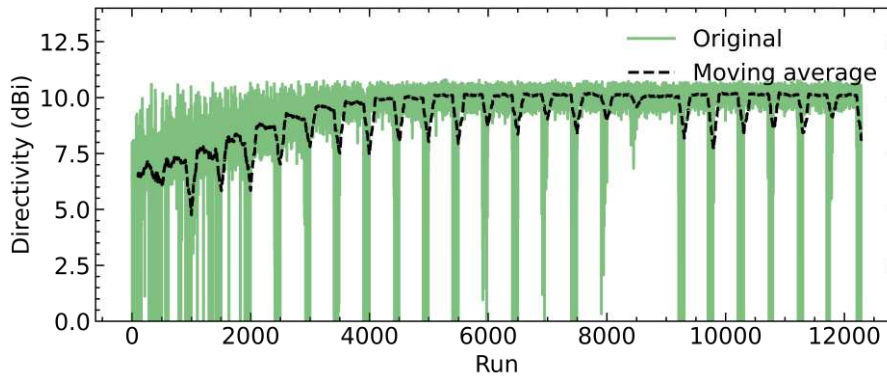
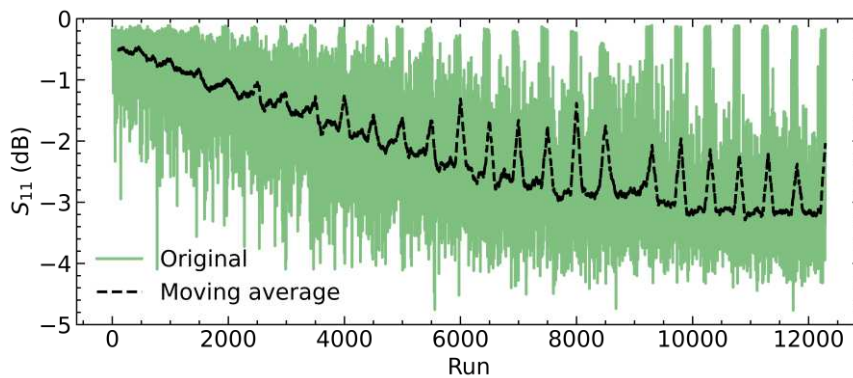


Figure 116. Evolution of the moving average of the free variables. a) Size of the trimmed edges. b) Size of the of the antennas and the array. c) Size of the coupling slot.

Figure 116c shows that the total dimensions of the slot ( $L_{wt}$  and  $W_w$ ) have not converged yet but the size of the effective length ( $L_w$ ) is converging. For the adaptation level, we observe a slow decrease during the first three quarters of the simulation process and its beginning to converge to a mean value of around -3 dB. However, an adaptation level smaller than -5 dB is never observed during the whole process with most solutions been worse than -4 dB in adaptation level. With this information, we suspect that there is no combination of parameters that will allow to match the antenna in this frequency band.



a.



b.

Figure 117. Evolution of the a) directivity and b) adaptation level of the array of antennas.

Taking into consideration all previous points, we believe that most efficient solutions for this problem have already been found and shown in the pareto front of Figure 115b. Given that not all variable has converged yet, there is a probability of finding slightly better solutions. However, we do not expect that these solutions will improve significantly the solutions already found. Furthermore, given that the algorithm is converging very slowly, we expect that the time needed to found better solutions will be very long therefore we do not consider worthy to find them. Therefore, we choose to put an end to this optimization problem. Next section will focus on choosing the most fitting solution from the pareto front and matching the antenna.

### III.3.4.1. Selection of the solution and performance

The final solution will be chosen by evaluating all the solutions in the pareto front. After discarding all the solutions whose axial ratio is bigger than 3 dB at boresight together with solutions that do not point in the axis, the Table 20 presents all the final candidates with the properties of interest arranged by “number of solutions” vector given by MATLAB. From this table we can observe that, for all the solutions, the directivity and matching level in both states

of polarization present very similar values. Unfortunately, none of these solutions are adapted at this frequency which will require a future post-design onto the chosen solutions. Another unfortunate situation is that none of the solutions presents directivities higher than 10 dBi in the axis, however they all presents directivities higher than 9 dBi. Considering the fact that we are using a very high permittivity substrate, we consider that the directivity values found are satisfactory. From the desired characteristics of the antenna exposed in Table 16, we will choose the solution number 2 since this configuration presents the largest aperture in axial ratio with an acceptable value of the boresight axial ratio. Additionally, since this configuration presents the lowest found value for  $f_1(x)$ , we can expect that this solution is the most symmetrical one since the other candidate solutions presents similar axial ratio values and aperture.

Table 20. Acceptable solutions for the array of antennas taken from the pareto front.

| Solution number | $f_1(x)$ value | $f_2(x)$ value | Axial ratio at boresight (dB) |            | Axial ratio angular aperture (°) |           | Directivity at boresight (dBi) |            | S <sub>11</sub> (dB) |             |
|-----------------|----------------|----------------|-------------------------------|------------|----------------------------------|-----------|--------------------------------|------------|----------------------|-------------|
|                 |                |                | LHCP                          | RHCP       | LHCP                             | RHCP      | LHCP                           | RHCP       | LHCP                 | RHCP        |
| <b>2</b>        | <b>54.7</b>    | <b>-2.8</b>    | <b>2.2</b>                    | <b>2.4</b> | <b>67</b>                        | <b>67</b> | <b>9.3</b>                     | <b>9.4</b> | <b>-2.5</b>          | <b>-2.6</b> |
| 6               | 69.0           | -3.6           | 2.8                           | 2.7        | 64                               | 64        | 9.6                            | 9.6        | -2.8                 | -2.8        |
| 7               | 65.2           | -3.3           | 2.3                           | 2.2        | 61                               | 62        | 9.5                            | 9.5        | -2.8                 | -2.9        |
| 19              | 61.0           | -2.9           | 2.1                           | 2.4        | 64                               | 67        | 9.4                            | 9.4        | -2.6                 | -2.6        |
| 30              | 116.3          | -4.8           | 2.9                           | 2.6        | 60                               | 59        | 9.7                            | 9.7        | -3.0                 | -3.0        |
| 33              | 181.1          | -5.5           | 2.4                           | 2.1        | 64                               | 61        | 9.6                            | 9.5        | -2.8                 | -2.7        |
| 39              | 58.7           | -2.7           | 2.2                           | 2.3        | 66                               | 64        | 9.3                            | 9.3        | -2.3                 | -2.3        |

The axial ratio of both CP configurations for the chosen solution is shown in Figure 118 for the  $\Phi$  planes at  $0^\circ$ ,  $45^\circ$ ,  $90^\circ$  and  $135^\circ$ . From Figure 118a we can see that the RHCP antenna presents a very symmetric AR lower than 3 dB in the angular range  $-37^\circ \leq \theta \leq 30^\circ$ . Similarly, from Figure 118b we observe that the LHCP antenna also presents a very symmetric AR lower than 3 dB in the angular range  $-35^\circ \leq \theta \leq 32^\circ$ . It is also worth noting that both arrays present a direction where the AR is lower than 3 dB for all angles between  $-90^\circ$  and  $90^\circ$  in the theta direction (at  $\Phi = 135^\circ$  for the LHCP antenna and  $\Phi = 45^\circ$  for the RHCP antenna).

Finally, Figure 120 presents the broadband behavior of the chosen solution from which it can be seen that both CP configurations presents very similar performances with a 3 dB axial ratio bandwidth of 1.8 GHz in both states. It is also observed that the minimum value of the axial ratio is not at 30 GHz but at 30.5 GHz where both configurations presents an axial ratio of around 1.2 dB and the maximum directivity is at 32 GHz with a value of 9.8 dBi. However, none of the antennas are matched therefore, in the next section we will concentrate in designing a strategy in order to match the antenna without perturbing the radiating performances.

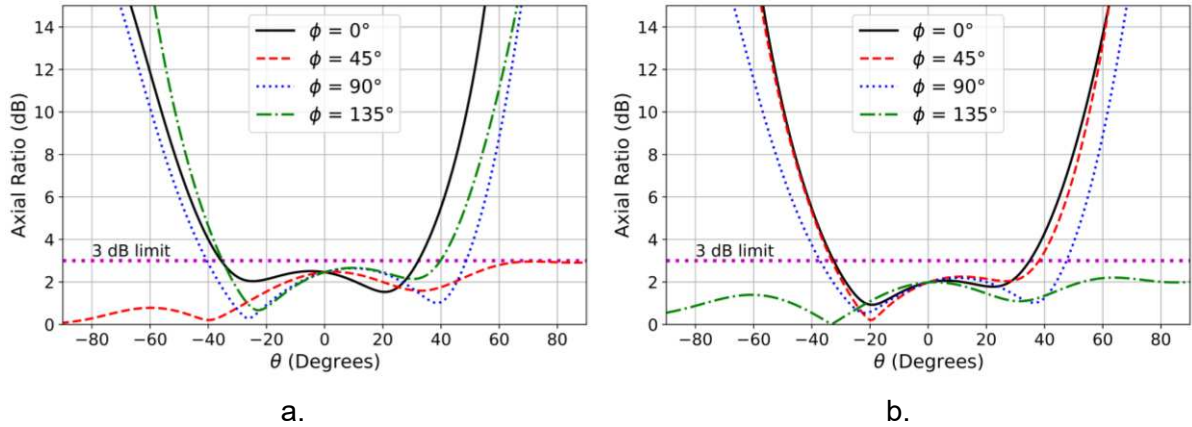


Figure 118. Simulated axial ratio at four cuts on the  $\Phi$  plane for the current best configuration.  
 a) RHCP antenna b) LHCP antenna.

Similarly, the directivity of both CP configurations for the chosen solution is shown in Figure 119 for the  $\Phi$  planes at  $0^\circ$ ,  $45^\circ$ ,  $90^\circ$  and  $135^\circ$ . From this figure we can see that, both configuration points in the axis.

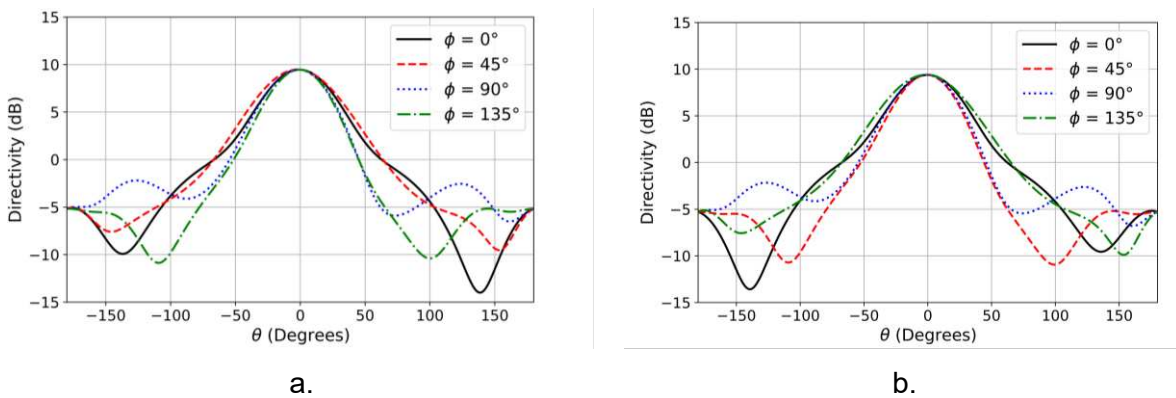


Figure 119. Simulated directivity at four cuts on the  $\Phi$  plane for the current best configuration.  
 a) RHCP antenna b) LHCP antenna.

As mentioned previously, the solution presented in Figure 120 may not be the best possible solution nor that is close to the best solution. In addition, due to the randomness of the process, there is no guarantee of getting the same results if the algorithm is run again nor that it takes the same time to converge to a solution. Normally, these kind of algorithms should be run multiple times in order to have statistically significant results. However, due to the time required to “complete” the optimization and the fact that the solution presented is judged as satisfactory, the authors do not consider that multiple runs of the algorithm are required.

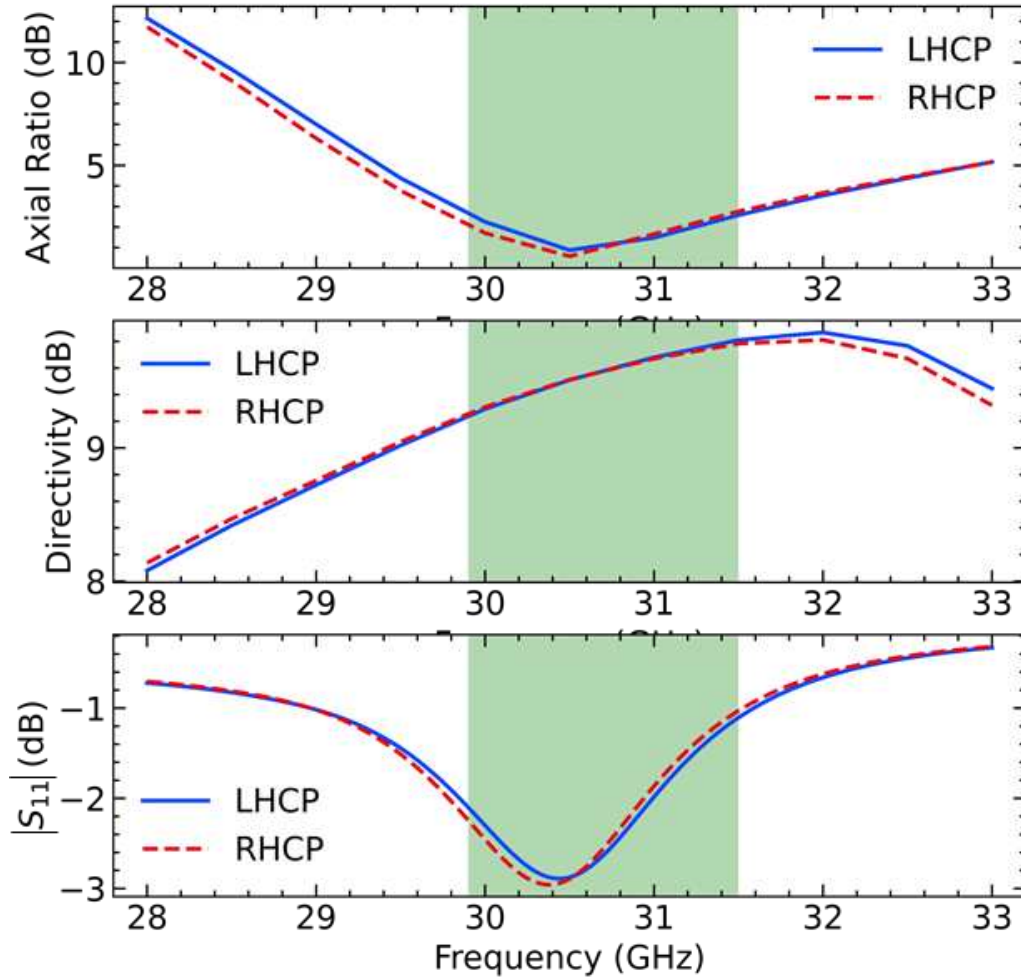


Figure 120. Simulated broadband performances of both CP configurations. The green rectangle corresponds to the frequency range where the AR of both circular polarizations is lower than 3dB.

### III.3.5. Antenna matching

The next step is, therefore, searching an appropriated matching strategy for the antenna. This has to be done carefully in order to not degrade significantly the solution already presented. From the broadband performances, we see that the minimum value of axial ratio is obtained at the frequency of 30.5 GHz.

Figure 121 shows the impedance of the de-embedded line at the slot reference plane of the previously selected antenna. The current adaptation level is around -2.5 dB at 31 GHz as shown previously in Figure 120. From the smith chart of Figure 121, we observe that the impedance of the antenna crosses the real axis at 31.2 GHz. Since the impedance is purely real at this point, we propose the use of a quarter-wavelength resonator to move the resonance frequency point close to 50  $\Omega$ .

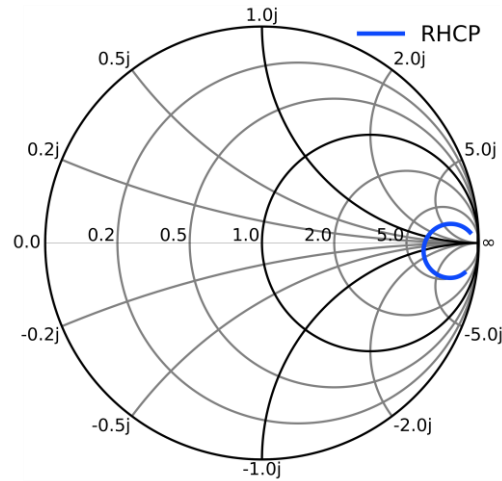


Figure 121. De-embedded matching characteristics of the selected antenna.

In order to match the load to a 50  $\Omega$  impedance source, the matching line between the source and the load must be of length  $\lambda/4$  at the operational frequency. Furthermore, the impedance of the quarter-wavelength line should be such that

$$Z_1 = \sqrt{Z_0 Z_L} \quad (103)$$

where  $Z_1$  is the characteristic impedance of the quarter-wave matching line,  $Z_0$  is the impedance of the source and  $Z_L$  is the impedance of the load. The impedance at the resonance frequency is around 350  $\Omega$ , thus according to equation (103), the impedance of the matching line needs to be 132  $\Omega$  in order to match the antenna to a 50  $\Omega$  impedance source.

However, this is a huge step in impedance involving a high difference in dimensions between the quarter-wave lines and the 50  $\Omega$  impedance line. This abrupt transition in the impedance can cause unwanted radiation which will result in perturbations in the radiation pattern of the antenna such as lower gain, a decrease of the front-to-back ratio and maybe influencing the pointing direction of the antenna. Moreover, these transitions will influence the matching characteristics resulting in a reduction the  $|S_{11}|$  level. To avoid abrupt transitions in the line impedance, a taper transmission line can be used where, instead of a step impedance (Figure 122a), a continuous deformation in the width of the line is used in order to smoothly change the impedance of the line over its length (Figure 122b) [155] [34].

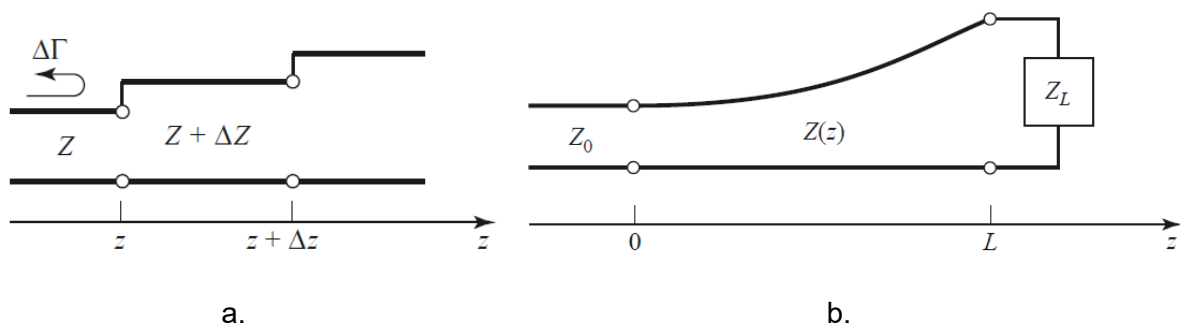


Figure 122. a) Model of an impedance step change. b) Model of a smooth change in impedance using a taper line.

The magnitude of the reflection coefficient as a function of the length of the taper line is given by:

$$|\Gamma(L)| = \frac{1}{2} \ln \left( \frac{Z_L}{Z_0} \right) \left( \frac{\sin(\beta L/2)}{\beta L/2} \right)^2 \quad (104)$$

where  $\beta$  is the propagation constant of the line.

From equation ( 104 ) we observe that the reflection coefficient decreases as the length of the taper increases. In fact, we can achieve zero reflection coefficient every time the length of the taper is an integer multiple of the wavelength. Unfortunately, at 31 GHz the wavelength is around 7mm which is much longer than the available space in the ground plane (little less than 5 mm). This is without even taking into consideration the need of a certain length of a 50  $\Omega$  line needed for the TEM mode to be installed correctly in the line. Another observation to equation ( 104 ) reveals that, for a given length  $L$ , the reflection coefficient can also be reduced by decreasing the ratio  $Z_L$  to  $Z_0$ . However, in order to reduce the ratio, either the  $Z_L$  must be reduced or  $Z_0$  must be increased. In order to match the antenna to a 50  $\Omega$  line, we propose the geometry shown in Figure 123.

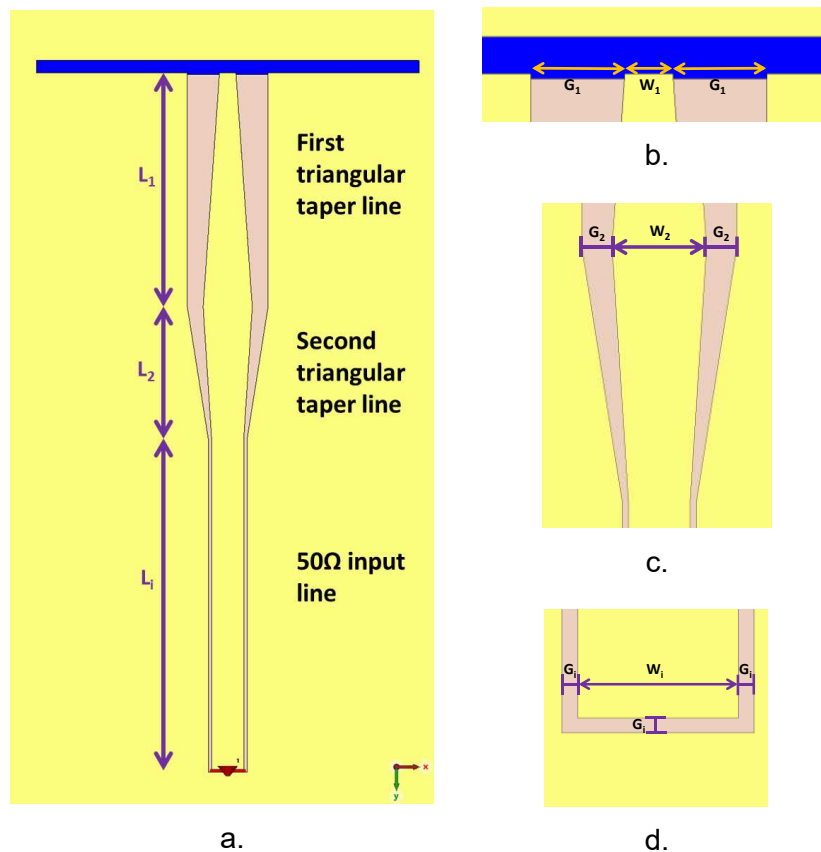


Figure 123. Proposed geometry for matching the antenna using two triangular taper lines a) Full view of the model. b) Dimensions of the CPW at the slot window plane integrating amorphous GeTe to obtain frequency reconfiguration. c) Dimensions of the CPW at the transition between the first and second triangular taper line. d) Dimensions of the 50  $\Omega$  input feeding line of the antenna.

First a CPW taper of length  $L_1$  will gradually transform the high impedance of the antenna to an intermediary lower impedance (in this case around 70  $\Omega$ ) then, a second CPW taper line of

length  $L_2$  will connect both the first CPW taper and the  $50 \Omega$  impedance. Since the magnitude of the reflection coefficient decreases with the length  $L$ , the first taper will need to be longer in order to balance higher  $Z_L$  to  $Z_0$  ratio.

The dimensions for the end the first taper were fixed to a gap of  $150 \mu\text{m}$  and central conductor width of  $100 \mu\text{m}$ . The impedance at the junction of the first and second tapered line is chosen such that the impedance is  $70\Omega$ . The final dimensions of the feeding line are finely tuned by optimization to achieve the minimum possible reflection coefficient for a slot window of length of  $0.6 \text{ mm}$  without perturbing significantly the axial ratio. The Figure 123d shows the dimensions of the  $50\Omega$  input line. The final dimensions of the antenna are shown in Table 21 while the feeding line dimensions are presented in Table 22.

Table 21. Final dimensions of the array of antennas.

| Parameter | Dimension        | Parameter | Dimension         |
|-----------|------------------|-----------|-------------------|
| $D_x$     | 3.95 mm          | $S_{L1x}$ | $610 \mu\text{m}$ |
| $D_y$     | 3.69 mm          | $S_{L1y}$ | $482 \mu\text{m}$ |
| $X_a$     | 1.39 mm          | $S_{L2x}$ | $462 \mu\text{m}$ |
| $Y_a$     | 1.74 mm          | $S_{L2y}$ | $519 \mu\text{m}$ |
| $X_e$     | 1.10 mm          | $S_{R1x}$ | $566 \mu\text{m}$ |
| $Y_e$     | 2.00 mm          | $S_{R1y}$ | $669 \mu\text{m}$ |
| $W_w$     | $78 \mu\text{m}$ | $S_{R2x}$ | $369 \mu\text{m}$ |
| $L_{wt}$  | 2.39 mm          | $S_{R2y}$ | $613 \mu\text{m}$ |

Table 22. Final dimensions of the proposed matching line.

| Parameter | Dimensions        |
|-----------|-------------------|
| $L_1$     | 1.46 mm           |
| $L_2$     | 0.83 mm           |
| $L_i$     | 2.00 mm           |
| $W_1$     | $100 \mu\text{m}$ |
| $G_1$     | $200 \mu\text{m}$ |
| $W_2$     | $306 \mu\text{m}$ |
| $G_2$     | $98 \mu\text{m}$  |
| $W_i$     | $200 \mu\text{m}$ |
| $G_i$     | $20 \mu\text{m}$  |

Figure 124 shows the results of matching the antenna using the two tapered line strategy on a RHCP antenna where an adaptation level of -12 dB is observed at 31 GHz which is still an acceptable matching level. The Figure 125 shows the impedance evolution with frequency showing a parallel type resonance at 31 GHz. These matching characteristics are satisfying therefore we will proceed with this strategy.

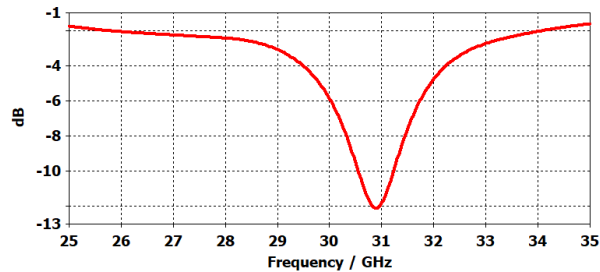


Figure 124. S-parameters of the antenna using two triangular tapered transmission lines as simulated in CST-Microwave for a  $L_w = 0.6$  mm.

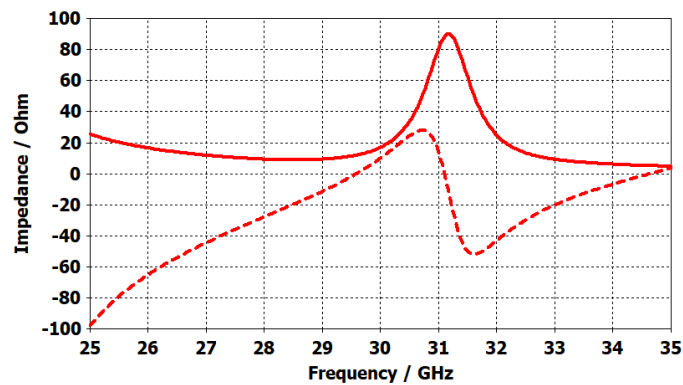


Figure 125. Simulated behavior of input impedance of the matched antenna using the proposed matching network in for a  $L_w = 0.6$  mm.

Figure 126 shows the response of both CP configurations to the change in effective length of the slot window (Crystallization/amorphization of the GeTe inside the slot). It is observed that both configurations are equally tuned by the change in the slot window presenting the same resonance frequency. At the same time a very slight (almost negligible) difference in the matching level of both circularly polarized configurations is observed.

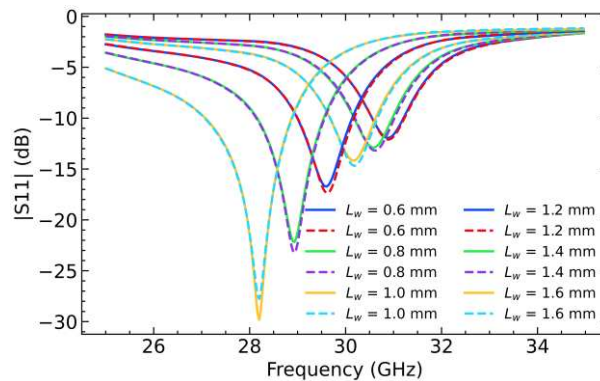


Figure 126. Performance of the adaptation level of the RHCP configuration (solid lines) and the LHCP configuration (dashed lines) circularly polarized configuration as the effective length of the slot is changed.

Figure 127a and Figure 127b shows the effect of the window tuning on the far-field characteristics. The former shows that the directivity is slightly perturbed for both cases with a clear trending in reducing the maximal directivity as the slot window is increased. Nonetheless the directivity in all cases (for both polarizations) is greater than 9 dBi. As for the case of the axial ratio, Figure 127b shows a slight degradation on the axial ratio level as the slot window is increased, this time, the axial ratio is lower than 2 dB for all cases. Since the axial ratio is almost not perturbed by the frequency reconfiguration, the simulation shows that a continuous frequency reconfigurability for the both circular polarized cases can go up to 31.1 GHz with directivities greater to 9 dBi for both cases.

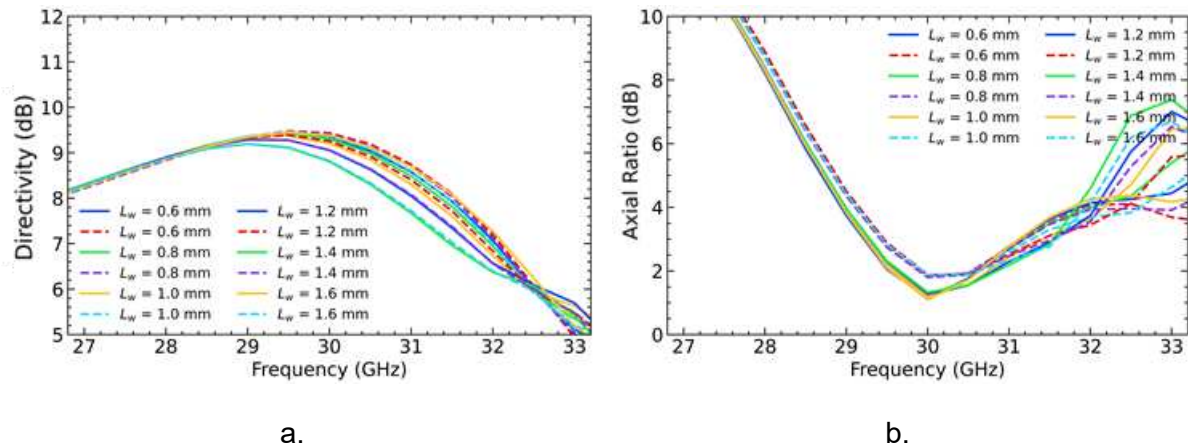


Figure 127. Performance of the far-field properties of the RHCP configuration (solid lines) and the LHCP configuration (dashed lines) as the effective length of the slot is changed. a) Directivity in the axis. b) Axial ratio in the axis.

For both linearly polarized configurations, Figure 128 shows the effect of changing the size of the slot on the matching level (Figure 128a) and directivity (Figure 128b), respectively for the configuration where all the edges are crystalline (dashed lines) and amorphous (solid lines). We can observe that the matching level can be continuously tuned by changing the length of the window (which is achieved by crystallizing the GeTe at the sides of the window) while presenting very good adaptation levels while the directivity is slightly reduced as the size of the slot is reduced. For the case when all edges are amorphous, we can observe that the minimum matching level is better than -14 dB for all lengths of the slot window while the directivity is almost unperturbed. Figure 128b shows that the maximal directivity is found at higher frequencies for the case where all GeTe edges are amorphous. This suggests that the resonant frequency of the structure is at higher frequencies which can be explain by the fact that the antenna is effectively smaller (due to the trimmed edges) therefore its resonance frequency should be higher than the case where all edges are crystalline.

The previous simulated results have proved very satisfactory. Therefore, we will proceed with the fabrication of the structure and the evaluation of their performances.

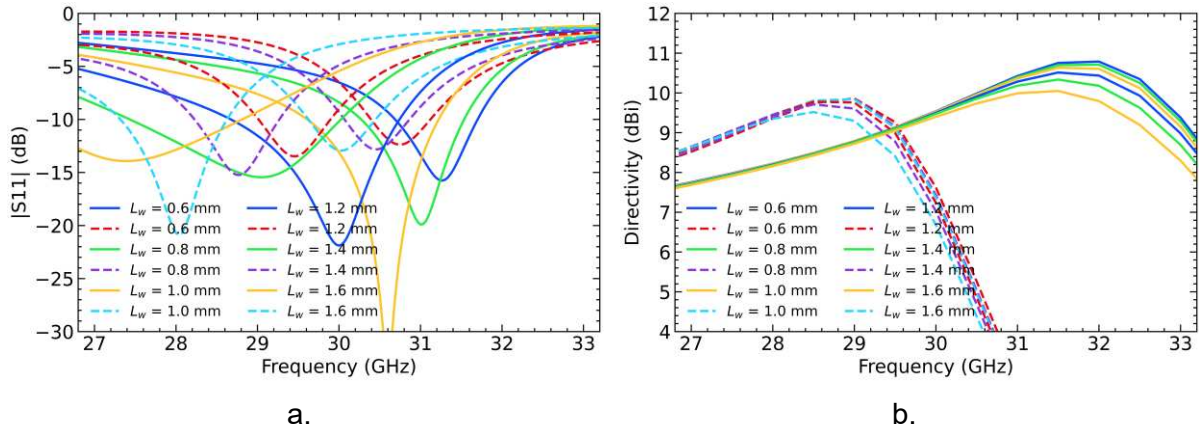


Figure 128. Performance linearly polarized configuration as the effective length of the slot is changed when all GeTe edges are in the crystalline state (dashed lines) and all the GeTe edges are in the amorphous state (solid lines). A) S-parameters b) Directivity.

### III.4. Fabrication and measurement

The structure shown in Figure 113 was fabricated at the clean room facilities in XLIM laboratory. The device needs to be fabricated as three separate circuits over two different wafers (substrates) and then bonded together with a thin glue layer. The three circuits to be fabricate are: 1) the array of antennas at the top of the superstrate, 2) the exciter antenna at the top of the substrate and 3) the ground plane with the input transmission line at the bottom of the substrate. Since the total size of the device is  $10 \times 10 \text{ mm}^2$ , multiple devices can be fabricated at once on a  $50 \times 50 \text{ mm}^2$  squared wafers, this is with the intention of increasing the success rate of fabrication procedure. In a substrate of this size, we can fabricate up to 16 devices at the time.

The array of antennas and the ground plane were fabricated by deposition of a 200-nm thin layer of GeTe using the DC magnetron sputtering of a 50:50 GeTe target, on  $50 \times 50 \text{ mm}^2$  wafers. The thickness of the GeTe layers was chosen after the conclusions obtained from II.5.1. The patterning of the structure was created using optical lithography followed by dry etching by means of a RIE process. The metallic structure of the devices was fabricated using the electron beam evaporation of Ti/Au layers with thicknesses of 40 nm and  $1.7 \text{ }\mu\text{m}$ , respectively. Then, the patterning was done by optical lithography with a lift-off technique. The exciter antenna does not possess any GeTe pattern within, therefore only the metallic pattern needs to be fabricated using the same steps and parameters as the other two devices.

After the three devices are fabricated, the superstrate and the substrate are bonded together with a glue layer, as previously mentioned. The glue used for this bonding is a thermally activated NOA 83H from Norland Products Incorporated [156] [35] which needs to be applied between the surfaces to be glued and then baked at  $80^\circ\text{C}$  for 3 hours in an oven in order to be cured and activated. This step needs to be performed very carefully in order to ensure that both substrates remain as aligned as possible with a layer that is as homogeneous as possible. Any deviation due to an unwanted misaligning or uneven bonding can result in the degradation of the performances of the device. Furthermore, the actual thickness of the glue layer can have an influence on the performance of the device as shown in Figure 129a alongside with the permittivity of the glue in these frequency ranges as shown in Figure 129b. From this simulation we can conclude that the parameters of the glue layer will have an influence on the resonance frequency as well as the matching level.

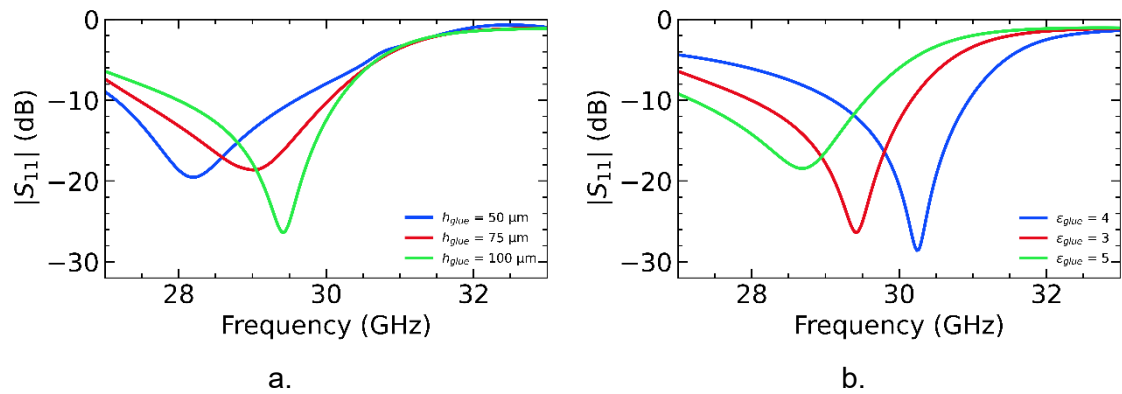
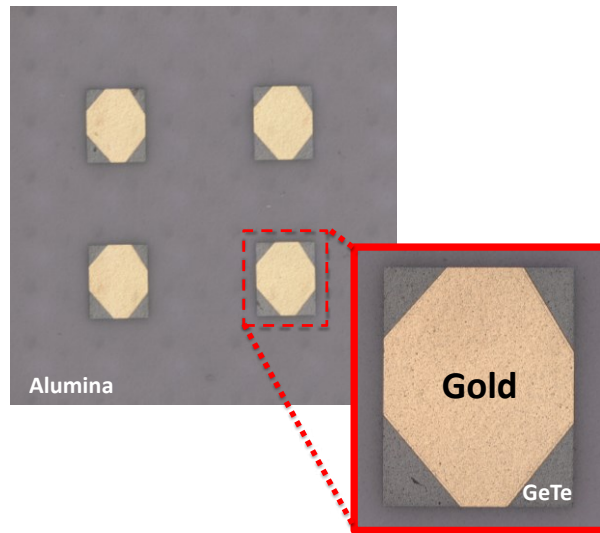


Figure 129. Simulated influence on the evolution of the matching properties of devices as a function of a) The thickness of the glue and, b) the permittivity of the glue layer.

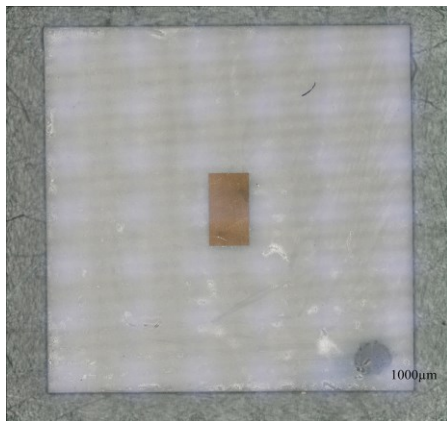
After the two wafers have been bonded, the individual arrays of antennas are cut by using a semi-automatic saw cutter. The complete structure after bonding is shown in Figure 130 where Figure 130a show an array of antennas on an alumina substrate and with the edges replaced with amorphous GeTe. Figure 130b shows the exciter antenna at the surface of the substrate and Figure 130c shows the ground plane with a slot filled with amorphous GeTe. In order to validate the design presented in this section, full metallic devices were also fabricated. This means that the amorphous GeTe layers are taken away while the crystallized GeTe parts are replaced with a metallic layer of the same thickness as the antennas as shown in Figure 131.

Additionally, a ground plane with a slot window of length of 1.1 mm was also fabricated in order to evaluate the performance of the antenna close to the 30 GHz zone as shown in Figure 132. These full metallic antennas will also serve as references to evaluate the losses induced by the GeTe regions.

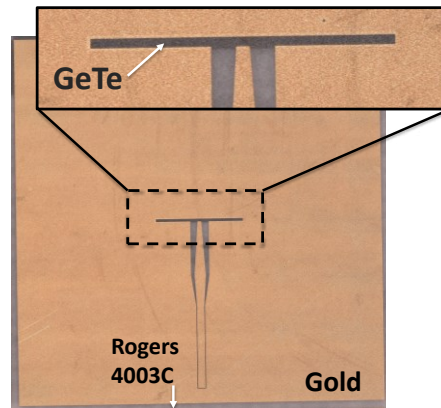
It should be noticed that the color of the metallic patterns in Figure 130a and Figure 130c is not the same although they are the same metal. This is because the high rugosity on the ROGERS 4003C causes the incident light to diffuse much more resulting in the metal to appear opaquer than the one over the alumina superstrate. As explained previously the rugosity of a material will induce very high losses at millimeter wave frequency bands. In order to mitigate the losses due to the roughness of the substrate, the Rogers substrate can be replaced by a quartz substrate who presents a much lower rugosity profile. Although, as mentioned in III.2.1, this substrate also presents a slightly higher permittivity and it is also very fragile with can results in the destruction of the circuit if not handled with precaution during the fabrication process.



a.

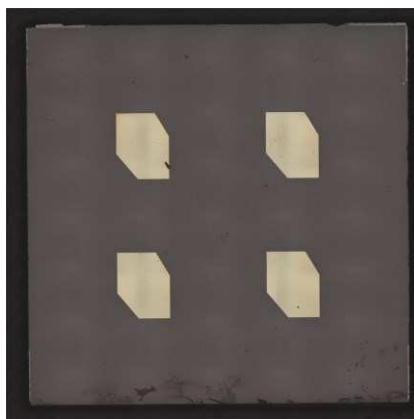


b.

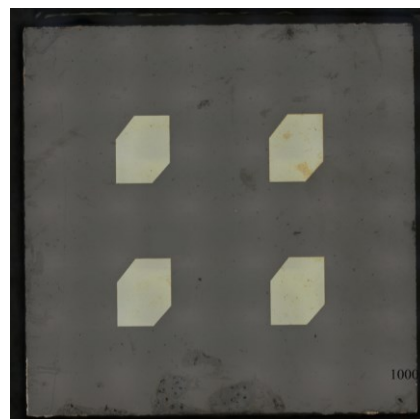


c.

Figure 130. Fabricated antenna. a) Array of antennas integrating amorphous GeTe at the top of the alumina substrate. b) Exciter antenna at the top of the ROGERS 4003C substrate (The dark dot at the bottom right is an ink marker for orientation purposes). c) Ground planes, input transmission line and slot window integrating amorphous GeTe.



a.



b.

Figure 131. Fabricated full metallic array of antennas. a) RHCP array. b) LHCP array.

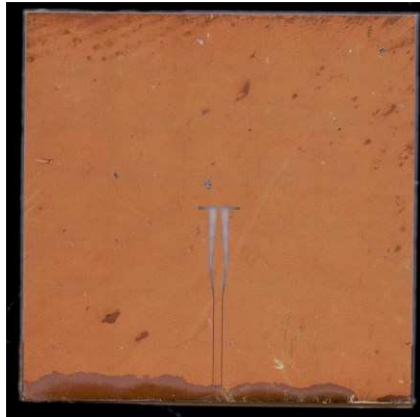


Figure 132. Fabricated ground plane over a ROGERS 4003C substrate with an empty slot of 1.1 mm length. The darker region at the bottom is part of the glue that overflow during the bonding process and could not be removed.

Therefore, a new batch of arrays of antennas were fabricated using the procedure as the previous batch except that the Rogers substrate has been replaced with a quartz substrate. Figure 133 shows the ground plane and exciter antenna of this new batch from which it can be observed that the metal in the ground plane is much brighter than the metal deposited over the Rogers substrate. It is worth nothing that in Figure 133a, the ground plane and the input transmission line are also visible which is due to the fact that the quartz is transparent at the visible wavelength regime. As mentioned previously, the permittivity of this substrate is slightly higher than the Rogers substrate, however the thickness of the substrate is also lower (thickness of 250  $\mu\text{m}$ ) which can compensate for the rise in permittivity in terms of the antenna performances.

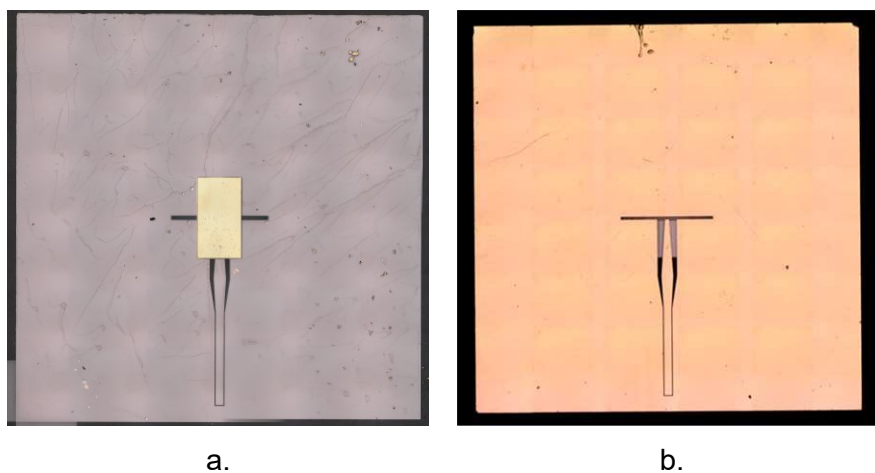


Figure 133. Fabricated antenna using a quartz substrate. a) Exciter antenna at the top of the substrate. b) Ground plane, input transmission line and slot window integrating amorphous GeTe.

#### III.4.1. Measure of S parameters

The S-parameters of the fabricated devices were measured using a 200- $\mu\text{m}$  pitch GSG probe and a vector network analyzer (ZVA Rohde Schwarz). The set-up used to measure the antenna is shown in Figure 134. The antennas are placed and measured over a Rohacell foam support in order to avoid perturbing the radiation characteristics of the antenna. This is thanks to the very low permittivity of the Rohacell foam (around 1.06) [157].

The permittivity of the glue layer as well as its thickness were obtained by retrosimulation of all measured antenna. The values obtained were around 2.0 and 50  $\mu\text{m}$  for the permittivity and the thickness, respectively.

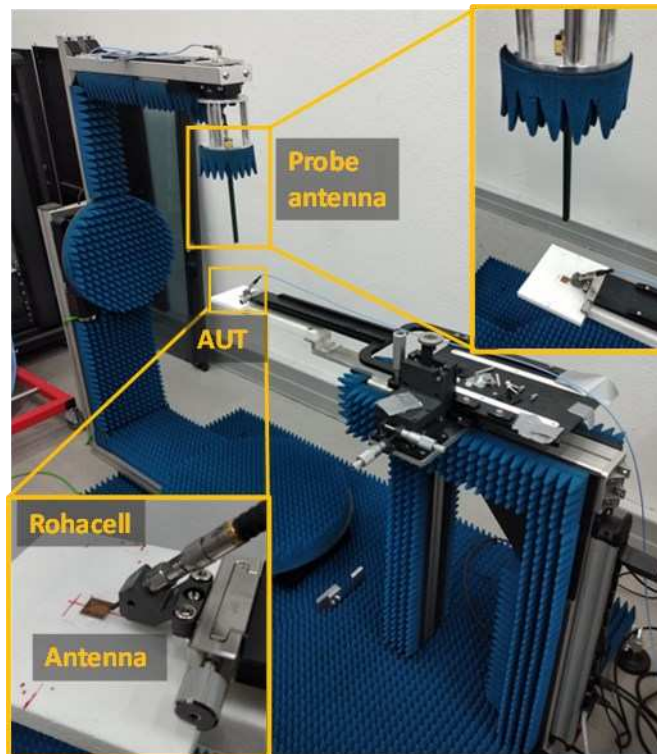


Figure 134. Image of the compact test range system used to measure the RF performance (matching and radiation) of the antenna under test (AUT).

#### III.4.1.1. Measures of S parameters on Rogers substrate

The  $S_{11}$  parameters of all the antennas were measured in the 20 – 40 GHz band. Figure 135a shows the measured performance of an array of antenna integrating GeTe on a ground plane with a slot window of  $L_w = 2.4$  mm fill with amorphous GeTe. The blue curve shows the expected results from simulation and the red trace shows the measured results together with the 10-dB bandwidth (red box). The difference in S parameters will be explained in the next section. The measured antenna shows a resonance frequency at 23.3 GHz. The matching performance are good as the  $|S_{11}|$  can arrive to values close to -30 dB in adaptation with a 10-dB bandwidth of 1.3 GHz (around 5% of fractional bandwidth).

Figure 135b shows the S parameters measured from the same array of antennas but with a slot window of  $L_w = 1.1$  mm. The matching level is around -18 dB at the resonance frequency with a bandwidth of 1.7 GHz (around 5.6% fractional bandwidth). From Figure 135 we can conclude that the frequency reconfiguration is achievable by tuning the length of the slot window will retaining good matching performances.

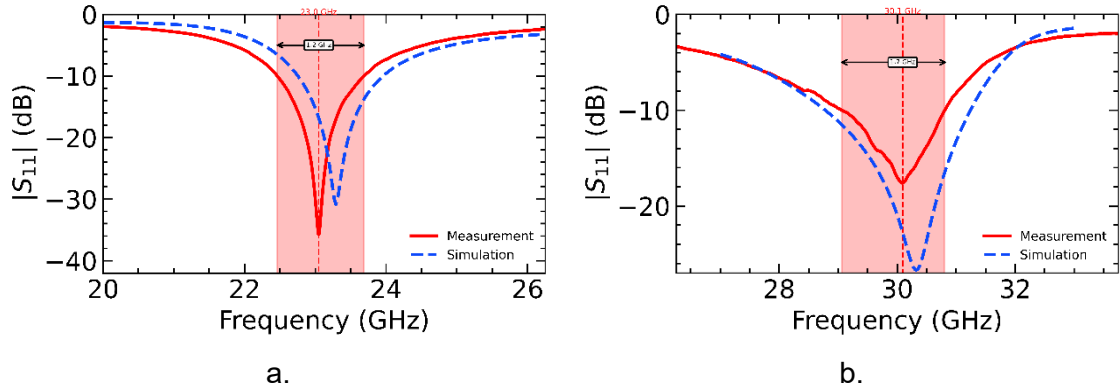


Figure 135. Measured matching performance of an array of antennas with a ROGERS 4003C substrate and a ground plane with a slot window of a) 2.4 mm length and, b) 1.1 mm length.

Figure 136a shows the measured performance of the full metal RHCP array of antennas for two different slot window lengths ( $L_w = 2.4$  mm and  $L_w = 1.1$  mm). The resonance frequency of this antenna is around 23.0 GHz which is very close to the previously measured antenna. A shift down in resonance frequency of the measurement with respect to the simulated performance is also observed. From Figure 136b we can also observe a disagreement between simulation and measurement, this time for a slot window of  $L_w = 1.1$  mm where a resonance frequency of 29.4 GHz is observed. This resonance frequency is also very close to the previously measured case with a slot window of  $L_w = 1.1$  mm.

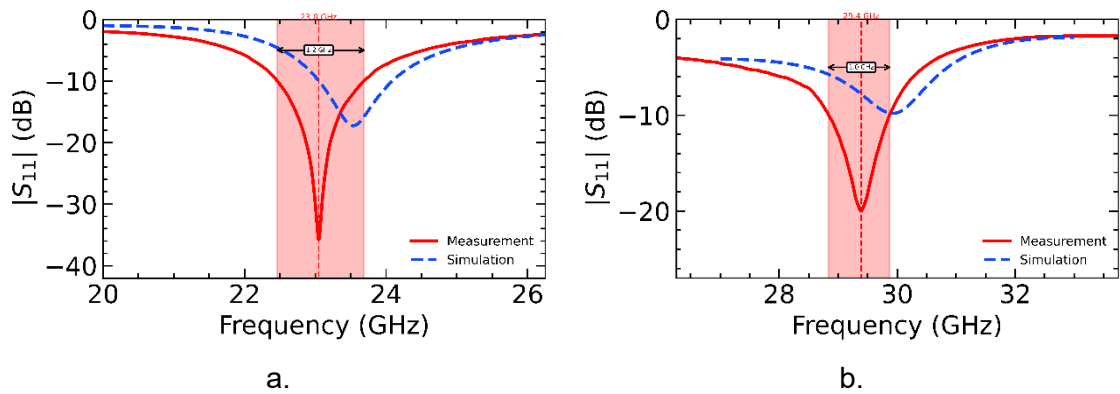


Figure 136. Measured and simulated matching performance of full-metallic RHCP array of antennas with a ROGERS 4003C substrate and a ground plane with a slot window of a) 2.4 mm length and, b) 1.1 mm length.

Figure 137 shows a comparison between the matching performances of a RHCP, LHCP and LP (when all edges are in amorphous state) array of antennas, all with the slot window length of  $L_w = 1.1$  mm. From this figure, it can be seen that the three states are very close in resonance frequency, although the CP antennas are shifted down in frequency. The overlapping 10 dB range goes from 29.3 GHz to 30 GHz. Since the LHCP antenna with a slot window length of 2.4 mm is not available, the comparison cannot be made thus is not shown.

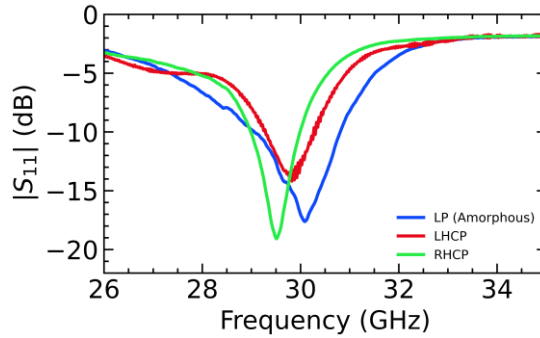


Figure 137. Comparison of the measured matching performance of the three states of polarization with a ROGERS 4003C substrate.

### III.4.1.2. Measures of S parameters on quartz substrate

As in the previous case, the S parameters of all the antennas fabricated on a quartz substrate were also measured in the 20 – 40 GHz band. Figure 138a show the measured performance of an array of antenna integrating GeTe on a ground plane with a slot window of  $L_w = 2.4$  mm filled with amorphous GeTe. The measured performance shows a resonance frequency at around 22.8 GHz, very close to the resonance frequency measured on the Rogers substrate (around 23.0 GHz) As in the case of the antennas over a Rogers substrate, the measured performances of the antennas also shown a shift down in resonance frequency. However, this time the matching performance are not as good as in the Rogers case as the matching level of the array of antennas has barely arrived to -11 dB at the resonance frequency.

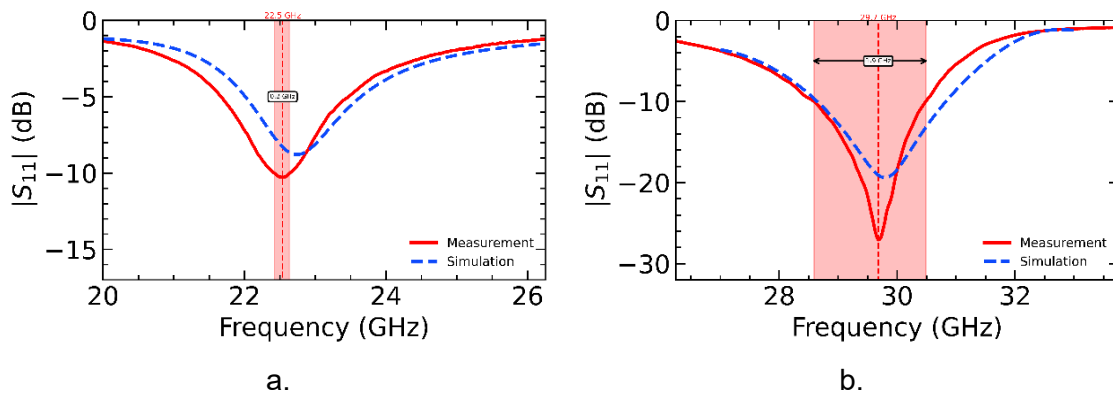


Figure 138. Measured and simulated matching performance of an array of antennas fabricated with a quartz substrate and a ground plane with a slot window of a) 2.4 mm length and, b) 1.1 mm length.

Figure 138b shows the S parameters measured from the same array of antennas but with a slot window of  $L_w = 1.1$  mm. The matching level is around -18 dB at the resonance frequency with a bandwidth of 1.7 GHz (around 5.6% fractional bandwidth). From Figure 138 we can conclude that the frequency reconfiguration is achievable by tuning the length of the slot window will retaining its matching performances.

Figure 139 shows the measured performance of full metal RHCP array of antennas fabricated on a quartz substrate for two different slot window lengths (and  $L_w = 2.4$  mm and  $L_w = 1.1$  mm). From Figure 139a we can see a measured resonance frequency of 22.4 GHz. But this time the matching performances are not as good as expected as the adaptation level has barely arrived to -10 dB at the resonance. From Figure 139b we can observe a resonance frequency of 29.4

GHz and also observe that the adaptation level at resonance is at -8 dB which is lower than the same antenna over a Rogers substrate.

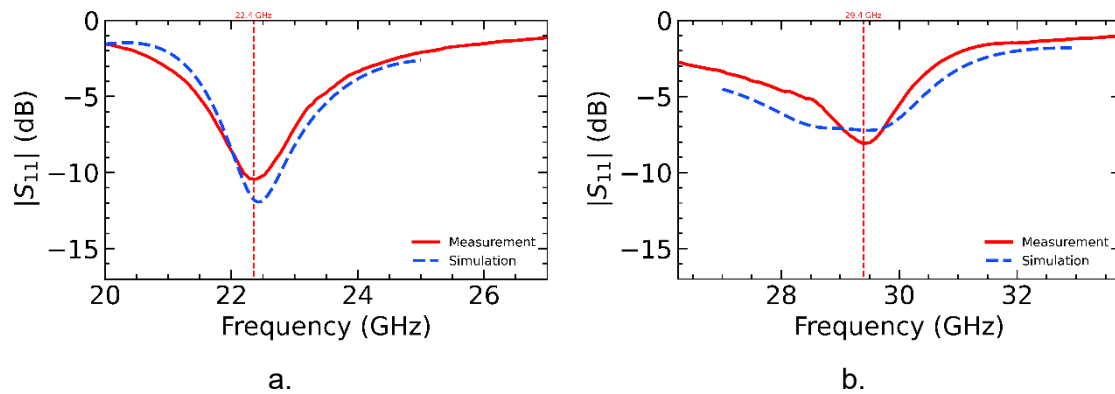


Figure 139. Measured matching performance of a full-metallic RHCP array of antennas with a quartz substrate and a ground plane with a slot window of a) 2.4 mm length and, b) 1.1 mm length.

Finally, Figure 140 shows a comparison between the matching performances of a RHCP, LHCP and LP array of antennas, all with the slot window length of  $L_w = 2.4$  mm for the quartz substrate. From this figure, it can be seen that the three states are very close in resonance frequency but the matching level is not enough as it barely arrives to -10 dB. Similar to the Rogers4003C, the LHCP antenna with a slot window length of 1.1 mm is not available thus the comparison is not shown.

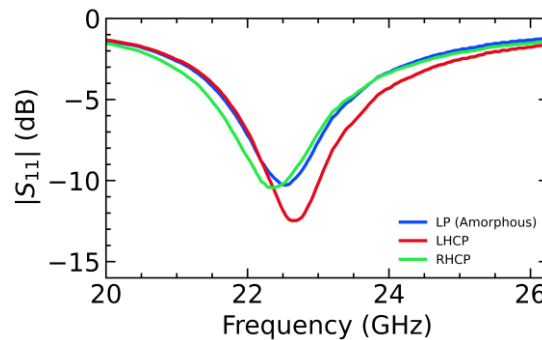


Figure 140. Comparison of the measured matching performance of the three states of polarization with a quartz substrate with a ground plane with a slot window of  $L_w = 2.4$  mm.

### III.4.1.3. Summary and comparison of the measured S parameters on both substrates

Figure 141 shows a comparison of the same antenna over the two different substrates with a slot window of length  $L_w = 1.1$  mm. Figure 141a shows the comparison of the measured S-parameters where we can observe that both devices present very similar resonance frequencies with very similar profiles except that the matching characteristics are not the same. This effect is more pronounced in Figure 141b where we can observe a comparison of the measured S-parameters of the full metallic RHCP antennas over the two different substrates. The two arrays of antennas present the same resonance frequency but the matching level differs by 12 dB.

The difference between the matching performance may be explained by the difference in rugosity of both ground planes. Indeed, in [158] it has been observed that the presence of a rough surface decreases the effective conductivity of the metal which can in turn affect the

matching of the line as shown in Figure 142. From this figure it can also be seen that the decrease in conductivity also decreases the resonance frequency which can explain the difference in simulation and measurement in Figure 135 and Figure 136.

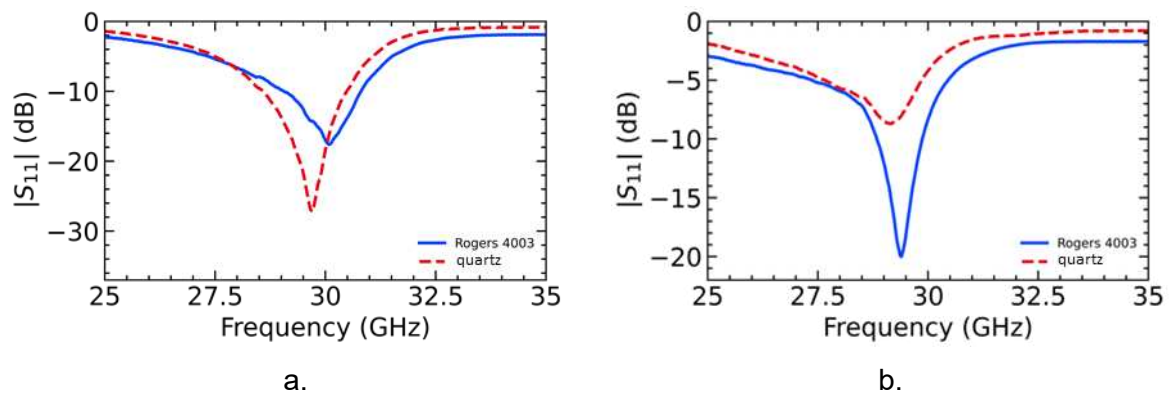


Figure 141. Comparison of the measured matching performance with a ROGERS 4003C and quartz substrates for the a) linearly polarized antenna (all edges amorphous) and, b) Full-metal RHCP array.

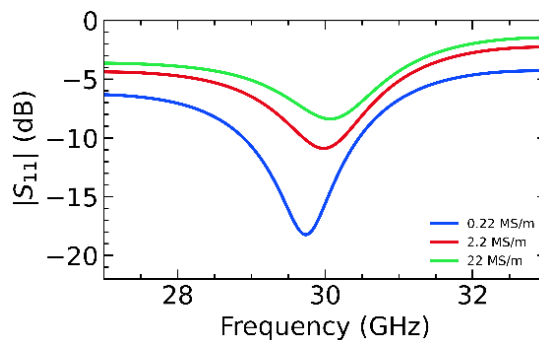


Figure 142. Simulated influence of the metal conductivity in the S-parameters of the RHCP antenna.

Since the full-metal reference antennas in circular polarization with a quartz substrate are not well matched at the resonance frequency. We will proceed to only measure the far-field of the antennas fabricated in ROGERS 4003C.

### III.4.2. Far-Field measurements of the reference antennas

The radiation characteristics were measured in the frequency band from 28 GHz to 32 GHz every 400 MHz. The antenna is placed at a distance such that we only measured the far-field radiation plane implying that the radial component of the field  $E_r \approx 0$ . The electric field in both directions ( $E_\theta$  and  $E_\phi$ ) was recorded using a horn antenna every  $5^\circ$  in both theta and phi planes at a constant radius.

Figure 143 shows the broadband performances of the three full-metal measured antennas with their respective adaptation levels. The individual 3-dB bandwidth of each circular polarized antenna goes as large as 2 GHz with directivities greater than 8.5 dB in the axis. Although both CP configurations presents excellent performance in terms of axial ratio we can observe that the frequency performance of both cases are not aligned. This can be explained by a difference in the size of the glue layer as the thickness of this layer can influence the overall effective permittivity of the antenna thus shifting the frequency behavior. The magenta box shows the region where the 3-dB axial ratio bandwidth of both CP configurations overlaps. The yellow bow shows the region where all the configurations are adapted with values less than -10 dB

(the overlapping region is 500 MHz) which is very close to 30 GHz, although in an ideal case, the matched frequency can be moved by tuning the length of the slot filled with GeTe.

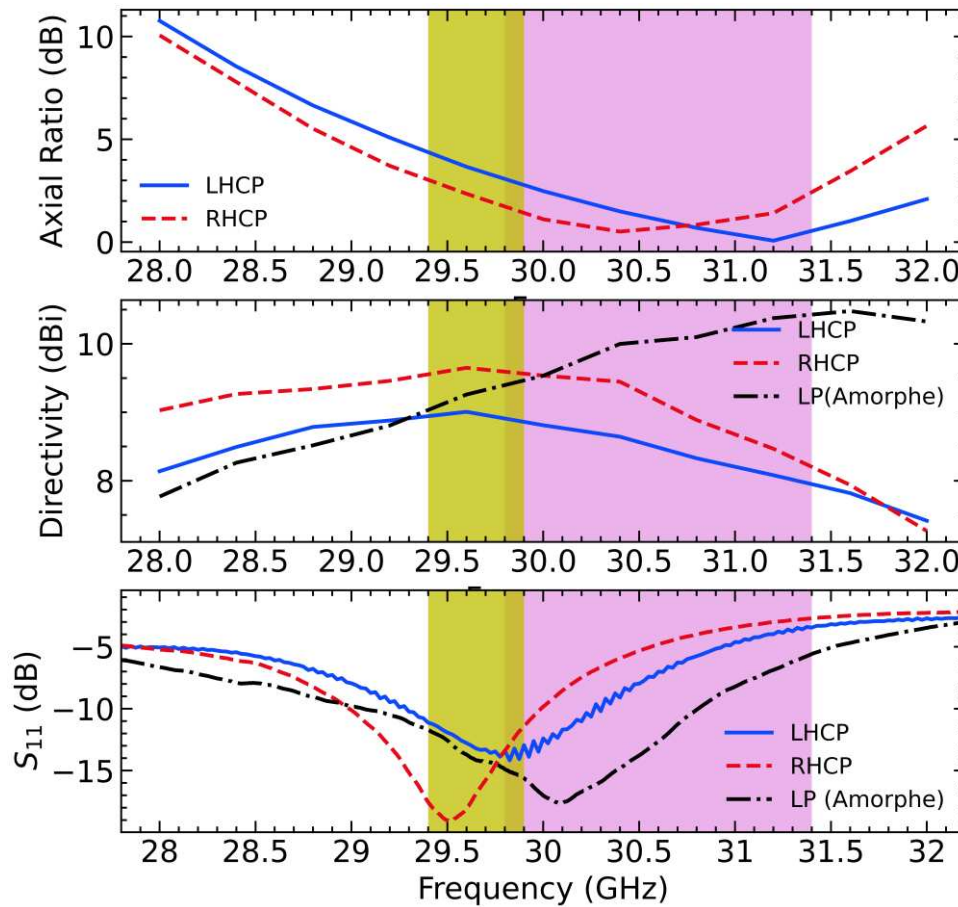


Figure 143. Measured maximal directivity, axial ratio and matching level of a full-metal RHCP and LHCP configuration and LP (with all edges in amorphous state) with a ROGERS 4003C substrate.

Figure 144 shows the realized gain and efficiency of the measured array of antennas. From this figure it can be seen that, at 30 GHz, the maximum efficiency of the LP case can be as high as 70% while is around 55% for the LHCP case and 45% for the RHCP case. It can be observed that the LP case is more efficient than the CP cases which is expected since the asymmetric trimmed edges in the CP antennas reduces the overall quality factor of the antenna implying a lower radiation efficiency than the LP case [136] [138].

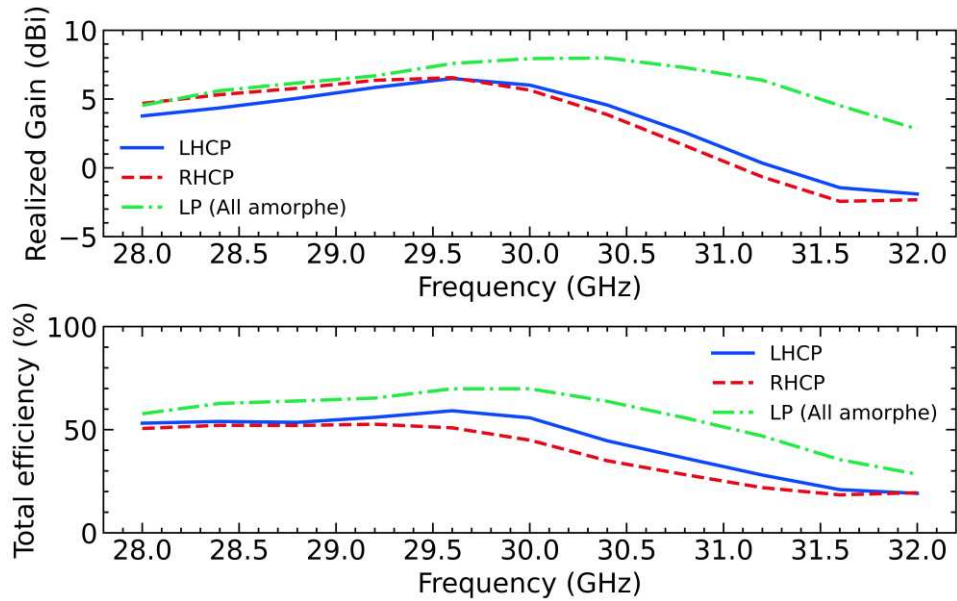


Figure 144. Measured realized gain and total efficiency of the full-metallic reference antennas.

Figure 145 shows the calculated directivity for a LP antenna integrating a GeTe composition on a ROGERS 4003C substrate at its resonance frequency of 29.6 GHz. Figure 145a shows the full picture of the measured directivity of the array while the Figure 145b shows the directivity at phi planes 0°, 45°, 90° and 135°. From this measure we can observe that the antenna radiates mostly in the boresight direction and that the maximum directivity is 9.4 dBi at 29.6 GHz.

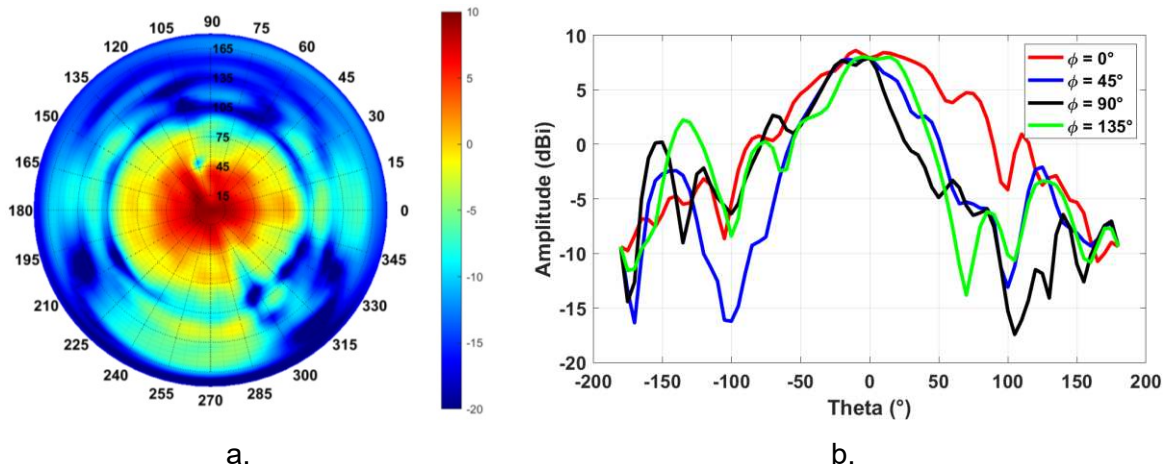


Figure 145. Measured directivity of the LP (all GeTe edges in amorphous state) array of antenna at 29.6 GHz. a) Full picture. b) Directivity at planes  $\phi = 0, 45, 90$  and  $135^\circ$ .

Figure 146 shows the measured directivity of the LHCP case of a full metallic antenna with a ROGERS 4003C substrate. As for the previous case, we can observe that this configuration mostly points in the axis of the antenna with a maximum directivity of 9.1 dBi at 29.6 GHz. We can also observe the appearing of what looks like a side lobe appearing at the  $\theta = 75^\circ$  in the  $\phi$  planes between  $225^\circ$  to  $30^\circ$ . Additionally, the radiation at the back ( $\theta = 180^\circ$ , at the axis of the slot window) is significantly higher than the LP case.

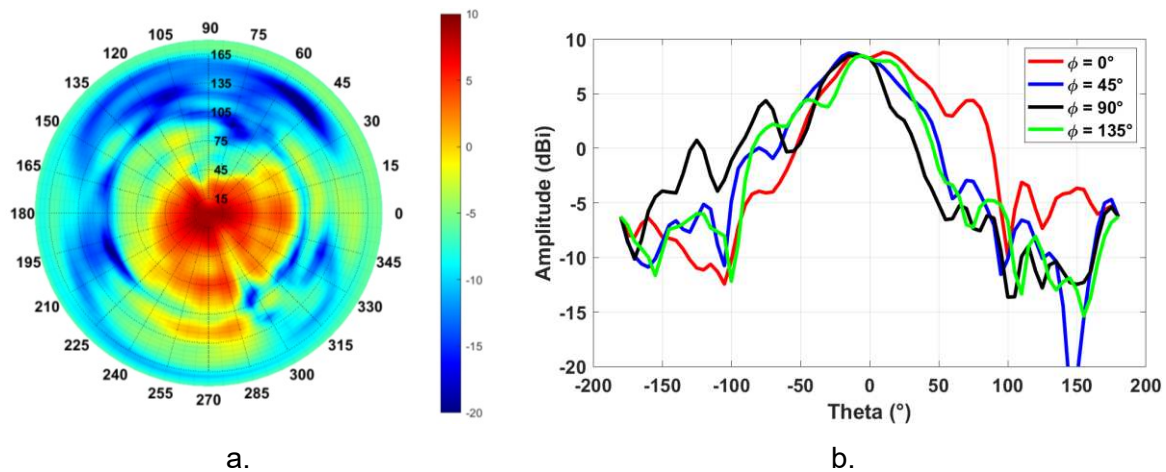


Figure 146. Measured directivity of a full-metal LHCP array of antennas at 29.6 GHz. a) Full picture. b) Directivity at planes  $\phi = 0, 45, 90$  and  $135^\circ$ .

Figure 147 shows the measured directivity of the RHCP case of a full metallic antenna with a ROGERS 4003C substrate. For this configuration, we can also observe that it mostly points in the axis of the antenna with a maximum directivity of 9.4 dBi at 29.6 GHz. We can also observe the appearing of a side lobe appearing at the  $\theta = 75^\circ$  in the  $\phi$  planes between  $240^\circ$  and  $285^\circ$ , although much smaller than LHCP case. Similar to the LHCP configuration, the radiation at the back is also significantly higher than the LP case.

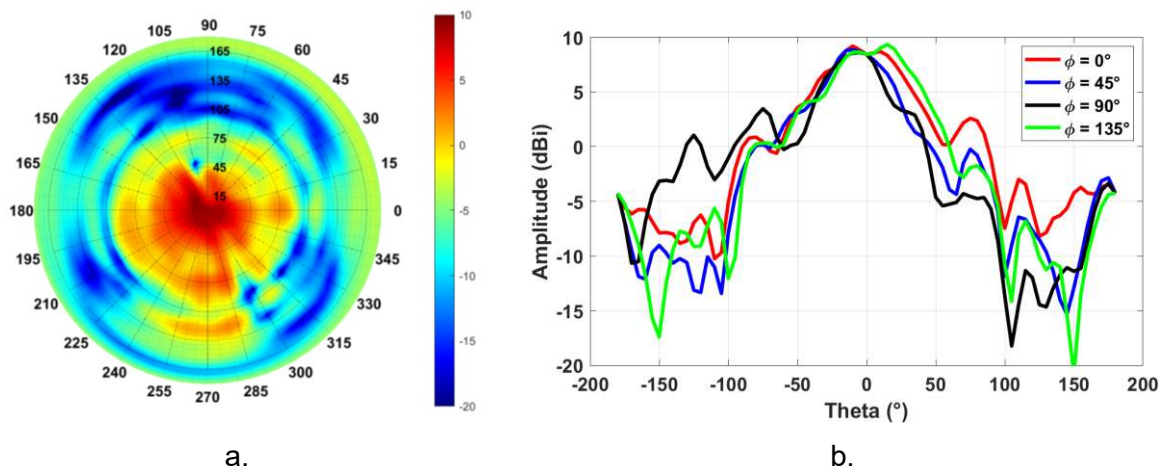


Figure 147. Measured directivity of a full-metal RHCP array of antennas at 29.6 GHz. a) Full picture. b) Directivity at planes  $\phi = 0, 45, 90$  and  $135^\circ$ .

Figure 148 shows the axial ratio at the frequency of 30 GHz where we can observe an axial ratio smaller than 3dB is achieved for all angles  $\theta < 30^\circ$  for all  $\phi$ -planes (lower limit) for the RHCP case.

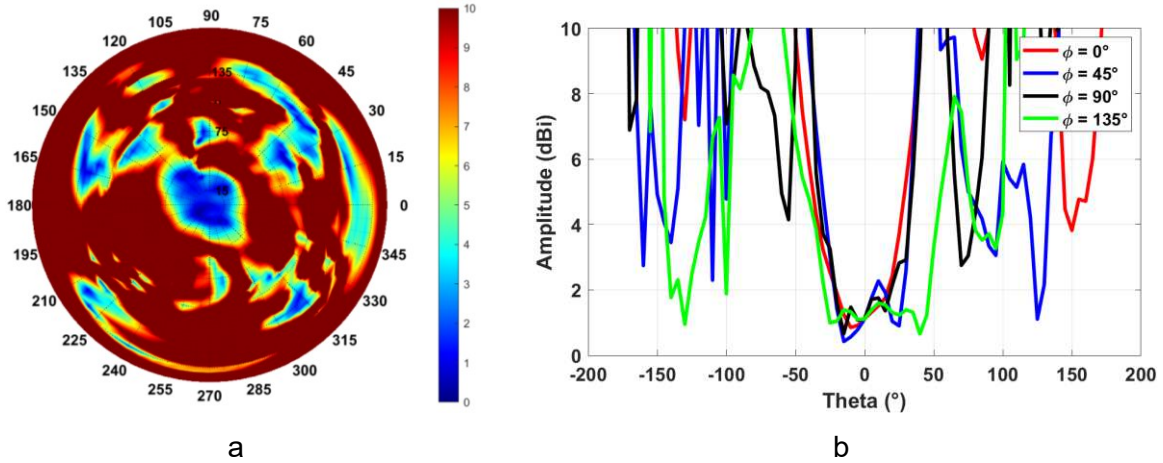


Figure 148. Measured axial ratio of a full-metal RHCP array of antennas at 30 GHz. a) Full picture. b) At planes  $\phi = 0, 45, 90$  and  $135^\circ$ .

Figure 149 shows the axial ratio at the frequency of 30.4 GHz (where the axial ratio is the smallest). From this figure we can observe that an axial ratio smaller than 3 dB is achieved for all angles  $\theta < 20^\circ$  (lower limit) for all  $\phi$ -planes which is a smaller angular aperture than the case of 30 GHz.

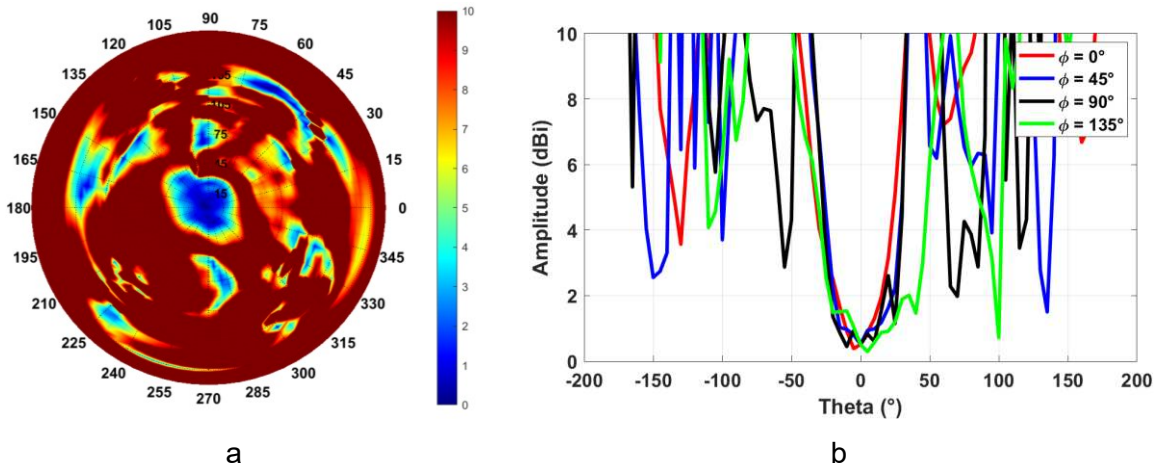


Figure 149. Measured axial ratio of a full-metal RHCP array of antennas at 30.4 GHz. a) Full picture. b) At planes  $\phi = 0, 45, 90$  and  $135^\circ$ .

At the matched frequency for the RHCP case, Figure 150 shows the axial ratio. From this figure we can observe that an axial ratio smaller than 3dB is achieved for all angles  $\theta$  between  $-40$  and  $25^\circ$  for all  $\phi$ -planes which represents a significantly bigger angular aperture than the case where the axial ratio is minimum at the axis.

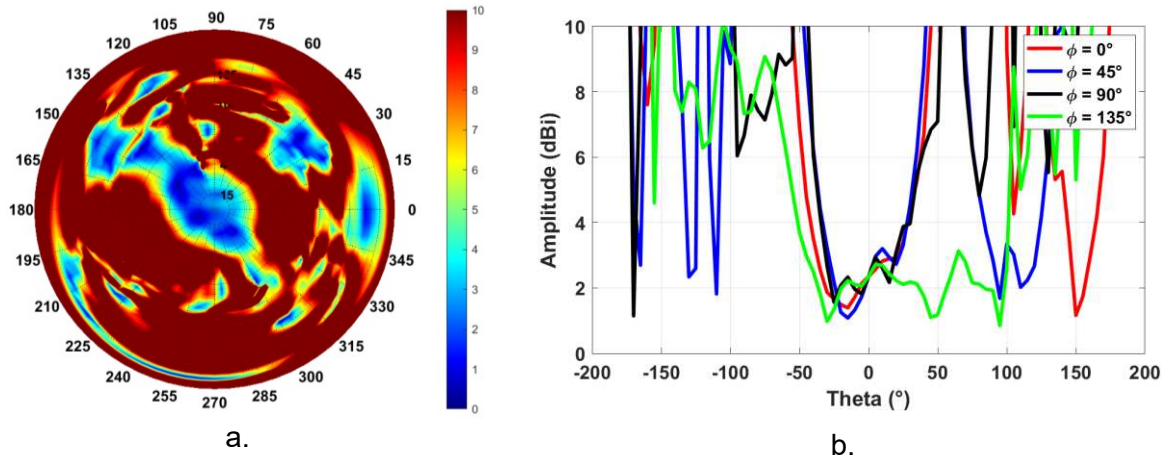


Figure 150. Measured axial ratio of a full-metal RHCP array of antennas at 29.6 GHz. a) Full picture. b) At planes  $\phi = 0, 45, 90$  and  $135^\circ$ .

Figure 151 shows the axial ratio of the LHCP configuration at the frequency of 30 GHz where we can observe that an axial ratio smaller than 3 dB is achieved for all angles  $\theta$  between  $-35^\circ$  and  $15^\circ$  for all  $\phi$ -planes.

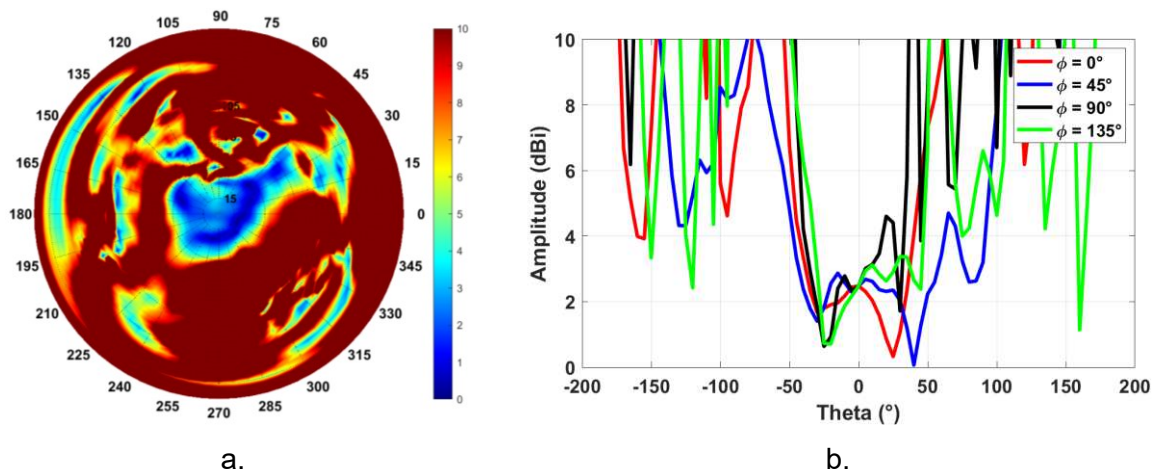


Figure 151. Measured axial ratio of a full-metal LHCP array of antennas at  $f = 30$  GHz. a) Full picture. b) At planes  $\phi = 0, 45, 90$  and  $135^\circ$ .

Figure 152 shows the axial ratio at the frequency of 31.2 GHz where the axial ratio is the smallest. From this figure we can observe that an axial ratio smaller than 3 dB is achieved for all angles  $\theta < 15^\circ$  for all  $\phi$ -planes which, similar to the RHCP configuration, this is a smaller angular aperture than the case of 30 GHz.

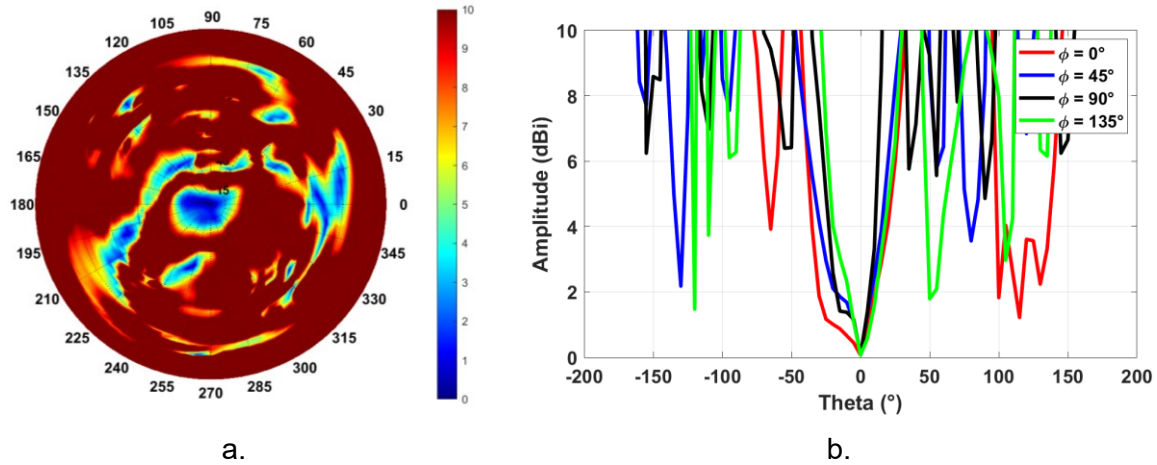


Figure 152. Measured axial ratio of a full-metal LHCP array of antennas at 30.4 GHz. a) Full picture. b) At planes  $\phi = 0, 45, 90$  and  $135^\circ$ .

Figure 153 shows the axial ratio close to the matched resonant frequency (at 29.6 GHz). From this figure we can observe a wider 3 dB axial ratio aperture, unfortunately the axial ratio at the axis is around 3.8 dB which do not comply with objectives demanded for this design.

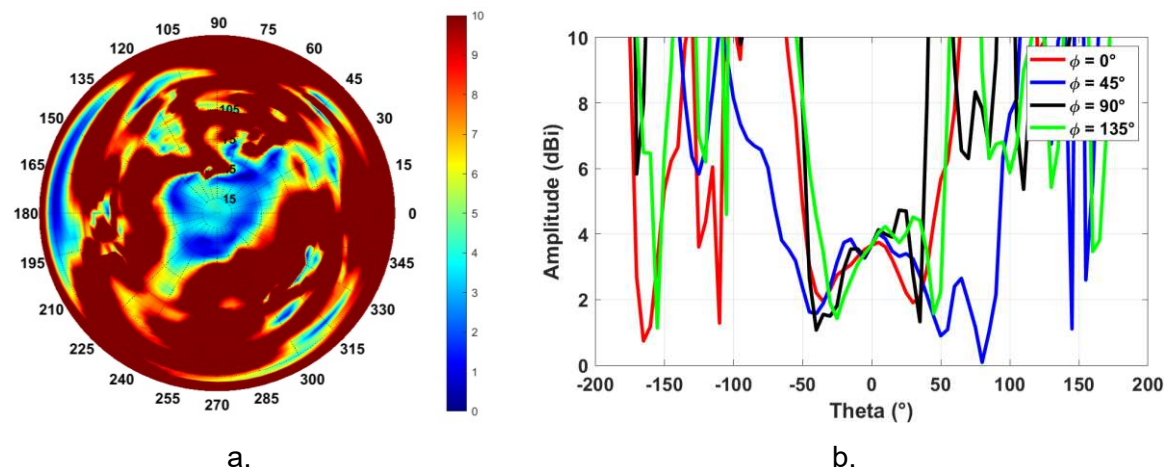


Figure 153. Measured axial ratio of a full-metal LHCP array of antennas at 29.6 GHz. a) Full picture. b) At planes  $\phi = 0, 45, 90$  and  $135^\circ$ .

Based on the far-field results as well as the measured matching performance, we can conclude that the proposed designed array of antennas has acceptable performances in both states of CP as well as the linear case with directivities greater than 8.5 dBi at 29.6 GHz, a wide broadband axial ratio and matching better than -10 dB at the frequency where all configuration presents acceptable performances. Although the arrays of antennas are not matched at the frequency where the axial ratio is minimal, we can observe that these points where the AR is minimal also presents a much narrower angular aperture, indeed the higher the AR at the axis direction, the bigger the angular aperture of the antenna. Since the antennas were optimized with the idea of possessing the biggest angular aperture, the fact that the matched resonant frequency is not aligned with the minimal value of AR can be justified and accepted. Therefore, we have demonstrated that the design array of antennas is able to work in three different states of polarization with acceptable performances, thus validating the design. In the next section,

we will present the performances of the array of antennas integrating GeTe for the polarization reconfigurability.

### III.4.3. Reconfiguration of the antenna polarization states

The GeTe edges of the antenna were transformed into their crystalline state using the laser irradiation setup used in II.5.3 with the corresponding found parameters. First, two opposite corners were irradiated using ten impulsions to transform the LP antenna into a RHCP antenna and the surface resistance was measured using a two-probe measuring system. Figure 154 shows the optical images of the resulting irradiation on the antennas.



Figure 154. Optical image of the irradiated GeTe edge of the array of antennas. The black features are the out-of-focus probes.

From Figure 154 is observed that the GeTe shows a distinctive change in appearance compared to the as-deposited (amorphous) state. However, the surface resistance measurement does not show a significant improvement of the resulting state after irradiation meaning that the GeTe was not crystallized. The same behavior was observed for the GeTe in the slot window of the substrate.

This failure in the crystallization can be explained by three possibilities:

1. The GeTe has oxidized due to a prolonged exposure to the environment causing a change in the chemical and structural properties of the GeTe.
2. A misadjust of the parameters during the magnetron sputtering deposition caused a change in the stoichiometric composition of the GeTe thus a change in the properties of the material.
3. The GeTe suffered a chemical and structural change during the photolithography process (due to the use of reactive ion etching) which may have result in an unwanted doping of the material.

An irradiation test on an alumina substrate with a GeTe layer deposited at the same time as the antenna GeTe layer resulted in a good quality crystallization alike to the results shown in II.5.4. This result makes us reject the first and second possibility as an explanation for the failed crystallization. The possibility number three can be confirmed or rejected by a Raman spectroscopy analysis. However, due to time constraints, this experiment was not performed.

In order to avoid using reactive ion etching, a new array of antennas was fabricated using a lift-off technique for the GeTe patterning, an example of the resulting array of antennas is shown in Figure 155a. Unfortunately, the lift-off step on the GeTe pattern resulted in a damage in the outer edges of the GeTe resulting in a smaller feature which can perturb the radiation pattern. Following the deposition, the edges of the GeTe were crystallized by laser irradiation, the results of the irradiation are shown in Figure 155b. A two-probes surface resistance measurement shows a change in resistance of around 4 orders of magnitude which confirms a successful transformation of the GeTe to a crystalline state.

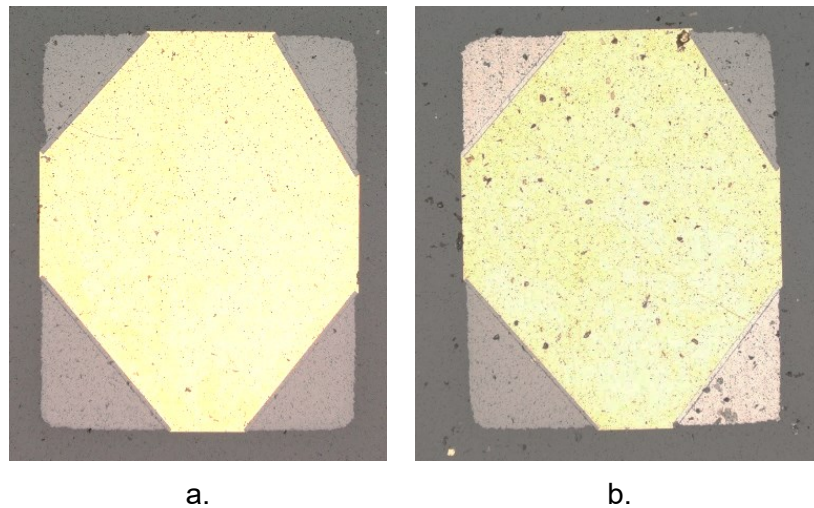


Figure 155. Examples of the new fabricated array of antennas using a lift-off technique. a) As-deposited (amorphous) state. b) After laser irradiation (RHCP state).

Figure 156 shows the broadband far-field measurement of the RHCP configuration. From Figure 156a it can be seen that the axial ratio has decreased significantly to not be considered as linear polarization although not to the level expected from the full metal antenna references while Figure 156b shows a maximal directivity of 9.7 dBi at 30.5 GHz which is very close to the expected performance from simulation shown in Figure 119.

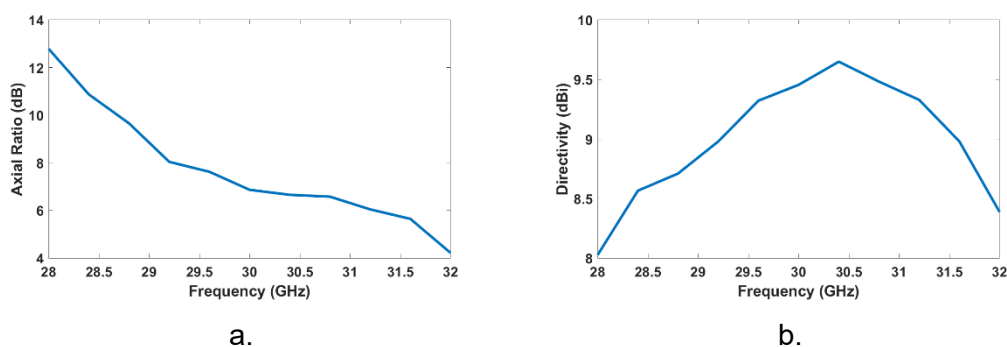


Figure 156. Measured far-field performances of the array of antennas after optical irradiation (as shown in Figure 155). a) Axial ratio in the axis and, b) Maximal directivity.

The degradation of the axial ratio can be mostly explained by the perturbation in the GeTe edges as shown in the results simulation shown in Figure 157. The simulation assumed that all GeTe pattern are perturbed equally in all directions by a factor  $\Delta$  as shown in Figure 157a. Figure 157b shows that deviations as little as 10  $\mu\text{m}$  from a perfect alignment ( $\Delta = 0 \mu\text{m}$ ) can cause significant changes in the axial ratio. Although the simulation shows similar trending as

the measured axial ratio, the difference between simulation and measurement can be attributed to the fact that, in reality, not all GeTe edges are perturbed equally in all directions.

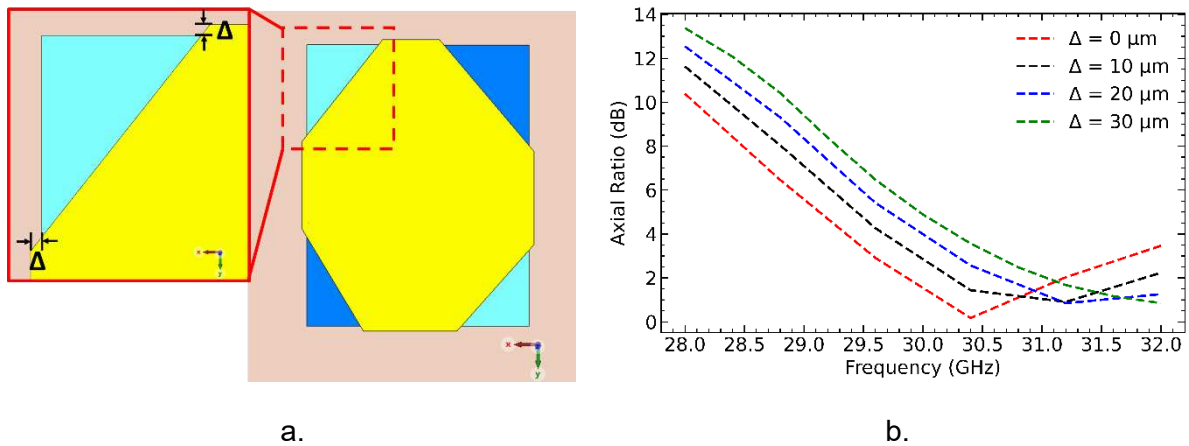


Figure 157. Simulation of the perturbation effect on the axial ratio of a RHCP antenna from a misalignment of the GeTe pattern. a) Geometry of the perturbation. b) Simulated axial ratio.

Then, the leftover amorphous GeTe were irradiated and transformed into their crystalline state in order to re-transform the antenna back to a LP state. Figure 158 shows the broadband far-field measurement of the current LP configuration. From Figure 158a it can be seen that the axial ratio has increased significantly compared to the previous case indicating a sufficiently good LP quality. Figure 158b shows a maximum directivity of 9.6 dBi at 30 GHz which is very closed to maximum directivity of the previous state. The sudden increase in directivity after 31 GHz is caused by the apparition of a secondary lobe.

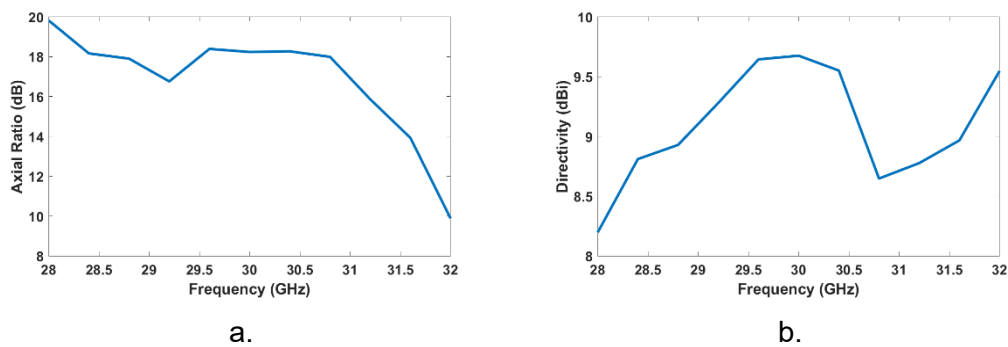


Figure 158. Measured far-field performances of the array of antenna shown in Figure 155 after crystallizing the remaining amorphous GeTe patterns. a) Axial ratio in the axis and, b) Maximal directivity

Since, according to simulation, the RHCP and LHCP states are identical in their broadband far-field characteristics, the LHCP state was not measured and their performances are assumed to be very similar (if not equal) the RHCP state.

### III.5. Conclusions

This chapter focus on the design, fabrication, measurement and optical activation of a reconfigurable array of antennas. The main objective is to design a multi-reconfigurable (in frequency and polarization state) antenna working at 30 GHz. The reconfiguration is done by integrating a GeTe composition and activate it using a laser pulse.

First, a suitable geometry was proposed such that the array of antennas is reconfigurable in polarization state and operational frequency. The antenna is composed of two wafers bonded together with a thin layer of glue. The superstrate contains the array of antennas while the substrate possesses an exciter patch to excite the array of antennas as well as the coupling slot. The polarization reconfiguration is created by replacing the edges of the patch antennas with a GeTe composition such that the polarization state depends on the state of the GeTe (amorphous or crystalline). The frequency reconfiguration is created by filling with a GeTe composition the coupling slot window in the ground plane. Then, by choosing the amount of crystalline GeTe, the length of the coupling slot can be changed and therefore the resonance frequency is changed.

The choice of the materials for the superstrate and substrate is very important since these materials need to be suitable for the integration of the GeTe while being performant in the millimeter-wave band frequencies for antenna applications. For the superstrate, an alumina substrate was chosen due to its high thermal conductivity and isotropic nature, however this material possesses a very high permittivity value that can complexify the design of the antenna. For the substrate, a ROGERS 4003C was chosen due to its low permittivity and low losses. Although this material possesses a very low thermal conductivity, the surrounding gold layer can also act as a high thermal conductor which can help to rapidly cool the GeTe.

The use of very distinct materials as superstrate and substrate together with the fact that the antenna must present acceptable performances in all states of polarization result in a very complex problem with a substantial number of free variables. Therefore, numerical optimization combined with 3D electromagnetic simulations were used to find a suitable configuration that minimizes the axial ratio with the widest angular aperture and with a maximum gain for all states. A review on current optimization methods was presented and compared in order to choose the most suitable one. Finally, due to the vast number of free variables and the non-linear nature of the objective functions, a genetic algorithm was chosen. The numerical optimization was implemented in MATLAB and evaluated for over 24 generations with more than 24000 simulations. The best solutions were obtained from the Pareto front of the problem in order to solve unavoidable trade-offs between the objectives. The simulation results of the final geometry present a wide axial ratio with symmetric performances in the RHCP and LHCP states and good performances in the LP state.

To validate the design, full metallic prototypes were fabricated in the clean room facilities of XLIM laboratory. The S-parameters measurements show that frequency reconfiguration is possible by changing the length of slot window. However, the matching level is sensitive to the parameters of the glue layer as well as the roughness of the substrate (due to the change of effective conductivity of the rough metal).

The far-field measurements of the metallic references show that the polarization reconfiguration is possible with a wide axial ratio in both circular polarized states and high directivity in the LP state with efficiencies greater than 50% in all states. This validates the design and proves the effectiveness of genetic algorithms as a tool for antenna design. However, important differences are observed between the performances of LHCP and RHCP states which can be attributed to a difference in the thickness of the glue layer.

The initial test on optical reconfiguration of the antenna failed due to the unsuccessful transformation of the GeTe to its crystalline state. This failure is mostly attributed to the reactive ion etching process which can cause a change in the properties of the GeTe layer, although this is yet to be confirmed by spectroscopy analysis.

The second test of optical activation using a GeTe patterned by lift-off shows a successful transformation into the crystalline state. The far-field measurements resulted in a significant change in polarization state between the LP and the RHCP state. However, the use of this technique results in a damage in the form of the GeTe pattern thus degrading severely the quality of polarization state.

## Conclusion and perspectives

---

This work consisted in the study, characterization (optical and electromagnetic) and optical activation of phase change materials using laser irradiation for their integration into high frequency systems, especially arrays of antennas. This with the objective of proposing an alternative solution to provide reconfiguration capabilities to high frequency systems. The results on this manuscript required a vast number of multiple domains of physics (such as electromagnetism, optics, material science and heat transfer) and engineering (such as clean room microfabrication, telecommunications and antennas) as well as the use of multiple measurement techniques combined with theoretical analysis and mathematical models to extract useful information from the measured data.

The first half of chapter I and Appendix 1 introduced the basic notions and metrics regarding antennas (with particular focus on patch antennas) and the reconfigurable actions that can be performed on an antenna. The state of the art on reconfigurable antennas was presented as well as the most common and current techniques used to provide reconfigurability capabilities to these systems such as PIN diodes, varactors, MEMS, ferroelectrics and PTMs. Although these strategies have proven very performant, they present several inconveniences such as reconfiguration in discrete states (using PIN diodes and MEMS) or requiring high polarization voltages (using MEMS, varactors and ferroelectrics) or a constant power supply in order to retain their states or very high losses in the mmWave band.

This is in this context that an interest in PCM compositions has emerged as a promising alternative to reconfigurable high frequency devices working in the millimeter-wave frequency band. In particular their non-volatile nature and high contrast in electrical resistivity allow the fabrication of very efficient high frequency RF-switches. Therefore, in the second half of chapter I the basic theory regarding the PCM compositions is introduced as well as the state of the art in PCM-based RF-switches. In particular, compositions based of germanium telluride (GeTe) and germanium antimonium telluride ( $\text{Ge}_2\text{Sb}_2\text{Te}_5$ ) have been extensively studied due to their very high resistivity contrast (up to 6 order of magnitude), fast switching (as fast 30 ns with optical excitations) and stability. In particular, the use of optical excitations is of great interest since this allows the elimination of the heater and its excitation bias thus massively reducing the complexity of the design and fabrication of devices integrating PCMs. However, as seen in Chapter I, the properties of the PCMs are sensible to fabrication process and environment thus attention must be exercised when fabricating the devices as well as proper characterization of the material.

The Chapter II is also divided into two main parts. The first part deals with the study and characterization of some promising PCM compositions (GeTe, GST and  $\text{Sb}_2\text{Te}_3$ ). We concluded that GeTe possess the biggest contrast in resistivity while the  $\text{Sb}_2\text{Te}_3$  presents the lowest crystallization temperature. Although a lower crystallization temperature implies the use of lower energies it also means that this composition is less stable compared to the GeTe and not suitable for applications such as memories thus we focus our efforts on GeTe and GST compositions. We proceed to the characterization of the DC-conductivity, dielectric permittivity and loss tangent of the GeTe and GST compositions. The main difficulty lies in the fact that PCM layers are very thin (in the order of hundreds of nanometers). To achieve this, it was proposed to use a differential approach combined with RF device measurements. The data obtained from this characterization were exploited in order to accurately design an array of antennas integration a PCM composition.

The second part of Chapter II focused on the reversible activation of a GeTe sample using a laser system. In order to efficiently activate a GeTe sample, we characterized the optical properties of this sample using an ellipsometry method. The data obtained from this measurement were used in multiphysics simulations employing the software COMSOL from which is concluded that green lasers ( $\lambda = 532 \text{ nm}$ ) produces the most efficient activation with the deeper optical penetration. This simulation also shows that thinner PCM layers (less than 250 nm) are easier to amorphise using laser pulses.

For the test of crystallization and amorphization, an optical irradiation banc consisting of a green laser and optical scanner was set-up and characterized. The experiments show that a laser pulse of 10 ns is enough to crystallize and amorphise a GeTe sample deposited over a sapphire substrate. This set-up allows to create arbitrary pattern in GeTe samples.

Finally, chapter III deals with the design of a multi-reconfigurable array of antennas integrating a GeTe composition. The proposed array of antennas can work in RHCP, LHCP and LP as well as multiple frequencies. The electromagnetic data obtained in the first half of chapter II was used to perform accurate electromagnetic simulations of the array of antennas. The integration of PCM requires the use of substrates with a high thermal conductivity such as alumina. Unfortunately, these kind of substrates often have high permittivity values that add a substantial amount of complexity to the design. Due to the vast number of free variables and lack of analytical formulations, the final design of the antenna was optimized by a genetic algorithm with a minimax approach in order to find a suitable configuration that works in all states of polarization for all frequencies. Simulation results show that the antenna possess directivities greater than 8.5 dBi at 30 GHz in all states and an axial ratio lower than 3 dB with a bandwidth of 1.8 GHz in RHCP and LHCP state. A continuous frequency reconfiguration is obtained by changing the size of the coupling slot by crystallizing the GeTe sample on the slot.

Some fully metallic test antennas (the crystalline GeTe was replaced by gold) were fabricated in order to validate the proposed design. The measurement of the far-field properties shows promising and acceptable results with efficiencies greater than 45% at the resonance frequency of 29.6 GHz and directivities greater than 8.5 dBi for all states. The axial ratio shows a broadband behavior of 1.8 GHz in both LHCP and RHCP. However, some important differences are observed between the LHCP and RHCP states which can be mostly attributed to a misjudgment of the properties of the glue layer such as its permittivity and thickness and the very rough profile of the substrate. The optical activation of the antennas shows a significant change in the polarization state of the antenna, depending on the state of the GeTe. However, the quality of the CP was severely degraded due uneven GeTe edges.

The results presented in this work represent promising advances for the integration of PCM into reconfigurable RF devices however some issues need to be addressed in order to enhance their performances and quality of the results:

- The proposed method for characterizing thin films of PCM compositions presented in chapter II presents non-negligible error margins (in particular in the loss tangent extraction) which can be minimized by using thicker films or longer CPW lines. In addition, it may be of interest to characterize other useful PCM compositions such as  $\text{Sb}_2\text{Te}_3$  or  $\text{InSbTe}$ .
- The multiphysics simulations of electromagnetic heating of GeTe performed in II.5.2 used a simple model in which the properties of the material are a function of temperature and does not takes into consideration the amorphization mechanism,

therefore the results obtained are mostly of qualitative nature. The results and predictions obtained from this simulation can be enhanced by using the crystallization theory explored in chapter I as well as an amorphization model. This can be done by exploiting COMSOLs modeling properties.

- The use of a laser with gaussian spatial profile is not completely adequate for using with a scanner system due to circular imprint of the crystallized area which can lead to gaps when the scanner irradiates big surfaces. In addition, in a gaussian profile, most of the energy is concentrated in the center of the laser spot which can results in unwanted damage to the irradiated region and wasted energy in the borders of the spot. These two issues can be fixed by using a “flat top” beam shaper with a square spatial profile which produces a square imprint with an even distribution of energy through the whole profile.
- During laser irradiation, part of the energy of the laser is reflected back by the PCM layer which results in wasted energy. This issue can be address by using anti-reflective coatings over the PCM layers. In addition, this coating can protect the PCM from the environment and delaying oxidation.
- The methodology presented in Chapter III for optimizing the antenna in both CP states proved to be an effective tool. However, the long time needed to find a solution for the problem can be a huge detriment and counterargument for the use of it. The optimization time can be drastically reduced by using parallel computation techniques or surrogate models.
- At millimeter-wave frequencies, the roughness of the material can have a significant influence on the performances of the antenna as shown by the measures of antennas over a quartz substrate and a Rogers 4003C substrate. Therefore, future devices at millimeter-wave band should prioritize the use of smooth surfaces or take into consideration the profile of the substrate.
- The properties of the materials seem to be altered by the photolithography process. Thus, an optimization of the RIE process needs to be carried out such that the GeTe is not affected.

## Journal publications

R. Carrizales-Juarez, L. Huitema, D. Passerieux, P. Daquin and A. Crunteanu, "Dielectric Properties of Phase Change Thin Films at Millimeter Waves," in IEEE Transactions on Microwave Theory and Techniques, vol. 71, no. 9, pp. 3852-3864, Sept. 2023, doi: 10.1109/TMTT.2023.3252722.

## International conferences

R. Carrizales-Juarez, L. Huitema, P. Daquin, E. Arnaud and A. Crunteanu "Simultaneous Optimization of a Right-handed and Left-handed Circular Polarization Array of Antennas Using Genetic Algorithms", 17<sup>th</sup> EuCAP, 2023, Florence, Italy.

R. Carrizales-Juarez, L. Huitema, D. Passerieux, P. Daquin and A. Crunteanu "Electromagnetic Properties of Phase Change Materials for Reconfigurable RF Systems in the Millimeter-Wave Frequency Band", 1<sup>st</sup> European Space Microwave Week, 2023, ESA-ESTEC, Noordwijk, The Netherlands.

## National conferences

R. Carrizales-Juarez, L. Huitema, D. Passerieux, P. Daquin and A. Crunteanu "Propriétés diélectriques des couches minces de GeTe à changement de phase dans le domaine des ondes millimétriques ", Journées Nationales Microondes, Limoges, 8-10 Juin 2022.

R. Carrizales-Juarez, L. Huitema, D. Passerieux, P. Daquin and A. Crunteanu "Propriétés diélectriques des couches minces amorphes de GeTe à changement de phase dans le domaine des ondes millimétriques ", 17<sup>èmes</sup> Journées de Caractérisation Microondes et Matériaux, Tours, 3-5 Avril 2023

## Prices and distinctions

- 2<sup>nd</sup> place at the IEEE France Antenna design competition – JNM 2022.
- 3<sup>rd</sup> place at the Innovation Student Competition - University of Limoges

## Appendices

---

|   |     |
|---|-----|
| Appendix 1. Fundamental theory of antennas .....                                | 175 |
| Appendix 2. Fundamental theory of the “equivalent network representation” ..... | 182 |
| Appendix 3. Error analysis of the characterization of PCM.....                  | 184 |

## Appendix 1. Fundamental theory of antennas

The overall performances of antenna devices can be divided into two main categories. The first is their capacity to transmit and receive power in the form of electromagnetic waves while the second is their performances as part of a high frequency electrical circuit.

### Antennas as circuit elements

From an electrical point of view, planar antennas can be considered as resonant cavities and modeled as RLC parallel resonators. Since we consider a cavity model, different resonant modes can exist within the structure. Microstrip antennas work on the fundamental resonance mode TM<sub>01</sub> since this is the lowest frequency resonant mode. The resonance can be modeled by a circuit as shown in Figure 159.

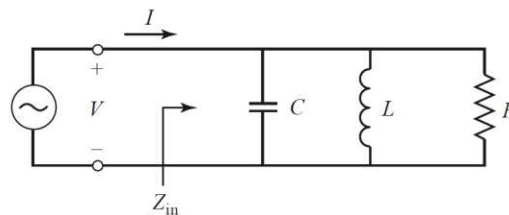


Figure 159. Equivalent RLC electrical model of a patch antenna.

The  $C$  and  $L$  components represent the electric and magnetic energy that are stored in the antenna. The resistance represents the losses of the circuit that can be divided into three contributors: the ohmic losses attributed to the metal losses in the antenna, the dielectric losses attributed to the substrate, and the losses due to the radiation. The impedance behavior of the  $C$  and  $L$  components varies with frequency and therefore, the impedance  $Z_{in}$  seen by the source also varies. The typical evolution of the input impedance  $Z_{in}$  as a function of frequency is represented in Figure 160a as an impedance plot and in Figure 160b as a (normalized) Smith chart plot. It is considered that the antenna resonates at the point where the imaginary part of  $Z_{in}$  is equal to zero or, equivalently when the magnitude of  $Z_{in}$  is maximum (this later definition is more helpful when the imaginary part never crosses the zero point). In circuit terms, the resonance frequency is given by:

$$f_r = \frac{1}{\sqrt{L \cdot C}} \quad (60)$$

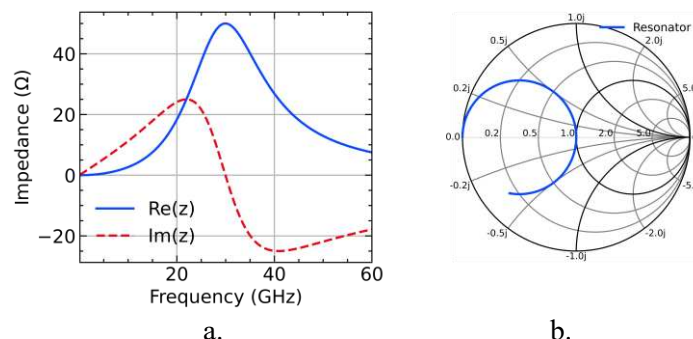


Figure 160. Evolution of the input impedance of a parallel RLC circuit as a function of frequency.

a) Impedance plot. b) Smith chart representation.

Like any other high-frequency circuit, not all the power delivered by the source arrives at the antenna since some part of this power is reflected back to the source. The amount of reflected

power is characterized by the reflection coefficient  $\Gamma$  (or, more commonly, the  $S_{11}$  parameter). The reflection coefficient of the resonator is a function of the impedance of the source and is given by :

$$S_{11} = \Gamma = \frac{Z_{in}(f) - Z_0^*}{Z_{in}(f) + Z_0^*} \quad (61)$$

where  $Z_0^*$  is the complex conjugate of the impedance of the source. Since  $Z_{in}$  is a complex function that depends on the frequency, so is the reflection coefficient. The ideal case implies a zero-reflection coefficient at the operating frequency of the antenna, which only occurs when  $Z_{in}$  is equal to the complex conjugate of  $Z_0$ . However, practically, this is very rarely the case thus is considered that the matching of an antenna is of good quality when  $|S_{11}| < 0.316$  (or in a logarithmic scale, less than -10 dB) in the frequency band of interest. If the impedance  $Z_{in}$  at the frequency of interest is higher than -10 dB, then impedance transformation techniques must be used in order to approach  $Z_{in}$  as close as possible to  $Z_0^*$ .

Once the power that enters into the antenna is known (called the “accepted power”,  $P_a$ ), the power radiated from the antenna can be calculated by:

$$P_r = \frac{1}{2} R_r |I|^2 \quad (62)$$

where  $R_r$  is the radiation resistance and  $I$  is the current entering into the resonator. The radiation resistance depends on the geometry of the antenna as well as on the dimensions and properties of the substrate and is usually very difficult to calculate unless the antenna has a very simple geometry. Ideally, for an antenna, all the power injected into the antenna would be radiated, however, the presence of ohmic and dielectric losses will reduce the amount of available power to radiate due to power losses within the substrate or dissipated by Joule effect in the metal structures. We can define the radiation efficiency  $\eta$  of the antenna as:

$$\eta = \frac{R_r}{R} = \frac{R_r}{R_r + R_o + R_d} \quad (63)$$

where  $R_o$  are the ohmic losses within the antenna and  $R_d$  are the losses in the substrate.

Another important aspect from the circuit point of view is the quality factor  $Q$  of the antenna. This is a figure of merit that is representative of the losses in the resonator, however, it can be used to estimate the bandwidth of the antenna. Assuming the bandwidth of the antenna is given by the frequency band where the matching is better than -10 dB, the fractional bandwidth is given by the equation:

$$\frac{\Delta f}{f_r} = \frac{1}{\sqrt{2}Q} \quad (64)$$

where  $\Delta f$  is the -10-dB bandwidth of the antenna.

In general, the  $Q$  factor is a direct function of the losses in the circuit: the bigger the losses, the higher the bandwidth of the antenna. The total losses in the circuit are proportional to the volume of the antenna meaning that one can increase the bandwidth of the antenna by using thicker substrates. However, as the total losses increase, the radiation efficiency decreases implying that a trade-off must be made between bandwidth and efficiency.

Figure 161 shows a comparison of the evolution of the radiation efficiency and the bandwidth as a function of the height of the substrate for different permittivity values. From this figure, it can be noticed that, indeed, radiation efficiency decreases as the thickness of the substrate

increases, however, the rate at which  $\eta$  decreases depends on the permittivity of the substrate: the higher the permittivity the lower the radiation efficiency of the antenna. On the other hand, as the substrate becomes thicker, the fractional bandwidth increases. Similarly, the rate at which the fractional bandwidth increases depends on the permittivity of the substrate: the lower the permittivity, the higher the bandwidth. Due to this trade-off, the standard choice for microstrip antennas is to use thick substrates with a low permittivity value and with low dielectric losses.

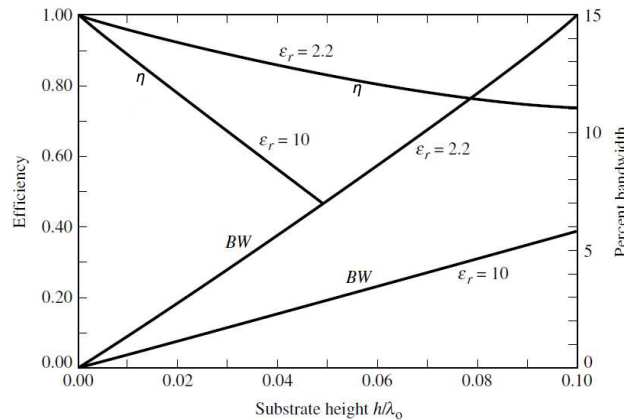


Figure 161. Evolution of the radiation efficiency and fractional bandwidth of an antenna as a function of the thickness of the substrate. Adapted from [12].

### Antennas as electromagnetic radiators

From an electromagnetic point of view, an antenna is a source of electromagnetic waves that extends radially towards infinity. For mathematical convenience, the space surrounding the antenna is represented in spherical coordinates, as shown in Figure 162. The  $\theta$ -plane is called the “elevation plane” while the  $\phi$ -plane is called the “azimuth plane”.

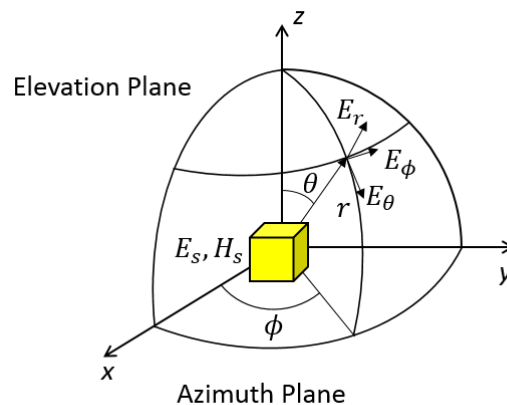


Figure 162. Geometrical representation of the space surrounding an antenna.

At any point in space, the electric field surrounding the antenna can be described by a three-component vector as:

$$E(r, \theta, \phi) = E_r(r, \theta, \phi)\hat{r} + E_\theta(r, \theta, \phi)\hat{\theta} + E_\phi(r, \theta, \phi)\hat{\phi} \quad (65)$$

The amplitude variation of each component in equation ( 65 ) can be described by spherical harmonics that vary in the form  $1/r^n$  for  $n = 1, 2, 3 \dots$ . At short distances from the antenna, the

higher order modes dominate the amplitude variation of the EM-field but at longer distances, these higher order modes are negligible. Therefore, we can divide the region surrounding the antenna into three different zones:

- **Reactive near-field region:** This region corresponds to the immediate surroundings of the antennas (generally, distances lower than the wavelength) and is characterized by a mostly reactive field.
- **Radiating near field:** This region corresponds to the region between the reactive near-field and far-field regions where radiation fields predominate but the angular distribution is still dependent on the distance to the antenna.
- **Far-field region:** This region corresponds to a distance very far from the antenna (where  $r > 2D^2/\lambda_0$ , with  $D$  –the principal dimension of the antenna and  $\lambda_0$  – the free space wavelength), where the angular field distribution is independent of the distance from the antenna and where the spherical waves can be approximate locally as plane waves.

Various criteria's have been used to define the boundaries separating each region since it depends on the radiating element [159] [160]. For the far-field radiation it is commonly accepted that it ranges at distances where  $r \gg 2D^2/\lambda_0$  (although this is only valid when  $D \gg \lambda_0$  [161]).

For most of the antennas, the far-field region is the preferred zone of operation since there are no reactive fields. In this region, the variation in the radial component is negligible, thus equation ( 65 ) can be rewritten as:

$$E(r, \theta, \varphi) \cong E_\theta(\theta, \varphi)\hat{\theta} + E_\varphi(\theta, \varphi)\hat{\varphi} \quad ( 66 )$$

The radiation properties of an antenna are graphically represented by the **antenna radiation pattern** which is a trace of the amplitude of the electric field (or equivalently, the radiated power) as a function of the angular direction. This representation can be done in a 3D representation or by a 2D image where the amplitude of the electric field as a function of  $\theta$  is represented for a constant angle  $\varphi$ . The chosen angles to represent the radiation pattern are  $\varphi = 0$  (commonly called the E-plane) and  $\varphi = 90$  (commonly called the H-plane). The radiation patterns depend on the geometry and the field distribution within the antenna and is usually represented in a logarithmic scale. The Figure 163 shows the typical radiation pattern of a microstrip patch antenna radiating at the fundamental mode TM01.

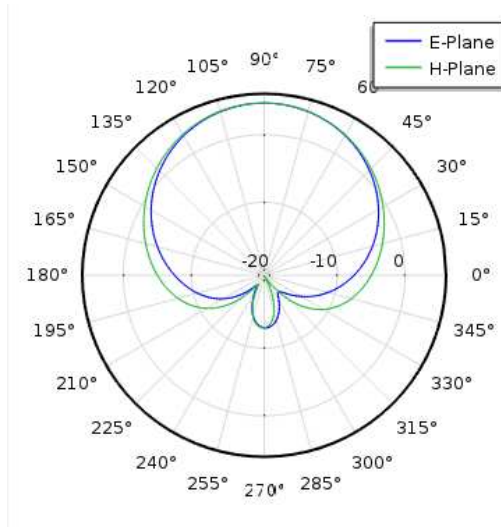


Figure 163. Normalized radiation pattern of a patch antenna.

In order to study the far-field characteristics of any antenna, the radiation intensity represents a convenient parameter from which all the relevant properties of the antenna can be derived. The radiation intensity  $U$  is defined as “the power radiated from an antenna per unit solid angle” and is related to the electric field of the antenna by:

$$U(\theta, \varphi) \cong \frac{1}{2\eta} \left( |E_{\theta}(\theta, \varphi)|^2 + |E_{\varphi}(\theta, \varphi)|^2 \right) \quad (67)$$

where  $\eta$  in the vacuum impedance.

From the radiation intensity, the total radiated power  $P_r$  by the antenna is calculated by:

$$P_r = \int_0^{2\pi} \int_0^{\pi} U(\theta, \varphi) \sin \theta \, d\theta \, d\varphi \quad (68)$$

As seen from Figure 163 the antenna does not radiate equally in all directions as the radiated electric field at the back of the antenna ( $\theta = 270^\circ$ ) is much lower than the radiation in the front ( $\theta = 90^\circ$ ). The capacity of an antenna to focus the radiated field in a particular direction is measured by the **directivity** parameter. This parameter is defined as “the ratio of the radiation intensity in a given direction from the antenna to radiation intensity of an isotropic source” where an isotropic source is a hypothetical antenna that would radiate equally in all directions. The directivity can be written as:

$$D(\theta, \varphi) = \frac{U(\theta, \varphi)}{U_0} = \frac{4\pi U(\theta, \varphi)}{P_r} \quad (69)$$

where  $U_0$  is the radiation intensity of an isotropic radiator. When the direction is not specified, the directivity of the antenna is taken to be the maximum directivity.

As previously mentioned, not all the power that is accepted by the antenna is radiated away. In order to account for the power loss within the antenna, the parameter “**gain**” of the antenna is defined as:

$$G(\theta, \varphi) = \frac{4\pi U(\theta, \varphi)}{P_a} \quad (70)$$

where  $P_a$  is the power accepted by the antenna.

The ratio between the radiated power and the accepted power is given by the **radiation efficiency  $\eta$  of the antenna**. Therefore, the directivity and the gain of the antenna are related by:

$$G(\theta, \varphi) = \eta D(\theta, \varphi) \quad (71)$$

Additionally, when the antenna is connected to a power source, not all power generated by the source is accepted by the antenna as seen in the previous section due to impedance mismatching of the antenna. To consider this impedance mismatch, we defined the parameter “**realized gain**” which is defined as:

$$G_r(\theta, \varphi) = (1 - |S_{11}|^2) G(\theta, \varphi) = \eta (1 - |S_{11}|^2) D(\theta, \varphi) \quad (72)$$

The parameter  $G_r$  translates the actual available electromagnetic power at the receiver station generated by the transmission station.

In the far-field region, the radiated wave propagates radially with only two perpendicular components, as indicated by equation ( 66 ). At any time  $t$ , the direction and magnitude of the resulting vector  $E$  changes as a function of the instantaneous value of each of its components. The state and behavior of the resulting instantaneous electric field are described by the “**state of polarization**” of the radiated wave. Although the electric field in the far-field zone is expressed in terms of the  $\theta$  and  $\varphi$  components of the electric field, the concept of polarization is understood better by using rectangular components  $x$  and  $y$ . There are three possible states of polarization of the antenna depending on the relationship between each component:

- **Linear polarization:** Occurs when the two components  $E_x$  and  $E_y$  are in phase. More generally, the linear polarization occurs when the time-phase difference between each component is a multiple of  $\pi$ .
- **Circular polarization:** Occurs only when the time-phase difference between  $E_x$  and  $E_y$  is an odd multiple of  $\pi/2$  while the magnitude of both components is the same.
- **Elliptical polarization:** Any other combination of phase and magnitude that is not the previous ones is considered elliptical polarization.

For any elliptically and circularly polarized wave, the curve that is traced in a plane perpendicular to the propagation of the wave by the instantaneous electric field is usually a tilted ellipse as shown in Figure 164.

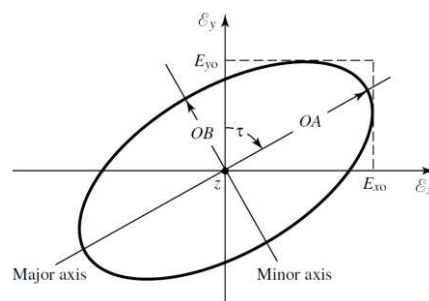


Figure 164. Polarization ellipse. Adapted from [11]

The ratio of the major axis to the minor axis is referred to as the **axial ratio** (usually measured in dB) and is used as a measure of the state of polarization of the antenna. The AR is calculated by :

$$AR = \sqrt{\frac{|E_\theta|^2 + |E_\phi|^2 + |E_\theta^2 + E_\phi^2|}{|E_\theta|^2 + |E_\phi|^2 - |E_\theta^2 + E_\phi^2|}} \quad (73)$$

If the axial ratio is infinity, the antenna is linearly polarized. If the axial ratio of the antenna is less than 2 (or 3dB) we consider that the antenna is circularly polarized. For every other value, it is considered that the wave is elliptically polarized. For the circular and elliptically polarized waves, the sense of rotation of the electric vector defines two cases: Right- Hand Polarization (RHP) if the electric vector rotates clockwise, and Left-Hand Polarization (LHP) if the electric vector rotates anti-clockwise.

An antenna receiver is able to extract the maximum available power of an incoming electromagnetic wave when the polarization state of the receiving antenna matches the polarization state of the incoming wave. If not, power is lost due to a polarization mismatch and is characterized by the **polarization loss factor** defined as:

$$PLF = |\rho_w \cdot \rho_a|^2 \quad (74)$$

where  $\rho_w$  and  $\rho_a$  are the polarization unit vectors defined from the electric field vector of the incoming wave and antenna, respectively. If the receiving antenna is linearly polarized and the incoming wave is linearly polarized in the orthogonal direction, no power is extracted from the incoming wave. If the receiving antenna is linearly polarized and the incoming wave is circularly polarized, only half of the power can be extracted from the incoming wave. If the incoming wave is Right- Hand polarized and the receiver is Left- Hand polarized, no power is extracted from the incoming wave. When the polarization state of the receiver antenna is not known, then a circularly polarized antenna emitter is to be preferred.

## Appendix 2. Fundamental theory of the “equivalent network representation”

Although this technique requires the circuit to be encapsulated in a metallic waveguide, the addition of the metallic walls should not perturb the behavior of the circuit provided that the circuit does not radiate and that the walls are sufficiently far from the circuit to study, therefore we consider that the circuit is encapsulated in a square waveguide of 1 mm side length. The electromagnetic structure to study is the one shown in Figure 56c and Figure 56d, respectively, where  $w$  is the size of the gap,  $s$  is the width of the central line,  $h_s$  is the height of the substrate, and  $h_{pcm}$  is the thickness of the PCM layer deposited on the substrate. The substrate is characterized by its permittivity  $\epsilon_r$  and the PCM is characterized by its permittivity  $\epsilon_{PCM}$ .

To transform the geometry of Figure 56c and Figure 56d to an equivalent network representation, we must first identify the boundary separating two regions of the space. For this case, this boundary is the plane where the metallization of the CPW is defined. This plane represents a mixed boundary (a plane where we have, at the same time, a conductive surface and a dielectric surface) that can be modelled as a variable source  $\mathbf{E}_e$  (called “Virtual source”) such that  $\mathbf{E}_e = \mathbf{0}$  at the conductive surfaces (The CPW lines) and  $\mathbf{E}_e \neq \mathbf{0}$  at the dielectric surface (the gap in the CPW). It is worth noticing that this virtual source does not deliver any power into the structure because the boundary conditions at the discontinuity plane impose that, in the metallic boundary the tangential electric field is zero and surface density current is non-zero, therefore the power delivered by the virtual source is zero. In the dielectric boundary, the tangential electric field is non-zero while the surface current density is zero and therefore the power delivered by the virtual source is, again, zero.

The boundary conditions imposed to the electromagnetic field at both sides of the boundary are represented by a dipole with an admittance operator  $\hat{Y}$  such that

$$\hat{Y}_i \vec{E}_e = \vec{J}_i \quad (75)$$

where  $i$  is the considered region. This admittance operator is also characterized by the permittivity of the material in the considered region. The general expression for the admittance operator is given by:

$$\hat{Y}_i = \sum_n (|f_n^{TE}\rangle Y_{i,n}^{TE} \langle f_n^{TE}| + |f_n^{TM}\rangle Y_{i,n}^{TM} \langle f_n^{TM}|) \quad (76)$$

where  $Y_{i,n}^{TE}$  and  $Y_{i,n}^{TM}$  are given in [28] and the functions  $f_n^{TE}$  and  $f_n^{TM}$  are the modal basis functions given in [26] for the TE and TM modes in the waveguide. The precise form of the admittance operators is given in our principal discussion as their particular form depends on if the structure is a single layer or multilayer substrate.

Finally, the virtual source and the dipoles can be joined together to form the circuit represented in Figure 165.

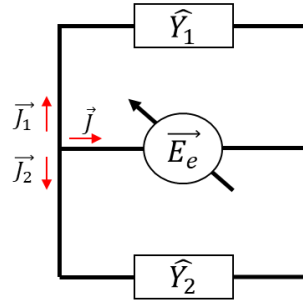


Figure 165. Equivalent circuit representation of the coplanar waveguide shown in Figure 56.

The application of Kirchhoff's and Ohm laws to the circuit in Figure 165 gives the following equation:

$$(\hat{Y}_1 + \hat{Y}_2)\vec{E}_e = \vec{J} \quad (77)$$

But because  $\vec{E}_e$  is zero when  $\vec{J}$  is non-zero (and vice versa), (77) reduces to:

$$(\hat{Y}_1 + \hat{Y}_2)\vec{E}_e = 0 \quad (78)$$

Equation (78) represents an integral equation that can be solved applying Galerkin's method by decomposing the virtual source  $\vec{E}_e$  into a set of trial functions  $\vec{g}_e$  defined such that:

$$\vec{E}_e = v_e \vec{g}_e \quad (79)$$

where  $v_e$  is designated unknown coefficients and  $\vec{g}_e$  is defined as:

$$\vec{g}_e = \begin{cases} g_{ex} = \begin{cases} -1 & \text{for } x \in \left[ \frac{a-s}{2} - w, \frac{a-s}{2} \right] \\ +1 & \text{for } x \in \left[ \frac{a+s}{2}, \frac{a+s}{2} + w \right] \\ 0 & \text{elsewhere} \end{cases} \\ g_{ez} = 0 & \text{for } x \in [0, a] \end{cases} \quad (80)$$

Note that  $g_{ex}$  represents a rough approximation of an odd mode propagating in the CPW line. The fact the  $g_{ez}$  is zero means that we are consideration a pure TEM mode in the line.

Then (78) has a solution, other than the trivial one ( $v_e = 0$ ), if and only if

$$\langle \vec{g}_e | (\hat{Y}_1 + \hat{Y}_2) \vec{g}_e \rangle = 0 \quad (81)$$

where  $\langle . | . \rangle$  represents the Hermitian scalar product.

### Appendix 3. Error analysis of the characterization of PCM

The accuracy of the proposed procedure to extract the permittivity of thin layers of PCMs lies in the fact that one can accurately deduce the effective permittivity of the devices using either ( 13 ) or ( 25 ). Therefore, it is of interest to evaluate how small changes in the parameters of the deposited layer of PCM may affect the effective permittivity of the line. For this purpose, we can calculate the partial derivative of the effective permittivity of the coplanar line device with respect to different parameters of the PCM using either ( 25 ) or 3D electromagnetic simulation. The partial derivatives were calculated numerically using the nominal parameters of the CPW line.

The first quantity of interest is how sensitive is the effective permittivity of the CPW to the permittivity of the obtained PCM. The changes of  $\epsilon_{PCM}$  due to small changes in  $\epsilon_{eff}$  can be calculated using

$$\Delta\epsilon_{PCM} = \Delta\epsilon_{eff} \left( \frac{\partial\epsilon_{eff}}{\partial\epsilon_{PCM}} \right)^{-1} \quad (82)$$

As an example, a CPW with a PCM thickness of 500 nm, has a numerical value for the partial derivative of 0.021 using the analytical method and 0.019 using the 3D EM simulation. Then, using ( 82 ), we can deduce that an error of 0.1 in the  $\epsilon_{eff}$  produces an error of 5 in the value of  $\epsilon_{PCM}$ .

The uncertainty on the effective permittivity due to small deviations on the parameters of the can be evaluated using:

$$\Delta\epsilon_{eff} = \sqrt{\left( \Delta h_{PCM} \frac{\partial\epsilon_{eff}}{\partial h_{PCM}} \right)^2 + \left( \Delta s \frac{\partial\epsilon_{eff}}{\partial s} \right)^2 + \left( \Delta w \frac{\partial\epsilon_{eff}}{\partial w} \right)^2 + \left( \Delta h_s \frac{\partial\epsilon_{eff}}{\partial h_s} \right)^2} \quad (83)$$

where  $\Delta h_{pcm}$ ,  $\Delta s$ ,  $\Delta w$ ,  $\Delta h_s$  are small changes in the thickness of the PCM, the width of the central conductor of the CPW, the gap of the CPW and the height of the substrate, respectively. Since optical lithography presents an accuracy of around 1  $\mu\text{m}$ , and the devices were fabricated on substrates cut from the same wafer and lithographically processed at the same time, the terms  $\Delta s$  and  $\Delta w$  can be neglected. Moreover, since the height of the substrate is much bigger than the dimensions of the CPW, small variations of its value can be neglected also. Therefore, ( 83 ) can be written as:

$$\Delta\epsilon_{eff} = \Delta h_{PCM} \frac{\partial\epsilon_{eff}}{\partial h_{PCM}} \epsilon_{eff} \quad (84)$$

This means that the uncertainties in the value of the effective permittivity of the line can be attributed mostly to uncertainties in the thickness of the PCM layer. A similar analysis can be done for the attenuation constant of the CPW by replacing  $\epsilon_{eff}$  with  $\alpha_t$ .

For the stub resonators, there is an additional parameter: the length of the resonator which can be solved analytically taking the partial derivative of ( 13 ):

$$\frac{d\epsilon_{eff}}{dL} = -2 \frac{\epsilon_{eff}^n}{L} \quad (85)$$

where  $\epsilon_{eff}^n$  is the effective permittivity calculated from ( 13 ) using the nominal values of the resonators. From ( 85 ), we can see that a larger resonator is less sensitivity to small variations of the length of the resonator.

These errors are calculated using ( 82 ), ( 83 ) and ( 84 ) which requires the evaluation of partial derivatives. Since we do not dispose of an explicit equation for evaluating the value of the partial derivatives, these values were calculated numerically by adding small perturbations to the geometric parameters of the CPW and looking at their influence in the effective permittivity of the line. The numerical values of the partial derivatives are shown, for each sample, in Table I from which it can be noticed that sample 4 is the most sensitive to errors in the thickness of the deposited PCM, which can be attributed to the low permittivity of the substrate. From samples 1 and 2 we observe that their sensitivity to errors in thickness of the PCM layer is independent of the thickness of the layer (sample 1 has a nominal PCM thickness of 500 nm and sample 2 has a nominal PCM thickness of 800 nm). But this sensitivity is inversely proportional to the permittivity of the substrate, which can be seen from sample 4 (GeTe over a SiO<sub>2</sub> substrate) who has a smaller permittivity value than the alumina substrate. From samples 2 (800-nm thick GeTe layer) and 4 (800-nm thick GST layer), we can observe that the bigger the permittivity of the PCM, the more sensible is the effective permittivity to deviations on the thickness of the PCM.

TABLE I.

| Sample | $\left(\frac{\partial \epsilon_{eff}}{\partial \epsilon_{PCM}}\right)^{-1}$ | $\frac{\partial \epsilon_{eff}}{\partial h_{PCM}} (\mu\text{m})^{-1}$ |
|--------|---|---|
| 1      | 66.7  | 0.336   |
| 2      | 41.7  | 0.348   |
| 3      | 76.9  | 2.68  |
| 4      | 50.0  | 0.654   |

The sensitivity of the extracted permittivity of the PCM to errors in the effective permittivity is quantified by ( 82 ) which requires knowledge of the derivative of effective permittivity to the permittivity of the PCM. Comparing sample 1 and sample 3, we conclude that the lower the permittivity of the substrate, the more sensible is the extracted value of the PCM to errors in the value of the effective permittivity. From samples 1 and 2 we observe that, the bigger the thickness of the PCM layer, the smaller the sensitivity of the extracted PCM permittivity. While from samples 2 and 4, we note that the bigger the permittivity of the PCM, the more sensitive is the extracted permittivity of the PCM to errors in the value of the effective permittivity.

## Bibliography

---

- [1] W. Hong, K.-H. Baek, et S. Ko, « Millimeter-Wave 5G Antennas for Smartphones: Overview and Experimental Demonstration », *IEEE Trans. Antennas Propag.*, vol. 65, n° 12, p. 6250-6261, déc. 2017, doi: 10.1109/TAP.2017.2740963.
- [2] T. S. Rappaport *et al.*, « Millimeter Wave Mobile Communications for 5G Cellular: It Will Work! », *IEEE Access*, vol. 1, p. 335-349, 2013, doi: 10.1109/ACCESS.2013.2260813.
- [3] T. S. Rappaport, Y. Xing, G. R. MacCartney, A. F. Molisch, E. Mellios, et J. Zhang, « Overview of Millimeter Wave Communications for Fifth-Generation (5G) Wireless Networks—With a Focus on Propagation Models », *IEEE Trans. Antennas Propag.*, vol. 65, n° 12, p. 6213-6230, déc. 2017, doi: 10.1109/TAP.2017.2734243.
- [4] M. T. Moayyed, F. Restuccia, et S. Basagni, « Comparative Performance Evaluation of mmWave 5G NR and LTE in a Campus Scenario », in *2020 IEEE 92nd Vehicular Technology Conference (VTC2020-Fall)*, nov. 2020, p. 1-5. doi: 10.1109/VTC2020-Fall49728.2020.9348727.
- [5] V. Dahiya et A. Kumar, « Performance Evaluation of Millimeter-wave Considering Rain Fade using NYUSIM Model », in *2022 International Conference on Industry 4.0 Technology (I4Tech)*, sept. 2022, p. 1-6. doi: 10.1109/I4Tech55392.2022.9952994.
- [6] P. Pawar, N. Pawar, et A. Trivedi, « How Atmospheric Attenuation affects the UAV Communication Network? », in *2023 2nd International Conference on Paradigm Shifts in Communications Embedded Systems, Machine Learning and Signal Processing (PCEMS)*, Nagpur, India: IEEE, avr. 2023, p. 1-6. doi: 10.1109/PCEMS58491.2023.10136103.
- [7] « ESA - Eduspace EN - Home - Atmospheric interference ». Consulté le: 9 octobre 2023. [En ligne]. Disponible sur: [https://www.esa.int/SPECIALS/Eduspace\\_EN/SEMUY3Z2OF\\_0.html](https://www.esa.int/SPECIALS/Eduspace_EN/SEMUY3Z2OF_0.html)
- [8] F. J. Wentz et T. Meissner, « Atmospheric absorption model for dry air and water vapor at microwave frequencies below 100 GHz derived from spaceborne radiometer observations: Atmospheric Absorption Model », *Radio Sci.*, vol. 51, n° 5, p. 381-391, mai 2016, doi: 10.1002/2015RS005858.
- [9] P. S. B. G, P. R. Mane, P. Kumar, T. Ali, et M. G. Nabi Alsath, « Planar MIMO antenna for mmWave applications: Evolution, present status & future scope », *Heliyon*, vol. 9, n° 2, p. e13362, févr. 2023, doi: 10.1016/j.heliyon.2023.e13362.
- [10] B. G. P. Shariff, T. Ali, P. R. Mane, et P. Kumar, « Array Antennas for mmWave Applications: A Comprehensive Review », *IEEE Access*, vol. 10, p. 126728-126766, 2022, doi: 10.1109/ACCESS.2022.3226272.
- [11] G. Maral, M. Bousquet, et Z. Sun, *Satellite communications systems: systems, techniques and technology*, 5th ed. revised. Chichester: Wiley, 2009.
- [12] M. Bouabdellah, E. Illi, F. E. Bouanani, et M.-S. Alouini, « Hybrid Very High Throughput Satellites: Potential, Challenges, and Research Directions », in *2020 IEEE Eighth International Conference on Communications and Networking (ComNet)*, oct. 2020, p. 1-6. doi: 10.1109/ComNet47917.2020.9306099.
- [13] E. Gill, J. Morton, P. Axelrad, D. M. Akos, M. Centrella, et S. Speretta, « Overview of Space-Capable Global Navigation Satellite Systems Receivers: Heritage, Status and the

Trend towards Miniaturization », *Sensors*, vol. 23, n° 17, Art. n° 17, janv. 2023, doi: 10.3390/s23177648.

[14] M. Höyhtyä, S. Boumard, A. Yastrebova, P. Järvensivu, M. Kiviranta, et A. Anttonen, « Sustainable Satellite Communications in the 6G Era: A European View for Multilayer Systems and Space Safety », *IEEE Access*, vol. 10, p. 99973-100005, 2022, doi: 10.1109/ACCESS.2022.3206862.

[15] Z. Yan *et al.*, « Topology Design for GNSSs Under Polling Mechanism Considering Both Inter-Satellite Links and Ground-Satellite Links », *IEEE Trans. Veh. Technol.*, vol. 71, n° 2, p. 2084-2097, févr. 2022, doi: 10.1109/TVT.2021.3135563.

[16] M. Srinivasan et V. Tsontos, « Satellite Altimetry for Ocean and Coastal Applications: A Review », *Remote Sens.*, vol. 15, n° 16, Art. n° 16, janv. 2023, doi: 10.3390/rs15163939.

[17] F. Rinaldi *et al.*, « Non-Terrestrial Networks in 5G & Beyond: A Survey », *IEEE Access*, vol. 8, p. 165178-165200, 2020, doi: 10.1109/ACCESS.2020.3022981.

[18] M. Giordani et M. Zorzi, « Non-Terrestrial Networks in the 6G Era: Challenges and Opportunities », *IEEE Netw.*, vol. 35, n° 2, p. 244-251, mars 2021, doi: 10.1109/MNET.011.2000493.

[19] M. N. Sweeting, « Modern Small Satellites-Changing the Economics of Space », *Proc. IEEE*, vol. 106, n° 3, p. 343-361, mars 2018, doi: 10.1109/JPROC.2018.2806218.

[20] F. Massimi, P. Ferrara, et F. Benedetto, « Deep Learning Methods for Space Situational Awareness in Mega-Constellations Satellite-Based Internet of Things Networks », *Sensors*, vol. 23, n° 1, Art. n° 1, janv. 2023, doi: 10.3390/s23010124.

[21] « Design and Implementation of Continuous Bounded Finite-Time Attitude Control of Reusable Launch Vehicle | IEEE Journals & Magazine | IEEE Xplore ». Consulté le: 3 mars 2024. [En ligne]. Disponible sur: <https://ieeexplore-ieee-org.ezproxy.unilim.fr/document/10083076>

[22] « State-of-the-Art Passive Beam-Steering Antenna Technologies: Challenges and Capabilities | IEEE Journals & Magazine | IEEE Xplore ». Consulté le: 25 février 2024. [En ligne]. Disponible sur: <https://ieeexplore-ieee-org.ezproxy.unilim.fr/document/10130278>

[23] « Satellite Communication (SATCOM) Market Size Report 2030 ». Consulté le: 26 février 2024. [En ligne]. Disponible sur: <https://www.grandviewresearch.com/industry-analysis/satellite-communication-market>

[24] C. A. Balanis, *Antenna theory: analysis and design*, Fourth edition. Hoboken, New Jersey: Wiley, 2016.

[25] G. Mackertich-Sengerdy, S. D. Campbell, et D. H. Werner, « Tailored compliant mechanisms for reconfigurable electromagnetic devices », *Nat. Commun.*, vol. 14, n° 1, Art. n° 1, févr. 2023, doi: 10.1038/s41467-023-36143-6.

[26] S. Lee, S. I. H. Shah, H. L. Lee, et S. Lim, « Frequency-Reconfigurable Antenna Inspired by Origami Flasher », *IEEE Antennas Wirel. Propag. Lett.*, vol. 18, n° 8, p. 1691-1695, août 2019, doi: 10.1109/LAWP.2019.2928302.

[27] M. Patriotis, F. N. Ayoub, Y. Tawk, J. Costantine, et C. G. Christodoulou, « A Millimeter-Wave Frequency Reconfigurable Circularly Polarized Antenna Array », *IEEE Open J. Antennas Propag.*, vol. 2, p. 759-766, 2021, doi: 10.1109/OJAP.2021.3090908.

- [28] I. Serhsouh, M. Himdi, H. Lebbar, et H. Vettikalladi, « Reconfigurable SIW Antenna for Fixed Frequency Beam Scanning and 5G Applications », *IEEE Access*, vol. 8, p. 60084-60089, 2020, doi: 10.1109/ACCESS.2020.2983001.
- [29] D. Rodrigo, B. A. Cetiner, et L. Jofre, « Frequency, Radiation Pattern and Polarization Reconfigurable Antenna Using a Parasitic Pixel Layer », *IEEE Trans. Antennas Propag.*, vol. 62, n° 6, p. 3422-3427, juin 2014, doi: 10.1109/TAP.2014.2314464.
- [30] J. J. Yao, « RF MEMS from a device perspective », *J. Micromechanics Microengineering*, vol. 10, n° 4, p. R9, déc. 2000, doi: 10.1088/0960-1317/10/4/201.
- [31] M. S. Gaikwad, N. K. Deshmukh, V. B. Sawant, et S. S. Mohite, « Evaluating Thermal Contact Resistance for Ohmic type RF MEMS switch », in *2019 International Conference on Nascent Technologies in Engineering (ICNTE)*, Navi Mumbai, India: IEEE, janv. 2019, p. 1-5. doi: 10.1109/ICNTE44896.2019.8945809.
- [32] Z. Deng, Y. Wang, et C. Lai, « Design and Analysis of Pattern Reconfigurable Antenna Based on RF MEMS Switches », *Electronics*, vol. 12, n° 14, Art. n° 14, janv. 2023, doi: 10.3390/electronics12143109.
- [33] K. Rajasekhar, K. GirijaSravani, et K. Srinivasa Rao, « Design and performance analysis of ohmic contact based SPMT RF MEMS switch », *Microsyst. Technol.*, vol. 29, n° 9, p. 1307-1318, sept. 2023, doi: 10.1007/s00542-023-05503-z.
- [34] A. J. Alazemi et Y. T. Alsaleh, « An ultrawideband antenna with two independently tunable notch bands », *Alex. Eng. J.*, vol. 79, p. 402-410, sept. 2023, doi: 10.1016/j.aej.2023.07.082.
- [35] Q. Chen, J. Ala-Laurinaho, A. Khripkov, J. Ilvonen, R. M. Moreno, et V. Viikari, « Varactor-Based Frequency-Reconfigurable Dual-Polarized mm-Wave Antenna Array for Mobile Devices », *IEEE Trans. Antennas Propag.*, vol. 71, n° 8, p. 6628-6638, août 2023, doi: 10.1109/TAP.2023.3287679.
- [36] T. Y. Kim, S. K. Kim, et S.-W. Kim, « Application of ferroelectric materials for improving output power of energy harvesters », *Nano Converg.*, vol. 5, n° 1, p. 30, nov. 2018, doi: 10.1186/s40580-018-0163-0.
- [37] H. Jiao, X. Wang, S. Wu, Y. Chen, J. Chu, et J. Wang, « Ferroelectric field effect transistors for electronics and optoelectronics », *Appl. Phys. Rev.*, vol. 10, n° 1, p. 011310, févr. 2023, doi: 10.1063/5.0090120.
- [38] M. V. Carballo, D. Borah, et T. S. Kalkur, « U-Slot Dual-band Frequency Reconfigurable Patch Antenna Tuned With Commercial Ferroelectric BST capacitors », in *2019 IEEE International Conference on Microwaves, Antennas, Communications and Electronic Systems (COMCAS)*, nov. 2019, p. 1-6. doi: 10.1109/COMCAS44984.2019.8958124.
- [39] V. Muzzupapa *et al.*, « Frequency Reconfigurable Millimeter Wave Antenna Integrating Ferroelectric Interdigitated Capacitors », in *2023 17th European Conference on Antennas and Propagation (EuCAP)*, Florence, Italy: IEEE, mars 2023, p. 1-4. doi: 10.23919/EuCAP57121.2023.10133761.
- [40] H.-Y. Li, C.-T. Yeh, J.-J. Huang, C.-W. Chang, C.-T. Yu, et J.-S. Fu, « CPW-Fed Frequency-Reconfigurable Slot-Loop Antenna With a Tunable Matching Network Based on Ferroelectric Varactors », *IEEE Antennas Wirel. Propag. Lett.*, vol. 14, p. 614-617, 2015, doi: 10.1109/LAWP.2014.2375334.

- [41] T. Alejo, L. Uson, et M. Arruebo, « Reversible stimuli-responsive nanomaterials with on-off switching ability for biomedical applications », *J. Controlled Release*, vol. 314, p. 162-176, nov. 2019, doi: 10.1016/j.jconrel.2019.10.036.
- [42] E. Haddad *et al.*, « Review of the VO<sub>2</sub> smart material applications with emphasis on its use for spacecraft thermal control », *Front. Mater.*, vol. 9, 2022, Consulté le: 10 octobre 2023. [En ligne]. Disponible sur: <https://www.frontiersin.org/articles/10.3389/fmats.2022.1013848>
- [43] L. Wang *et al.*, « A Review of THz Modulators with Dynamic Tunable Metasurfaces », *Nanomaterials*, vol. 9, n° 7, Art. n° 7, juill. 2019, doi: 10.3390/nano9070965.
- [44] E.-N. Sirjita, A. Boulle, J.-C. Orlianges, R. Mayet, et A. Crunteanu, « Structural and electrical properties of high-performance vanadium dioxide thin layers obtained by reactive magnetron sputtering », *Thin Solid Films*, vol. 759, p. 139461, oct. 2022, doi: 10.1016/j.tsf.2022.139461.
- [45] L. Huitema, A. Crunteanu, H. Wong, et E. Arnaud, « Highly integrated VO<sub>2</sub>-based tunable antenna for millimeter-wave applications », *Appl. Phys. Lett.*, vol. 110, n° 20, p. 203501, mai 2017, doi: 10.1063/1.4983364.
- [46] S. R. Ovshinsky, « Reversible Electrical Switching Phenomena in Disordered Structures », *Phys. Rev. Lett.*, vol. 21, n° 20, p. 1450-1453, nov. 1968, doi: 10.1103/PhysRevLett.21.1450.
- [47] L. Chen, D. Rende, L. S. Schadler, et R. Ozisik, « Polymer nanocomposite foams », *J. Mater. Chem. A*, vol. 1, n° 12, p. 3837, 2013, doi: 10.1039/c2ta00086e.
- [48] J. S. Blázquez, F. J. Romero, C. F. Conde, et A. Conde, « A Review of Different Models Derived from Classical Kolmogorov, Johnson and Mehl, and Avrami (KJMA) Theory to Recover Physical Meaning in Solid-State Transformations », *Phys. Status Solidi B*, vol. 259, n° 6, p. 2100524, 2022, doi: 10.1002/pssb.202100524.
- [49] S. Vyazovkin et N. Sbirrazzuoli, « Nonisothermal Crystallization Kinetics by DSC: Practical Overview », *Processes*, vol. 11, n° 5, Art. n° 5, mai 2023, doi: 10.3390/pr11051438.
- [50] S. Raoux et M. Wuttig, Éd., *Phase Change Materials*. Boston, MA: Springer US, 2009. doi: 10.1007/978-0-387-84874-7.
- [51] S. Raoux, J. L. Jordan-Sweet, et A. J. Kellock, « Crystallization properties of ultrathin phase change films », *J. Appl. Phys.*, vol. 103, n° 11, p. 114310, juin 2008, doi: 10.1063/1.2938076.
- [52] W. Chong et Z. Koon, « Thickness Dependent Nano-Crystallization in Ge<sub>2</sub>Sb<sub>2</sub>Te<sub>5</sub> Films and Its Effect on Devices », *Jpn. J. Appl. Phys.*, vol. 46, n° 4S, p. 2211, avr. 2007, doi: 10.1143/JJAP.46.2211.
- [53] H. C. F. Martens, R. Vlutters, et J. C. Prangma, « Thickness dependent crystallization speed in thin phase change layers used for optical recording », *J. Appl. Phys.*, vol. 95, n° 8, p. 3977-3983, mars 2004, doi: 10.1063/1.1667606.
- [54] N. El-Hinnawy *et al.*, « 18.15 Improvements in GeTe-Based Inline Phase-Change Switch Technology for RF Switching Applications », 2014.
- [55] T. Singh et R. R. Mansour, « Chalcogenide Phase-Change Material Germanium Telluride for Radio-Frequency Applications: An overview », *IEEE Nanotechnol. Mag.*, vol. 16, n° 3, p. 26-41, juin 2022, doi: 10.1109/MNANO.2022.3160772.

- [56] A. Mennai, A. Bessaudou, F. Cosset, C. Guines, P. Blondy, et A. Crunteanu, « Bistable RF switches using Ge<sub>2</sub>Sb<sub>2</sub>Te<sub>5</sub> phase change material », in *2015 European Microwave Conference (EuMC)*, Paris, France: IEEE, sept. 2015, p. 945-947. doi: 10.1109/EuMC.2015.7345920.
- [57] M. Zhang *et al.*, « Tunable Terahertz Wavefront Modulation Based on Phase Change Materials Embedded in Metasurface », *Nanomaterials*, vol. 12, n° 20, p. 3592, oct. 2022, doi: 10.3390/nano12203592.
- [58] R. Tsu, W. E. Howard, et L. Esaki, « Optical and Electrical Properties and Band Structure of GeTe and SnTe », *Phys. Rev.*, vol. 172, n° 3, p. 779-788, août 1968, doi: 10.1103/PhysRev.172.779.
- [59] J. Goldak, C. S. Barrett, D. Innes, et W. Youdelis, « Structure of Alpha GeTe », *J. Chem. Phys.*, vol. 44, n° 9, p. 3323-3325, mai 2004, doi: 10.1063/1.1727231.
- [60] G. Bruns *et al.*, « Nanosecond switching in GeTe phase change memory cells », *Appl. Phys. Lett.*, vol. 95, n° 4, p. 043108, juill. 2009, doi: 10.1063/1.3191670.
- [61] M. Le Gallo et A. Sebastian, « An overview of phase-change memory device physics », *J. Phys. Appl. Phys.*, vol. 53, n° 21, p. 213002, mai 2020, doi: 10.1088/1361-6463/ab7794.
- [62] D. Lencer, M. Salinga, et M. Wuttig, « Design Rules for Phase-Change Materials in Data Storage Applications », *Adv. Mater.*, vol. 23, n° 18, p. 2030-2058, 2011, doi: 10.1002/adma.201004255.
- [63] S. Raoux, B. Muñoz, H.-Y. Cheng, et J. L. Jordan-Sweet, « Phase transitions in Ge-Te phase change materials studied by time-resolved x-ray diffraction », *Appl. Phys. Lett.*, vol. 95, n° 14, p. 143118, oct. 2009, doi: 10.1063/1.3236786.
- [64] M. Chen, K. A. Rubin, et R. W. Barton, « Compound materials for reversible, phase-change optical data storage », *Appl. Phys. Lett.*, vol. 49, n° 9, p. 502-504, sept. 1986, doi: 10.1063/1.97617.
- [65] J.-S. Moon *et al.*, « 11 THz figure-of-merit phase-change RF switches for reconfigurable wireless front-ends », in *2015 IEEE MTT-S International Microwave Symposium*, Phoenix, AZ, USA: IEEE, mai 2015, p. 1-4. doi: 10.1109/MWSYM.2015.7167005.
- [66] A. N. D. Kolb *et al.*, « Understanding the Crystallization Behavior of Surface-Oxidized GeTe Thin Films for Phase-Change Memory Application », *ACS Appl. Electron. Mater.*, vol. 1, n° 5, p. 701-710, mai 2019, doi: 10.1021/acsaelm.9b00070.
- [67] M. Gallard *et al.*, « New insights into thermomechanical behavior of GeTe thin films during crystallization », *Acta Mater.*, vol. 191, p. 60-69, juin 2020, doi: 10.1016/j.actamat.2020.04.001.
- [68] Y. Yuan, Z. Xu, S. Song, Z. Song, R. Liu, et J. Zhai, « Crystallization behavior of MnTe/GeTe stacked thin films for multi-level phase change memory », *Appl. Surf. Sci.*, vol. 640, p. 158362, déc. 2023, doi: 10.1016/j.apsusc.2023.158362.
- [69] L. Gao *et al.*, « Nano-Scanning Calorimetry Applied to Phase Change Processes in GeTe Thin Films », *IEEE Trans. Electron Devices*, vol. 70, n° 8, p. 4128-4132, août 2023, doi: 10.1109/TED.2023.3283233.

- [70] J.-W. Park *et al.*, « Optical properties of (GeTe, Sb<sub>2</sub>Te<sub>3</sub>) pseudobinary thin films studied with spectroscopic ellipsometry », *Appl. Phys. Lett.*, vol. 93, n° 2, p. 021914, juill. 2008, doi: 10.1063/1.2959818.
- [71] S. Raoux, H.-Y. Cheng, M. A. Caldwell, et H.-S. P. Wong, « Crystallization times of Ge–Te phase change materials as a function of composition », *Appl. Phys. Lett.*, vol. 95, n° 7, p. 071910, août 2009, doi: 10.1063/1.3212732.
- [72] R. J. Warzoha, B. F. Donovan, N. T. Vu, J. G. Champlain, S. Mack, et L. B. Ruppalt, « Nanoscale thermal transport in amorphous and crystalline GeTe thin-films », *Appl. Phys. Lett.*, vol. 115, n° 2, p. 023104, juill. 2019, doi: 10.1063/1.5098334.
- [73] V. V. Ionin, A. V. Kiselev, N. N. Eliseev, V. A. Mikhalevsky, M. A. Pankov, et A. A. Lotin, « Multilevel reversible laser-induced phase transitions in GeTe thin films », *Appl. Phys. Lett.*, vol. 117, n° 1, p. 011901, juill. 2020, doi: 10.1063/5.0014375.
- [74] W. Gawelda, J. Siegel, C. N. Afonso, V. Plausinaitiene, A. Abrutis, et C. Wiemer, « Dynamics of laser-induced phase switching in GeTe films », *J. Appl. Phys.*, vol. 109, n° 12, p. 123102, juin 2011, doi: 10.1063/1.3596562.
- [75] R. E. Simpson, P. Fons, A. V. Kolobov, M. Krbal, et J. Tominaga, « Enhanced crystallization of GeTe from an Sb<sub>2</sub>Te<sub>3</sub> template », *Appl. Phys. Lett.*, vol. 100, n° 2, p. 021911, janv. 2012, doi: 10.1063/1.3675635.
- [76] N. Yamada, E. Ohno, K. Nishiuchi, N. Akahira, et M. Takao, « Rapid-phase transitions of GeTe-Sb<sub>2</sub>Te<sub>3</sub> pseudobinary amorphous thin films for an optical disk memory », *J. Appl. Phys.*, vol. 69, n° 5, p. 2849-2856, mars 1991, doi: 10.1063/1.348620.
- [77] V. Meli *et al.*, « Multi Level Cell Reliability in Ge-rich GeSbTe-based Phase Change Memory Arrays », in *2023 IEEE International Reliability Physics Symposium (IRPS)*, Monterey, CA, USA: IEEE, mars 2023, p. 1-5. doi: 10.1109/IRPS48203.2023.10118339.
- [78] I. Friedrich, V. Weidenhof, W. Njoroge, P. Franz, et M. Wuttig, « Structural transformations of Ge<sub>2</sub>Sb<sub>2</sub>Te<sub>5</sub> films studied by electrical resistance measurements », *J. Appl. Phys.*, vol. 87, n° 9, p. 4130-4134, mai 2000, doi: 10.1063/1.373041.
- [79] I.-D. Simandan *et al.*, « Influence of Deposition Method on the Structural and Optical Properties of Ge<sub>2</sub>Sb<sub>2</sub>Te<sub>5</sub> », *Materials*, vol. 14, n° 13, p. 3663, juin 2021, doi: 10.3390/ma14133663.
- [80] W. P. Risk, C. T. Rettner, et S. Raoux, « Thermal conductivities and phase transition temperatures of various phase-change materials measured by the 3 $\omega$  method », *Appl. Phys. Lett.*, vol. 94, n° 10, p. 101906, mars 2009, doi: 10.1063/1.3097353.
- [81] E. K. Chua *et al.*, « Low resistance, high dynamic range reconfigurable phase change switch for radio frequency applications », *Appl. Phys. Lett.*, vol. 97, n° 18, p. 183506, nov. 2010, doi: 10.1063/1.3508954.
- [82] A. Ghalem *et al.*, « Arrays of GeTe electrically activated RF switches », in *2017 IEEE MTT-S International Microwave Workshop Series on Advanced Materials and Processes for RF and THz Applications (IMWS-AMP)*, Pavia: IEEE, sept. 2017, p. 1-3. doi: 10.1109/IMWS-AMP.2017.8247380.
- [83] N. El-Hinnawy, G. Slovin, J. Rose, et D. Howard, « A 25 THz F<sub>CO</sub> (6.3 fs R\_ON\*C\_OFF) Phase-Change Material RF Switch Fabricated in a High Volume Manufacturing Environment

with Demonstrated Cycling > 1 Billion Times », in *2020 IEEE/MTT-S International Microwave Symposium (IMS)*, août 2020, p. 45-48. doi: 10.1109/IMS30576.2020.9223973.

[84] P. Borodulin *et al.*, « Recent advances in fabrication and characterization of GeTe-based phase-change RF switches and MMICs », in *2017 IEEE MTT-S International Microwave Symposium (IMS)*, juin 2017, p. 285-288. doi: 10.1109/MWSYM.2017.8059098.

[85] A. Crunteanu, L. Huitema, J.-C. Orlianges, C. Guines, et D. Passerieux, « Optical switching of GeTe phase change materials for high-frequency applications », in *2017 IEEE MTT-S International Microwave Workshop Series on Advanced Materials and Processes for RF and THz Applications (IMWS-AMP)*, sept. 2017, p. 1-3. doi: 10.1109/IMWS-AMP.2017.8247379.

[86] J. L. Valdes, L. Huitema, E. Arnaud, D. Passerieux, et A. Crunteanu, « A Polarization Reconfigurable Patch Antenna in the Millimeter-Waves Domain Using Optical Control of Phase Change Materials », *IEEE Open J. Antennas Propag.*, vol. 1, p. 224-232, 2020, doi: 10.1109/OJAP.2020.2996767.

[87] J. R. L. Valdes, « Antennes agiles reconfigurables optiquement dans le domaine millimétrique avec l'intégration de matériaux à changement de phase », phdthesis, Université de Limoges, 2020. Consulté le: 21 février 2024. [En ligne]. Disponible sur: <https://theses.hal.science/tel-03129887>

[88] A. Ghalem, C. Guines, D. Passerieux, J.-C. Orlianges, L. Huitema, et A. Crunteanu, « Reversible, Fast Optical Switching of Phase Change Materials for Active Control of High-Frequency Functions », in *2018 IEEE/MTT-S International Microwave Symposium - IMS*, juin 2018, p. 839-842. doi: 10.1109/MWSYM.2018.8439247.

[89] S. Franssila, *Introduction to microfabrication*. Chichester, West Sussex, England ; Hoboken, NJ: J. Wiley, 2004.

[90] A. Ghalem, C. Guines, D. Passerieux, J.-C. Orlianges, L. Huitema, et A. Crunteanu, « Reversible, Fast Optical Switching of Phase Change Materials for Active Control of High-Frequency Functions », in *2018 IEEE/MTT-S International Microwave Symposium - IMS*, juin 2018, p. 839-842. doi: 10.1109/MWSYM.2018.8439247.

[91] A. Ghalem *et al.*, « Arrays of GeTe electrically activated RF switches », in *2017 IEEE MTT-S International Microwave Workshop Series on Advanced Materials and Processes for RF and THz Applications (IMWS-AMP)*, sept. 2017, p. 1-3. doi: 10.1109/IMWS-AMP.2017.8247380.

[92] T. Singh et R. R. Mansour, « Chalcogenide Phase-Change Material Germanium Telluride for Radio-Frequency Applications: An overview », *IEEE Nanotechnol. Mag.*, vol. 16, n° 3, p. 26-41, juin 2022, doi: 10.1109/MNANO.2022.3160772.

[93] S. Raoux, « Phase Change Materials », *Annu. Rev. Mater. Res.*, vol. 39, n° 1, p. 25-48, août 2009, doi: 10.1146/annurev-matsci-082908-145405.

[94] S. Raoux et M. Wuttig, Éd., *Phase change materials: science and applications*. New York, NY: Springer, 2009.

[95] M. Wuttig et N. Yamada, « Phase-change materials for rewriteable data storage », *Nat. Mater.*, vol. 6, n° 11, p. 824-832, nov. 2007, doi: 10.1038/nmat2009.

- [96] J. Plante et B. Lee, « Environmental Conditions for Space Flight Hardware: A Survey ». 1 janvier 2005. Consulté le: 23 juillet 2023. [En ligne]. Disponible sur: <https://ntrs.nasa.gov/citations/20060013394>
- [97] U. Russo, D. Ielmini, et A. L. Lacaita, « Analytical Modeling of Chalcogenide Crystallization for PCM Data-Retention Extrapolation », *IEEE Trans. Electron Devices*, vol. 54, n° 10, p. 2769-2777, oct. 2007, doi: 10.1109/TED.2007.904976.
- [98] M. L. Lee, K. T. Yong, C. L. Gan, L. H. Ting, S. B. Muhamad Daud, et L. P. Shi, « Crystallization and thermal stability of Sn-doped Ge<sub>2</sub>Sb<sub>2</sub>Te<sub>5</sub> phase change material », *J. Phys. Appl. Phys.*, vol. 41, n° 21, p. 215402, nov. 2008, doi: 10.1088/0022-3727/41/21/215402.
- [99] M. Rütten, M. Kaes, A. Albert, M. Wuttig, et M. Salinga, « Relation between bandgap and resistance drift in amorphous phase change materials », *Sci. Rep.*, vol. 5, n° 1, Art. n° 1, déc. 2015, doi: 10.1038/srep17362.
- [100] C. Y. Khoo *et al.*, « Impact of deposition conditions on the crystallization kinetics of amorphous GeTe films », *J. Mater. Sci.*, vol. 51, n° 4, p. 1864-1872, févr. 2016, doi: 10.1007/s10853-015-9493-z.
- [101] M. Zhu *et al.*, « N-doped Sb<sub>2</sub>Te phase change materials for higher data retention », *J. Alloys Compd.*, vol. 509, n° 41, p. 10105-10109, oct. 2011, doi: 10.1016/j.jallcom.2011.08.050.
- [102] C. Chen *et al.*, « Dielectric properties of amorphous phase-change materials », *Phys. Rev. B*, vol. 95, n° 9, p. 094111, mars 2017, doi: 10.1103/PhysRevB.95.094111.
- [103] E. Prokhorov, J. J. Gervacio-Arciniega, G. Luna-Bárceñas, Y. Kovalenko, F. J. Espinoza-Beltrán, et G. Trápaga, « Dielectric properties of Ge<sub>2</sub>Sb<sub>2</sub>Te<sub>5</sub> phase-change films », *J. Appl. Phys.*, vol. 113, n° 11, p. 113705, mars 2013, doi: 10.1063/1.4795592.
- [104] F. Kadlec, C. Kadlec, et P. Kužel, « Contrast in terahertz conductivity of phase-change materials », *Solid State Commun.*, vol. 152, n° 10, p. 852-855, mai 2012, doi: 10.1016/j.ssc.2012.02.018.
- [105] V. Bovtun *et al.*, « Microwave characterization of dielectric substrates for thin films deposition », in *2013 IEEE XXXIII International Scientific Conference Electronics and Nanotechnology (ELNANO)*, avr. 2013, p. 17-20. doi: 10.1109/ELNANO.2013.6552081.
- [106] C. D. Easton, M. V. Jacob, et J. Krupka, « Non-destructive complex permittivity measurement of low permittivity thin film materials », *Meas. Sci. Technol.*, vol. 18, n° 9, p. 2869-2877, juill. 2007, doi: 10.1088/0957-0233/18/9/016.
- [107] U. C. Hasar, « Determination of Complex Permittivity of Low-Loss Samples From Position-Invariant Transmission and Shorted-Reflection Measurements », *IEEE Trans. Microw. Theory Tech.*, vol. 66, n° 2, p. 1090-1098, févr. 2018, doi: 10.1109/TMTT.2017.2772864.
- [108] U. C. Hasar, Y. Kaya, J. J. Barroso, et M. Ertugrul, « Determination of Reference-Plane Invariant, Thickness-Independent, and Broadband Constitutive Parameters of Thin Materials », *IEEE Trans. Microw. Theory Tech.*, vol. 63, n° 7, p. 2313-2321, juill. 2015, doi: 10.1109/TMTT.2015.2431685.
- [109] V. Laur *et al.*, « Wide-Band Characterization of Ferroelectric Thin-Films: Applications to KTN-based Microwave Agile Devices », in *2006 European Microwave Conference*, sept. 2006, p. 929-932. doi: 10.1109/EUMC.2006.281073.

- [110] T. Itoh, « Spectral Domain Immitance Approach for Dispersion Characteristics of Generalized Printed Transmission Lines », *IEEE Trans. Microw. Theory Tech.*, vol. 28, n° 7, p. 733-736, juill. 1980, doi: 10.1109/TMTT.1980.1130158.
- [111] R. B. Marks, « A multiline method of network analyzer calibration », *IEEE Trans. Microw. Theory Tech.*, vol. 39, n° 7, p. 1205-1215, juill. 1991, doi: 10.1109/22.85388.
- [112] H. Baudrand, « Representation by Equivalent circuit of the Integral methods in Microwave passive elements », in *1990 20th European Microwave Conference*, sept. 1990, p. 1359-1364. doi: 10.1109/EUMA.1990.336256.
- [113] F. Bouzidi, H. Aubert, D. Bajon, et H. Baudrand, « Equivalent network representation of boundary conditions involving generalized trial quantities-application to lossy transmission lines with finite metallization thickness », *IEEE Trans. Microw. Theory Tech.*, vol. 45, n° 6, p. 869-876, juin 1997, doi: 10.1109/22.588594.
- [114] Y. Morimoto, T. Motegi, W. Kasai, et K. Niwano, « Transmission Line Loss Properties of Dielectric Loss Tangent and Conductive Surface Roughness in 5G Millimeter Wave Band », in *2020 IEEE Asia-Pacific Microwave Conference (APMC)*, déc. 2020, p. 776-778. doi: 10.1109/APMC47863.2020.9331571.
- [115] X. Guo, D. R. Jackson, et J. Chen, « An analysis of copper surface roughness effects on signal propagation in PCB traces », in *2013 Texas Symposium on Wireless and Microwave Circuits and Systems (WMCS)*, avr. 2013, p. 1-4. doi: 10.1109/WMCaS.2013.6563552.
- [116] C.-Y. Lee, Y. Liu, et T. Itoh, « The effects of the coupled slotline mode and air-bridges on CPW and NLC waveguide discontinuities », *IEEE Trans. Microw. Theory Tech.*, vol. 43, n° 12, p. 2759-2765, déc. 1995, doi: 10.1109/22.475632.
- [117] Abraham. Savitzky et M. J. E. Golay, « Smoothing and Differentiation of Data by Simplified Least Squares Procedures. », *Anal. Chem.*, vol. 36, n° 8, p. 1627-1639, juill. 1964, doi: 10.1021/ac60214a047.
- [118] W. Gawelda, J. Siegel, C. N. Afonso, V. Plausinaitiene, A. Abrutis, et C. Wiemer, « Dynamics of laser-induced phase switching in GeTe films », *J. Appl. Phys.*, vol. 109, n° 12, p. 123102, juin 2011, doi: 10.1063/1.3596562.
- [119] J. Siegel, A. Schropp, J. Solis, C. N. Afonso, et M. Wuttig, « Rewritable phase-change optical recording in Ge<sub>2</sub>Sb<sub>2</sub>Te<sub>5</sub> films induced by picosecond laser pulses », *Appl. Phys. Lett.*, vol. 84, n° 13, p. 2250-2252, mars 2004, doi: 10.1063/1.1689756.
- [120] A.-K. U. Michel, P. Zalden, D. N. Chigrin, M. Wuttig, A. M. Lindenberg, et T. Taubner, « Reversible Optical Switching of Infrared Antenna Resonances with Ultrathin Phase-Change Layers Using Femtosecond Laser Pulses », *ACS Photonics*, vol. 1, n° 9, p. 833-839, sept. 2014, doi: 10.1021/ph500121d.
- [121] M. Pinaud, G. Humbert, S. Engelbrecht, L. Merlat, B. M. Fischer, et A. Crunteanu, « Terahertz Devices Using the Optical Activation of GeTe Phase Change Materials: Toward Fully Reconfigurable Functionalities », *ACS Photonics*, vol. 8, n° 11, p. 3272-3281, nov. 2021, doi: 10.1021/acsp Photonics.1c01086.
- [122] Deepti, D. Gangwar, S. Singh, A. Sharma, et M. R. Tripathy, « Design of Terahertz PCM and its Application in Polarisation Conversion and RCS Reduction », in *2021 IEEE Indian Conference on Antennas and Propagation (InCAP)*, déc. 2021, p. 863-866. doi: 10.1109/InCAP52216.2021.9726453.

- [123] Y. Gutiérrez *et al.*, « Characterizing optical phase-change materials with spectroscopic ellipsometry and polarimetry », *Thin Solid Films*, vol. 763, p. 139580, déc. 2022, doi: 10.1016/j.tsf.2022.139580.
- [124] S. Yamanaka, S. Ogawa, I. Morimoto, et Y. Ueshima, « Electronic Structures and Optical Properties of GeTe and Ge<sub>2</sub>Sb<sub>2</sub>Te<sub>5</sub> », *Jpn. J. Appl. Phys.*, vol. 37, n° 6R, p. 3327, juin 1998, doi: 10.1143/JJAP.37.3327.
- [125] H. Tompkins et E. A. Irene, *Handbook of Ellipsometry*. William Andrew, 2005.
- [126] R. Castanet et C. Bergman, « Capacité calorifique du composé Ge<sub>0,5</sub>Te<sub>0,5</sub> à l'état liquide et solide », *J. Common Met.*, vol. 68, n° 2, p. 119-124, déc. 1979, doi: 10.1016/0022-5088(79)90047-X.
- [127] R. K. Quinn et R. T. Johnson, « Thermally-induced structural and electrical effects in Ge-Te-based amorphous alloys », *J. Non-Cryst. Solids*, vol. 12, n° 2, p. 213-231, juill. 1973, doi: 10.1016/0022-3093(73)90071-9.
- [128] G. Langer, J. Hartmann, et M. Reichling, « Thermal conductivity of thin metallic films measured by photothermal profile analysis », *Rev. Sci. Instrum.*, vol. 68, n° 3, p. 1510-1513, mars 1997, doi: 10.1063/1.1147638.
- [129] R. E. Collin, *Field theory of guided waves*, 2nd ed. New York: IEEE Press, 1991.
- [130] C. A. Balanis, *Balanis' advanced engineering electromagnetics*, Third edition. Hoboken, New Jersey: John Wiley & Sons, 2024.
- [131] I. Rana et N. Alexopoulos, « Current distribution and input impedance of printed dipoles », *IEEE Trans. Antennas Propag.*, vol. 29, n° 1, p. 99-105, janv. 1981, doi: 10.1109/TAP.1981.1142536.
- [132] N. Alexopoulos et I. Rana, « Mutual impedance computation between printed dipoles », *IEEE Trans. Antennas Propag.*, vol. 29, n° 1, p. 106-111, janv. 1981, doi: 10.1109/TAP.1981.1142531.
- [133] Y.-M. Zhang, X. Li, et S.-Q. Xiao, « A Simple Decoupling Method for Millimeter-Wave Aperture-Coupled Patch Antenna Arrays », in *2023 International Workshop on Antenna Technology (iWAT)*, Aalborg, Denmark: IEEE, mai 2023, p. 1-3. doi: 10.1109/iWAT57058.2023.10171657.
- [134] D. B. Petkova, T. S. Tsekov, et P. Z. Petkov, « Application of Electromagnetic Bandgap Structures for Mutual Coupling Reduction in Microstrip Antenna Arrays », in *2023 58th International Scientific Conference on Information, Communication and Energy Systems and Technologies (ICEST)*, Nis, Serbia: IEEE, juin 2023, p. 73-76. doi: 10.1109/ICEST58410.2023.10187394.
- [135] R. Mishra, S. M. S., et A. R. Harish, « Mutual coupling mitigation and bandwidth enhancement in 2x1 array using feed point modification and metamaterial superstrate », in *2023 First International Conference on Microwave, Antenna and Communication (MAC)*, Prayagraj, India: IEEE, mars 2023, p. 1-5. doi: 10.1109/MAC58191.2023.10177120.
- [136] I. J. Bahl et P. Bhartia, *Microstrip antennas*. in The Artech House microwave library. Dedham, Mass: Artech House, 1980.

- [137] J. Svacina, « Analysis of multilayer microstrip lines by a conformal mapping method », *IEEE Trans. Microw. Theory Tech.*, vol. 40, n° 4, p. 769-772, avr. 1992, doi: 10.1109/22.127530.
- [138] J. R. James et P. S. Hall, Éd., *Handbook of Microstrip Antennas, Volume 1*. Institution of Engineering and Technology, 1989. doi: 10.1049/PBEW028F.
- [139] L. Bottou, « Large-Scale Machine Learning with Stochastic Gradient Descent », in *Proceedings of COMPSTAT'2010*, Y. Lechevallier et G. Saporta, Éd., Heidelberg: Physica-Verlag HD, 2010, p. 177-186. doi: 10.1007/978-3-7908-2604-3\_16.
- [140] P. Netrapalli, « Stochastic Gradient Descent and Its Variants in Machine Learning », *J. Indian Inst. Sci.*, vol. 99, n° 2, p. 201-213, juin 2019, doi: 10.1007/s41745-019-0098-4.
- [141] M. J. Kochenderfer et T. A. Wheeler, *Algorithms for optimization*. Cambridge: The MIT press, 2019.
- [142] « What is Gradient Descent? | IBM ». Consulté le: 10 mars 2024. [En ligne]. Disponible sur: <https://www.ibm.com/topics/gradient-descent>
- [143] Z. Zhu, A. Li, et Y. Wang, « Study on two-stage fractional order gradient descend method », in *2021 40th Chinese Control Conference (CCC)*, Shanghai, China: IEEE, juill. 2021, p. 7960-7964. doi: 10.23919/CCC52363.2021.9549324.
- [144] R. Hooke et T. A. Jeeves, « `` Direct Search'' Solution of Numerical and Statistical Problems », *J. ACM*, vol. 8, n° 2, p. 212-229, avr. 1961, doi: 10.1145/321062.321069.
- [145] M. J. D. Powell, « An efficient method for finding the minimum of a function of several variables without calculating derivatives », *Comput. J.*, vol. 7, n° 2, p. 155-162, févr. 1964, doi: 10.1093/comjnl/7.2.155.
- [146] V. Torczon, « On the Convergence of Pattern Search Algorithms », *SIAM J. Optim.*, vol. 7, n° 1, p. 1-25, févr. 1997, doi: 10.1137/S1052623493250780.
- [147] F. Enache, F. Popescu, D. Deapareanu, A. Enache, et T. Oroian, « Multi-criteria optimization of non-uniform linear antenna array using genetic algorithms », in *2016 International Conference on Communications (COMM)*, Bucharest, Romania: IEEE, juin 2016, p. 121-124. doi: 10.1109/ICComm.2016.7528328.
- [148] D. Mandal, S. K. Ghoshal, S. Das, S. Bhattacharjee, et A. K. Bhattacharjee, « Improvement of Radiation Pattern for Linear Antenna Arrays Using Genetic Algorithm », in *2010 International Conference on Recent Trends in Information, Telecommunication and Computing*, Kochi, Kerala: IEEE, mars 2010, p. 126-129. doi: 10.1109/ITC.2010.17.
- [149] T.-Y. Han et L.-Y. Tseng, « Design of a Broad/Dual-Band Circularly Polarized Square Slot Antenna Using Genetic Local Search Algorithms », in *2009 WRI World Congress on Computer Science and Information Engineering*, Los Angeles, California USA: IEEE, 2009, p. 77-80. doi: 10.1109/CSIE.2009.533.
- [150] D. Zhou, S. Gao, R. A. Abd-Alhameed, C. Zhang, M. S. Alkhambashi, et J. D. Xu, « Design and optimisation of compact hybrid quadrifilar helical-spiral antenna in GPS applications using Genetic Algorithm », in *2012 6th European Conference on Antennas and Propagation (EuCAP)*, Prague, Czech Republic: IEEE, mars 2012, p. 1-4. doi: 10.1109/EuCAP.2012.6206315.

- [151] K. Deep, K. P. Singh, M. L. Kansal, et C. Mohan, « A real coded genetic algorithm for solving integer and mixed integer optimization problems », *Appl. Math. Comput.*, vol. 212, n° 2, p. 505-518, juin 2009, doi: 10.1016/j.amc.2009.02.044.
- [152] R. L. Haupt, « Optimum population size and mutation rate for a simple real genetic algorithm that optimizes array factors », in *IEEE Antennas and Propagation Society International Symposium. Transmitting Waves of Progress to the Next Millennium. 2000 Digest. Held in conjunction with: USNC/URSI National Radio Science Meeting (Cat. No.00CH37118)*, Salt Lake City, UT, USA: IEEE, 2000, p. 1034-1037. doi: 10.1109/APS.2000.875398.
- [153] J. T. Alander, « On optimal population size of genetic algorithms », in *CompEuro 1992 Proceedings Computer Systems and Software Engineering*, The Hague, Netherlands: IEEE Comput. Soc. Press, 1992, p. 65-70. doi: 10.1109/CMPEUR.1992.218485.
- [154] S. Gotshall et B. Rylander, « Optimal Population Size and the Genetic Algorithm ».
- [155] D. M. Pozar, *Microwave engineering*, 4th ed. Hoboken, NJ: Wiley, 2012.
- [156] « Flacon d'Application d'Adhésif Optique Norland, NOA 83H, 1 once ». Consulté le: 10 mars 2024. [En ligne]. Disponible sur: <https://www.edmundoptics.fr/p/1-oz-application-bottle-of-noa-83h/12431/>
- [157] « ROHACELL® A - Evonik Industries ». Consulté le: 10 mars 2024. [En ligne]. Disponible sur: <https://performance-foams.evonik.com/en/products-and-solutions/rohacell/rohacell-a-170034.html>
- [158] G. Gold et K. Helmreich, « A Physical Surface Roughness Model and Its Applications », *IEEE Trans. Microw. Theory Tech.*, vol. 65, n° 10, p. 3720-3732, oct. 2017, doi: 10.1109/TMTT.2017.2695192.
- [159] S. Laybras et P. F. Combes, « On radiating-zone boundaries of short,  $\lambda/2$ , and  $\lambda$  dipoles », *IEEE Antennas Propag. Mag.*, vol. 46, n° 5, p. 53-65, oct. 2004, doi: 10.1109/MAP.2004.1388826.
- [160] S. Fisahn, H. D. Pham, S. Sandmann, H. Garbe, et S. Koj, « Far Field Region of Radiated Emissions from Wind Energy Conversion Systems », in *2019 International Symposium on Electromagnetic Compatibility - EMC EUROPE*, sept. 2019, p. 450-455. doi: 10.1109/EMCEurope.2019.8872081.
- [161] Y. Rahmat-Samii, L. I. Williams, et R. G. Yaccarino, « The UCLA bi-polar planar-near-field antenna-measurement and diagnostics range », *IEEE Antennas Propag. Mag.*, vol. 37, n° 6, p. 16-35, déc. 1995, doi: 10.1109/74.482029.

## Radiation pattern reconfigurable antennas based on Phase Change Materials (PCM) integration

Ce travail porte sur l'étude, la caractérisation et activation optique de couches minces de matériaux à changement de phase (PCM) pour leur intégration dans des dispositifs reconfigurables haute fréquence, notamment des systèmes antennaires. Le principe de reconfiguration est obtenu en exploitant le contraste élevé de résistivité des PCMs entre son état amorphe (forte résistivité) et son état cristallin (faible résistivité). Ce changement d'état est non volatil et réversible et est obtenu par une courte impulsion laser. Les propriétés électromagnétiques du PCM ont également été caractérisées dans la bande des fréquences d'ondes millimétriques (environ 30 GHz) et utilisées pour la conception et la simulation précise d'un réseau d'antennes multi-reconfigurables (en état de polarisation et en fréquence de fonctionnement) fonctionnant à des fréquences autour de 30 GHz.

---

Mots-clés : Matériaux à changement de phase, réseau d'antennes, caractérisation électromagnétique, fréquences d'ondes millimétriques.

## Radiation pattern reconfigurable antennas based on Phase Change Materials (PCM) integration

This work focuses on the study, characterization and optical activation of thin films of phase change materials (PCM) for their integration in high-frequency reconfigurable devices, in particular antenna systems. The principle of reconfiguration is achieved by exploiting the high contrast in resistivity of PCMs between its amorphous state (high resistivity) and crystalline state (low resistivity). This change of state is non-volatile and reversible and is achieved by a short laser pulse. The electromagnetic properties of PCMs were also characterized in the millimeter-wave band frequency (around 30 GHz) and used for the design and accurate simulation of a multi-reconfigurable (in polarization state and operational frequency) array of antennas working at frequencies around 30 GHz.

---

Keywords: Phase change materials, array of antennas, electromagnetic characterization, millimeter-wave frequencies.